Title
Investigations of the Electrochemical Reduction of Carbon Dioxide

Author
Clark, Ezra Lee

Publication Date
2018

Peer reviewed|Thesis/dissertation

Investigations of the Electrochemical Reduction of Carbon Dioxide

By

Ezra L. Clark

A dissertation submitted in partial satisfaction of the

requirements for the degree of

Doctor of Philosophy

in

Chemical Engineering

in the

Graduate Division

of the

University of California, Berkeley

Committee in charge:

Professor Alexis T. Bell, Chair

Professor Bryan D. McCloskey

Professor Fiona M. Doyle

Summer 2018

Investigations of the Electrochemical Reduction of Carbon Dioxide

By

Ezra L. Clark

Abstract

Investigations of the Electrochemical Reduction of Carbon Dioxide

By

Ezra L. Clark

Doctor of Philosophy in Chemical Engineering

University of California, Berkeley

Professor Alexis T. Bell, Chair

The electrochemical reduction of CO_2 offers a potential means for producing carbon-neutral fuels and chemicals. Cu is the most effective contemporary electrocatalyst for reducing CO_2 to products such as methane, ethene, and ethanol. Unfortunately, the current efficiency of the process is limited by competition with the relatively facile H_2 evolution reaction. Thus, there is considerable interest in identifying ways to modify Cu that will suppress the evolution of H_2 and enhance the selectivity to desired products. Accomplishing this goal has proven difficult, partially because objective evaluation of CO_2 reduction electrocatalysts has been convoluted by a lack of standardized methods for measuring and reporting activity data. Furthermore, the electrochemical reduction of CO_2 is sensitive to electrolyte polarization, which is characterized by the formation of gradients in both pH and the concentration of CO_2 near the cathode surface. Since the intrinsic kinetics of CO_2 reduction depend on the composition of the local reaction environment it is desirable to measure the concentration of reaction-relevant species in the immediate vicinity of the cathode. However, meeting this objective has proven difficult since conventional analytical methods only sample species from the bulk electrolyte.

In the first study, we identify extraneous variables that influence the measured activity of CO_2 reduction electrocatalysts and propose procedures to improve the accuracy and precision of reported data. We demonstrate that when these proposed procedures are followed that the activity of Ag and Cu electrocatalysts prepared and tested in different laboratories exhibit little variation. We advocate that standardizing the experimental methods for measuring the activity of CO_2 reduction electrocatalysts will greatly facilitate the search for electrocatalysts with superior activity and selectivity.

In the second study, we investigate the impact of surface atomic structure on the CO evolution activity of Ag by conducting CO_2 reduction over Ag(111), Ag(100), and Ag(110) thin films. We directly observe the surface atomic structure of these Ag thin films under electrochemical conditions by conducting in-situ electrochemical scanning tunneling microscopy, which enables atom resolved images to be acquired under an applied potential. We find that the CO_2 reduction activity of the corrugated Ag(110) surface is roughly an order of magnitude higher than either Ag(111) or Ag(100). We have determined that these activity trends are caused by variations in the local electric field

strength, which stabilizes the polarizable intermediates of CO_2 reduction. The strength of these local electric fields is enhanced over undercoordinated surface atoms due to their elevated surface charge density when polarized to a given potential.

In the third study, we report a novel differential electrochemical mass spectrometer (DEMS) cell design that enables the partial current densities of volatile CO_2 reduction products to be quantified in real time. The capabilities of the novel DEMS cell are demonstrated by conducting CO_2 reduction over polycrystalline Cu. The reaction products are quantified in real time as a function of the applied potential during linear sweep voltammetry, demonstrating that the technique can determine the product distribution produced over a given electrocatalyst as a function of the applied potential on the timescale of roughly one hour.

In the fourth study, we utilize DEMS to measure the concentration of CO_2 and reaction products in the immediate vicinity of the cathode surface. This capability is achieved by coating the electrocatalyst directly onto the pervaporation membrane used to transfer volatile species into the mass spectrometer, thereby enabling these species to be sampled directly from the electrode-electrolyte interface. Using this approach, we observe the depletion of CO_2 within the local reaction environment due to reaction with hydroxide anions evolved from the cathode, providing insights into the detrimental effects of concentration polarization on the performance of CO_2 reduction electrocatalysts. Furthermore, we observe an abundance of aldehydes relative to alcohols within the local reaction environment over Cu, supporting their hypothesized role as intermediate reaction products in the mechanism of alcohol formation.

In the fifth study, we investigate CO_2 reduction over CuAg bimetallic electrodes and surface alloys, which we have found to be more selective for the formation of multi-carbon products than pure Cu. This selectivity enhancement is a result of the selective suppression of H_2 evolution, which occurs due to compressive strain induced by the incorporation of relatively large Ag atoms into the Cu surface. Furthermore, we report that these bimetallic electrocatalysts exhibit an unusually high selectivity for the formation of multi-carbon carbonyl-containing products, which we hypothesize to be the consequence of a reduced coverage of adsorbed H and the reduced oxophilicity of the compressively strained Cu.

Overall, these studies demonstrate that the activity and selectivity of CO_2 reduction electrocatalysts can be tuned by modifying both the surface atomic structure and elemental composition of the electrocatalyst. Furthermore, they demonstrate that the composition of the electrolyte near the cathode surface varies substantially from the bulk and contains a substantial concentration of transient reaction products that are typically reduced further.

To my family and friends that have supported me on this journey.

Table of Contents

Acknowledgements

I would like to acknowledge my graduate research advisor, Professor Alexis T. Bell, first and foremost. Alex has made untold contributions to my development as a scientist over the past 6 years. He has given me both the freedom to explore my scientific curiosities as well as the guidance to turn them into definitive scientific investigations. Through his example I learned how to dissect complex problems into clearly defined questions that can be approached creatively with first principles. His energy and sharp mind never cease to impress me.

I would also like to acknowledge my undergraduate research advisor, Professor Mahendra K. Sunkara. Mahendra not only provided me with an early outlet for my scientific curiosities but also encouraged me to continue exploring them in graduate school. He was willing to give me the opportunity to contribute to world-class science early in my academic career and taught me the values of fundamental science and entrepreneurship.

I would also like to acknowledge all of my colleagues and collaborators that I have had the pleasure of working with since embarking on this academic journey. Our discussions and comradery have contributed immensely to my professional development. Specifically, I would like to acknowledge Professor Praveen Meduri, Dr. Chandrashekar Pendyala, Dr. Jacek Jasinski, Dr. Vivekanand Kumar, Jeong-Hoon Kim, and Franz G. Petzold from the University of Louisville. Furthermore, I would like to acknowledge Professor Meenesh Singh, Professor Mu-Jeng Cheng, Dr. Joaquin Resasco, Dr. Youngkook Kwon, Dr. Peter Lobacarro, Dr. Yanwei Lum, and Dr. Alejandro Garza from the University of California at Berkeley. Additionally, I would like to acknowledge Professor Thomas F. Jaramillo, Professor Karen Chan, Dr. Christopher Hahn, Dr. Stefan Ringe, Alan Landers, John Lin, and Michael Tang from Stanford University. Finally, I would like to acknowledge Professor Manuel P. Soriaga, Dr. Youn-Geun Kim, and Dr. Jack H. Baricuatro from the California Institute of Technology.

I would also like to acknowledge the undergraduate mentees that I have had the pleasure to work with throughout graduate school. Specifically, I would like to acknowledge Jaeyoung Park, Fillary Susanto, Linh Thao-Chung, and Amber Walton. I sincerely appreciate your patience with me as I learned how to serve as an effective mentor. I hope that each of you finds success and fulfillment in your future career.

I would also like to thank my friends, who have provided me with many good memories. Specifically, I would like to acknowledge John David Baumgarten, Garrett Tuggle, Dr. Jason Absher, and Dr. Alejandro Martinez-Garcia from Louisville. Furthermore, I would like to acknowledge Dr. Joaquin Resasco, Professor Cory Simon, Dr. John Stevens, Dr. Rishi Ganeriwala, and Dr. David Rolfe from Berkeley.

I would also like to acknowledge Ariel Kuhn for making graduate school more than just an accomplishment. I look forward to watching your scientific metamorphosis over the next few years, as you have watched mine.

Finally, I would like to acknowledge my family. My father, Jimmy Clark, and my mother, Roxanne Clark, instilled me with a desire to make the world a better place from a young age. Their lesson of compassion for all creatures will surely keep me on the right path for years to come. I would also like to acknowledge my brother, Jordan Clark, who has taught me that perseverance is the only way to make daunting dreams a reality. Furthermore, I would like to acknowledge my grandpa, Edward Clark, and my grandma, Edna Clark, who taught me the value of higher education and hard work. Finally, I would like to acknowledge my dog, Stella, who has been looking after my family since I have been away.

Chapter 1

Introduction to the Electrochemical Reduction of Carbon Dioxide

1.1 Motivation

The extensive use of fossil fuels over the past century has led to the progressive accumulation of carbon dioxide (CO_2) in the atmosphere.[1,2] Since CO_2 is a greenhouse gas, the increase in the concentration of atmospheric CO_2 has contributed to the gradual warming of the global climate.[2] Concern over global climate change has motivated significant interest in increasing the utilization of carbon-neutral forms of energy, such as wind and solar.[3,4] Unfortunately, energy production from these renewable sources is intermittent and offset from the energy demand of modern society.[5,6] In fact, the intermittency of these renewable energy sources limits the extent to which they can currently be incorporated into the existing energy infrastructure without compromising grid stability.[6] Thus, energy storage strategies need to be developed before the utilization of renewable energy can be significantly increased.

Grid-scale electrochemical energy storage has received significant interest in recent decades.[6–8] However, electrochemical batteries currently account for a negligible quantity of the global grid-scale energy storage capacity due to their relatively low volumetric energy density, high capital costs, and low device lifetimes. Alternatively, renewable electricity can be utilized to directly synthesize potential fuels using an electrolyzer, effectively converting the electrical energy into chemical fuels. While hydrogen (H_2) is the most widely investigated target fuel of this energy storage approach,[5,9] it is not an ideal fuel due to its low volumetric energy density. Furthermore, the electrolytic synthesis of H_2 does not address the need to establish a carbon-neutral chemical industry nor the need to recycle a portion of the CO_2 already in the atmosphere, which could be accomplished via electrochemical reduction after capture and concentration. Conversely, electrochemical CO_2 reduction offers a potential means of synthesizing carbon-neutral fuels and chemicals using renewable electricity, as shown in Figure 1.1. It is advantageous to other forms of energy storage because it produces fuels that are directly compatible with our existing energy infrastructure. Furthermore, it is a potential approach to recycling the CO_2 already in the atmosphere for useful means.

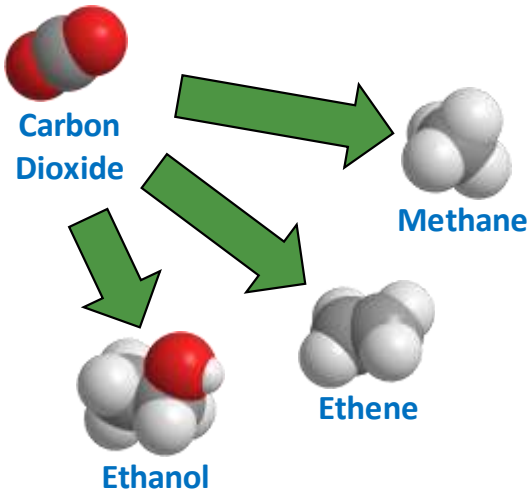

Figure 1.1 *– Useful products generated by the electrochemical reduction of carbon dioxide.*

1.2 Process Overview

Electrolyzers for CO_2 reduction consist of an anode, a cathode, and an electrolyte, as shown on Figure 1.2. Oxygen evolution (E^0 = +1.23 V vs SHE) is typically performed at the anode:[10,11]

Acid: $2H_2O \rightarrow O_2 + 4H^+ + 4e^-$

Base: $4OH^- \rightarrow O_2 + 2H_2O + 4e^-$

However, other electrochemical oxidations can also be conducted, such as chloride oxidation (E^0 = +1.36 V vs SHE) or wastewater (glucose) oxidation (E^0 = -0.01 V vs SHE):

$$2Cl^- \rightarrow Cl_2 + 2e^-$$

$$C_6H_{12}O_6 + 6H_2O \rightarrow 6CO_2 + 24H^+ + 24e^-$$

The advantage of these alternative oxidation reactions is that they either produce more economically valuable products or require less oxidizing potentials than O_2 evolution. The electrons liberated from the oxidation reaction are increased in potential using an external power supply, such as a photovoltaic device, and are utilized to reduce CO_2 at the cathode. Many different products can be produced by the reduction of CO_2:[10,11]

Acid:
$$CO_2 + H^+ + 2e^- \rightarrow HCOO^-$$
$$CO_2 + 2H^+ + 2e^- \rightarrow CO + H_2O$$
$$CO_2 + 8H^+ + 8e^- \rightarrow CH_4 + 2H_2O$$
$$2CO_2 + 12H^+ + 12e^- \rightarrow C_2H_5OH + 3H_2O$$
$$2CO_2 + 12H^+ + 12e^- \rightarrow C_2H_4 + 4H_2O$$

Base:
$$CO_2 + H_2O + 2e^- \rightarrow HCOO^- + OH^-$$
$$CO_2 + H_2O + 2e^- \rightarrow CO + 2OH^-$$
$$CO_2 + 6H_2O + 8e^- \rightarrow CH_4 + 8OH^-$$
$$2CO_2 + 9H_2O + 12e^- \rightarrow C_2H_5OH + 12OH^-$$
$$2CO_2 + 8H_2O + 12e^- \rightarrow C_2H_4 + 12OH^-$$

It should be noted that the reactants at the anode and cathode depend on the composition of the electrolyte, with protons and water serving as the direct H source for CO_2 reduction in acid and base, respectively. If O_2 and CH_4 are evolved at the anode and cathode, respectively, the overall reaction can be written as:

$$CO_2 + 2H_2O \rightarrow CH_4 + 2O_2$$

The free energy of this reaction is +800.6 kJ/mol, which corresponds to a thermodynamic voltage requirement of 1.037 V.

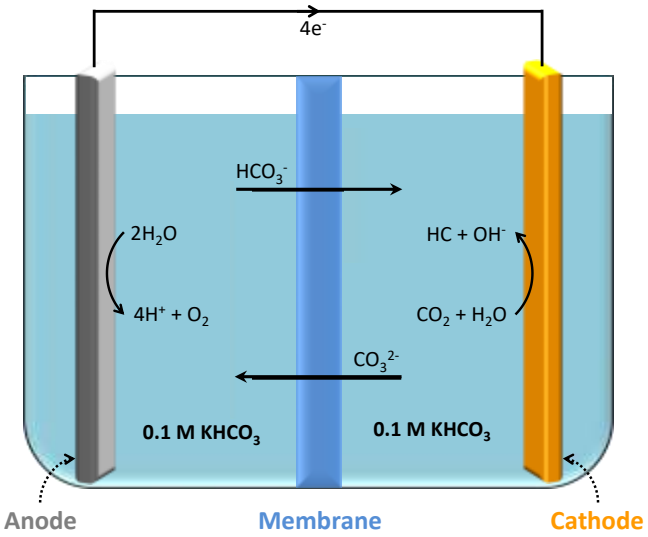

Figure 1.2 *– Schematic of a generic CO_2 reduction electrolyzer.*

The electrolyte provides a pathway for ion conduction between the electrodes. The electrolyte can be a liquid, a solid, or a combination of both. It is common practice to incorporate an ion-exchange membrane into the electrochemical cell when utilizing liquid electrolytes so that the anolyte and catholyte are physically separated into distinct zones. This prevents electrical shorting of the electrochemical cell as well as the crossover of electrochemical reaction products produced over one electrode to the oppositely charged electrode. Preventing such crossover eliminates the possibility of several parasitic side reactions, such as the oxidation of CO_2-derived products at the anode and the reduction of O_2 at the cathode.

The H required for the reduction of CO_2 must be derived from water for the process to be sustainable. As a result, conducting CO_2 reduction in aqueous electrolytes has received greater contemporary interest than conducting CO_2 reduction in nonaqueous electrolytes.[12,13] However, acidic aqueous electrolytes must be avoided to prevent the

excessive H_2 evolution that occurs when conducting CO_2 reduction in electrolytes with high proton activity.[14,15] Furthermore, alkaline electrolytes must also be avoided because dissolved CO_2 reacts with hydroxide anions to form electrochemically inert bicarbonate and carbonate anions.[16,17] Thus, aqueous CO_2 reduction must be conducted in a near-neutral electrolyte. Unfortunately, this makes these electrolyzers susceptible to concentration polarization, wherein the electrolyte composition near the electrodes deviates substantially from that found in the bulk electrolyte.[17] As a result, buffered electrolytes are utilized to suppress the magnitude of these concentration gradients, which would otherwise result in excessive Nernstian voltage loss and uncertainty in electrocatalytic activity measurements.[17–19] However, because buffers with high proton availability (low pK_a) result in excessive H_2 evolution,[20] bicarbonate anions (pK_a = 10.3) are typically utilized as the buffering media. Finally, the electrolyte concentration is generally kept low to prevent the "salting out" of dissolved CO_2.[17] Under these conditions, bicarbonate anions have been identified as the primary charge carrier in the electrolyte.[17]

1.3 Challenges

1.3.1 Reaction Selectivity

The electrochemical reduction of CO_2 must compete with the relatively facile H_2 evolution reaction:[10,11]

Acid: $2H^+ + 2e^- \rightarrow H_2$

Base: $2H_2O + 2e^- \rightarrow H_2 + 2OH^-$

As a result, electrocatalysts that are selective for CO_2 reduction must be inactive for H_2 evolution to minimize the fraction of current lost to this parasitic side reaction. Unfortunately, most transition metals are too active for H_2 evolution to be highly selective electrocatalysts for CO_2 reduction.[21,22] However, late transition and p-block metals have exceptionally low H binding energies, which makes them among the worst electrocatalysts for H_2 evolution.[23] As a result, most contemporary studies of CO_2 reduction have investigated electrocatalysts consisting of these elements.

The coinage metals exhibit exceptional selectivity for the evolution of CO while the p-block metals are selective for the evolution of $HCOO^-$, as shown in Figure 1.3.[21,22] Cu is the only monometallic electrocatalyst that exhibits high selectivity for the production of hydrocarbons and alcohols,[21,22] which are derived from a CO intermediate.[10,24–28] Unfortunately, Cu does not evolve a single reaction product during CO_2 reduction selectively. Instead, Cu produces a mixture of up to 16 different reaction products at any given potential.[10,11] Furthermore, Cu evolves excessive quantities of H_2 during CO_2 reduction, with a typical H_2 Faradaic efficiency of 30%.[10,11] Thus, there is contemporary interest in discovering methods of suppressing H_2 evolution and enhancing the selectivity to the desired products obtained over Cu. Current strategies for modifying the selectivity observed over Cu include modulating the applied potential,[10,11,29] surface morphology,[30–34] cation identity,[35–38] and buffer concentration.[20,39–41] Unfortunately, these strategies

have only yielded marginal improvements in reaction selectivity. While alloying is another means for tuning the product distribution,[42] no multi-metallic electrocatalyst has been discovered with a multi-carbon product selectivity superior to pure Cu.[43–46] The lack of a validated mechanism by which CO_2 is reduced to hydrocarbons and alcohols over Cu has hindered the search for superior electrocatalysts. Thus, elucidating these mechanisms is a contemporary goal of researchers seeking to conduct rational electrocatalyst development for CO_2 reduction.

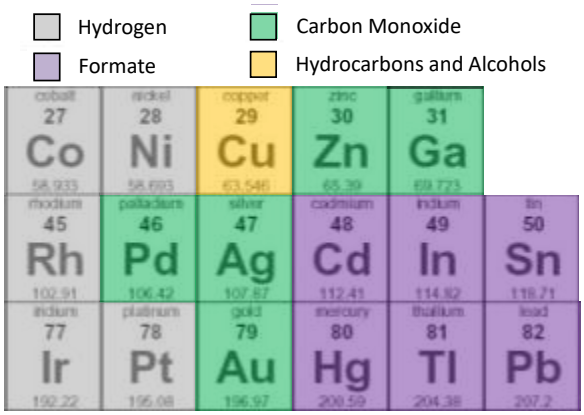

Figure 1.3 *– Reaction selectivity observed over the late transition and p-block metals during CO_2 reduction.*

1.3.2 Electrocatalyst Activity

CO_2 reduction requires roughly the same applied potential as H_2 evolution thermodynamically. However, in practice overpotentials of roughly 1 V are required to produce hydrocarbons and alcohols over Cu. This excessive overpotential requirement results in low cathodic energy conversion efficiency and is one of the primary factors preventing commercial implementation of the technology. Thus, a primary goal of contemporary CO_2 reduction studies is improving electrocatalytic activity. Unfortunately, it is currently difficult to establish electrocatalyst design principles based on data in the published literature because each research group has its own method of analyzing and reporting activity data. Without the ability to accurately compare the activity of electrocatalysts reported in the literature it is difficult to establish electrocatalyst design principles that result in improved activity for CO_2 reduction. There is a need to standardize these research practices so that accurate activity comparisons can be made between research groups. Only then can fair comparisons between electrocatalysts reported in the literature be made and electrocatalyst design principles established.

1.4 Outline

In Chapter 2 we present a series of suggestions for standardizing electrocatalytic activity measurements and data reporting for studies of CO_2 reduction. Furthermore, we identify several previously unrecognized extraneous variables that significantly influence the measured activity of CO_2 reduction electrocatalysts. In Chapter 3 we report our investigation of CO_2 reduction over Ag(111), Ag(100), and Ag(110) thin films, which we

have utilized to study the impact of surface atomic structure on the CO evolution activity of Ag electrocatalysts. We observe that step sites exhibit nearly an order of magnitude higher CO evolution activity than the basal planes. This superior activity is attributed to stronger local electric fields near undercoordinated surface atoms, which stabilize the activation of CO_2. In Chapter 4 we present a novel cell design for differential electrochemical mass spectrometry (DEMS) that enables the product distribution produced by an electrocatalysts during CO_2 reduction to be probed in real time. In Chapter 5 we present another DEMS cell design that enables the composition of the local reaction environment to be probed in real time. Using this approach, we have observed the reaction of CO_2 with hydroxide anions evolved over Ag and an abundance of aldehydes within the local reaction environment over Cu. These observations provide insights into both the detrimental effects of concentration polarization as well as the role of aldehydes as transient reaction products in the mechanism of alcohol formation over Cu. Finally, in Chapter 6 we report our investigation of CO_2 reduction over Cu+Ag surface alloys, which we have found to be less active for H_2 evolution and more selective for the formation of multi-carbon oxygenated products than pure Cu. The reduced activity for H_2 evolution is a result of compressive strain introduced by the incorporation of relatively large Ag atoms into the Cu surface, which selectively weakens the H adsorption energy. The enhanced oxygenate selectivity is a result of the reduced H_2 evolution activity and the reduced oxophilicity of the compressively strained Cu.

1.5 References

(1) Falkowski, P.; Scholes, R. J.; Boyle, E.; Canadell, J.; Canfield, D.; Elser, J.; Gruber, N.; Hibbard, K.; Hogberg, P.; Linder, S.; et al. The Global Carbon Cycle: A Test of Our Knowledge of Earth as a System. *Science (80-.).* **2000**, *290* (5490), 291–296.

(2) Davis, S. J.; Caldeira, K.; Matthews, H. D. Future CO2 Emissions and Climate Change from Existing Energy Infrastructure. *Science (80-.).* **2010**, *329* (5997), 1330–1333.

(3) Pacala, S.; Socolow, R. Stabilization Wedges: Solving the Climate Problem for the next 50 Years with Current Technologies. *Science (80-.).* **2004**, *305* (5686), 968–972.

(4) Chu, S.; Majumdar, A. Opportunities and Challenges for a Sustainable Energy Future. *Nature* **2012**, *488* (7411), 294–303.

(5) Cook, T. R.; Dogutan, D. K.; Reece, S. Y.; Surendranath, Y.; Teets, T. S.; Nocera, D. G. Solar Energy Supply and Storage for the Legacy and Non Legacy Worlds. *Chem. Rev.* **2010**, *110* (11), 6474–6502.

(6) Yang, Z.; Zhang, J.; Kintner-Meyer, M. C. W.; Lu, X.; Choi, D.; Lemmon, J. P.; Liu, J. Electrochemical Energy Storage for Green Grid. *Chem. Rev.* **2011**, *111* (5), 3577–3613.

(7) Chen, H.; Cong, T. N.; Yang, W.; Tan, C.; Li, Y.; Ding, Y. Progress in Electrical Energy Storage System: A Critical Review. *Prog. Nat. Sci.* **2009**, *19* (3), 291–312.

(8) Gu, S.; Xu, B.; Yan, Y. Electrochemical Energy Engineering: A New Frontier of Chemical Engineering Innovation. *Annu. Rev. Chem. Biomol. Eng.* **2014**, *5* (1), 429–454.

(9) Turner, J.; Sverdrup, G.; Mann, M. K.; Maness, P.-C.; Kroposki, B.; Maria, G.; Evans, R. J.; Blake, D. Renewable Hydrogen Production. *Int. J. Energy Res.* **2007**, *32*, 379–407.

(10) Hori, Y.; Murata, A.; Takahashi, R. Formation of Hydrocarbons in the Electrochemical Reduction of Carbon Dioxide at a Copper Electrode in Aqueous Solution. *J. Chem. Soc. Faraday Trans. I* **1989**, *85* (8), 2309–2326.

(11) Kuhl, K. P.; Cave, E. R.; Abram, D. N.; Jaramillo, T. F. New Insights into the Electrochemical Reduction of Carbon Dioxide on Metallic Copper Surfaces. *Energy*

Environ. Sci. **2012**, *5* (5), 7050–7059.
(12) Gattrell, M.; Gupta, N.; Co, A. A Review of the Aqueous Electrochemical Reduction of CO2 to Hydrocarbons at Copper. *J. Electroanal. Chem.* **2006**, *594* (1), 1–19.
(13) Hori, Y. Electrochemical CO2 Reduction on Metal Electrodes. In *Modern Aspects of Electrochemistry*; Vayenas, C. G., White, R. E., Gamboa-Aldeco, M. E., Eds.; Springer: New York, 2008; pp 89–189.
(14) Durst, J.; Siebel, A.; Simon, C.; Hasché, F.; Herranz, J.; Gasteiger, H. A. New Insights into the Electrochemical Hydrogen Oxidation and Evolution Reaction Mechanism. *Energy Environ. Sci.* **2014**, *7* (7), 2255–2260.
(15) Sheng, W.; Zhuang, Z.; Gao, M.; Zheng, J.; Chen, J. G.; Yan, Y. Correlating Hydrogen Oxidation and Evolution Activity on Platinum at Different pH with Measured Hydrogen Binding Energy. *Nat. Commun.* **2015**, *6*, 1–6.
(16) Gupta, N.; Gattrell, M.; MacDougall, B. Calculation for the Cathode Surface Concentrations in the Electrochemical Reduction of CO2 in KHCO3 Solutions. *J. Appl. Electrochem.* **2006**, *36* (2), 161–172.
(17) Singh, M. R.; Clark, E. L.; Bell, A. T. Effects of Electrolyte, Catalyst, and Membrane Composition and Operating Conditions on the Performance of Solar-Driven Electrochemical Reduction of Carbon Dioxide. *Phys. Chem. Chem. Phys.* **2015**, *17* (29), 18924–18936.
(18) Dunwell, M.; Yang, X.; Setzler, B. P.; Anibal, J.; Yan, Y.; Xu, B. Examination of Near-Electrode Concentration Gradients and Kinetic Impacts on the Electrochemical Reduction of CO_2 Using Surface-Enhanced Infrared Spectroscopy. *ACS Catal.* **2018**, 3999–4008.
(19) Clark, E. L.; Resasco, J.; Landers, A.; Lin, J.; Chung, L.-T.; Walton, A.; Hahn, C.; Jaramillo, T. F.; Bell, A. T. Data Acquisition Protocols and Reporting Standards for Studies of the Electrochemical Reduction of Carbon Dioxide. *ACS Catal.* **2018**, *8*, 6560–6570.
(20) Resasco, J.; Lum, Y.; Clark, E. L.; Zeledon, J.; Bell, A. T. Effects of Anion Identity and Concentration on the Electrochemical Reduction of CO2. *ChemElectroChem* **2018**, *5*, 1–10.
(21) Hori, Y.; Kikuchi, K.; Suzuki, S. Production of CO and CH4 in Electrochemical Reduction of CO2 at Metal Electrodes in Aqueous Hydrogencarbonate Solution. *Chem. Lett.* **1985**, *14* (11), 1695–1698.
(22) Noda, H.; Ikeda, S.; Oda, Y.; Imai, K.; Maeda, M.; Ito, K. Electrochemical Reduction of Carbon Dioxide at Various Metal Electrodes in Aqueous Potassium Hydrogen Carbonate Solution. *Bull. Chem. Soc. Jpn.* **1990**, *63* (9), 2459–2462.
(23) Nørskov, J. K.; Bligaard, T.; Logadottir, A.; Kitchin, J. R.; Chen, J. G.; Pandelov, S.; Stimming, U. Trends in the Exchange Current for Hydrogen Evolution. *J. Electrochem. Soc.* **2005**, *152* (3), J23–J26.
(24) Hori, Y.; Murata, A.; Takahashi, R.; Suzuki, S. Electrochemical Reduction of Carbon Monoxide to Hydrocarbons at Various Metal Electrodes in Aqueous Solution. *Chem. Lett.* **1987**, *16* (8), 1665–1668.
(25) Hori, Y.; Takahashi, R.; Yoshinami, Y.; Murata, A. Electrochemical Reduction of CO at a Copper Electrode. *J. Phys. Chem. B* **1997**, *101* (36), 7075–7081.
(26) Peterson, A. A.; Abild-Pedersen, F.; Studt, F.; Rossmeisl, J.; Nørskov, J. K. How Copper Catalyzes the Electroreduction of Carbon Dioxide into Hydrocarbon Fuels. *Energy Environ. Sci.* **2010**, *3* (9), 1311.
(27) Peterson, A. A.; Nørskov, J. K. Activity Descriptors for CO2 Electroreduction to Methane on Transition-Metal Catalysts. *J. Phys. Chem. Lett.* **2012**, *3*, 251–258.
(28) Nie, X.; Esopi, M. R.; Janik, M. J.; Asthagiri, A. Selectivity of CO2 Reduction on Copper Electrodes: The Role of the Kinetics of Elementary Steps. *Angew. Chemie - Int. Ed.* **2013**, *52* (9), 2459–2462.
(29) Noda, H.; Ikeda, S.; Oda, Y.; Ito, K. Potential Dependencies of the Products on

Electrochemical Reduction of Carbon Dioxide at a Copper Electrode. *Chem. Lett.* **1989**, *2*, 289–292.
(30) Li, C. W.; Kanan, M. W. CO2 Reduction at Low Overpotential on Cu Electrodes Resulting from the Reduction of Thick Cu2O Films. *J. Am. Chem. Soc.* **2012**, *134* (17), 7231–7234.
(31) Tang, W.; Peterson, A. a; Varela, A. S.; Jovanov, Z. P.; Bech, L.; Durand, W. J.; Dahl, S.; Nørskov, J. K.; Chorkendorff, I. The Importance of Surface Morphology in Controlling the Selectivity of Polycrystalline Copper for CO2 Electroreduction. *Phys. Chem. Chem. Phys.* **2012**, *14* (1), 76–81.
(32) Manthiram, K.; Beberwyck, B. J.; Alivisatos, A. P. Enhanced Electrochemical Methanation of Carbon Dioxide with a Dispersible Nanoscale Copper Catalyst. *J. Am. Chem. Soc.* **2014**, *136* (38), 13319–13325.
(33) Roberts, F. S.; Kuhl, K. P.; Nilsson, A. High Selectivity for Ethylene from Carbon Dioxide Reduction over Copper Nanocube Electrocatalysts. *Angew. Chemie - Int. Ed.* **2015**, *54* (17), 5179–5182.
(34) Feng, X.; Jiang, K.; Fan, S.; Kanan, M. W. A Direct Grain-Boundary-Activity Correlation for CO Electroreduction on Cu Nanoparticles. *ACS Cent. Sci.* **2016**, *2* (3), 169–174.
(35) Murata, A.; Hori, Y. Product Selectivity Affected by Cationic Species in Electrochemical Reduction of CO2 and CO at a Cu Electrode. *Bull. Chem. Soc. Jpn.* **1991**, *64*, 123–127.
(36) Kyriacou, G. Z.; Anagnostopoulos, A. K. Influence CO2 Partial Pressure and the Supporting Electrolyte Cation on the Product Distribution in CO2 Electroreduction. *J. Appl. Electrochem.* **1993**, *23* (5), 483–486.
(37) Singh, M. R.; Kwon, Y.; Lum, Y.; Ager, J. W.; Bell, A. T. Hydrolysis of Electrolyte Cations Enhances the Electrochemical Reduction of CO2 over Ag and Cu. *J. Am. Chem. Soc.* **2016**, *138* (39), 13006–13012.
(38) Resasco, J.; Chen, L. D.; Clark, E.; Tsai, C.; Hahn, C.; Jaramillo, T. F.; Chan, K.; Bell, A. T. Promoter Effects of Alkali Metal Cations on the Electrochemical Reduction of Carbon Dioxide. *J. Am. Chem. Soc.* **2017**, *139* (32), 11277–11287.
(39) Hori, Y.; Murata, A.; Takahashi, R.; Suzuki, S. Enhanced Formation of Ethylene and Alcohols at Ambient Temperature and Pressure in Electrochemical Reduction of Carbon Dioxide at a Copper Electrode. *J. Am. Chem. Soc. Chem. Commun.* **1988**, *1*, 17–19.
(40) Kas, R.; Kortlever, R.; Yilmaz, H.; Koper, M. T. M.; Mul, G. Manipulating the Hydrocarbon Selectivity of Copper Nanoparticles in CO2 Electroreduction by Process Conditions. *ChemElectroChem* **2015**, *2* (3), 354–358.
(41) Varela, A. S.; Kroschel, M.; Reier, T.; Strasser, P. Controlling the Selectivity of CO 2 Electroreduction on Copper: The Effect of the Electrolyte Concentration and the Importance of the Local pH. *Catal. Today* **2016**, *260*, 8–13.
(42) Hansen, H. A.; Shi, C.; Lausche, A.; Peterson, A.; Nørskov, J. K. Bifunctional Alloys for the Electroreduction of CO2 and CO. *Phys. Chem. Chem. Phys.* **2016**, *18* (111), 9194–9201.
(43) Hahn, C.; Abram, D. N.; Hansen, H. A.; Hatsukade, T.; Jackson, A.; Johnson, N. C.; Hellstern, T. R.; Kuhl, K. P.; Cave, E. R.; Feaster, J. T.; et al. Synthesis of Thin Film AuPd Alloys and Their Investigation for Electrocatalytic CO2 Reduction. *J. Mater. Chem. A* **2015**, *3*, 20185–20194.
(44) Ren, D.; Ang, B. S. H.; Yeo, B. S. Tuning the Selectivity of Carbon Dioxide Electroreduction toward Ethanol on Oxide-Derived CuxZn Catalysts. *ACS Catal.* **2016**, *6* (12), 8239–8247.
(45) Torelli, D. A.; Francis, S. A.; Crompton, J. C.; Javier, A.; Thompson, J. R.; Brunschwig, B. S.; Soriaga, M. P.; Lewis, N. S. Nickel–Gallium-Catalyzed Electrochemical Reduction of CO2 to Highly Reduced Products at Low Overpotentials. *ACS Catal.* **2016**, *6*, 2100–2104.
(46) Ma, S.; Sadakiyo, M.; Heim, M.; Luo, R.; Haasch, R. T.; Gold, J. I.; Yamauchi, M.; Kenis, P. J. A. Electroreduction of Carbon Dioxide to Hydrocarbons Using Bimetallic Cu-Pd Catalysts with Different Mixing Patterns. *J. Am. Chem. Soc.* **2017**, *139* (1), 47–50.

Chapter 2

Data Acquisition Protocols and Reporting Standards for Studies of the Electrochemical Reduction of Carbon Dioxide

Adapted from:
Clark, E. L.; Resasco, J.; Landers, A.; Lin, J.; Chung, L.-T.; Walton, A.; Hahn, C.; Jaramillo, T. F.; Bell, A. T. *ACS Catal.* **2018**, 8, 6560-6570.

Abstract

Objective evaluation of the performance of electrocatalysts for CO_2 reduction has been complicated by a lack of standardized methods for measuring and reporting activity data. In this perspective, we advocate that standardizing these practices can aid in advancing research efforts toward the development of efficient and selective CO_2 reduction electrocatalysts. Using information taken from experimental studies, we identify variables that influence the measured performance of CO_2 reduction electrocatalysts and propose procedures to improve the accuracy and reproducibility of reported data. We recommend that catalysts be measured under conditions which do not introduce artifacts from impurities, either from the electrolyte or counter electrode, and advocate the acquisition of data measured in the absence of mass transport effects. Furthermore, measured rates of electrochemical reactions should be normalized to both the geometric electrode area as well as the electrochemically active surface area to facilitate the comparison of reported catalysts with those previously known. We demonstrate that when these factors are accounted for, the CO_2 reduction activity of Ag and Cu measured in different laboratories exhibit little difference. Adoption of the recommendations presented in this perspective would greatly facilitate the identification of superior catalysts for CO_2 reduction arising solely from changes in their composition and pretreatment.

2.1 Introduction

The electrochemical reduction of CO_2 offers a means of producing transportation fuels and commodity chemicals using intermittent renewable electricity.[1-3] Motivated by this objective, numerous publications have appeared in recent years aimed at identifying

electrocatalysts that can efficiently and selectively reduce CO_2 to desired products.[4-10] However, objective evaluation of the activity and selectivity of different catalysts and operating conditions has proven difficult due to a lack of standardized protocols for preparing catalysts and evaluating their electrocatalytic activity. These issues are significant because the performance of electrocatalyts is influenced not only by the composition and morphology of the electrocatalyst itself, but also by the composition of the electrolyte, the hydrodynamics of the electrochemical cell, and the purity of both the electrocatalyst and the electrolyte.

This perspective identifies some of the key variables that influence the measured activity and selectivity of CO_2 reduction electrocatalysts with the aim of proposing procedures to obtain reproducible data that can be attributed solely to properties of the catalyst. We show how each factor affects the measured electrocatalytic activity and selectivity and provide recommendations for the preparation of electrocatalysts and the design of electrochemical cells. We demonstrate that interinstitutional reproducibility is observed over independently prepared and tested catalyst materials when these recommendations are considered. Finally, we stress the importance of reporting electrocatalyst activity normalized by the electrochemically active surface area and caution against claims of superior catalyst performance based solely on Faradaic efficiency.

2.2 Benchmarking Electrocatalytic Performance

Comparing catalytic data from different laboratories can be convoluted because each tends to use its own sources of catalyst and electrolyte, method of catalyst preparation and pretreatment, and design of the electrochemical cell used for catalyst evaluation. As we show below, these differences can introduce unintended consequences that impact the observed activity of CO_2 reduction electrocatalysts. To minimize the effects of factors other than catalyst composition and morphology, we recommend that research groups benchmark their ability to accurately and consistently reproduce the published activity for a well-studied planar monometallic catalyst prior to reporting data for new catalysts.

The choice of electrocatalyst to be used for benchmarking purposes requires careful consideration. Cu is the most well studied catalyst for CO_2 reduction because it is the only monometallic catalyst that can reduce CO_2 to hydrocarbons and alcohols with reasonably high Faradaic efficiencies.[11-14] However, it should be noted that Cu produces a wide variety of products, the distribution of which is sensitive to the manner of catalyst preparation. To illustrate this point, the CO_2 reduction activity observed over Cu(111) and Cu(100) are compared in Figure 2.1A.[13,15,16] Experimental details of the preparation and testing of these epitaxial thin films can be found in the Supporting Information (see 2.9.1 and 2.9.2). The Cu(100) surface exhibits an activity for generating C_{2+} products roughly an order of magnitude higher than that for Cu(111), as reported elsewhere.[13,16] This atomic structure dependence can cause polycrystalline Cu foils obtained from different vendors or even different batches from the same vendor to exhibit large differences in electrocatalytic activity and selectivity that arise due to variations in surface atomic

structure. In contrast to Cu, Ag predominately produces H_2 and CO, with CO Faradaic efficiencies exceeding 90% at an applied potential of -1 V vs RHE.[17,18] Furthermore, the product distribution obtained over Ag is less dependent on the surface atomic structure than Cu.[17] To illustrate this point the CO_2 reduction activity of Ag(111) and Ag(100) are compared in Figure 2.1B. While the CO evolution activity exhibits a slight surface atomic structure dependence, the variation observed is only a factor of ~2. The relatively similar activity observed over Ag(111) and Ag(100) means that the activity observed over polycrystalline Ag foils will exhibit less variation from sample to sample. Thus, we recommend that Ag be used as a benchmarking electrocatalyst to assess the ability of a research group to carry out accurate and reproducible activity measurements.

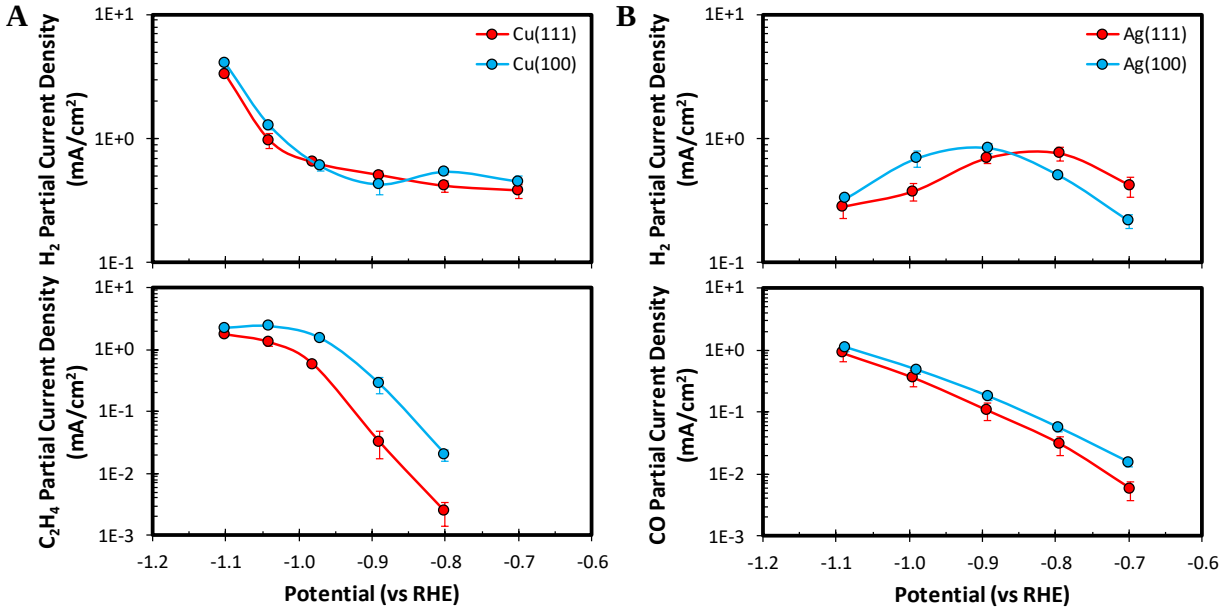

Figure 2.1 *– Structure sensitivity of CO_2 reduction activity of monometallic electrocatalysts in 0.1 M $KHCO_3$: (A) Cu(111) vs Cu(100) and (B) Ag(111) vs Ag(100).*

Surface preparation methods can also introduce additional variations in activity and selectivity between samples of the same metal due to the impact that these pretreatments have on the purity and distribution of undercoordinated sites at the electrode surface.[19,20] Mechanical polishing can introduce contaminants onto the catalyst surface from the polish residue (see 2.9.3). These polish residues can be susceptible to electrochemical reduction under the conditions of CO_2 reduction and may exhibit background activity in the metallic state, as is the case for alumina-based polishing compounds.[21] As a result, SiC and diamond-based polishing compounds should be favored over alumina-based polishing compounds since residues from these compounds will be largely electrochemically inert. Electropolishing can also be utilized but thorough rinsing of the electrocatalyst should be practiced to prevent carryover of specifically adsorbing anions into the reaction vessel.

Comparisons between different catalysts should only be done if their activity was measured in identical electrolyte solutions. Several studies have demonstrated that the identity of the cations and anions in the electrolyte affect both the activity and selectivity

of CO_2 reduction catalysts. For example, the activity and selectivity of both polycrystalline foils and epitaxial thin films of Ag and Cu have been demonstrated to change as the size of the electrolyte cation is increased from Li^+ to Cs^+.[22] Larger cations, such as Cs^+, favor the formation of CO over Ag and C_{2+} products over Cu due to electrostatic field-stabilization of species involved in the formation of CO in the case of Ag and of C-C bonds, such as adsorbed OCCO and OCCHO, in the case of Cu.[23] Conversely, cation size has no effect on the partial current densities for H_2 or CH_4 because their mechanistic pathways do not involve reaction intermediates with significant dipole moments and there are insignificant changes in the dipole moment between the reactant and transition state.[23] The composition of the anionic component of the supporting electrolyte can also affect CO_2 reduction selectivity. For example, in the case of CO_2 reduction over Cu, phosphate-based electrolytes result in higher partial currents for H_2 and CH_4 than are observed in bicarbonate-based electrolytes, but the choice electrolyte anion has little effect on the partial currents for CO, $HCOO^-$, C_2H_4, or C_2H_5OH. Furthermore, changes in the buffer concentration also impact catalyst selectivity.[24-27] As a result of these influences, researchers should only compare catalytic data obtained using identical electrolyte solutions. Obtaining catalytic data in either 0.1 M $KHCO_3$ or 0.1 M $CsHCO_3$ will enable the greatest comparison to published catalytic data, since the majority of CO_2 reduction studies have been conducted using these electrolytes.

2.3 Impact of Electrochemical Cell Hydrodynamics on Electrocatalytic Activity

The electrochemical reduction of CO_2 is highly susceptible to concentration polarization, wherein Faradaic processes induce concentration gradients near the electrode surface. These concentration gradients arise because bicarbonate solutions are weak buffers and CO_2 has a low mass transfer coefficient through aqueous solutions.[28,29] Even modest current densities cause the pH and CO_2 concentration near the cathode surface to vary significantly from that in the bulk electrolyte.[30,31] The magnitude of the concentration gradients depends largely on the hydrodynamics of the electrochemical cell. As a result, the electrolyte needs to be mixed vigorously to ensure sufficient mass transport to and from the cathode. Electrolyte mixing in small electrochemical cells is usually accomplished by agitation of the electrolyte with a column of CO_2 bubbles, although pump-driven recirculation of CO_2-saturated electrolyte has also been employed.[32,33] Activity data acquired in a regime where significant concentration polarization occurs does not reflect the intrinsic activity or selectivity of the catalyst, but rather the convolution of the properties of the catalyst and the effects of mass transfer. Therefore, researchers should avoid measuring catalytic activity under conditions where mass transfer effects are significant because correcting for these effects is nontrivial. Researchers should also only consider the portion of their data that has been shown to be free of the effects of mass transfer when making conclusions about intrinsic reaction kinetics.

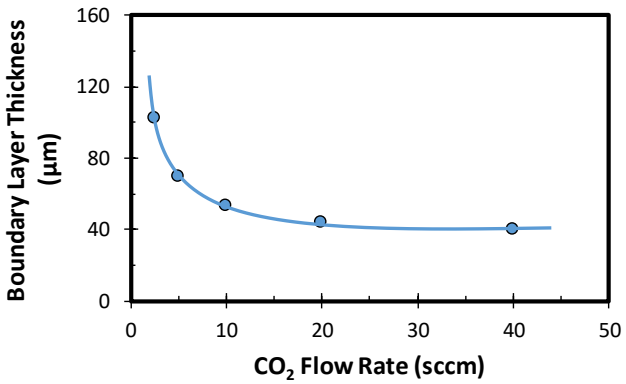

Figure 2.2 *– Hydrodynamic boundary layer thicknesses at the cathode surface as a function of the CO_2 flow rate utilized to mix the catholyte calculated by measuring the diffusion-limited current density of ferricyanide reduction over polycrystalline Au.*

The mass transfer boundary layer thickness of an electrochemical cell can be quantified by measuring the diffusion-limited current density for ferricyanide reduction (see 2.9.4). As shown in Figure 2.2, increasing the CO_2 flow rate reduces the hydrodynamic boundary layer thickness but has a diminishing effect as the CO_2 flow rate is increased. Activity measurements were conducted as a function of the applied potential for different CO_2 flow rates to demonstrate the impact that the mass transfer boundary layer thickness has on the measured activity of polycrystalline Ag. Figure 2.3 shows the partial current densities for H_2 and CO as a function of the mass transfer boundary layer thickness, which was systematically varied by varying the CO_2 flow rate through the cell. The variation in the partial currents for H_2 and CO are direct results of the variation in the mass transfer boundary layer thickness at the cathode surface and is not due to changes in the bulk CO_2 concentration. The latter statement is supported by the observation that electrochemical cells incorporating gas dispersion frits maintain saturation of the bulk electrolyte with CO_2 during prolonged electrolysis.[32]

We note that the tested Ag films were completely free of contaminants within the detection limits of XPS and ISS (see 2.9.5). Thus, the observed variations in electrocatalytic activity are a direct result of the degree to which concentration polarization influences the observed electrocatalytic activity. As shown in Figure 2.3, the hydrodynamic regime in which the activity of polycrystalline Ag is measured dictates what is observed at potentials more negative than -1 V vs RHE, the potential for which mass transfer effects become significant (see 2.9.6). As the hydrodynamic boundary layer thickness is reduced, less H_2 and more CO is produced at a given applied potential, resulting in a CO Faradaic efficiency swing of ~60% at -1.4 V vs RHE. As a result, the maximum rate of CO_2 consumption over the cathode increases inversely with the hydrodynamic boundary layer thickness, as expected for a diffusion-limited process (see 2.9.6).

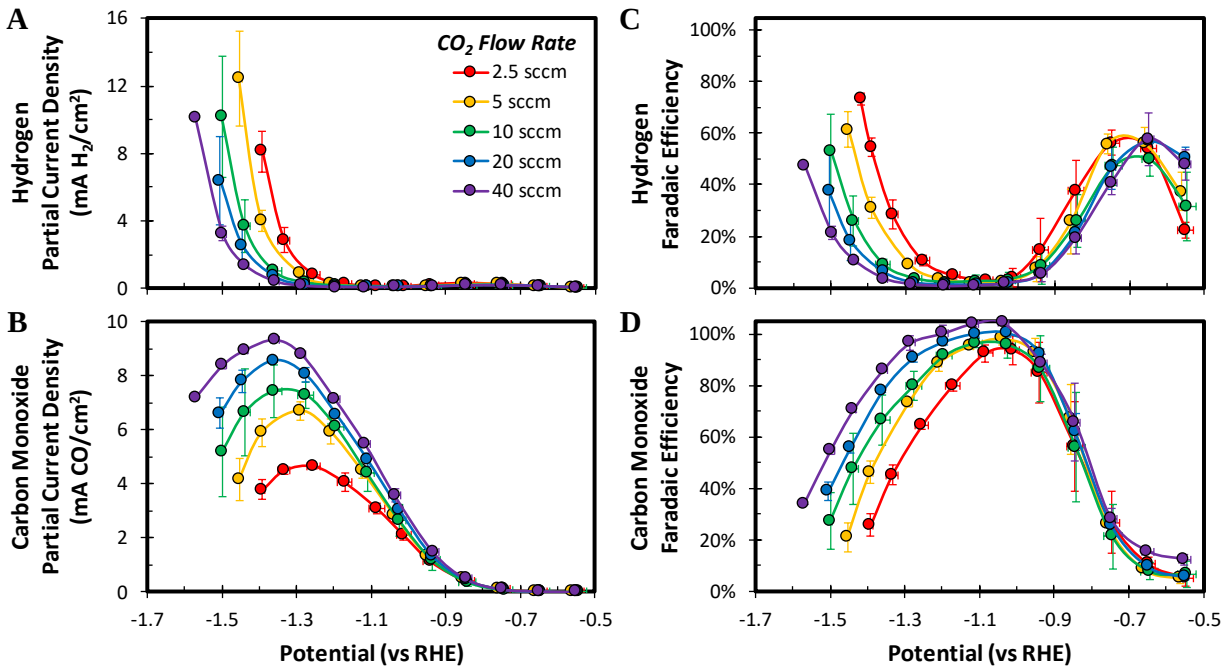

Figure 2.3 *– Dependence of the measured activity of polycrystalline Ag on the CO_2 flow rate utilized to mix the electrochemical cell: (A) H_2 partial current density, (B) CO partial current density, (C) H_2 Faradaic efficiency, and (D) CO Faradaic efficiency.*

This demonstration of the influence of the hydrodynamics of the electrochemical cell on the measured activity of polycrystalline Ag indicates the importance of designing electrochemical cells with adequate electrolyte mixing and conducting catalytic activity measurements in a regime that is minimally influenced by mass transfer to the cathode surface. Only under such conditions is it possible to definitively measure the intrinsic activity of the catalyst and obtain data that is directly comparable across research institutions. For the electrochemical cell and polycrystalline Ag catalyst utilized here, the impact of concentration polarization becomes significant for applied potentials below -1 V vs RHE, as indicated by the deviation of the CO partial current density from Tafel kinetics (see 2.9.6). As a result, the measured activity is minimally affected by the mass transfer boundary layer thickness at potentials more positive than -1 V vs RHE. It should be noted, though, the potential at which concentration polarization becomes significant is a function of the overall current density and not the applied potential. As a result, catalysts with high surface areas are more susceptible to mass transfer limitations than planar catalysts, which complicates obtaining an accurate measurement of their intrinsic activity. Another point to realize is that concentration polarization introduces error when reporting data on a RHE scale because the local pH deviates substantially from that in the bulk, as shown in Figure 2.4.[34] This error can become significant when comparing catalysts that suffer from concentration polarization to different extents. Examples include comparing catalysts with vastly different surface roughness or comparing planar catalysts evaluated in electrochemical cells with different hydrodynamic boundary layer thicknesses.[35] These differences can lead to divergent local reaction environments that convolute accurate activity comparisons.

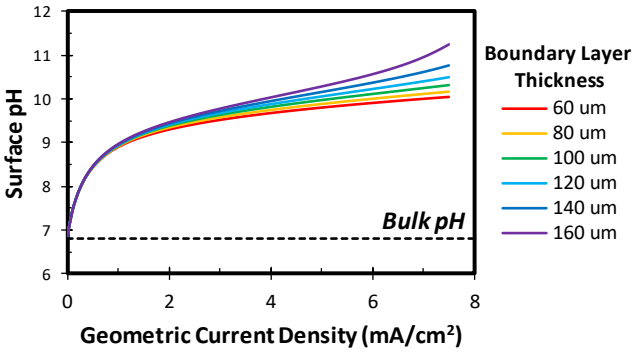

Figure 2.4 *– Calculated pH at the surface of a planar cathode as a function of the geometric current density and the hydrodynamic boundary layer thickness in 0.1 M bicarbonate electrolyte.*

2.4 Impact of Impurities on Electrocatalytic Activity

The steady-state activity and selectivity of a material should be measured in the absence of surface contamination to assess its intrinsic catalytic properties. If surface contamination occurs, it is important to distinguish whether it is a consequence of catalytic intermediates that poison the surface or whether it is the result of impurities inadvertently introduced onto the surface.[36] We note that the high overpotentials typically utilized to evaluate the activity of CO_2 reduction electrocatalysts are sufficiently negative to reduce nearly any transition metal cation that might be present in the catholyte. In general, transition metal impurities will increase the activity of the electrocatalyst for the H_2 evolution reaction (HER), since the late transition and p-block metals typically studied as CO_2 reduction electrocatalysts have very low HER activity.[37,38] Even trace quantities (<1 μM) of transition metal cations in the electrolyte can cause CO_2 reduction electrocatalysts to lose their activity on the timescale of a typical experiment.[38,39] Metallic impurities in the catholyte can originate from the solvent, the electrolyte salts, and from the other components of the electrochemical cell.

The purity of the electrode surface is often validated using X-ray photoelectron spectroscopy (XPS). This analytical method probes the composition of the top 0.5 to 2 nm of the sample, depending on the collection angle and the kinetic energy of the relevant photoelectrons.[40] The detection limit of XPS for transition metals is typically between 0.1 and 1 atomic percent, depending on the sample morphology and the combination of elements.[41] While this detection limit may be adequate for certain applications, it is inadequate for validating the purity of catalyst surfaces since even ~20% of a monolayer of impurities can go undetected by XPS.[40, 41] Thus, the lack of observable contamination by XPS does not indicate that the electrode surface is free of contamination. Ion scattering spectroscopy (ISS) can be used to more accurately validate the purity of the catalyst surface since it only probes the top layer of atoms on the sample surface.[42] However, because ISS is a line-of-sight technique it can be difficult to obtain quantitative information about the relative abundance of constituent elements due to their nonequivalent coverage by adventitious adsorbates, such as ambient oxygen. Despite this, ISS is a very useful

analytical technique because of its enhanced sensitivity for detecting impurities on an electrode surface.

Researchers have recently demonstrated that Pt and other noble metals typically used as anode electrocatalysts can dissolve under typical operating conditions.[43-48] The transition metal cations evolved from the anode can reach the cathode even when an anion exchange membrane is utilized to separate the electrode chambers.[49] Whether this crossover occurs during operation or during the storage and cleaning of the electrochemical cell has yet to be resolved conclusively. The effect of inadvertent Pt contamination on the activity of Cu(100) is shown in Figure 2.5, which compares the transient activity observed over Cu(100) when Pt and glassy carbon (GC) are employed as anodes. Figure 2.5A shows that the activity for producing H_2 and C_2H_4 increase and decrease, respectively, over the course of 1 hr when Pt is used as the anode. However, Figure 2.5A also shows that the activity for all products is remarkably stable when GC is used as the anode. The differences in the ethene to methane ratio observed at the

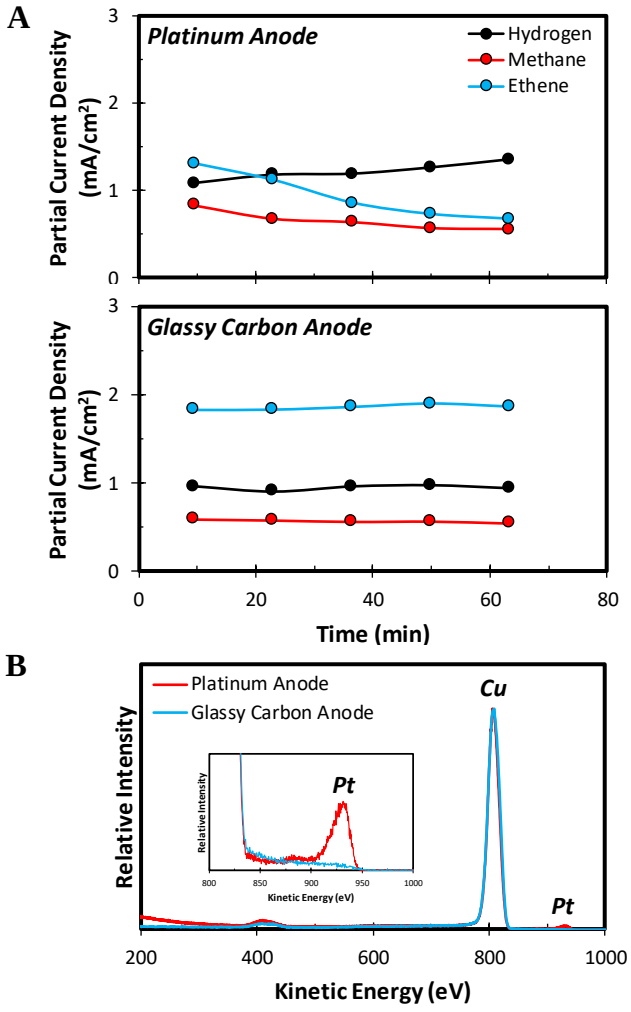

Figure 2.5 *– (A) Comparison of the transient activity observed over Cu(100) at an applied potential of −1.0 V vs RHE using Pt anode and glass carbon anodes. (B) Comparison of the ISS spectra of Cu(100) tested using Pt and glassy carbon anodes.*

beginning of the experiments could be a result of Pt promotion of the Cu surface. In fact, it has been demonstrated that the reduction of a small quantity of a HER active metal onto the surface of Cu results in a decrease in the ethene to methane ratio during CO_2 reduction. While both surfaces appeared to be free of contamination by XPS, Pt was detected by ISS on the Cu(100) electrode tested using a Pt anode. Thus, researchers should employ a sacrificial GC anode when measuring the intrinsic activity of CO_2 reduction electrocatalysts to prevent inadvertent surface contamination.

The degree to which impurities impact the observed activity depends strongly on the surface area of the cathode relative to the volume of the catholyte. Since the cathodic potential needed to drive CO_2 reduction is usually much more negative than the standard reduction potential of transition metal cations, it can be assumed that over a long period of time most of the metal impurities present in the electrolyte will be electrodeposited onto the cathode surface. Figure 2.6 demonstrates that even very small concentrations (<1 µM) of electrolyte impurities can result in a significant coverage (0.1 ML) on the electrocatalyst surface (see 2.9.7). Furthermore, the calculation indicates that contamination will be especially problematic for systems where the catholyte volume is large compared to the electrode surface area. This means that the tolerance for impurities increases with the roughness of the catalyst surface. Therefore, researchers should be mindful of the different extents to which impurities could influence the observed activity when comparing two catalysts with significantly different roughness factors. For instance, lower rates of HER over a high surface area catalyst in comparison to a low surface area standard could potentially be the result of a smaller fraction of surface sites being covered by electrodeposited impurities.

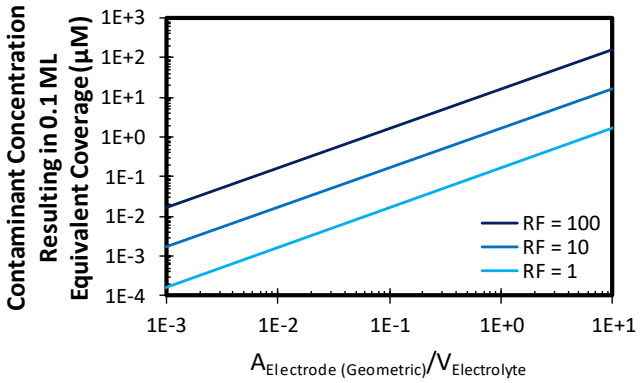

Figure 2.6 *– Calculated electrolyte impurity concentration required to cover 10% of the electrocatalyst surface based on the geometric cathode surface area to electrolyte volume ratio and the roughness factor of the cathode surface.*

2.5 Interinstitutional Reproducibility

Consistent and reproducible reports of CO_2 reduction electrocatalysis are critical to advancing the field. By first benchmarking electrochemical systems against standard catalysts researchers can be assured that results obtained from testing a novel catalyst formulation will be repeatable at other institutions and that measured activity can be

confidently attributed to the properties of the catalyst itself. The entire electrochemical system, including catalyst, electrolyte, electrochemical cell, and operating conditions, needs to be considered before making comparisons with the literature.

With careful experimentation, electrocatalyst activity can be accurately and reliably reproduced at different academic institutions. This point is nicely illustrated by the data presented in Figure 2.7, which shows the activity for selected products obtained over polycrystalline silver and epitaxial Cu(100) thin films, prepared and tested independently at Berkeley and Stanford. Similar experimental protocols were used at both institutions to avoid artifacts from impurities, and a potential range was chosen for comparison in which the effects of concentration polarization were minimized. Further details of the cell design and experimental protocols at each institution are included in the Supporting Information (see 2.9.1 and 2.9.2). The close agreement in observed activity demonstrates that reproducibility can be achieved with careful experimentation.

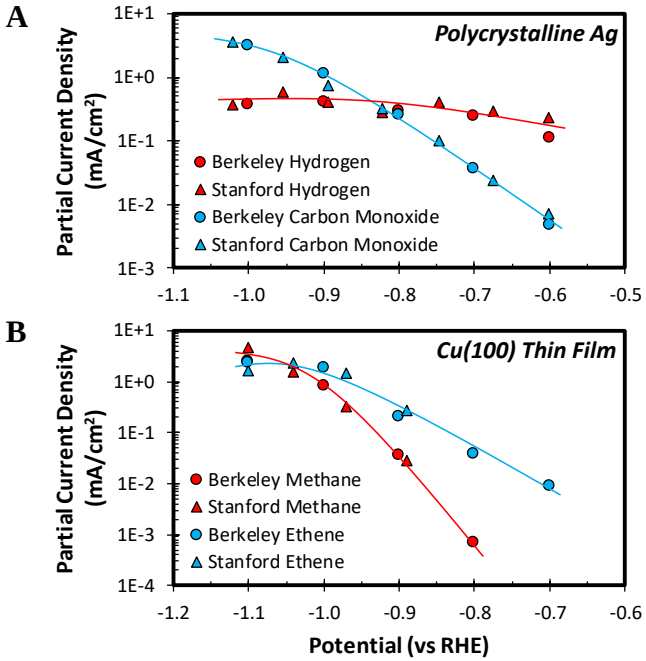

Figure 2.7 *– Interinstitutional reproducibility of activity data measured over electrocatalysts independently prepared and tested at two different academic institutions: (A) polycrystalline Ag and (B) Cu(100) thin films.*

2.6 Reporting Electrocatalytic Activity

Several figures of merit can be utilized to report the activity and selectivity observed over an electrocatalyst. One commonly used metric for selectivity is Faradaic efficiency, which is defined as the fraction of Faradaic charge utilized to produce a given product. While Faradaic efficiency is useful for describing the selectivity of a catalyst, it is problematic when comparing catalysts with drastically different activities. For example, it is tempting to conclude that the catalyst that is more selective for producing a specific product is more active for producing that product. However, an increase in selectivity to

a product may or may not be accompanied by an increase in the rate at which that product is produced. In these cases, only comparing Faradaic efficiencies can obscure the true differences between two catalysts. The rate of product production, which is proportional to its partial current density, is a much less ambiguous descriptor of catalytic activity. Figure 2.8 compares the Faradaic efficiencies and partial current densities observed over Cu(100) as a function of the alkali cation in 0.1 M bicarbonate electrolytes.[23] The trends in Faradaic efficiency exhibit a decrease in selectivity to HER as the size of the alkali metal cation increases. Based on this metric alone, one might conclude that larger cations suppress HER. However, Figure 2.8B shows that the rate of HER is unaffected by the identity of the electrolyte cation, as the decrease in selectivity is accompanied by an increase in the total current density. This example demonstrates that only comparing Faradaic efficiencies can give an incomplete picture of catalyst performance, and in some cases can even provide a qualitatively incorrect description of catalytic behavior as properties of the system change.

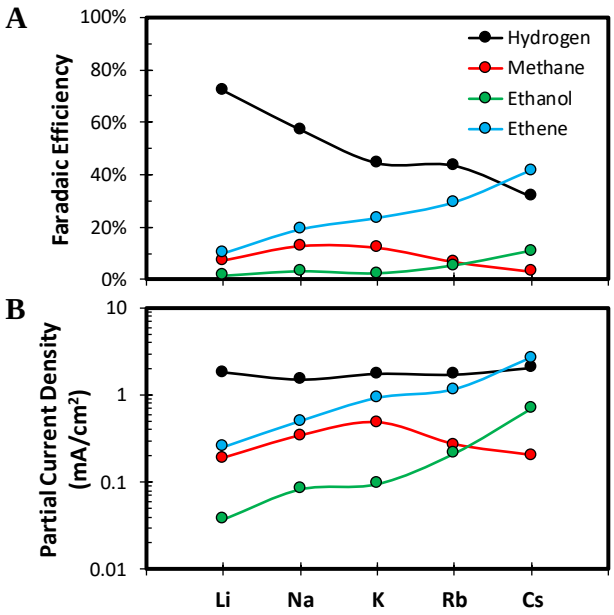

Figure 2.8 *– (A) Faradaic efficiencies and (B) partial current densities for selected products observed over Cu(100) at an applied potential of −1.0 V vs RHE in 0.1 M bicarbonate electrolytes as a function of the identity of the alkali cation.*

Measured rates must be normalized by the number of available catalytic sites when making comparisons between different catalysts.[50] For thermally activated reactions, and for other well studied electrocatalytic reactions, it is common to normalize observed rates by the number of active sites.[51-54] This procedure has not yet been adopted for CO_2 reduction, and catalytic activity is typically reported on the basis of the geometric area of the cathode. This is problematic because it makes it difficult to determine if reported activity improvements are the result of intrinsic activity improvements or simply higher catalyst surface area. While normalization to the number of active sites is a preferable metric it can be difficult to identify what the active site is. However, normalizing the measured activity by the electrochemically active surface area

is a straightforward way to normalize catalytic activity that is meaningful and applicable to a wide variety of different electrocatalysts.[55]

The electrochemically active surface area (ECSA) of a electrocatalytic material can be estimated by measuring the double-layer capacitance of the electrode-electrolyte interface.[56] The double layer capacitance can be measured by conducting cyclic voltammetry (CV) in a potential range where no Faradaic processes occur, typically a 100 mV window centered at the open-circuit potential (OCP). In this potential region, any measured current can be ascribed to the non-Faradaic process of charging the electrochemical double layer. The charging current, i_c, measured during CV is related linearly to the scan rate v with a slope equal to the double layer capacitance:

$$C_{DL} = \frac{i_c}{v}$$

This measured capacitance (C_{DL}) can be compared to that of a smooth planar surface (C_{REF}) to obtain a relative roughness factor for the electrocatalyst:

$$ESCA = \frac{C_{DL}}{C_{REF}}$$

Since the reference sample is unlikely to be atomically flat and/or have the same surface termination as the sample of interest, comparisons on this basis or using a published reference capacitance value may not give accurate absolute values for the total surface area of the catalyst. However, this is generally acceptable since differences between a novel catalyst and a well-known benchmark are typically of interest. However, it is important to realize that in some cases the entire surface area of the electrode is not electrocatalytically active. As a result, normalizing the measured activity by the total ECSA would be inappropriate. One example is when nanoparticles are supported on an inert support, such as GC or Toray paper. For these systems underpotential deposition can give a more accurate estimate of the catalytically relevant surface area. However, this approach is dependent on the elemental composition of the electrocatalyst and must be tailored to fit the application.

The importance of reporting current densities normalized to the ECSA is illustrated in Figure 2.9, which compares the CO_2 reduction activity observed over two polycrystalline Ag electrodes with different roughness factors. The first sample was polished mechanically while the second was roughened by electrochemical cycling in 1 M KCl. Figure 2.9A shows that the geometric CO partial current densities of the electrodes vary by nearly an order of magnitude. However, the electrocatalysts also exhibit drastically different surface areas (see 2.9.8). As a result, when the CO partial current densities are normalized by the ECSA the catalysts are identical at low overpotentials (Figure 2.9B). At high overpotentials, the relatively smooth Ag catalyst performs better because mass transfer is limiting the supply of CO_2 to the roughened electrode. The effects of mass transfer can be mitigated by increasing the CO_2 flow rate, thereby increasing the potential window over which the two samples show identical activity. These

data suggest that differences in ECSA do not lead to differences in the intrinsic activity in this case. This example highlights the importance of proper data treatment and normalization, as comparisons solely based on Faradaic efficiency or geometric partial current densities can be misleading. These results also demonstrate that care should be taken in using onset potential as a metric of intrinsic catalytic activity, since it is entirely dependent on the detection limits of the experimental setup.

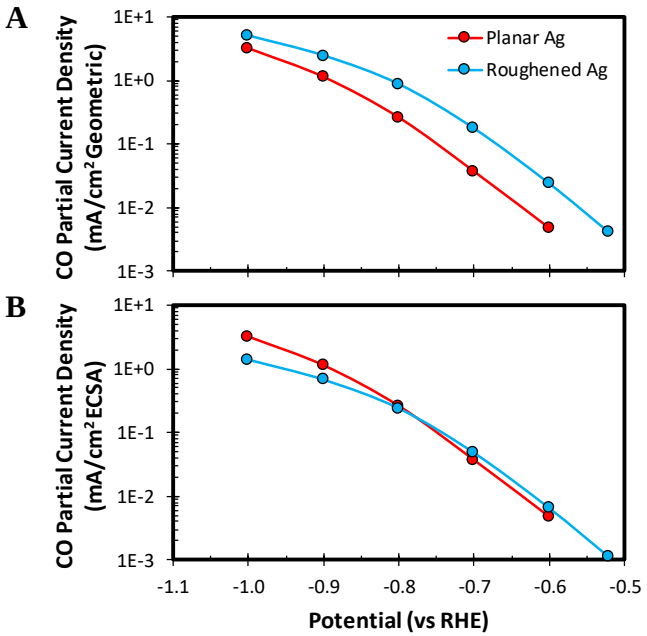

Figure 2.9 *– Comparison of the CO evolution activity observed over mechanically polished and electrochemically roughened Ag catalysts normalized to (A) geometric area and (B) electrochemically active surface area (ECSA).*

The ECSA-normalized CO evolution activities of Au-based electrocatalysts have recently been compared, leading to the conclusion that no Au-based catalyst formulation reported in the literature exhibits a superior activity to polycrystalline Au foils.[57] There has also been substantial interest in high surface area Cu-based catalysts for CO_2 reduction, and in particular those derived from the reduction of oxidized Cu.[4,7,58-64] It has been reported that pre-oxidized Cu catalysts exhibit an exceptionally high activity for producing multi-carbon products, such as C_2H_4 and C_2H_5OH. These studies have stimulated efforts aimed at understanding the origin of the seemingly superior catalytic activity of these oxide-derived catalysts compared to polycrystalline Cu foils.[65-72] However it has not been clearly demonstrated if the enhanced activity is due to an increase in the total surface area of the catalyst or to an enhancement of the intrinsic activity.[61-68] Using the metrics discussed above, we show in Figure 2.10 an example of an activity comparison between Cu standards (polycrystalline Cu foil and epitaxial Cu thin films) and a plasma treated Cu catalyst for which surface area measurements are available.[7] We see that the ECSA-normalized partial currents for C_2H_4, the most abundant multi-carbon product produced by Cu, reported for this high surface area electrocatalyst are comparable to those observed over polycrystalline Cu and Cu(100), indicating that the intrinsic activity of this electrocatalyst for producing multi-carbon products is not significantly affected by the way in which the catalyst is prepared. A more extensive comparison of high surface area Cu

catalysts is shown in Figure S2.9, from which the same conclusion can be drawn (see 2.9.8). The different methods of producing Cu catalysts may result in preferential exposure of different low Miller index planes, as the variation in the data is similar to the differences in activity of Cu(111) and Cu(100); however, there is no evidence that these preparations yield sites substantially more active for producing C_2H_4 than those present on these two crystallographic faces.

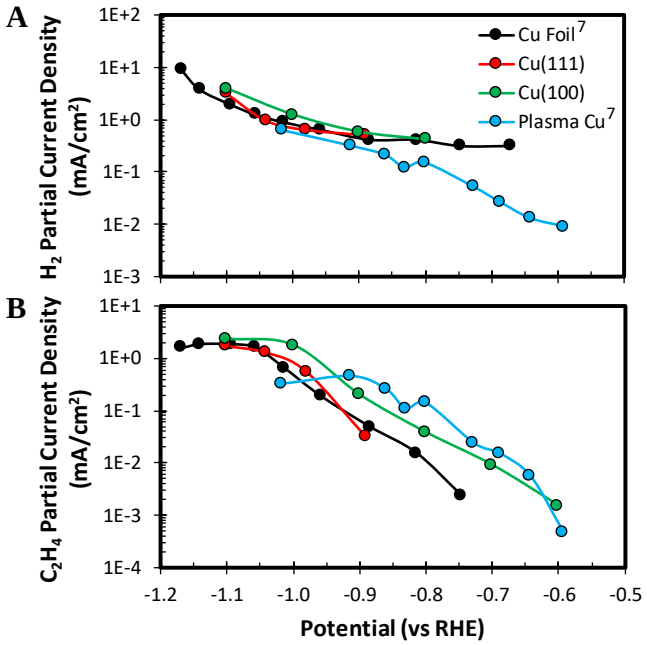

Figure 2.10 *– Comparison of ECSA-normalized partial currents observed over Cu-based catalysts: (A) C_2H_4 and (B) H_2. Plasma-treated Cu data are taken from Mistry et al.*[7]

Although high surface area Cu catalysts do not show higher intrinsic activity for multi-carbon product formation than polycrystalline Cu foils, their selectivity to these products is generally higher. In Figure 2.10B we show the specific partial current for producing H_2 over the same Cu-base catalysts analyzed above. We see that the normalized rate of HER is lower on the high surface area electrocatalyst relative to planar Cu foil and Cu(100), especially at low overpotentials. A similar trend is observed in general in Figure S2.7B. A lower per site rate for HER with a constant rate of multi-carbon product formation leads to a higher selectivity to the multi-carbon products. This reduced rate of HER could be the result of intrinsic differences in reactivity between the catalysts. However, it is also possible that the lower rates of HER on high surface area catalysts relative to polycrystalline Cu is a consequence of other differences, e.g. mass transport effects, or a smaller fraction of surface sites being covered by electrolyte impurities. For example, it has recently been demonstrated that bicarbonate anions can act as an H source for the cathode, with the rates of HER scaling with the concentration of bicarbonate anions near the cathode.[27] Since the onset of concentration polarization occurs at relatively positive potentials over high surface area catalysts, the reduced HER activity might be a consequence of a lower bicarbonate concentration near the cathode.

2.7 Conclusions

In this perspective, we have demonstrated that standardizing the methods used to measure and report electrocatalytic data can aid research efforts aimed at developing novel catalysts for CO_2 reduction. We recommend that catalyst activity and selectivity be measured under conditions which do not introduce artifacts from metallic impurities originating from either the electrolyte or a metallic counter electrode. Furthermore, to understand the behavior of the catalyst itself, the measured data should be taken under conditions in which rates are not a convolution of intrinsic kinetics and the effects of mass transport. Finally, catalytic data should be reported as rates normalized to the electrochemically active area or some specific measure of geometric active site. Adoption of the recommendations presented in this perspective would greatly facilitate meaningful comparisons of catalysts between different research groups and would facilitate the advancement of the field.

2.8 References

(1) Lewis, N. S.; Nocera, D. G. Powering the Planet: Chemical Challenges in Solar Energy Utilization. *Proc. Natl. Acad. Sci.* **2006,** 103, 15729-15735.

(2) Chu, S.; Majumdar, A. Opportunities and Challenges for a Sustainable Energy Future. *Nature* **2012,** 488, 294-303.

(3) Seh, Z. W.; Kibsgaard, J.; Dickens, C. F.; Chorkendorff, I.; Nørskov, J. K.; Jaramillo, T. F. Combining Theory and Experiment in Electrocatalysis: Insights into Materials Design. *Science* **2017,** 355, 1-12.

(4) Li, C.; Kanan, M. CO_2 Reduction at Low Overpotential on Cu Electrodes Resulting from the Reduction of Thick Cu_2O Films. *J. Am. Chem. Soc.* **2012,** 134, 7231-7234.

(5) Kim, D.; Resasco, J.; Yu, Y.; Asiri, A. M.; Yang, P. Synergistic Geometric and Electronic Effects for Electrochemical Reduction of Carbon Dioxide using Gold-Copper Bimetallic Nanoparticles. *Nat. Commun.* **2014,** 5, 1-8.

(6) Lu, Q.; Rosen, J.; Zhou, Y.; Hutchings, G. S.; Kimmel, Y. C.; Chen, J. G.; Jiao, F. A Selective and Efficient Electrocatalyst for Carbon Dioxide Reduction. *Nat. Commun.* **2014,** 5, 1-6.

(7) Mistry, H.; Varela, A. S.; Bonifacio, C. S.; Zegkinoglou, I.; Sinev, I.; Choi, Y.-W.; Kisslinger, K.; Stach, E. A.; Yang, J. C.; Strasser, P.; Cuenya, B. R. Highly Selective Plasma-Activated Copper Catalysts for Carbon Dioxide Reduction to Ethylene. *Nat. Commun.* **2016,** 7, 1-9.

(8) Kortlever, R.; Shen, J.; Schouten, K. J. P.; Calle-Vallejo, F.; Koper, M. T. M. Catalysts and Reaction Pathways for the Electrochemical Reduction of Carbon Dioxide. *J. Phys. Chem. Lett.* **2015,** 6, 4073-4082.

(9) Qiao, J.; Liu, Y.; Hong, F.; Zhang, J. A Review of Catalysts for the Electroreduction of Carbon Dioxide to Produce Low-Carbon Fuels. *Chem. Soc. Rev.* **2014,** 43, 631-675.

(10) Costentin, C.; Robert, M.; Saveant, J.-M. Catalysts for the Electrochemical Reduction of Carbon Dioxide. *Chem. Soc. Rev.* **2013,** 42, 2423-2436.

(11) Hori, Y.; Vayenas, C.; White, R.; Gamboa Aldeco, M. Electrochemical CO_2 Reduction on Metal Electrodes In *Modern Aspects of Electrochemistry,* Springer: New York, **2008**; 42, 89-189.

(12) Kuhl, K.; Cave, E.; Abram, D.; Jaramillo, T. New Insights into the Electrochemical Reduction of Carbon Dioxide on Metallic Copper Surfaces. *Energy Environ. Sci.* **2012,** 5, 7050-7059.
(13) Hori, Y.; Wakebe, H.; Tsukamoto, T.; Koga, O. Adsorption of CO Accompanied with Simultaneous Charge-Transfer on Copper Single-Crystal Electrodes Related with Electrochemical Reduction of CO_2 to Hydrocarbons. *Surf. Sci.* **1995,** 335, 258-263.
(14) Reske, R.; Mistry, H.; Behafarid, F.; Cuenya, B.; Strasser, P. Particle Size Effects in the Catalytic Reduction of CO_2 on Cu Nanoparticles. *J. Am. Chem. Soc.* **2014,** 136, 6978-6986.
(15) Hori, Y.; Takahashi, I.; Koga, O.; Hoshi, N. Selective Formation of C2 Compounds from Electrochemical Reduction of CO_2 at a Series of Copper Single Crystal Electrodes. *J. Phys. Chem. B* **2002,** 106, 15-17.
(16) Hahn, C.; Hatsukade, T.; Kim, Y.; Vailionis, A.; Baricuatro, J.; Higgins, D.; Nitopi, S.; Soriaga, M.; Jaramillo, T. Engineering Cu Surfaces for the Electrocatalytic Conversion of CO_2: Controlling Selectivity toward Oxygenates and Hydrocarbons. *Proc. Natl. Acad. Sci.* **2017,** 114, 5918-5923.
(17) Hoshi, N.; Kato, M.; Hori, Y. Electrochemical Reduction of CO_2 on Single Crystal Electrodes of Silver Ag(111), Ag(100) and Ag(110). *J. Electroanal. Chem.* **1997,** 440, 283-286.
(18) Hatsukade, T.; Kuhl, K.; Cave, E.; Abram, D.; Jaramillo, T. Insights into the Electrocatalytic Reduction of CO_2 on Metallic Silver Surfaces. *Phys. Chem. Chem. Phys.* **2014,** 16, 13814-13819.
(19) Tang, W.; Peterson, A.; Varela, A.; Jovanov, Z.; Bech, L.; Durand, W.; Dahl, S.; Norskov, J.; Chorkendorff, I. The Importance of Surface Morphology in Controlling the Selectivity of Polycrystalline Copper for CO_2 Electroreduction. *Phys. Chem. Chem. Phys.* **2012,** 14, 76-81.
(20) Terunuma, Y.; Saitoh, A.; Momose, Y. Relationship Between Hydrocarbon Production in the Electrochemical Reduction of CO_2 and the Characteristics of the Cu Electrode. *J. Electroanal. Chem.* **1997,** 434, 69-75.
(21) Vijh, A. K. Electrolytic hydrogen evolution reaction on aluminum, oxide-covered electrodes. *J. Phys. Chem.* **1969**, 73, 506-513.
(22) Akira, M.; Yoshio, H. Product Selectivity Affected by Cationic Species in Electrochemical Reduction of CO_2 and CO at a Cu Electrode. *Bull. Chem. Soc. Jpn.* **1991,** 64, 123-127.
(23) Resasco, J.; Chen, L.; Clark, E.; Tsai, C.; Hahn, C.; Jaramillo, T.; Chan, K.; Bell, A. Promoter Effects of Alkali Metal Cations on the Electrochemical Reduction of Carbon Dioxide. *J. Am. Chem. Soc.* **2017,** 139, 11277-11287.
(24) Hori, Y.; Murata, A.; Takahashi, R. Formation of Hydrocarbons in the Electrochemical Reduction of Carbon Dioxide at a Copper Electrode in Aqueous Solution. *J. Chem. Soc. Faraday Trans. I* **1989,** 85, 2309-2326.
(25) Varela, A. S.; Kroschel, M.; Reier, T.; Strasser, P. Controlling the Selectivity of CO_2 Electroreduction on Copper: The Effect of Electrolyte Concentration and the Importance of the Local pH. *Catal. Today* **2016,** 260, 8-13.
(26) Kas, R.; Kortlever, R.; Yılmaz, H.; Koper, M. T. M.; Mul, G. Manipulating the Hydrocarbon Selectivity of Copper Nanoparticles in CO_2 Electroreduction by Process Conditions. *ChemElectroChem* **2015,** 2, 354-358.
(27) Resasco, J.; Lum, Y.; Clark, E. L.; Zeledon, J. Z.; Bell, A. T. Effects of Anion Identity and Concentration on Electrochemical Reduction of CO_2. *ChemElectroChem.* **2018,** 5, 1064-1072.
(28) Butler, J. N., The Basic Equations In *Carbon dioxide equilibria and their applications*. Addison-Wesley series in Civil Engineering; Addison-Wesley: Reading, Mass. **1982,** 1, 15-43.

(29) Haynes, W. M., Ed. Diffusion of Gases in Water In *Handbook of chemistry and physics*. 94th Edition, CRC press: Boca Raton, FL. **2014**, 6-250.
(30) Singh, M. R.; Clark, E. L.; Bell, A. T. Effects of Electrolyte, Catalyst, and Membrane Composition and Operating Conditions on the Performance of Solar-Driven Electrochemical Reduction of Carbon Dioxide. *Phys. Chem. Chem. Phys.* **2015,** 17, 18924-18936.
(31) Gupta, N.; Gattrell, M.; MacDougall, B. Calculation for the Cathode Surface Concentrations in the Electrochemical Reduction of CO_2 in $KHCO_3$ Solutions. *J. Appl. Electrochem.* **2006,** 36, 161-172.
(32) Lobaccaro, P.; Singh, M. R.; Clark, E. L.; Kwon, Y.; Bell, A. T.; Ager, J. W. Effects of Temperature and Gas-Liquid Mass Transfer on the Operation of Small Electrochemical Cells for the Quantitative Evaluation of CO_2 Reduction Electrocatalysts. *Phys. Chem. Chem. Phys.* **2016,** 18, 26777-26785.
(33) Clark, E. L.; Singh, M. R.; Kwon, Y.; Bell, A. T. Differential Electrochemical Mass Spectrometer Cell Design for Online Quantification of Products Produced During Electrochemical Reduction of CO_2. *Anal. Chem.* **2015,** 87, 8013-8020.
(34) Dunwell, M.; Yang, X.; Setzler, B. P.; Anibal, J.; Yan, Y.; Xu, B.; Examination of Near-Electrode Concentration Gradients and Kinetic Impacts on the Electrochemical Reduction of CO_2 using Surface-Enhanced Infrared Spectroscopy. *ACS Catal.* **2018**, 8, 3999-4008.
(35) Clark, E. L.; Bell, A. T. Direct Observation of the Local Reaction Environment during the Electrochemical Reduction of CO_2. *J. Am. Chem. Soc.* Just Accepted Manuscript. DOI: 10.1021/jacs.8b04058
(36) Butt, J. B.; Petersen, E. E., Physical & Chemical Description of Deactivation In *Activation, Deactivation, and Poisoning of Catalysts*, Academic Press Inc.: San Diego, **1988**, 4-25.
(37) Kuhl, K. P.; Hatsukade, T.; Cave, E. R.; Abram, D. N.; Kibsgaard, J.; Jaramillo, T. F. Electrocatalytic Conversion of Carbon Dioxide to Methane and Methanol on Transition Metal Surfaces. *J. Am. Chem. Soc.* **2014,** 136, 14107-14113.
(38) Hori, Y.; Konishi, H.; Futamura, T.; Murata, A.; Koga, O.; Sakurai, H.; Oguma, K. "Deactivation of Copper Electrode" in Electrochemical Reduction of CO_2. *Electrochim. Acta* **2005,** 50, 5354-5369.
(39) Wuttig, A.; Surendranath, Y. Impurity Ion Complexation Enhances Carbon Dioxide Reduction Catalysis. *ACS Catal.* **2015,** 5, 4479-4484.
(40) Seah, M. P.; Dench, W. A. Quantitative Electron Spectroscopy of Surfaces: A Standard Data Base for Electron Inelastic Mean Free Paths in Solids. *Surf. Interface Anal.* **1979,** 1, 2-11.
(41) Shard, A. G. Detection Limits in Xps for More Than 6000 Binary Systems Using Al and Mg Kα X-Rays. *Surf. Interface Anal.* **2014,** 46, 175-185.
(42) Cushman, C. V.; Bruner, P.; Zakel, J.; Major, G. H.; Lunt, B. M.; Smith, N. J.; Grehl, T.; Linford, M. R. Low Energy Ion Scattering (LEIS). A Practical Introduction to Its Theory, Instrumentation, and Applications. *Anal. Methods* **2016,** 8, 3419-3439.
(43) Lopes, P. P.; Strmcnik, D.; Tripkovic, D.; Connell, J. G.; Stamenkovic, V.; Markovic, N. M. Relationships between Atomic Level Surface Structure and Stability/Activity of Platinum Surface Atoms in Aqueous Environments. *ACS Catal.* **2016,** 6, 2536-2544.
(44) Chen, R.; Yang, C.; Cai, W.; Wang, H.-Y.; Miao, J.; Zhang, L.; Chen, S.; Liu, B. Use of Platinum as the Counter Electrode to Study the Activity of Nonprecious Metal Catalysts for the Hydrogen Evolution Reaction. *ACS Energy Lett.* **2017,** 2, 1070-1075.
(45) Dong, G.; Fang, M.; Wang, H.; Yip, S.; Cheung, H.-Y.; Wang, F.; Wong, C.-Y.; Chu, S. T.; Ho, J. C. Insight into the Electrochemical Activation of Carbon-Based Cathodes for Hydrogen Evolution Reaction. *J. Mater. Chem. A* **2015,** 3, 13080-13086.

(46) Cherevko, S.; Zeradjanin, A. R.; Topalov, A. A.; Kulyk, N.; Katsounaros, I.; Mayrhofer, K. J. J. Dissolution of Noble Metals During Oxygen Evolution in Acidic Media. *ChemCatChem* **2014,** 6, 2219-2223.
(47) Cherevko, S.; Zeradjanin, A. R.; Keeley, G. P.; Mayrhofer, K. J. J. A Comparative Study on Gold and Platinum Dissolution in Acidic and Alkaline Media. *J. Electrochem. Soc.* **2014,** 161, 822-830.
(48) Chen, J. G.; Jones, C. W.; Linic, S.; Stamenkovic, V. R. Best Practices in Pursuit of Topics in Heterogeneous Electrocatalysis. *ACS Catal.* **2017,** 7, 6392-6393.
(49) Dunwell, M.; Lu, Q.; Heyes, J. M.; Rosen, J.; Chen, J. G.; Yan, Y.; Jiao, F.; Xu, B. The Central Role of Bicarbonate in the Electrochemical Reduction of Carbon Dioxide on Gold. *J. Am. Chem. Soc.* **2017,** 139, 3774-3783.
(50) Boudart, M. Turnover Rates in Heterogeneous Catalysis. *Chem. Rev.* **1995,** 95, 661-666.
(51) Gasteiger, H. A.; Kocha, S. S.; Sompalli, B.; Wagner, F. T. Activity Benchmarks and Requirements for Pt, Pt-Alloy, and Non-Pt Oxygen Reduction Catalysts for PEMFCs. *Appl. Catal. B: Environ.* **2005,** 56, 9-35.
(52) McCrory, C. C. L.; Jung, S.; Peters, J. C.; Jaramillo, T. F. Benchmarking Heterogeneous Electrocatalysts for the Oxygen Evolution Reaction. *J. Am. Chem. Soc.* **2013,** 135, 16977-16987.
(53) McCrory, C. C. L.; Jung, S.; Ferrer, I. M.; Chatman, S. M.; Peters, J. C.; Jaramillo, T. F. Benchmarking Hydrogen Evolving Reaction and Oxygen Evolving Reaction Electrocatalysts for Solar Water Splitting Devices. *J. Am. Chem. Soc.* **2015,** 137, 4347-4357.
(54) Bligaard, T.; Bullock, R. M.; Campbell, C. T.; Chen, J. G.; Gates, B. C.; Gorte, R. J.; Jones, C. W.; Jones, W. D.; Kitchin, J. R.; Scott, S. L. Toward Benchmarking in Catalysis Science: Best Practices, Challenges, and Opportunities. *ACS Catal.* **2016,** 6, 2590-2602.
(55) Benck, J. D.; Hellstern, T. R.; Kibsgaard, J.; Chakthranont, P.; Jaramillo, T. F. Catalyzing the Hydrogen Evolution Reaction (HER) with Molybdenum Sulfide Nanomaterials. *ACS Catal.* **2014,** 4, 3957-3971.
(56) Trasatti, S.; Petrii, O. A., Real surface area measurements in electrochemistry. *Pure Appl. Chem.*, 1991; 63, 711-734.
(57) Jovanov, Z. P.; Hansen, H. A.; Varela, A. S.; Malacrida, P.; Peterson, A. A.; Nørskov, J. K.; Stephens, I. E. L.; Chorkendorff, I. Opportunities and challenges in the electrocatalysis of CO_2 and CO reduction using bifunctional surfaces: A theoretical and experimental study of Au-Cd alloys. *J. Catal.* **2016,** 343, 215-231.
(58) Chen, Y.; Li, C. W.; Kanan, M. W. Aqueous CO_2 Reduction at Very Low Overpotential on Oxide-Derived Au Nanoparticles. *J. Am. Chem. Soc.* **2012,** 134, 19969-19972.
(59) Chen, Y.; Kanan, M. W. Tin Oxide Dependence of the CO_2 Reduction Efficiency on Tin Electrodes and Enhanced Activity for Tin/Tin Oxide Thin-Film Catalysts. *J. Am. Chem. Soc.* **2012,** 134, 1986-1989.
(60) Roberts, F. S.; Kuhl, K. P.; Nilsson, A. Electroreduction of Carbon Monoxide over a Copper Nanocube Catalyst: Surface Structure and pH Dependence on Selectivity. *ChemCatChem* **2016,** 8, 1119-1124.
(61) Kwon, Y.; Lum, Y.; Clark, E. L.; Ager, J. W.; Bell, A. T. CO_2 Electroreduction with Enhanced Ethylene and Ethanol Selectivity by Nanostructuring Polycrystalline Copper. *ChemElectroChem* **2016,** 3, 1012-1019.
(62) Ma, M.; Djanashvili, K.; Smith, W. A. Controllable Hydrocarbon Formation from the Electrochemical Reduction of CO_2 over Cu Nanowire Arrays. *Angew. Chem. Int. Ed.* **2016,** 55, 6680-6684.
(63) Ren, D.; Deng, Y.; Handoko, A. D.; Chen, C. S.; Malkhandi, S.; Yeo, B. S. Selective Electrochemical Reduction of Carbon Dioxide to Ethylene and Ethanol on Copper(I) Oxide Catalysts. *ACS Catal.* **2015,** 5, 2814-2821.

(64) Raciti, D.; Livi, K. J.; Wang, C. Highly Dense Cu Nanowires for Low-Overpotential CO_2 Reduction. *Nano Lett.* **2015,** 15, 6829-6835.
(65) Verdaguer-Casadevall, A.; Li, C. W.; Johansson, T. P.; Scott, S. B.; McKeown, J. T.; Kumar, M.; Stephens, I. E. L.; Kanan, M. W.; Chorkendorff, I. Probing the Active Surface Sites for CO Reduction on Oxide-Derived Copper Electrocatalysts. *J. Am. Chem. Soc.* **2015,** 137, 9808-9811.
(66) Feng, X.; Jiang, K.; Fan, S.; Kanan, M. W. A Direct Grain-Boundary-Activity Correlation for CO Electroreduction on Cu Nanoparticles. *ACS Cent. Sci.* **2016,** 2, 169-174.
(67) Gao, D.; Zegkinoglou, I.; Divins, N. J.; Scholten, F.; Sinev, I.; Grosse, P.; Roldan Cuenya, B. Plasma-Activated Copper Nanocube Catalysts for Efficient Carbon Dioxide Electroreduction to Hydrocarbons and Alcohols. *ACS Nano* **2017,** 11, 4825-4831.
(68) Cheng, T.; Xiao, H.; Goddard, W. A. Nature of the Active Sites for CO Reduction on Copper Nanoparticles; Suggestions for Optimizing Performance. *J. Am. Chem. Soc.* **2017,** 139, 11642-11645.
(69) Favaro, M.; Xiao, H.; Cheng, T.; Goddard, W. A.; Yano, J.; Crumlin, E. J. Subsurface Oxide Plays a Critical Role in CO_2 Activation by Cu(111) Surfaces to Form Chemisorbed CO_2, the First Step in Reduction of CO_2. *Proc. Natl. Acad. Sci.* **2017,** 114, 6706-6711.
(70) Cavalca, F.; Ferragut, R.; Aghion, S.; Eilert, A.; Diaz-Morales, O.; Liu, C.; Koh, A. L.; Hansen, T. W.; Pettersson, L. G. M.; Nilsson, A. Nature and Distribution of Stable Subsurface Oxygen in Copper Electrodes During Electrochemical CO_2 Reduction. *J. Phys. Chem. C* **2017,** 121, 25003-25009.
(71) Eilert, A.; Cavalca, F.; Roberts, F. S.; Osterwalder, J.; Liu, C.; Favaro, M.; Crumlin, E. J.; Ogasawara, H.; Friebel, D.; Pettersson, L. G. M.; Nilsson, A. Subsurface Oxygen in Oxide-Derived Copper Electrocatalysts for Carbon Dioxide Reduction. *J. Phys. Chem. Lett.* **2017,** 8, 285-290.
(72) Liu, C.; Lourenço, M. P.; Hedström, S.; Cavalca, F.; Diaz-Morales, O.; Duarte, H. A.; Nilsson, A.; Pettersson, L. G. M. Stability and Effects of Subsurface Oxygen in Oxide-Derived Cu Catalyst for CO_2 Reduction. *J. Phys. Chem. C* **2017**, 121, 25010-25017.

2.9 Supplementary Information

2.9.1 Experimental Methods at the University of California at Berkeley

2.9.1.1 Electrode Preparation

Epitaxial Cu and Ag thin films were prepared by sputter disposition onto single-side polished Si(111), (100), or (110) wafers (Virginia semiconductor, 1-10 Ω cm). The native oxide was removed from the surface of the Si substrates prior to deposition by submerging them in a 10 wt. % HF solution for 5 min. Immediately after HF etching the Si wafers were transferred into an AJA ATC Orion-5 sputtering system for deposition. The Cu (99.999% Kurt Lesker) and Ag (99.999% Kurt Lesker) were deposited under Ar at a pressure of 2 mTorr at a rate of 1 Å/s, which was calibrated using a quartz crystal monitor. The total film thickness deposited was 100 nm. Cu deposition was conducted at ambient temperature whereas Ag deposition was conducted at 300 °C by heating the sample stage using an IR lamp. Cu(111) and (100) oriented thin films were obtained by deposition onto Si(110) and (100) substrates, respectively, whereas Ag(111) and (100) oriented thin films were obtained by deposition onto Si(111) and (100) substrates, respectively. Ag foils (99.999% Alfa Aesar) were mechanically polished with a series of sandpapers (600, 1200, and 2500 grit 3M) and sonicated in DI water for 30 min before electrochemical testing.

2.9.1.2 Electrode Characterization

The structure of the Cu and Ag thin films were characterized by X-ray diffraction. The orientation and epitaxial quality of the films were determined using symmetric θ-2θ scans, in plane ϕ scans, ω scans or rocking curves, and pole figures. XRD patterns were taken with a PANanalytical X'Pert diffractometer using Cu Kα radiation (λ = 1.54056 Å). Symmetric θ-2θ scans were collected on samples fixed onto a flat glass slide in locked-coupled mode with a goniometer resolution of 0.001°. The near-surface composition of electrodes was measured using a Kratos Axis Ultra DLD X-ray photoelectron spectrometer (XPS). All spectra were acquired using monochromatized Al Kα radiation (15 kV, 15 mA). Ar sputtering of the sample surface was avoided to prevent surface composition changes. The kinetic energy scale of the measured core level spectra was calibrated by setting the C 1s binding energy to 284.8 eV. Further analysis of surface composition was done using ion scattering spectroscopy (ISS) using the same instrument. All ISS spectra were acquired using a focused He ion beam (1 kV).

2.9.1.3 Electrochemical Measurements

All electrochemical experiments were conducted in a gas-tight electrochemical cell machined from polyether ether ketone (PEEK). A schematic of the cell is shown below in Figure S2.1. Further details of this electrochemical cell are described in previous works.[1] The cell was sonicated in 20 wt. % nitric acid and thoroughly rinsed with DI water prior to all experimentation. The working and counter electrodes were parallel and separated by an anion-conducting membrane (Selemion AMV AGC Inc.). Gas dispersion frits were incorporated into both electrode chambers to provide ample electrolyte mixing. The

exposed geometric surface area of each electrode was 1 cm^2 and the electrolyte volume of each electrode chamber was 1.8 mL. The counter electrode was a glassy carbon plate (Type 2 Alfa Aesar) that was also sonicated in 20 wt. % nitric acid prior to all experimentation. Platinum foil was also used as the anode. The working electrode potential was referenced against a Ag/AgCl electrode (Innovative Instruments Inc.) that was calibrated against a homemade standard hydrogen electrode. A 0.05 M M_2CO_3 (99.995% Sigma Aldrich) solution prepared using 18.2 MΩ DI water was used as the electrolyte. Metallic impurities in the as-prepared electrolyte were removed before electrolysis by chelating them with Chelex 100 (Na form Sigma Aldrich). Both electrode chambers were sparged with CO_2 (99.999% Praxair Inc.) at a rate of 2.5 to 40 sccm for 30 min prior to and throughout the duration of all electrochemical measurements. Upon saturation with CO_2 the pH of the electrolyte was 6.8, which was maintained throughout the duration of chronoamperometry.

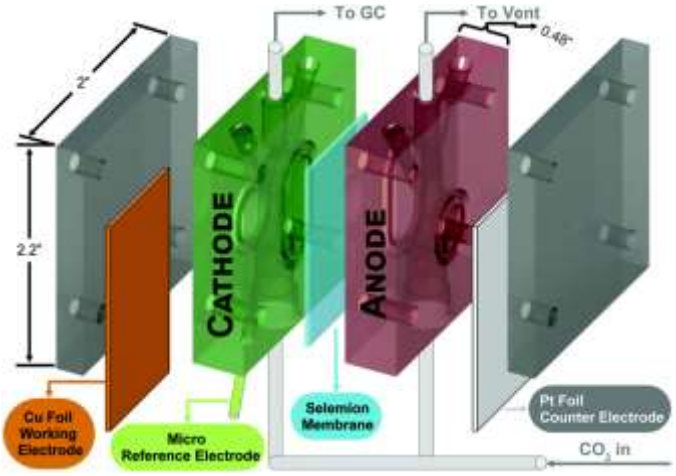

Figure S2.1 *– Schematic of the electrochemical cell used for testing at Berkeley. Reproduced from Lobaccaro et al[1]. Copyright 2016, Royal Society of Chemistry.*

Electrochemistry was performed using a Biologic VSP-300 potentiostat. All electrochemical measurements were recorded versus the reference electrode and converted to the RHE scale. Potentiostatic electrochemical impedance spectroscopy (PEIS) was used to determine the uncompensated resistance (R_u) of the electrochemical cell by applying voltage waveforms about the open circuit potential with an amplitude of 20 mV and frequencies ranging from 50 Hz to 500 kHz. The potentiostat compensated for 85% of R_u *in-situ* and the last 15% was post-corrected to arrive at accurate potentials. The electrocatalytic activity of each electrode was assessed by conducting a chronoamperometry staircase at increasingly negative applied potentials.

2.9.1.4 Product Analysis

The effluent from the electrochemical cell was introduced directly into the sampling loop of an Agilent 7890B gas chromatograph (GC) equipped with a pulsed-discharge helium ionization detector (PDHID). The effluent was sampled after the first 10 min of chronoamperometry and every 14 min thereafter. The constituents of the gaseous sample were separated in He (99.9999% Praxair Inc.) using a Hayesep-Q capillary column (Agilent) in series with a packed ShinCarbon ST column (Restek Co.). After sampling the reaction effluent the column oven was maintained at 50 °C for 1 min followed by a temperature ramp at 30 °C/min to 250 °C, which was maintained for the duration of the analysis. The signal response of the PDHID was calibrated by analyzing a series of NIST-traceable standard gas mixtures (Airgas Inc.).

The electrolyte from both electrode chambers was collected after electrolysis and analyzed using a Thermo Scientific UltiMate 3000 liquid chromatograph (HPLC) equipped with a refractive index detector (RID). The electrolyte samples were stored in a refrigerated autosampler until analyzed in order to minimize the evaporation of volatile liquid-phase reaction products. The liquid-phase products contained in a 10 µL aliquot were separated using a series of two Aminex HPX 87-H columns (Bio-Rad Inc.) and a 1 mM sulfuric acid eluent (99.999% Sigma Aldrich). The column oven was maintained at 60 °C for the duration of the analysis. The signal response of the RID was calibrated by analyzing standard solutions of each product at a concentration of 1, 10, and 50 mM.

2.9.2 Experimental Methods at Stanford University

The experimental methods employed at Stanford University have been fully described in previous works.[2, 3] The electrode preparation and electrochemical testing was conducted using similar methodologies as those employed at the University of California at Berkeley. The electrochemical experiments were conducted in a gas-tight electrochemical cell machined from polycarbonate. A schematic of the cell is shown in Figure S2.2. Further details of this electrochemical cell are described in previous works.[4] 0.1 M $KHCO_3$ (Sigma-Aldrich, 99.99% metals basis) was used as the electrolyte, which was constantly sparged with CO_2 (5.0, Praxair) at a flow rate of 20 sccm. The pH of the electrolyte was maintained at 6.8 during all experimentation. The effluent of the electrochemical cell was introduced directly into the sampling loop of a gas chromatograph (GC, SRI 8610C in the Multi-Gas #3 configuration). The compartments of the electrochemical cell were separated by an anion exchange membrane (Selemion AMV, AGC Inc.). A Ag/AgCl (Accumet) electrode was used as the reference electrode and a platinum foil was used as the counter electrode. Polycrystalline silver foil (Alfa Aesar, 0.1 mm thickness, 99.998% metals basis), was mechanically polished (3M, 400 grit) and rinsed with water until no discoloration was observed on the surface prior to each electrochemical experiment. Thin films of Cu were prepared inside a Temescal BJD-1800 chamber by electron beam evaporation. Si(100) and (110) were used as substrates to produce epitaxial Cu(100) and (111) thin films, respectively. The native oxide was removed with buffered hydrofluoric acid (BHF) before loading the samples into the chamber. After evacuating the chamber, 100 nm of Cu was deposited at 2 Å/s on the Si substrates.

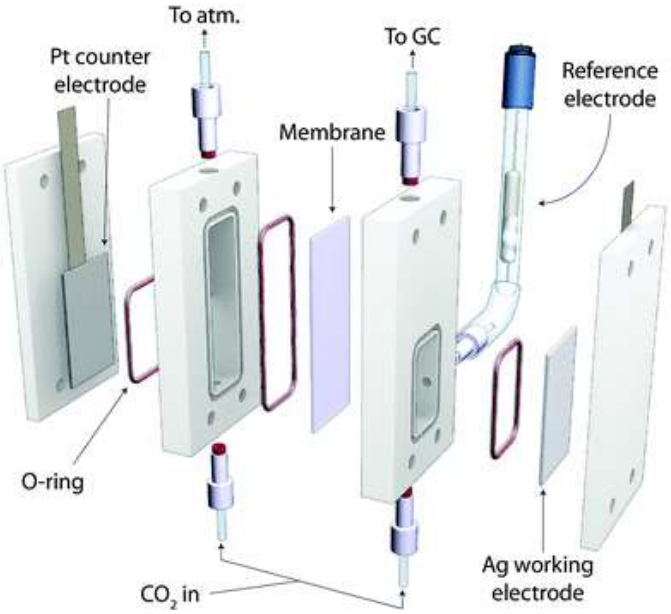

Figure S2.2 *– Schematic of the electrochemical cell used for testing at Stanford. Reproduced from Hatsukade et al.[2] Copyright 2014, Royal Society of Chemistry.*

2.9.3 Impact of Mechanical Polishing on Surface Purity

Different surface preparation methods can introduce variations in the activity and selectivity between samples of the same metal.[5, 6] Surface preparation methods reported in the literature include various forms of mechanical and electrochemical polishing. Understanding how these treatments affect the purity of the catalyst surface is critical to obtaining accurate and reproducible results. Figure S2.3 shows the surface composition of a Cu foil after various mechanical polishing treatments. Residues of the polishing compound are detected in the electrode surface after rising. This is especially problematic for alumina polishes as Al is an active HER metal. No attempt was made to characterize the impact that different surface preparation methods have on the morphology of the electrode surface, the distribution of undercoordinated sites, or its measured electrocatalytic activity.

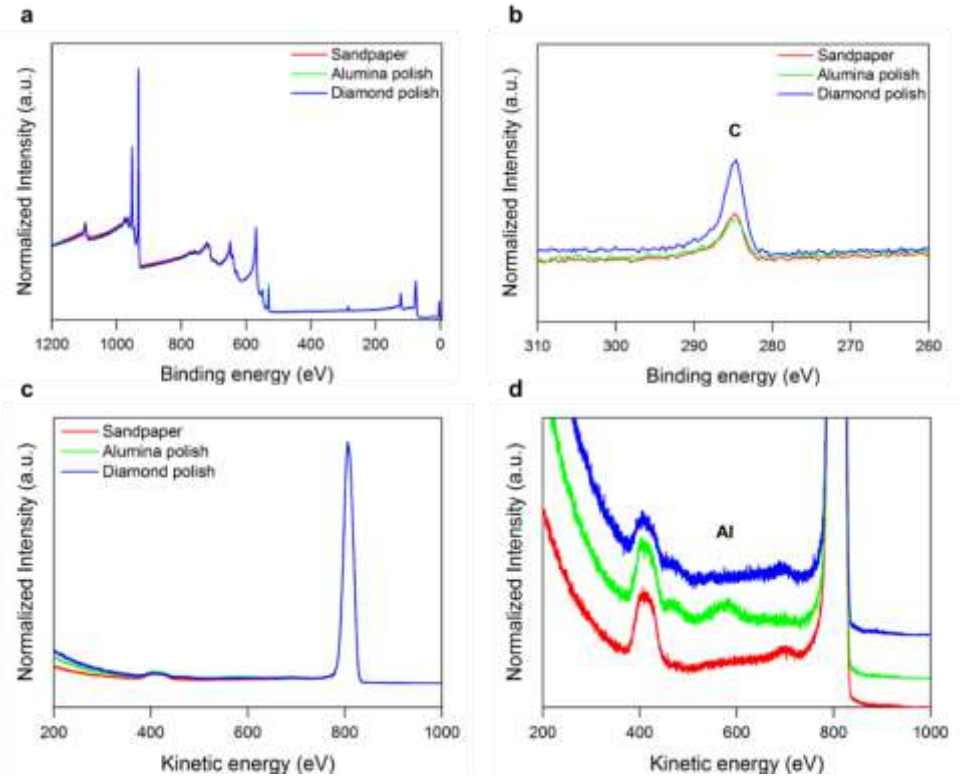

Figure S2.3 *– Surface characterization after different mechanical polishing pretreatments. (A) XPS survey scan, (B) C 1s scan, and (C)/(D) ISS scans for Cu foils mechanically polished with different polishing compounds.*

2.9.4 Quantification of the Hydrodynamic Boundary Layer Thickness

The hydrodynamic boundary layer thickness of an electrochemical cell can be quantified by measuring the diffusion-limited current of ferricyanide reduction:

$$Fe(CN)_6^{3-} + e^- \rightarrow Fe(CN)_6^{4-}$$

Ferricyanide reduction is an ideal reaction to probe the hydrodynamic boundary layer thickness due to its electrochemical reversibility, meaning that the reduction of ferricyanide is facile such that the observed rate is limited only by mass transfer regardless of the applied overpotential. When conducting this measurement, the total ferricyanide concentration should be minimized and the supporting electrolyte should be identical to that typically employed during CO_2 reduction. This will ensure that the fluid properties of the solution utilized to quantify the hydrodynamic boundary layer thickness accurately reflect those of the electrolytes typically employed to measure electrocatalytic activity. Furthermore, Au electrodes should be utilized to conduct the measurement to avoid Galvanic corrosion processes in which ferricyanide is the oxidizing agent. Figure S2.4A depicts cyclic voltammograms measured in 0.1 M $CsHCO_3$ electrolytes with and without the addition of 10 mM $K_3Fe(CN)_6$. There is a potential window of ~600 mV where the observed Faradaic current can be attributed entirely to ferricyanide reduction. Furthermore, the observed rate of ferricyanide reduction is independent of the applied voltage, which is a result of its electrochemical reversibility, as previously mentioned. Thus, the steady state diffusion-limited current density associated with ferricyanide reduction can be measured and utilized to calculate the average hydrodynamic boundary layer thickness at the cathode surface using Fick's law:

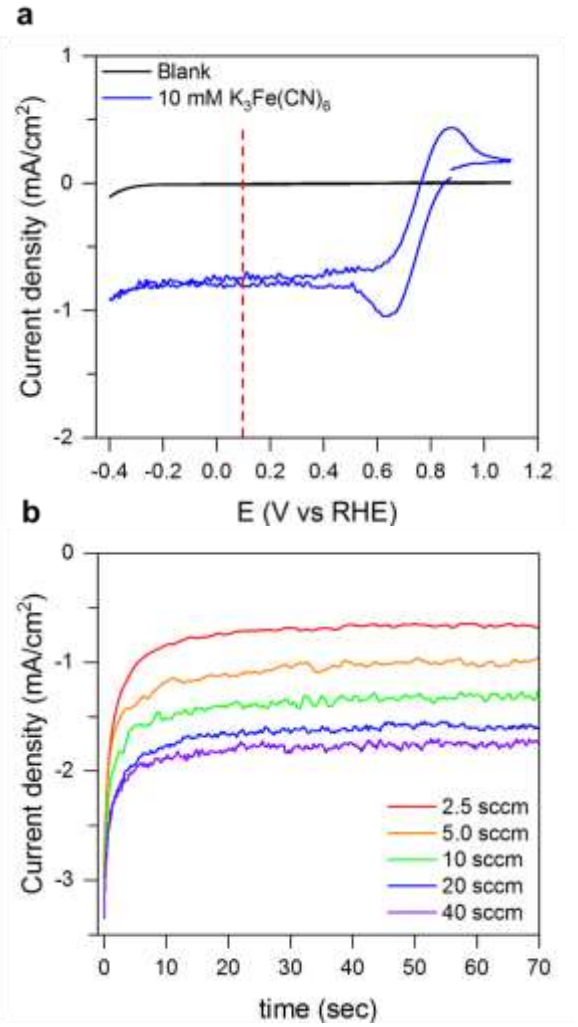

Figure S2.4 *– Quantification of the hydrodynamic boundary layer thickness of an electrochemical cell. (A) Cyclic voltammograms obtained in 0.1 M $CsHCO_3$ saturated with CO_2 with and without the addition of 10 mM $K_3Fe(CN)_6$. The dotted red line indicates the potential used in the subsequent chronoamperometry experiments. (B) Chronoamperometry experiments utilized to measure the diffusion-limited current density of ferricyanide reduction under a series of different hydrodynamic conditions.*

$$\delta_{BL} = \frac{F \times D_{Fe(CN)_6{}^{3-}} \times C^*_{Fe(CN)_6{}^{3-}}}{J_{SS}}$$

As shown in Figure S2.4B, the steady state current density associated with ferricyanide reduction increases as the flow rate of CO_2 through the cell increases, which occurs due to the enhanced mixing of the electrolyte by the column of CO_2 bubbles near the cathode.

2.9.5 XPS and ISS Analysis of Tested Polycrystalline Ag Films

XPS and ISS were conducted on the polycrystalline Ag thin films tested under different hydrodynamic conditions to confirm that the observed trends were not being influenced by varying impurity concentrations. As shown in Figure S2.5, all electrodes were observed to be completely free of contamination within the detection limits of XPS and ISS.

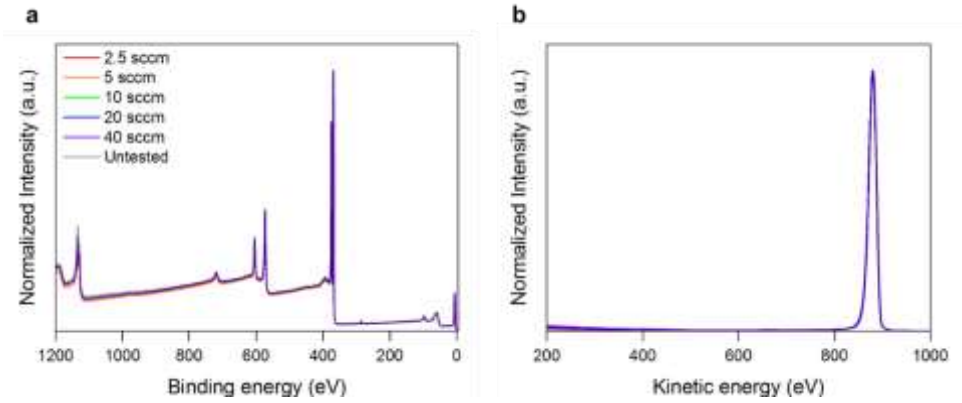

Figure S2.5 *– (A) XPS and (B) ISS characterization of the surface purity of polycrystalline Ag before and after chronoamperometry staircases in Chelex-pretreated 0.1 M $CsHCO_3$ using a glassy carbon anode.*

2.9.6 Dependence of the Measured Activity of Polycrystalline Ag on the Hydrodynamics of the Electrochemical Cell

The CO partial current density observed over polycrystalline Ag deviates from Tafel kinetics at roughly -1 V vs RHE, as shown in Figure S2.6. This deviation is due to concentration polarization of the electrode surface. As a result, the observed activity at potentials negative of -1 V vs RHE is dependent on the hydrodynamics of the electrochemical cell. To illustrate this the maximum rate of CO_2 consumption over polycrystalline Ag was measured under a series of different hydrodynamic conditions. The maximum rate of CO_2 consumption was found to scale inversely with the hydrodynamic boundary layer thickness, as shown on Figure S2.7. This is exactly what would be expected for a reaction that is limited by diffusive mass transfer of a reactant through a stagnant boundary layer.

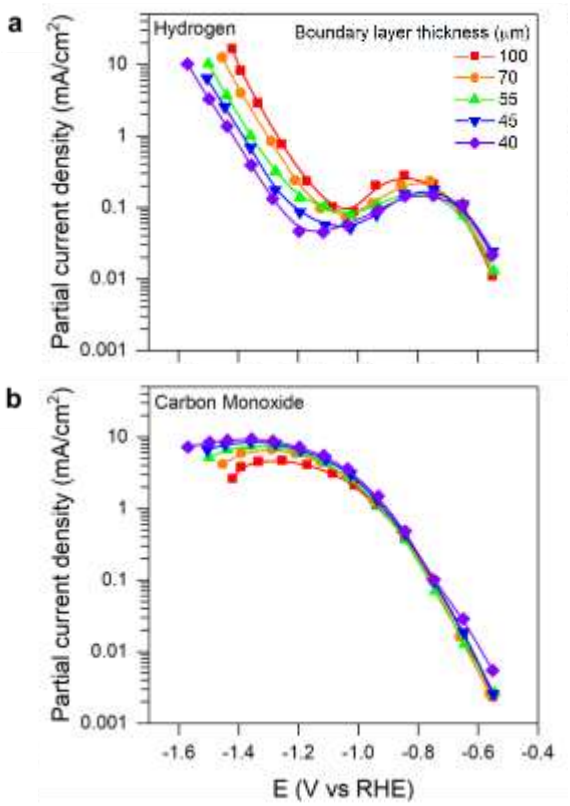

Figure S2.6 *– Dependence of the measured activity of polycrystalline Ag on the hydrodynamics of the electrochemical cell. (A) H_2 partial current density. (B) CO partial current density.*

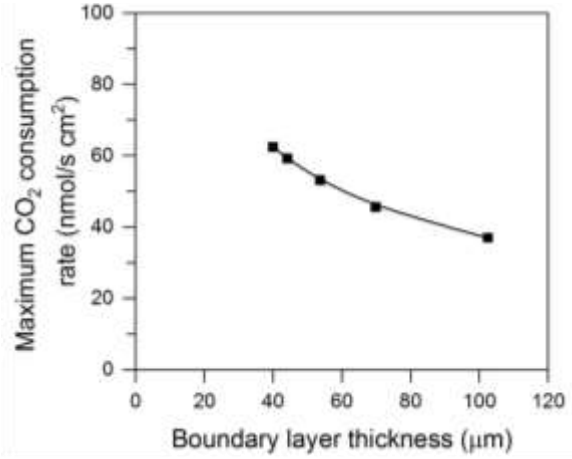

Figure S2.7 *– Maximum rate of CO_2 consumption observed over polycrystalline Ag in 0.1 M $CsHCO_3$ as a function of the hydrodynamic boundary layer thickness.*

2.9.7 Calculation of the Significance of Electrolyte Impurities

The concentration of contaminants in the catholyte that result in a coverage of 0.1 ML equivalents on the cathode surface was calculated assuming a surface atom density of 10^{15} atoms/cm^2 and that all the impurities in the electrolyte are deposited onto the cathode surface over the course of electrolysis using:

$$C = \frac{A/V * RF}{6.022}$$

Where:

C	Concentration of impurities resulting in 0.1 ML coverage
A	Geometric surface area of cathode
V	Catholyte volume
RF	Roughness factor of the cathode

2.9.8 Quantification of Surface Roughness by Capacitive Cycling

The surface roughness of the electrochemically cycled Ag electrode was determined relative to a mechanically polished Ag foil by taking the ratio of their double layer capacitances. The double layer capacitance was determined by measuring the charging current in a potential range where no Faradaic processes occur at a series of increasingly rapid scan rates, as shown in Figure S2.8A. The double layer capacitance was then determined by calculating the scan rate dependence of the observed charging current, as shown in Figure S2.8B. Finally, the roughness factor of the electrochemically cycled electrode was determined by normalizing the calculated double layer capacitance by that measured over the mechanically polished Ag foil.

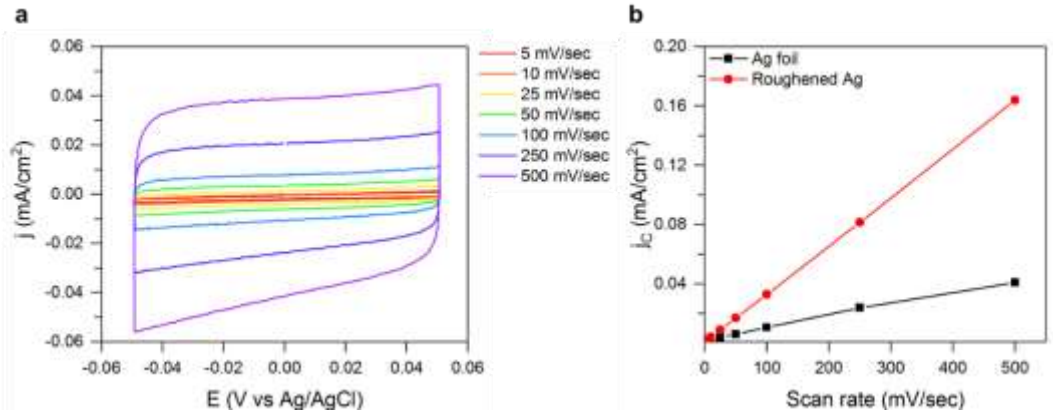

Figure S2.8 *– Determination of relative roughness of Ag catalysts (A) Capacitive cycling of a mechanically polished Ag foil over a 100 mV non-Faradaic region in a 0.1 M $HClO_4$ electrolyte. (B) Capacitive current vs scan rate.*

2.9.9 Comparison of ECSA Normalized Activity of Cu-Based Catalysts

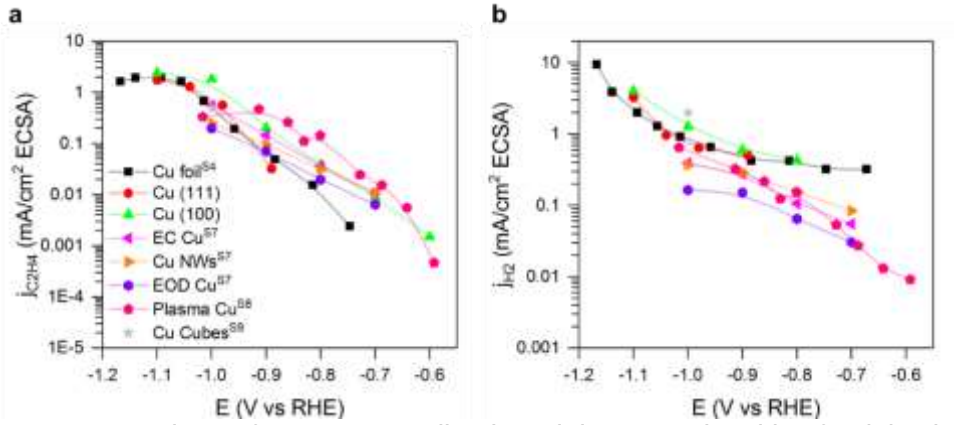

Figure S2.9 *– Comparison of ECSA normalized partial current densities for (A) ethylene and (B) hydrogen over different Cu-based catalysts.*

2.9.10 Supplementary Information References

(1) Lobaccaro, P.; Singh, M. R.; Clark, E. L.; Kwon, Y.; Bell, A. T.; Ager, J. W. Effects of Temperature and Gas-Liquid Mass Transfer on the Operation of Small Electrochemical Cells for the Quantitative Evaluation of CO_2 Reduction Electrocatalysts. *Phys. Chem. Chem. Phys.* **2016,** 18, 26777-26785.

(2) Hatsukade, T.; Kuhl, K. P.; Cave, E. R.; Abram, D. N.; Jaramillo, T. F. Insights into the Electrocatalytic Reduction of CO_2 on Metallic Silver Surfaces. *Phys. Chem. Chem. Phys.* **2014,** 16, 13814-13819.

(3) Hahn, C.; Hatsukade, T.; Kim, Y.-G.; Vailionis, A.; Baricuatro, J. H.; Higgins, D. C.; Nitopi, S. A.; Soriaga, M. P.; Jaramillo, T. F. Engineering Cu Surfaces for the Electrocatalytic Conversion of CO_2: Controlling Selectivity toward Oxygenates and Hydrocarbons. *Proc. Natl. Acad. Sci.* **2017,** 114, 5918-5923.

(4) Kuhl, K. P.; Cave, E. R.; Abram, D. N.; Jaramillo, T. F. New Insights into the Electrochemical Reduction of Carbon Dioxide on Metallic Copper Surfaces. *Energy Environ. Sci.* **2012,** 5, 7050-7059.

(5) Tang, W.; Peterson, A.; Varela, A.; Jovanov, Z.; Bech, L.; Durand, W.; Dahl, S.; Norskov, J.; Chorkendorff, I. The Importance of Surface Morphology in Controlling the Selectivity of Polycrystalline Copper for CO_2 Electroreduction. *Phys. Chem. Chem. Phys.* **2012,** 14, 76-81.

(6) Terunuma, Y.; Saitoh, A.; Momose, Y. Relationship Between Hydrocarbon Production in the Electrochemical Reduction of CO_2 and the Characteristics of the Cu Electrode. *J. Electroanal. Chem.* **1997,** 434, 69-75.

(7) Lum, Y.; Yue, B.; Lobaccaro, P.; Bell, A.T.; Ager, J. W.; Optimizing C–C Coupling on Oxide-Derived Copper Catalysts for Electrochemical CO_2 Reduction. *J. Phys. Chem.C.* **2017,** *121,* 14191-14203.

(8) Mistry, H.; Varela, A. S.; Bonifacio, C. S.; Zegkinoglou, I.; Sinev, I.; Choi, Y. W.; Kisslinger, K.; Stach, E. A.; Yang, J. C.; Strasser, P.; Cuenya, B. R. Highly Selective Plasma-Activated Copper Catalysts for Carbon Dioxide Reduction to Ethylene. *Nat. Commun.* **2016,** 7, 1-9.

(9) Roberts, F. S.; Kuhl, K. P.; Nilsson, A. Electroreduction of Carbon Monoxide over a Copper Nanocube Catalyst: Surface Structure and pH Dependence on Selectivity. *ChemCatChem* **2016,** 8, 1119-1124.

Chapter 3

Influence of Surface Atomic Structure on the Intrinsic CO_2 Reduction Activity of Ag Electrocatalysts

Abstract

The electrochemical reduction of carbon dioxide (CO_2) to carbon monoxide (CO) over silver (Ag) electrocatalysts has received substantial contemporary interest. This has resulted in the discovery of nanostructured Ag electrocatalysts with superior activity to polycrystalline Ag foils. Unfortunately, identifying the causes of the improved intrinsic activity exhibited by these electrocatalysts has been difficult, partially due to a lack of experimental and theoretical relationships between the surface atomic structure and intrinsic activity of Ag electrocatalysts for CO_2 reduction. Herein, we elucidate the impact of the surface atomic structure on the intrinsic CO evolution activity of Ag electrocatalysts by investigating CO_2 reduction over epitaxially grown Ag thin films with (111), (100), and (110) orientations. The surface atomic structures of the Ag thin films are validated under electrochemical conditions using *operando* electrochemical scanning tunneling microscopy. The CO_2 reduction activity of the Ag thin films is then investigated both theoretically and experimentally, leading to the conclusion that step edge defects substantially contribute to the activity observed over Ag(111) and Ag(100) thin films. Furthermore, the intrinsically superior activity of these step edge defects and the Ag(110) surfaces is hypothesized to be the result of enhanced electric field stabilization of polarizable intermediates of CO_2 reduction, which possess substantial dipole moments. The enhanced electric field stabilization over these undercoordinated surface sites is a result of an enhanced surface charge density, which leads to the formation of stronger local electric fields upon polarization to a given potential.

3.1 Introduction

Carbon dioxide (CO_2) can be electrochemically reduced to fuel precursors, such as carbon monoxide (CO).[1–3] Polycrystalline silver (Ag) has been identified as one of the only monometallic electrocatalysts capable of achieving Faradaic efficiencies for CO evolution approaching 100%, albeit over a narrow potential range.[4–7] Recently,

nanostructured Ag electrocatalysts have been developed with superior CO_2 reduction activity than polycrystalline Ag foils.[8–12] While such electrocatalysts exhibit superior Faradaic efficiencies for CO evolution than polycrystalline Ag foils, it is not always clear if they also exhibit intrinsically superior activity due to the lack of surface area normalized activity data. However, the hypothesized causes for the intrinsically superior CO evolution activity in the cases where it has been convincingly demonstrated vary from the presence of surface defects,[8,11] an elevated local pH,[10] and residual halide promotion.[9]

While the notion that the CO evolution activity of surface defects are superior to basal planes is supported by calculations of the CO evolution reaction thermodynamics over different Ag surfaces,[13] these models lack contemporary validation. In fact, the CO_2 reduction activity of Ag single crystals has only been reported in a potential regime that is now known to suffer from mass transfer limitations.[14,15] Thus, the present study was conducted to provide insights into the dependence of the CO evolution activity of Ag-based electrocatalysts on their surface atomic structure. This was accomplished by developing a method of epitaxially growing Ag thin films with (111), (100), and (110) orientations. We conclude that the presence of step edge defects in the Ag(111) and Ag(100) films significantly contributes to their observed activity, making their apparent activities more similar to Ag(110). The intrinsically superior activity of Ag(110) compared to either Ag(111) or Ag(100) is hypothesized to be the result of enhanced electric field stabilization of polarizable intermediates of CO evolution. The enhanced electric field stabilization is a result of an elevated surface charge density on undercoordinated Ag surface atoms.

3.2 Experimental

3.2.1 Electrode Preparation

Ag thin films were deposited onto polished single crystal Si wafers (1-10 Ω*cm Virginia Semiconductor) using an AJA ATC Orion-5 magnetron sputtering system. The Si wafers were etched immediately before deposition using 10 wt. % HF. An IR lamp was used to heat the Si wafers to 300 °C prior to deposition. Ag (99.999% Kurt J. Lesker) was then sputtered onto the etched Si wafers at a rate of 1 Å/s under Ar to a thickness of 100 nm.

3.2.2 Electrode Characterization

The crystal structures of the Ag thin films were analyzed with a Rigaku Smartlab x-ray diffractometer (XRD) using Cu Kα radiation (40 kV, 40 mA). Symmetric out-of-plane θ/2θ scans were conducted to identify the out-of-plane growth orientation of the Ag crystallites in the thin films. Symmetric in-plane φ scans at Bragg reflections corresponding to both Si and Ag were conducted to determine the orientation of the Ag crystallites with respect to the Si substrate. Symmetric out-of-plane Ω scans, or rocking curves, were conducted to determine the average degree of misorientation of the Ag crystallites with respect to the substrate normal. X-ray pole figures of the Ag thin films were acquired using a PANanalytical X'Pert diffractometer using Cu Kα radiation.

The near-surface composition of the Ag thin films was measured before and after electrolysis using a Kratos Axis Ultra DLD x-ray photoelectron spectrometer (XPS). All spectra were acquired using monochromatized Al Kα radiation (15 kV, 15 mA). Where applicable, Ar sputtering of the sample surface was conducted using a focused Ar ion beam (5 kV). The kinetic energy scale of the measured spectra was calibrated by setting the C 1s binding energy to 284.8 eV. The work functions of the Ag thin films were measured using an accelerating voltage of 9 V. The same instrument was also used to measure the surface composition of the Ag thin films before and after electrolysis by ion scattering spectroscopy (ISS). All spectra were acquired using a focused He ion beam (1 kV). No impurities were detected on the surface of the thin films before or after electrolysis by either XPS or ISS (see 3.6.1).

3.2.3 Electrochemical Scanning Tunneling Microscopy

Electrochemical scanning tunneling microscopy (EC-STM) was conducted using a Nanoscope E microscope (Digital Instruments, Veeco) equipped with a built-in three-electrode potentiostat. The experimental procedure was described in detail elsewhere.[16] All STM measurements were conducted in a custom electrochemical cell machined from Kel-F (Emco Industrial Plastics Inc.). The counter electrode was a Pt wire. The working electrode potential was referenced against a miniature leakless Ag/AgCl reference electrode (Innovative Instruments Inc.). The STM tips were prepared by electrochemically etching a tungsten wire (0.25 mm diameter Sigma-Aldrich) in 1.0 M KOH at 15 V_{ac}.

Ag thin film samples were prepared and used without pretreatment for the EC-STM experiments. The samples were immersed in 0.1 M $HClO_4$ (Sigma-Aldrich) and the potential scanned from OCV to -0.94 V vs RHE at 50 mV/s to reduce any invasive surface oxides to Ag metal. The EC-STM scans were then acquired at -0.2 V vs SHE using E_B = 300 mV and I_T = 2 nA for large-area (greater than 10 nm × 10 nm) images and E_B = 300 mV and I_T = 20 nA for atomic-resolution images. All solutions were prepared with 18.2 MΩ*cm Nanopure water (ThermoFisher Scientific).

3.2.4 Step Edge Density Analysis

The step edge density analysis of the EC-STM images was conducted using the FIJI software.[17] The raw images were processed with a median filter of 2px to reduce feedback artifacts. Step edges were identified using a pixel-valued threshold method and a Sobel-filtered edge detection method. First, the pixel-valued threshold method was employed with a threshold value above the height of a typical Ag step. The height scale of the EC-STM images is 30nm, with a 240 pixel-value range. As a result, the EC-STM depth resolution is 0.125 nm/pixel-value. The typical Ag step height was taken to be about 0.3nm, so a threshold of 4 pixels were used to identify step edges. Furthermore, distinct contours were drawn on each image manually. The Sobel-filtered edge detection method convolutes two 3x3 kernels to approximate the gradients of the EC-STM images.[18] The filtered images display the gradients on a green-purple color scale. To avoid noise and double counting, the gradients in the images were then segmented with a histogram-based threshold such that 70-75% of the pixel values are captured. The step density is

then calculated by taking the quotient between the identified step edge pixels with the total number of pixels in the images.

3.2.5 Electrochemical Characterization

All electrochemical measurements were conducted in a custom gas-tight electrochemical cell machined from PEEK.[19] The cell was sonicated in 20 wt. % nitric acid and thoroughly rinsed with DI water prior to all experimentation. The working and counter electrodes were parallel and separated by an anion-conducting membrane (Selemion AMV AGC Inc.). Gas dispersion frits were incorporated into both electrode chambers to provide ample electrolyte mixing. The exposed geometric surface area of each electrode was 1 cm^2 and the electrolyte volume of each electrode chamber was 1.8 mL. The counter electrode was a glassy carbon plate (Type 2 Alfa Aesar) that was also sonicated in 20 wt. % nitric acid prior to all experimentation. Platinum was not used as the anode due to the possibility of contaminating the cathode.[20,21] The working electrode potential was referenced against a miniature leakless Ag/AgCl electrode (Innovative Instruments Inc.) that was calibrated against a homemade standard hydrogen electrode. A 0.05 M K_2CO_3 (99.995% Sigma Aldrich) solution prepared using 18.2 MΩ*cm DI water was used as the electrolyte. Metallic impurities in the as-prepared electrolyte were removed before electrolysis by chelating them with Chelex 100 (Na form Sigma Aldrich).[21,22] Both electrode chambers were sparged with CO_2 (99.999% Praxair Inc.) at a rate of 10 sccm for 30 min prior to and throughout the duration of all electrochemical measurements unless explicitly stated otherwise. Upon saturation with CO_2 the pH of the electrolyte was 6.8, which was maintained throughout the duration of all electrocatalytic measurements. The hydrodynamic boundary layer thickness at the cathode surface was determined to be roughly 50 µm under these conditions by measuring the diffusion limited current of ferricyanide reduction (see 3.6.2).

Electrochemistry was performed using a Biologic VSP-300 potentiostat. All electrochemical measurements were recorded versus the reference electrode and converted to the RHE scale. Potentiostatic electrochemical impedance spectroscopy (PEIS) was used to determine the uncompensated resistance (R_u) of the electrochemical cell by applying voltage waveforms about the open circuit potential with an amplitude of 20 mV and frequencies ranging from 50 Hz to 500 kHz (see 3.6.3). The potentiostat compensated for 85% of R_u *in-situ* and the last 15% was post-corrected to arrive at accurate potentials. The redox properties of the Ag thin films were assessed by performing reversible chloride adsorption during cyclic voltammetry from -0.5 to +0.4 V vs SHE at a scan rate of 500 mV/s in 0.01 M KCl saturated with N_2 until a stable voltammogram was obtained, which occurred in approximately 10 cycles.[14] The electrocatalytic activity of each Ag thin film was assessed by conducting chronoamperometry staircases from -0.5 to -1.5 V vs RHE with a step size of 100 mV and a step length of 15 min. Each thin film orientation was tested at least three separate times to ensure the statistical relevance of the observed trends. The roughness factor of the tested Ag thin films was determined by dividing the double layer capacitance of the Ag thin films by the minimum double layer capacitance measured over the Ag thin films. The double layer capacitance of each tested Ag thin film was measured by conducting cyclic

voltammetry in a potential range where no Faradaic processes occur at a series of increasingly rapid scan rates immediately after chronoamperometry (see 3.6.4).

3.2.6 Product Analysis

The effluent from the electrochemical cell was introduced directly into the sampling loop of an Agilent 7890B gas chromatograph (GC) equipped with a pulsed-discharge helium ionization detector (PDHID). The effluent was sampled at least 10 min after each chronoamperometry potential step. The constituents of the gaseous sample were separated in He (99.9999% Praxair Inc.) using a Hayesep-Q capillary column (Agilent) in series with a packed ShinCarbon ST column (Restek Co.). After sampling the reaction effluent the column oven was maintained at 50 °C for 1 min followed by a temperature ramp at 30 °C/min to 250 °C, which was maintained for the duration of the analysis. The signal response of the PDHID was calibrated by analyzing a series of NIST-traceable standard gas mixtures (Airgas Inc.) (see 3.6.5).

The electrolyte from both electrode chambers was collected after electrolysis and analyzed using a Thermo Scientific UltiMate 3000 liquid chromatograph (HPLC) equipped with a refractive index detector (RID). The electrolyte samples were stored in a refrigerated autosampler until analyzed to minimize the evaporation of volatile liquid-phase reaction products. The liquid-phase products contained in a 10 µL aliquot were separated using a series of two Aminex HPX 87-H columns (Bio-Rad Inc.) and a 1 mM sulfuric acid eluent (99.999% Sigma Aldrich). The column oven was maintained at 60 °C for the duration of the analysis. The signal response of the RID was calibrated by analyzing standard solutions of each product at a concentration of 1, 10, and 50 mM (see 3.6.6).

3.2.7 Theory

Reaction energetics were calculated with density functional theory with a periodic plane-wave implementation and ultrasoft pseudopotentials using QUANTUM ESPRESSO version 5.1[23] interfaced with the Atomistic Simulation Environment (ASE).[24] We applied the BEEF-vdW functional, which provides a reasonable description of van der Waals forces while maintaining an accurate prediction of chemisorption energies.[25] Spin-polarized calculations were performed using plane-wave and density cutoffs of 500 and 5000 eV, respectively, as well as a Fermi-level smearing width of 0.1 eV.

Adsorption energies were evaluated using four-layer 4×4 (111 and 100) and three-layer 6×6 (110) supercells with all but the top two layers constrained, 20 Å separation of the surface slabs and [4×4×1] Monkhorst-Pack *k*-point grids[26]. All structures were relaxed using a BFGS line search algorithm until force components were less than 0.03 eV/Å. A dipole correction was applied to decouple the electrostatic interaction between the periodically repeated slabs. Zero-point energy and finite temperature corrections were evaluated from the harmonic adsorbate vibrations using ASE. We applied a correction of 0.33 eV to the energy of CO_2(g), which was determined from fits to experimental gas phase reaction energetics.[25]

A sawtooth-like external potential (homogeneous electric field) was applied to the relaxed structures along the z-direction (vertical to the slabs) with varying field strengths between –0.3 and 0.4 V/Å. The resulting field dependent adsorption energies were interpolated with a quadratic polynomial in order to calculate the dipole moments and polarizabilities. By this procedure, we obtained the field dependency of the adsorption energies which was added on top of the dipole-corrected field-free calculations performed before.

Calculations of the field distributions around the slabs were performed using VASP version 5.4.4[27–30] and applying Projector-Augmented-Wave based pseudo-potentials.[31,32] Solvation and charging effects were accounted for by the VASPsol module.[33] The revised Perdew-Burke-Ernzerhof (RPBE) exchange-correlation functional[34] was used, since this was shown to yield highly accurate predictions of Potential of Zero Charges using the default VASPsol parameters for water.[35] All calculations were performed using "accurate" numerical default settings, an energy cutoff of 800 eV, a [6×6×1] k-point grid and a Fermi level smearing with of 0.1 eV on unrelaxed surface slabs obtained from cutting the relaxed Ag fcc bulk structure. The surface slabs consisted of 7-layer 1×1 (111 and 100), 2×1 (110) and 3×1 (211) supercells separated by 160 Å. A large separation of the slabs is necessary to converge the electrostatic potential of the charged slabs.[36] The default VASPsol parameters were used to represent the water environment,[33] but the non-electrostatic parameter τ was set to zero due to known numerical instabilities in the electrostatic potential.[36] Ion distributions were included in all calculations in the solvent by means of the linearized Poisson-Boltzmann theory[37] using a Debye length of 3 Å. A constant electrode potential (Fermi level) was reached by applying a Newton scheme which optimized the number of electrons to reach a predefined electrode potential. A reference potential of 4.44 eV was subtracted from the Fermi level in order to reference the electrode potential to the Standard Hydrogen Electrode.[38]

3.3 Results and Discussion

3.3.1 Thin Film Deposition

Cu thin films can be grown epitaxially on Si single crystal substrates at room temperature.[39–42] This is possible because Cu diffuses rapidly through Si at room temperature, enabling a copper silicide interlayer to form during the deposition that relaxes the lattice mismatch between Cu and Si.[39] The epitaxial growth of Ag thin films on copper silicide interlayers has also been reported.[43,44] However, epitaxial Ag thin films prepared using copper silicide interlayers exhibited excessive hydrocarbon selectivities uncharacteristic of Ag at potentials cathodic of -1 V vs RHE (see 3.6.7). Furthermore, Cu was observed on the surface of these electrodes after CO_2 reduction using ion scattering spectroscopy (ISS). Thus, adsorbate induced segregation likely draws the Cu in the interlayer to the electrode surface.[45] As a result, a Cu-free method of epitaxially depositing Ag thin films on Si was developed. Specifically, Ag thin films were deposited onto Si single crystal substrates at an elevated temperature so that the Ag would diffuse rapidly enough

through Si to form a silver silicide interlayer. This interlayer relaxes the lattice mismatch between Ag and Si, which have lattice parameters of 4.08 and 5.43 Å, respectively.

3.3.2 Bulk Crystal Orientation

Symmetrical x-ray diffraction (XRD) scans were conducted over Ag thin films deposited onto Si(111), Si(100), and Si(110) to determine if the orientation of the Si substrate impacts the out-of-plane growth orientation of the Ag thin films. The only Ag diffraction peaks observed were those corresponding to the orientation as the substrate, indicating that the Ag thin films are textured out-of-plane with orientations matching the substrate (see 3.6.8). X-ray pole figures were conducted to determine both the out-of-plane and in-plane orientation of the Ag thin films and validate that they grow epitaxially on the Si substrates. The results are shown in Figure 3.1. The Ag(200) x-ray pole figure of the Ag thin film deposited onto Si(111) exhibits the threefold symmetry characteristic of Ag(111), confirming the epitaxial nature of the thin film with the relationship Si(111)‖Ag(111). Furthermore, the lack of sixfold symmetry indicates that the Ag(111) thin film does not exhibit twinning.[41] The Ag(111) x-ray pole figure of the Ag thin film deposited onto Si(100) exhibits the fourfold symmetry characteristic of Ag(100), confirming the epitaxial nature of the thin film with the relationship Si(100)‖Ag(100). Finally, the Ag(110) x-ray pole figure of the Ag thin film deposited onto Si(110) exhibits strong intensity parallel to the surface normal, confirming the epitaxial nature of the thin film with the relationship Si(110)‖Ag(110). Ag(111) and Ag(200) x-ray pole figures of the Ag(110) thin film were also conducted (see 3.6.9).

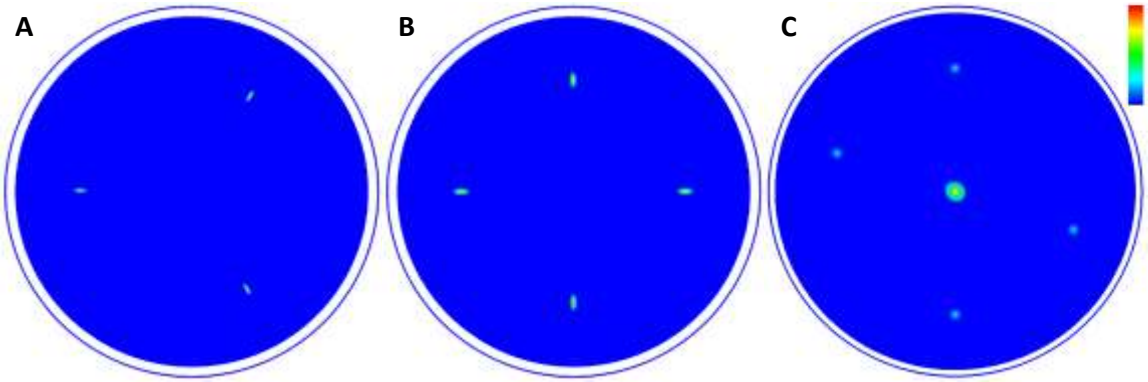

Figure 3.1 *– X-ray pole figures of (A) Si(111)‖Ag(111); Ag(200) intensities shown, (B) Si(100)‖Ag(100); Ag(111) intensities shown, and (C) Si(110)‖Ag(110); Ag(022) intensities shown.*

3.3.3 Surface Atomic Structure

Operando electrochemical scanning tunneling microscopy (EC-STM) was conducted to determine if the bulk crystal orientation of the Ag thin films impacts their surface atomic structure under an applied bias in an aqueous electrolyte.[16,46,47] To this end, atomically resolved EC-STM images were acquired at an applied potential of -0.2 V vs SHE in 0.1 M $HClO_4$ over the Ag(111), Ag(100), and Ag(110) thin films. The observed surface atomic structures were consistent with the bulk orientation of the Ag crystallites

in the thin films, as shown in Figure 3.2. Furthermore, the surfaces did not exhibit any signs of reconstruction and remained stable. Finally, reversible chloride adsorption was conducted over the Ag thin films to confirm their surface atomic structures under near-neutral electrochemical conditions.[14] The consistency of the reversible potentials for chloride adsorption measured over the Ag thin films with those reported over Ag single crystals supports the conclusion that the majority of Ag surface sites are consistent with the bulk orientation of the Ag thin films (see 3.6.10).

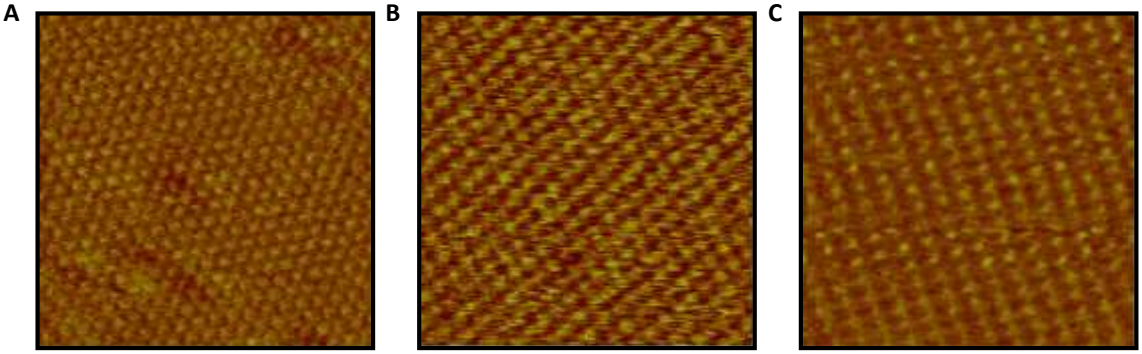

Figure 3.2 *– Atomically resolved in-situ electrochemical scanning tunneling micrographs of (A) Ag(111), (B) Ag(100), and (C) Ag(110) thin films obtained at -0.2 V vs SHE in 0.1 M $HClO_4$. Image size is 5 nm x 5 nm.*

3.3.4 Surface Defect Density

Low resolution operando EC-STM was conducted to determine the abundance of films defects, such as step edges. Step edges were identified using a pixel-valued threshold method and a Sobel-filtered edge detection method, as shown in Figure 3.3. The former identifies step edges using the pixel value as an atomic height indicator while the latter identifies step edges using the pixel value gradients across the images. The two approaches yield step edge density estimations within 2% of one another, which gives credence to the accuracy of the analysis. The step edge density was found to be ~8% over the Ag(111) and Ag(100) thin films and ~12% over the Ag(110) thin films, which is consistent with the higher electrochemical surface area observed over the Ag(110) thin films relative to either the Ag(111) or Ag(100) thin films.

The extent to which step edge defects contribute to the overall electrocatalytic activity observed over the Ag thin films is a function of their abundance and activity relative to terrace sites. As shown in Figure 3.4, defects with even slightly lower activation barriers than terrace sites will contribute disproportionately to the observed activity (see 3.6.11). This fact is often not acknowledged in studies that attempt to relate the surface faceting of electrocatalysts with their observed activity for CO_2 reduction.[14,47–49]

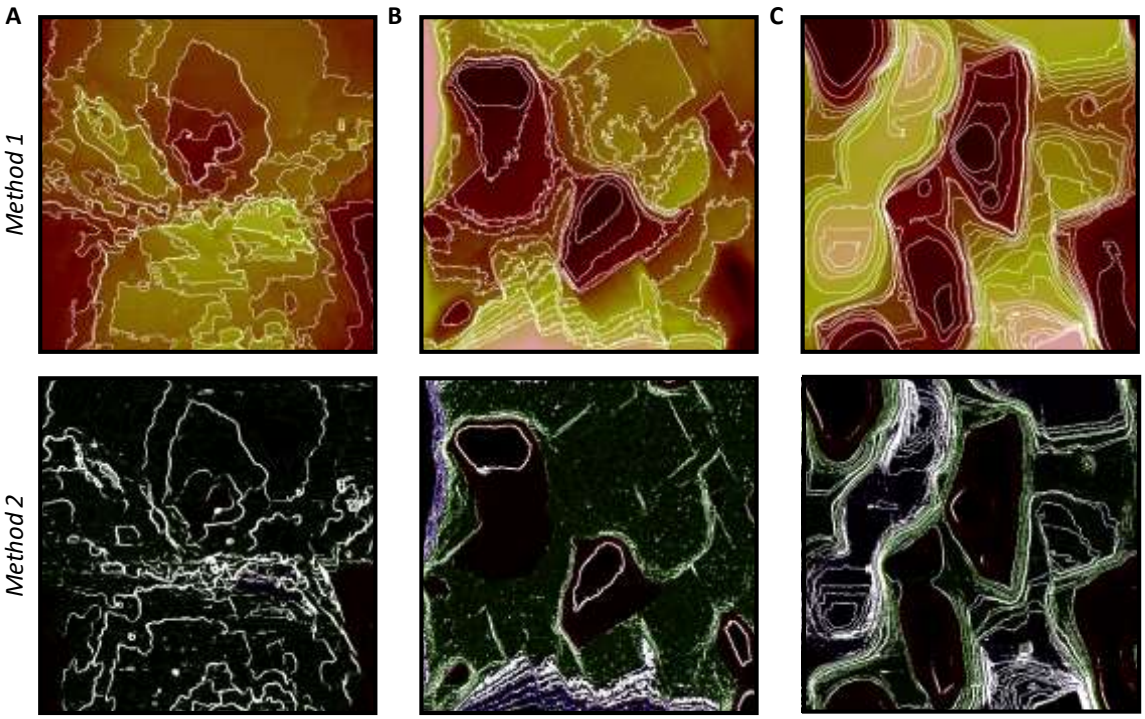

Figure 3.3 *– Step density analysis on in-situ EC-STM images of (A) Ag(111), (B) Ag(100), and (C) Ag(110) thin films. Analysis was performed using two methods: (1) a pixel-valued threshold method where step boundaries are delineated based on pixel values as an atomic height indicator; (2) a Sobel-filtered edge detection method which determines step boundaries based on pixel value gradients across the images. Image size is 500 nm x 500 nm.*

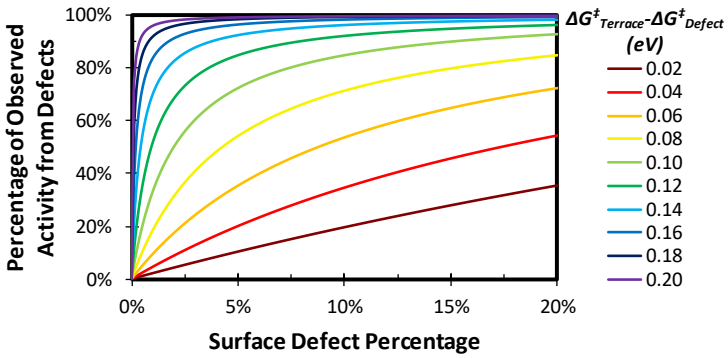

Figure 3.4 *– Calculated contribution of defects to the observed activity based on their abundance and activity relative to terrace sites.*

3.3.5 CO_2 Reduction Activity

The electrocatalytic activity of the Ag thin films was measured by conducting chronoamperometry staircases from -0.5 to -1.5 V vs RHE in 0.1 M $KHCO_3$, as shown in Figure 3.5. The observed activities were normalized by the roughness factors of the Ag thin films, which were calculated by taking the ratio of their double layer capacitances as measured during cyclic voltammetry immediately after the terminal potential of the

chronoamperometry staircase was reached. The CO evolution activity observed over the Ag thin films exhibited Tafel kinetics until approximately -1 V vs RHE, at which point mass transfer limitations inhibit the observed rate of CO evolution.[15,21,50] At this potential, the CO evolution activity of Ag(111) and Ag(100) are roughly equivalent. However, the Ag(110) surface exhibits a superior activity by a factor of ~5. The relative activities observed over the Ag thin films agree well with the relative activities of Ag(111), Ag(100), and Ag(110) single crystals.[14]

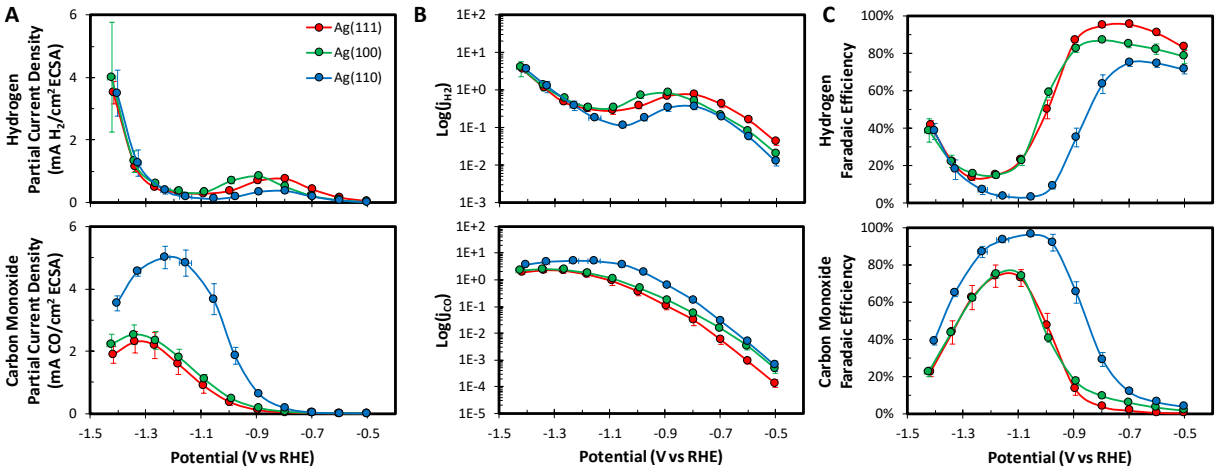

Figure 3.5 *– CO_2 reduction activity observed over Ag(111), Ag(100), and Ag(110) thin films vs applied potential. Partial current densities for H_2 and CO on (A) linear scale and (B) log scale. (C) H_2 and CO Faradaic efficiencies.*

The reaction thermodynamics for CO evolution were calculated over Ag(111), Ag(100), Ag(110), and Ag(211). The Ag(211) surface was calculated as a representative step edge defect. As shown in Figure 3.6, the CO evolution activity of Ag(110) is expected to be superior to both Ag(111) and Ag(100) based on the calculated reaction thermodynamics. However, the differences in their activities are expected to be much larger than observed experimentally. This apparent inconsistency can be understood by considering the activity of Ag(111), Ag(100), and Ag(110) terraces relative to Ag(211), a typical step edge defect. While the activity of Ag(110) is expected to be approximately equal to that of a typical step edge defect, Ag(111) and Ag(100) are expected to be significantly less active. Thus, a significant portion of the activity observed over the Ag(111) and Ag(100) thin films likely occurs over the step edge defects present at the electrode surface. Conversely, step edge defects are expected to contribute a smaller fraction of the activity observed over the Ag(110) thin films. Thus, the presence of step edge defects reduces the differences in the CO evolution activity observed over the Ag thin films by contributing more significantly to the activity observed over Ag(111) and Ag(100) than Ag(110).

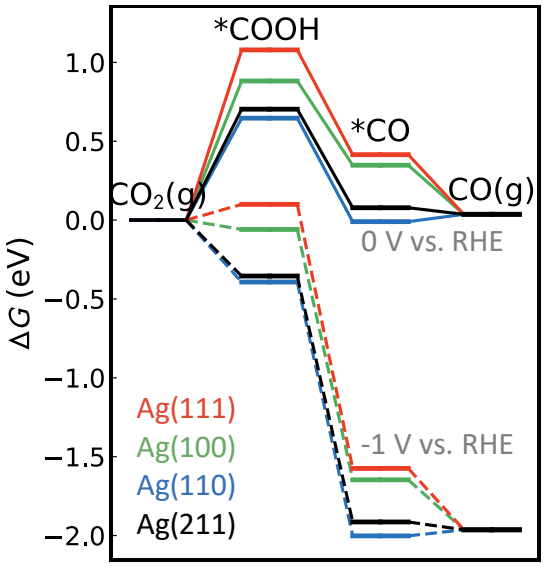

Figure 3.6 *– Homogeneous electric field corrected free energy diagram for CO evolution. A Stern capacitance of 25 μF/cm^2, a bulk dielectric permittivity of 2 and experimental (100, 111, 110) or theoretical (211) values for the PZCs were used to estimate the electric fields at specific applied potentials.*

The hydrogen evolution reaction (HER) activity observed over the Ag thin films exhibits 3 distinct regions. At potentials anodic of -0.7 V vs RHE the relative HER activities observed over the Ag thin films are consistent with what is observed in the absence of CO_2 (see 3.6.12). However, the HER activity observed in the absence of CO_2 does not agree with what would be expected based on the calculated reaction thermodynamics. This is again a result of step edge defects contributing more significantly to the activity observed over Ag(111) and Ag(100) than Ag(110). At potentials cathodic of -0.7 V vs RHE the HER activity is significantly inhibited over all surfaces compared to what would be expected based on an extrapolation of the initial Tafel kinetics. This suppression is likely due to the presence of adsorbates associated with CO evolution poisoning step edge defects, which is where the majority of the HER activity is likely to occur. Since CO accumulation on the Ag surface will weaken the H adsorption energy of neighboring Ag sites,[51] a high CO coverage may not be necessary to significantly suppress HER over Ag.[52] This hypothesis is supported by the fact that the HER activity observed over polycrystalline Ag in the presence of CO_2 during linear sweep voltammetry deviates from the activity observed in the absence of CO_2 at the potential where the evolution of CO is first detected (see 3.6.13).[50] Furthermore, microkinetic modeling has concluded that intermediates of CO evolution are present on the surface of polycrystalline Ag electrocatalysts during CO_2 reduction.[53] Finally, in-situ spectroscopy has been utilized to observe adsorbed CO on Ag electrocatalysts during CO_2 reduction.[54,55] The observed HER activity resumes Tafel behavior at potentials cathodic of -1 V vs RHE due to the liberation of adsorbates associated with the evolution of CO from the electrode surface. However, this phenomenon is not intrinsic and occurs due to mass transfer limitations inhibiting the rate of CO evolution, as previously discussed. This can be demonstrated by observing the dependence of the measured activity of polycrystalline Ag at potentials cathodic of -1 V vs RHE on the hydrodynamics of the electrochemical cell, which

demonstrates that the HER activity in this potential regime is dependent on the rate of mass transfer of CO_2 to the cathode surface.[21,50]

3.3.6 Local Electric Field Strength

The adsorption energies of polarizable reaction intermediates with significant dipole moments are influenced by the electric field strength, as shown in Figure 3.7.[56,57] The electric field strength will not significantly impact the adsorption energy of H since it is not polarizable and does not possess a dipole moment. Conversely, the electric field strength will significantly stabilize intermediates of CO evolution, such as COOH and CO. Furthermore, the relative magnitude of the stabilization is roughly independent of the surface atomic structure of the electrocatalyst for a given electric field strength. Thus, the differences in the intrinsic activity of Ag(110) and Ag(111)/Ag(100) may be due to differences in the strength of the local electric fields at a given potential.

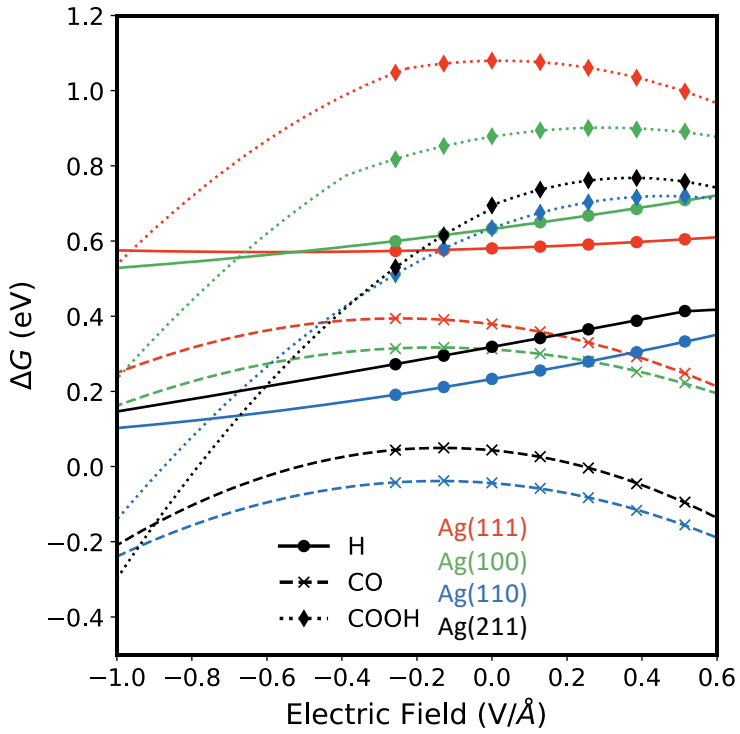

Figure 3.7 *– Homogeneous electric field dependent binding free energies of reaction intermediates over Ag(111), Ag(100), and Ag(110) given relative to H_2(g) and CO_2(g) In all cases the most stable adsorption sites were determined at each applied field value.*

The work functions of the Ag thin films decrease systematically with surface atom density, in agreement with what has been observed over the corresponding Ag single crystals (see 3.6.14).[58] As the work functions of the Ag thin films decrease, their potential of zero charge shifts to more cathodic potentials.[59,60] As a result, the total surface charge on the Ag thin films decreases with surface atom density when polarized to a given potential vs RHE. However, since the surface atom density also decreases the net effect is that the charge per surface atom increases (see 3.6.15). The higher surface charge

density results in a higher local electric field strength, as shown in Figure 3.8. A substantial portion of the local electric field distribution is oriented perpendicular to the electrode surface (see 3.6.16). As a result, Ag facets with lower surface atom densities exhibit superior intrinsic kinetics for CO evolution due to the elevated local electric field strength, which stabilizes the polarizable intermediates of CO evolution.

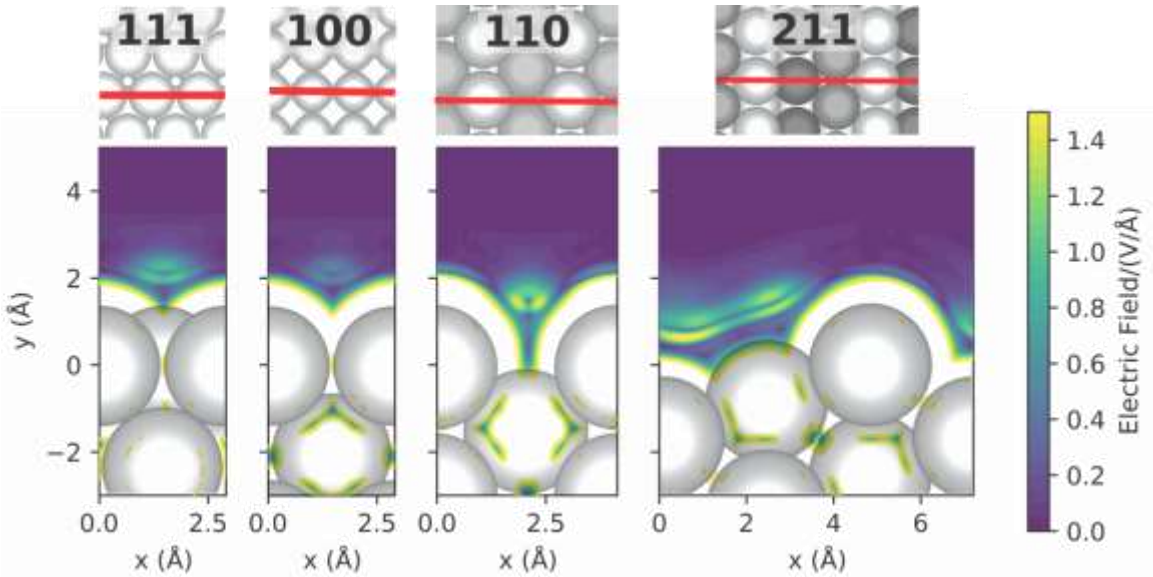

Figure 3.8 *– Absolute magnitude of the electric field distribution over Ag(111), Ag(100), Ag(110), and Ag(211) at an applied potential of -1 V vs RHE as obtained from DFT-LPB calculations using VASPsol. The electric field is plotted on an x-z cut through the 3D space as illustrated by the top views of the facets. Electric field magnitudes outside the limits of the color bar are represented in white.*

3.4 Conclusions

In conclusion, a method for growing Ag thin films epitaxially on Si single crystal substrates has been developed. The surface atomic structure of the epitaxial Ag thin films was found to be consistent with their bulk crystal orientation under electrochemical conditions using EC-STM. A combined theoretical and experimental study of the dependence of the CO evolution activity of Ag on the surface atomic structure led to the conclusion that step edge defects substantially contribute to the CO evolution activity observed over the Ag(111) and Ag(100) thin films but not Ag(110) thin films. Furthermore, Ag(110) exhibits superior intrinsic activity compared to either Ag(111) or Ag(100) due to an elevated surface charge density at a given potential. The elevated surface charge density results in stronger local electric fields, which significantly improve the reaction thermodynamics of CO evolution by stabilizing polarizable reaction intermediates.

3.5 References

(1) Jitaru, M.; Lowy, D. A.; Toma, M.; Toma, B. C.; Oniciu, L. Electrochemical Reduction of Carbon Dioxide on Flat Metallic Cathodes. *J. Appl. Electrochem.* **1997**, *27* (8), 875–889.

(2) Gattrell, M.; Gupta, N.; Co, A. A Review of the Aqueous Electrochemical Reduction of CO2 to Hydrocarbons at Copper. *J. Electroanal. Chem.* **2006**, *594* (1), 1–19.
(3) Hori, Y. Electrochemical CO2 Reduction on Metal Electrodes. In *Modern Aspects of Electrochemistry*; Vayenas, C. G., White, R. E., Gamboa-Aldeco, M. E., Eds.; Springer: New York, 2008; pp 89–189.
(4) Hori, Y.; Kikuchi, K.; Suzuki, S. Production of CO and CH4 in Electrochemical Reduction of CO2 at Metal Electrodes in Aqueous Hydrogencarbonate Solution. *Chem. Lett.* **1985**, *14* (11), 1695–1698.
(5) Noda, H.; Ikeda, S.; Oda, Y.; Imai, K.; Maeda, M.; Ito, K.; Ideka, S.; Oda, Y.; Imai, K.; Maeda, M.; et al. Electrochemical Reduction of Carbon Dioxide at Various Metal Electodes in Aqueous Potassium Hydrogen Carbonate Solution. *Bull. Chem. Soc. Jpn.* **1990**, *63* (9), 2459–2462.
(6) Hori, Y.; Wakebe, H.; Tsukamoto, T.; Koga, O. Electrocatalytic Process of CO Selectivity in Electrochemical Reduction of CO2 at Metal Electrodes in Aqueous Media. *Electrochim. Acta* **1994**, *39* (11–12), 1833–1839.
(7) Hatsukade, T.; Kuhl, K. P.; Cave, E. R.; Abram, D. N.; Jaramillo, T. F. Insights into the Electrocatalytic Reduction of CO2 on Metallic Silver Surfaces. *Phys. Chem. Chem. Phys.* **2014**, *16* (27), 13814–13819.
(8) Lu, Q.; Rosen, J.; Zhou, Y.; Hutchings, G. S.; Kimmel, Y. C.; Chen, J. G.; Jiao, F. A Selective and Efficient Electrocatalyst for Carbon Dioxide Reduction. *Nat. Commun.* **2014**, *5*, 1–6.
(9) Hsieh, Y.-C.; Senanayake, S. D.; Zhang, Y.; Xu, W.; Polyansky, D. E. Effect of Chloride Anions on the Synthesis and Enhanced Catalytic Activity of Silver Nanocoral Electrodes for CO_2 Electroreduction. *ACS Catal.* **2015**, *5* (9), 5349–5356.
(10) Ma, M.; Trześniewski, B. J.; Xie, J.; Smith, W. A. Selective and Efficient Reduction of Carbon Dioxide to Carbon Monoxide on Oxide-Derived Nanostructured Silver Electrocatalysts. *Angew. Chemie - Int. Ed.* **2016**, *55* (33), 9748–9752.
(11) Mistry, H.; Choi, Y. W.; Bagger, A.; Scholten, F.; Bonifacio, C. S.; Sinev, I.; Divins, N. J.; Zegkinoglou, I.; Jeon, H. S.; Kisslinger, K.; et al. Enhanced Carbon Dioxide Electroreduction to Carbon Monoxide over Defect-Rich Plasma-Activated Silver Catalysts. *Angew. Chemie - Int. Ed.* **2017**, *56* (38), 11394–11398.
(12) Peng, X.; Karakalos, S. G.; Mustain, W. E. Preferentially Oriented Ag Nanocrystals with Extremely High Activity and Faradaic Efficiency for CO2 Electrochemical Reduction to CO. *ACS Appl. Mater. Interfaces* **2018**, *10* (2), 1734–1742.
(13) Rosen, J.; Hutchings, G. S.; Lu, Q.; Rivera, S.; Zhou, Y.; Vlachos, D. G.; Jiao, F. Mechanistic Insights into the Electrochemical Reduction of CO2 to CO on Nanostructured Ag Surfaces. *ACS Catal.* **2015**, *5* (7), 4293–4299.
(14) Hoshi, N.; Kato, M.; Hori, Y. Electrochemical Reduction of CO2 on Single Crystal Electrodes of Silver Ag(111), Ag(100), and Ag(110). *J. Electroanal. Chem.* **1997**, *440* (1–2), 283–286.
(15) Singh, M. R.; Clark, E. L.; Bell, A. T. Effects of Electrolyte, Catalyst, and Membrane Composition and Operating Conditions on the Performance of Solar-Driven Electrochemical Reduction of Carbon Dioxide. *Phys. Chem. Chem. Phys.* **2015**, *17* (29), 18924–18936.
(16) Kim, Y. G.; Baricuatro, J. H.; Javier, A.; Gregoire, J. M.; Soriaga, M. P. The Evolution of the Polycrystalline Copper Surface, First to Cu(111) and Then to Cu(100), at a Fixed CO2RR Potential: A Study by Operando EC-STM. *Langmuir* **2014**, *30* (50), 15053–15056.
(17) Schindelin, J.; Arganda-Carreras, I.; Frise, E.; Kaynig, V.; Longair, M.; Pietzsch, T.; Preibisch, S.; Rueden, C.; Saalfeld, S.; Schmid, B.; et al. Fiji: An Open-Source Platform for Biological-Image Analysis. *Nat. Methods* **2012**, *9* (7), 676–682.
(18) Danielsson, P.-E.; Seger, O. Generalized and Separable Sobel Operators. *Mach. Vis.*

Three-Dimensional Scenes **1990**, 347–379.
(19) Lobaccaro, P.; Singh, M. R.; Clark, E. L.; Kwon, Y.; Bell, A. T.; Ager, J. W. Effects of Temperature and Gas-Liquid Mass Transfer on the Operation of Small Electrochemical Cells for the Quantitative Evaluation of CO2 Reduction Electrocatalysts. *Phys. Chem. Chem. Phys.* **2016**, *18* (38), 26777–26785.
(20) Dunwell, M.; Lu, Q.; Heyes, J. M.; Rosen, J.; Chen, J. G.; Yan, Y.; Jiao, F.; Xu, B. The Central Role of Bicarbonate in the Electrochemical Reduction of Carbon Dioxide on Gold. *J. Am. Chem. Soc.* **2017**, *139* (10), 3774–3783.
(21) Clark, E. L.; Resasco, J.; Landers, A.; Lin, J.; Chung, L.-T.; Walton, A.; Hahn, C.; Jaramillo, T. F.; Bell, A. T. Data Acquisition Protocols and Reporting Standards for Studies of the Electrochemical Reduction of Carbon Dioxide. *ACS Catal.* **2018**, *8*, 6560–6570.
(22) Wuttig, A.; Surendranath, Y. Impurity Ion Complexation Enhances Carbon Dioxide Reduction Catalysis. *ACS Catal.* **2015**, *5* (7), 4479–4484.
(23) Giannozzi, P.; Baroni, S.; Bonini, N.; Calandra, M.; Car, R.; Cavazzoni, C.; Ceresoli, D.; Chiarotti, G. L.; Cococcioni, M.; Dabo, I.; et al. QUANTUM ESPRESSO: A Modular and Open-Source Software Project for Quantum Simulations of Materials. *J. Phys. Condens. Matter* **2009**, *21* (39), 395502.
(24) Hjorth Larsen, A.; Jørgen Mortensen, J.; Blomqvist, J.; Castelli, I. E.; Christensen, R.; Dułak, M.; Friis, J.; Groves, M. N.; Hammer, B.; Hargus, C.; et al. The Atomic Simulation Environment---a Python Library for Working with Atoms. *J. Phys. Condens. Matter* **2017**, *29* (27), 273002.
(25) Studt, F.; Abild-Pedersen, F.; Varley, J. B.; Nørskov, J. K. CO and CO2 Hydrogenation to Methanol Calculated Using the BEEF-vdW Functional. *Catal. Lett.* **2013**, *143* (1), 71–73.
(26) Monkhorst, H. J.; Pack, J. D. Special Points for Brillouin-Zone Integrations. *Phys. Rev. B Condens. Matter* **1976**, *13* (12), 5188–5192.
(27) Kresse, G.; Hafner, J. Ab Initio Molecular Dynamics for Liquid Metals. *Phys. Rev. B Condens. Matter* **1993**, *47* (1), 558–561.
(28) Kresse, G.; Hafner, J. Ab Initio Molecular-Dynamics Simulation of the Liquid-Metal-Amorphous-Semiconductor Transition in Germanium. *Phys. Rev. B Condens. Matter* **1994**, *49* (20), 14251–14269.
(29) Kresse, G.; Furthmüller, J. Efficiency of Ab-Initio Total Energy Calculations for Metals and Semiconductors Using a Plane-Wave Basis Set. *Comput. Mater. Sci.* **1996**, *6* (1), 15–50.
(30) Kresse, G.; Furthmüller, J. Efficient Iterative Schemes for Ab Initio Total-Energy Calculations Using a Plane-Wave Basis Set. *Phys. Rev. B Condens. Matter* **1996**, *54* (16), 11169–11186.
(31) Kresse, G.; Hafner, J. Norm-Conserving and Ultrasoft Pseudopotentials for First-Row and Transition Elements. *J. Phys. Condens. Matter* **1994**, *6* (40), 8245.
(32) Vanderbilt, D. Soft Self-Consistent Pseudopotentials in a Generalized Eigenvalue Formalism. *Phys. Rev. B Condens. Matter* **1990**, *41* (11), 7892–7895.
(33) Mathew, K.; Sundararaman, R.; Letchworth-Weaver, K.; Arias, T. A.; Hennig, R. G. Implicit Solvation Model for Density-Functional Study of Nanocrystal Surfaces and Reaction Pathways. *J. Chem. Phys.* **2014**, *140* (8), 84106.
(34) Hammer, B.; Hansen, L. B.; Nørskov, J. K. Improved Adsorption Energetics within Density-Functional Theory Using Revised {Perdew-Burke-Ernzerhof} Functionals. *Phys. Rev. B Condens. Matter* **1999**, *59* (11), 7413–7421.
(35) Goodpaster, J. D.; Bell, A. T.; Head-Gordon, M. Identification of Possible Pathways for C-C Bond Formation during Electrochemical Reduction of CO2: New Theoretical Insights from an Improved Electrochemical Model. *J. Phys. Chem. Lett.* **2016**, *7* (8), 1471–1477.
(36) Steinmann, S. N.; Sautet, P. Assessing a First-Principles Model of an Electrochemical Interface by Comparison with Experiment. *J. Phys. Chem. C* **2016**, *120* (10), 5619–5623.
(37) Mathew, K.; Hennig, R. G. *Implicit Self-Consistent Description of Electrolyte in Plane-Wave*

Density-Functional Theory; 2016.
(38) Trasatti, S. The Absolute Electrode Potential: An Explanatory Note (Recommendations 1986). *J. Macromol. Sci. Part A Pure Appl. Chem.* **1986**, *58* (7), 955–966.
(39) Chang, C. A. Formation of Copper Silicides from Cu(100)/Si(100) and Cu(111)/Si(111) Structures. *J. Appl. Phys.* **1990**, *67* (1), 566–569.
(40) Jiang, H.; Klemmer, T. J.; Barnard, J. A.; Payzant, E. A. Epitaxial Growth of Cu on Si by Magnetron Sputtering. *J. Vac. Sci. Technol. B* **1998**, *16* (6), 3376–3383.
(41) Jiang, H.; Klemmer, T. J.; Barnard, J. A.; Doyle, W. D.; Payzant, E. A. Epitaxial Growth of Cu(111) Films on Si(110) by Magnetron Sputtering: Orientation and Twin Growth. *Thin Solid Films* **1998**, *315* (1–2), 13–16.
(42) Krastev, E. T.; Voice, L. D.; Tobin, R. G. Surface Morphology and Electric Conductivity of Epitaxial Cu(100) Films Grown on H-Terminated Si(100). *J. Appl. Phys.* **1996**, *79* (9), 6865–6871.
(43) Pedersen, K.; Kristensen, T. B.; Pederser, T. G.; Morgen, P.; Li, Z.; Hoffman, S. V. Optimum Cu Buffer Layer Thickness for Growth of Metal Overlayers on Si (111). *Phys. Rev. B* **2002**, *66* (15), 1–4.
(44) Pedersen, K.; Morgen, P.; Petersen, T. G.; Li, Z.; Hoffmann, S. V. Epitaxial Growth of Thin Ag and Au Films on Si(111) Using Thin Copper Silicide Buffer Layers. *J. Vac. Sci. Technol. A* **2003**, *21* (4), 1431–1435.
(45) Clark, E. L.; Hahn, C.; Jaramillo, T. F.; Bell, A. T. Electrochemical CO2 Reduction over Compressively Strained CuAg Surface Alloys with Enhanced Multi-Carbon Oxygenate Selectivity. *J. Am. Chem. Soc.* **2017**, *139* (44), 15848–15857.
(46) Kim, Y. G.; Javier, A.; Baricuatro, J. H.; Torelli, D.; Cummins, K. D.; Tsang, C. F.; Hemminger, J. C.; Soriaga, M. P. Surface Reconstruction of Pure-Cu Single-Crystal Electrodes under CO-Reduction Potentials in Alkaline Solutions: A Study by Seriatim ECSTM-DEMS. *J. Electroanal. Chem.* **2016**, *780*, 290–295.
(47) Hahn, C.; Hatsukade, T.; Kim, Y.-G.; Vailionis, A.; Baricuatro, J. H.; Higgins, D. C.; Nitopi, S. A.; Soriaga, M. P.; Jaramillo, T. F. Engineering Cu Surfaces for the Electrocatalytic Conversion of CO2: Controlling Selectivity Toward Oxygenates and Hydrocarbons. *Proc. Natl. Acad. Sci.* **2017**, *114* (23), 5918–5923.
(48) Hori, Y.; Takahashi, I.; Koga, O.; Hoshi, N. Selective Formation of C2 Compounds from Electrochemical Reduction of CO 2 at a Series of Copper Single Crystal Electrodes. *J. Phys. Chem. B* **2002**, *106* (1), 15–17.
(49) Hori, Y.; Takahashi, I.; Koga, O.; Hoshi, N. Electrochemical Reduction of Carbon Dioxide at Various Series of Copper Single Crystal Electrodes. *J. Mol. Catal. A Chem.* **2003**, *199* (1–2), 39–47.
(50) Clark, E. L.; Bell, A. T. Direct Observation of the Local Reaction Environment during the Electrochemical Reduction of CO2. *J. Am. Chem. Soc.* **2018**, *140* (22), 7012–7020.
(51) Zhang, Y.-J.; Sethuraman, V.; Michalsky, R.; Peterson, A. A. Competition between CO2 Reduction and H2 Evolution on Transition-Metal Electrocatalysts. *ACS Catal.* **2014**, *4* (10), 3742–3748.
(52) Nørskov, J. K.; Bligaard, T.; Logadottir, A.; Kitchin, J. R.; Chen, J. G.; Pandelov, S.; Stimming, U. Trends in the Exchange Current for Hydrogen Evolution. *J. Electrochem. Soc.* **2005**, *152* (3), J23–J26.
(53) Singh, M. R.; Goodpaster, J. D.; Weber, A. Z.; Head-Gordon, M.; Bell, A. T. Mechanistic Insights into Electrochemical Reduction of CO2 over Ag Using Density Functional Theory and Transport Models. *Proc. Natl. Acad. Sci.* **2017**, *114* (42), E8812–E8821.
(54) Oda, I.; Ogasawara, H.; Ito, M. Carbon Monoxide Adsorption on Copper and Silver Electrodes during Carbon Dioxide Electroreduction Studied by Infrared Reflection Absorption Spectroscopy and Surface-Enhanced Raman Spectroscopy. *Langmuir* **1996**, *12* (4), 1094–1097.

(55) Firet, N. J.; Smith, W. A. Probing the Reaction Mechanism of CO2 Electroreduction over Ag Films via Operando Infrared Spectroscopy. *ACS Catal.* **2017**, *7* (1), 606–612.
(56) Chen, L. D.; Urushihara, M.; Chan, K.; Nørskov, J. K. Electric Field Effects in Electrochemical CO2 Reduction. *ACS Catal.* **2016**, *6* (10), 7133–7139.
(57) Resasco, J.; Chen, L. D.; Clark, E.; Tsai, C.; Hahn, C.; Jaramillo, T. F.; Chan, K.; Bell, A. T. Promoter Effects of Alkali Metal Cations on the Electrochemical Reduction of Carbon Dioxide. *J. Am. Chem. Soc.* **2017**, *139* (32), 11277–11287.
(58) Chelvayohan, M.; Mee, C. H. B. Work Function Measurements on (110), (100) and (111) Surfaces of Silver. *J. Phys. C Solid State Phys.* **1982**, *15* (10), 2305–2312.
(59) Bachetta, M.; Trasatti, S.; Doubova, L.; Hamelin, A. The Dependence of the Potential of Zero Charge of Silver Electrodes on the Crystallographic Orientation of the Surface. *J. Electroanal. Chem.* **1986**, *200* (1–2), 389–396.
(60) Hamelin, A.; Stoicoviciu, L.; Doubova, L.; Trasatti, S. Influence of the Crystallographic Orientation of the Surface on the Potential of Zero Charge of Silver Electrodes. *Surf. Sci.* **1988**, *201* (3), 498–506.

3.6 Supplementary Information

3.6.1 Validating Surface Purity by Ion-Scattering Spectroscopy

The purity of the Ag thin films was measured before and after experimentation using ion scattering spectroscopy (ISS). As shown in Figure S3.1, no impurities were detected on the surfaces of the thin films after experimentation.

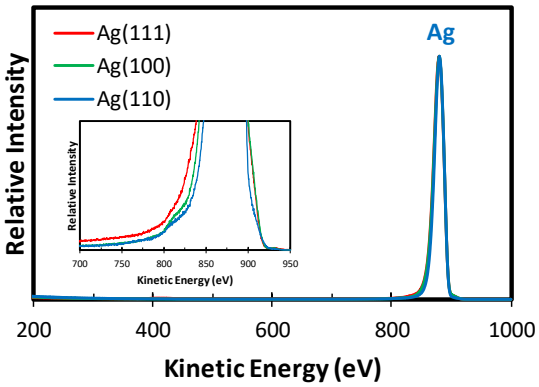

Figure S3.1 *– ISS analysis of the Ag thin films after experimentation.*

3.6.2 Quantification of the Hydrodynamic Boundary Layer Thickness

The hydrodynamic boundary layer thickness of an electrochemical cell can be quantified by measuring the diffusion-limited current density of ferricyanide reduction:

$$Fe(CN)_6^{3-} + e^- \rightarrow Fe(CN)_6^{4-}$$

Ferricyanide reduction is an ideal reaction to probe the hydrodynamic boundary layer thickness because it is electrochemically reversible, meaning that the reduction of ferricyanide is facile such that the observed rate is limited only by mass transfer regardless of the applied overpotential. When conducting this measurement, the total ferricyanide concentration should be minimized and the supporting electrolyte should be identical to that typically employed during CO_2 reduction. This will ensure that the fluid properties of the solution utilized to quantify the hydrodynamic boundary layer thickness accurately reflect those of the electrolytes employed to measure electrocatalytic activity. Furthermore, Au electrodes should be utilized to conduct the measurement to avoid Galvanic corrosion processes in which ferricyanide is the oxidizing agent. Figure S3.2A depicts cyclic voltammograms observed in 0.1 M $CsHCO_3$ with and without the addition of 10 mM $K_3Fe(CN)_6$. There is a potential window of ~600 mV where the observed Faradaic current can be attributed entirely to ferricyanide reduction. Furthermore, the observed rate of ferricyanide reduction is independent of the applied voltage, which is due to the electrochemical reversibility of the reaction, as previously mentioned. Thus, the steady state diffusion-limited current density associated with ferricyanide reduction can be measured

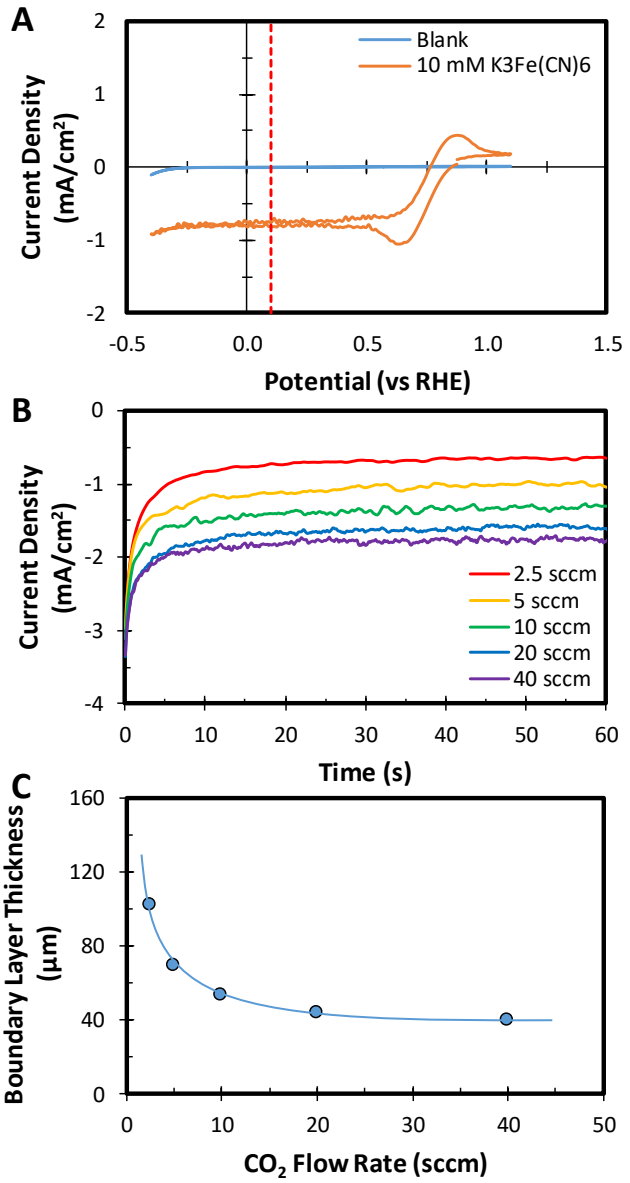

Figure S3.2 *– (A) Cyclic voltammograms obtained in 0.1 M $CsHCO_3$ saturated with CO_2 with and without the addition of 10 mM $K_3Fe(CN)_6$. The dotted red line indicates the potential used during chronoamperometry to measure the diffusion limited rate of ferricyanide reduction. (B) Diffusion limited current of ferricyanide reduction measured during chronoamperometry at a series of increasingly rapid CO_2 flow rates. (C) Calculated average hydrodynamic boundary layer thickness at the cathode surface as a function of the CO_2 flow rate utilized to mix the electrochemical cell.*

during chronoamperometry and utilized to calculate the average hydrodynamic boundary layer thickness at the cathode surface using Fick's law:

$$\delta_{BL} = \frac{F \times D_{Fe(CN)_6{}^{3-}} \times C^*_{Fe(CN)_6{}^{3-}}}{J_{SS}}$$

Where:

δ_{BL}	Average hydrodynamic boundary layer thickness
F	Faraday's constant
$D_{Fe(CN)_6{}^{3-}}$	Mass diffusivity of ferricyanide
$C^*_{Fe(CN)_6{}^{3-}}$	Bulk concentration of ferricyanide
J_{SS}	Steady state current density

As shown in Figure S3.2B, the steady state current density associated with ferricyanide reduction increases as the flow rate of CO_2 through the cell increases. As a result, the hydrodynamic boundary layer thickness at the cathode surface decreases as the flow rate of CO_2 increases, as shown in Figure S3.2C. The hydrodynamic boundary layer thickness decreases due to the enhanced mixing by the column of CO_2 bubbles near the cathode as the CO_2 flow rate increases.

3.6.3 Potentiostatic Electrochemical Impedance Spectroscopy

Potentiostatic electrochemical impedance spectroscopy (PEIS) was conducted to determine the total uncompensated resistance (R_u) of the electrochemical cell. Potential waveforms, centered at the open circuit potential, were applied to the electrochemical cell with a sinus amplitude of 20 mV and frequencies ranging from 50 Hz to 500 kHz, with 10 different frequencies tested per decade. The average of 10 measurements at each frequency were used to construct a Bode plot, as shown in Figure S3.3A. Using the Bode plot, the characteristic frequency and uncompensated resistance of the electrochemical cell were determined to be ~6 kHz and ~50 Ω, respectively.

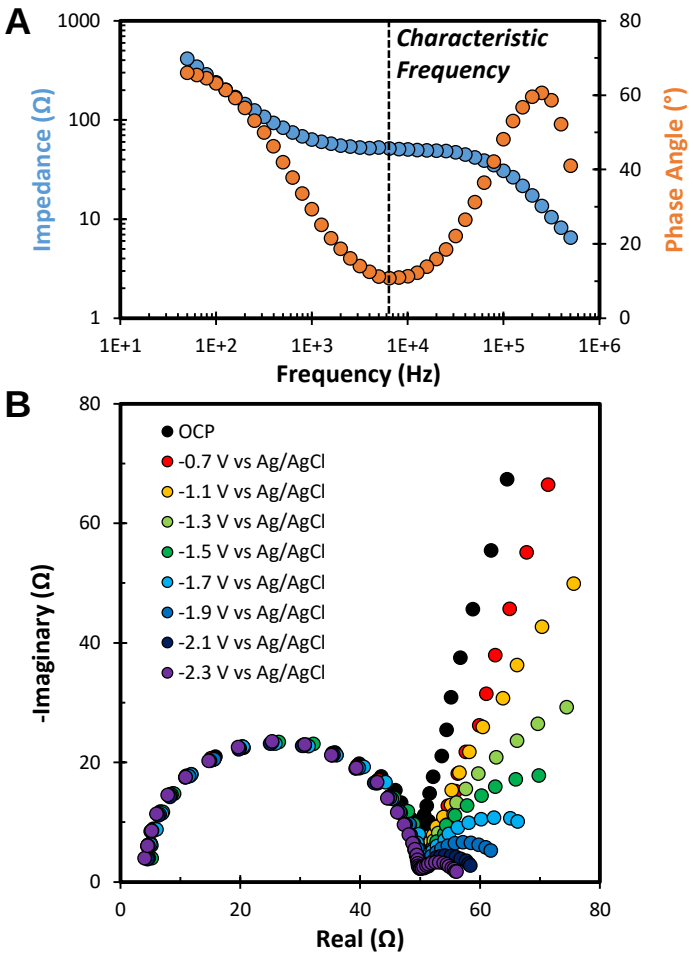

Figure S3.3 *– (A) Bode diagram obtained by applying voltage waveforms with the potential centered at the open circuit potential. (B) Nyquist plot obtained by applying voltage waveforms with the applied potential centered at increasingly negative values.*

The Bode plot obtained with the applied potential centered at the open circuit potential includes contributions from the uncompensated resistance as well as the working electrode-electrolyte interface. To confirm the value of the uncompensated resistance the PEIS measurements were repeated with the voltage waveforms centered at increasingly negative applied potentials. The resulting Nyquist plot, shown in Figure S3.3B, corroborates the conclusion that the correct value of the uncompensated resistance is ~50 Ω.

3.6.4 Electrochemically Active Surface Area of the Ag(hkl) Thin Films

The roughness factors of the Ag thin films were determined by taking the ratio of their double layer capacitances. The double layer capacitance of each thin film was determined by measuring the charging current in a potential range where no Faradaic processes occur at a series of increasingly rapid scan rates. As shown in Figure S3.4, the Ag(110) thin film exhibited slightly higher electrochemically active surface area than either the Ag(111) or Ag(100) thin films. The reproducibility of the roughness factors observed over the Ag thin films suggest that the surface step edge defect density does not vary substantially from sample to sample.

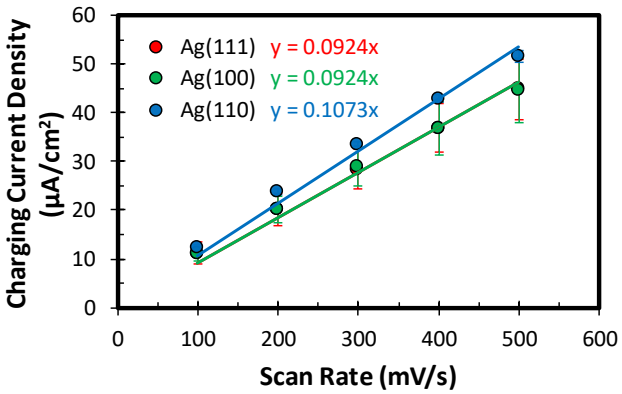

Figure S3.4 *– Comparison of the double layer capacitances of the Ag thin films measured by conducting cyclic voltammetry at a series of increasingly rapid scan rates.*

3.6.5 Gas Chromatography

Gas chromatography (GC) was utilized to quantify the concentration of reaction products in the effluent of the electrochemical cell, which was sampled 10 min after each voltage step. A typical gas chromatogram is depicted in Figure S3.5A. This chromatogram was obtained by analyzing a standard gas mixture containing 1000 ppm of H_2, CO, CH_4, C_2H_4, and C_2H_6 balanced in He. The signal response of the pulsed discharge helium ionization detector (PDHID) was calibrated by analyzing a series of standard gas mixtures. The resulting calibration curves are depicted in Figure S3.5B.

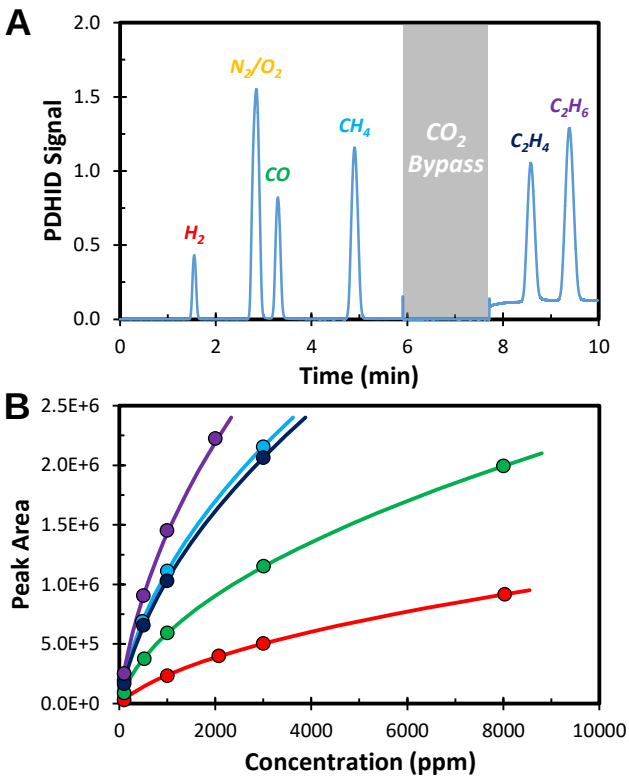

Figure S3.5 *– (A) Representative gas chromatogram containing all the gaseous products expected during CO_2 reduction over Cu. (B) Gaseous product calibration curves.*

3.6.6 High Performance Liquid Chromatography

High performance liquid chromatography (HPLC) was utilized to quantify the reaction products dissolved in the electrolyte. The electrolyte samples collected after chronoamperometry were stored in a refrigerated autosampler until analyzed to minimize the evaporation of volatile liquid-phase reaction products. A typical liquid chromatogram is depicted in Figure S3.6A. This chromatogram was obtained by analyzing a standard solution containing ~10 mM of every liquid-phase product expected during CO_2 reduction. The signal response of the refractive index detector was calibrated by analyzing standard solutions of each product at a concentration of 1, 10, and 50 mM. The resulting calibration curves are depicted in Figure S3.6B.

It is apparent from Figure S3.6A that most of the liquid-phase products are well resolved with the exception of allyl alcohol, ethanol, and propionaldehyde. To determine if peak overlap between these products compromises accurate quantification, standard solutions of these products were prepared at the maximum concentrations expected to be observed in the catholyte after conducting CO_2 reduction over Cu for 70 min. As shown in Figure S3.6C, these products can be resolved by dividing the signal response into three distinct regions.

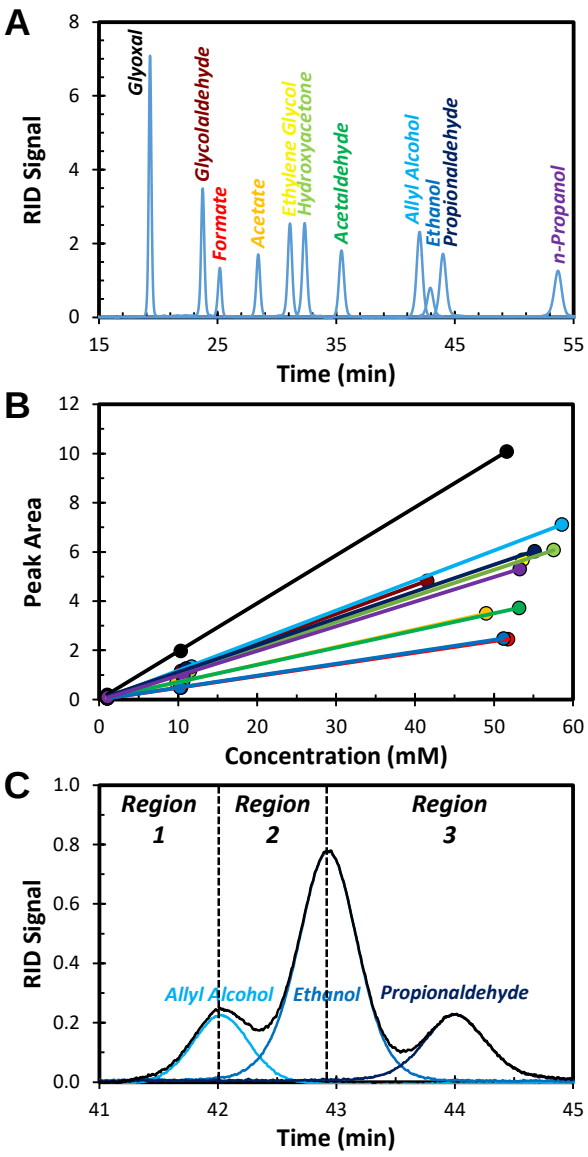

Figure S3.6 *– (A) Liquid chromatogram obtained by analyzing a standard solution containing ~10 mM of all liquid-phase products expected during CO_2 reduction over Cu. (B) Liquid-phase product calibration curves. (C) Deconvolution of the RID signal corresponding to allyl alcohol, ethanol, and propionaldehyde.*

3.6.7 Comparison of Epitaxial Growth Techniques

The electrocatalytic activity observed over Ag(100) thin films prepared using a Cu interlayer is shown in Figure S3.7A. Conversely, the electrocatalytic activity observed over Ag(100) thin films prepared using the Cu-free approach developed herein is shown in Figure S3.7B. Several differences in the electrocatalytic activity observed over the Ag(100) thin films are apparent. The H_2 partial current density is higher and the CO partial current density is lower at a given potential over the Ag(100) thin films prepared using a Cu interlayer. Furthermore, substantial methane formation is observed over the Ag(100) thin film prepared using a Cu interlayer, whereas the Cu-free Ag(100) thin film exhibits negligible activity for methane production. The cause for these observed discrepancies was determined to be the presence of trace amounts of Cu on the surface of the Ag(100) thin film prepared using a Cu interlayer. This was concluded by conducting ISS over both Ag(100) thin films after experimentation, as shown in Figure S3.7C.

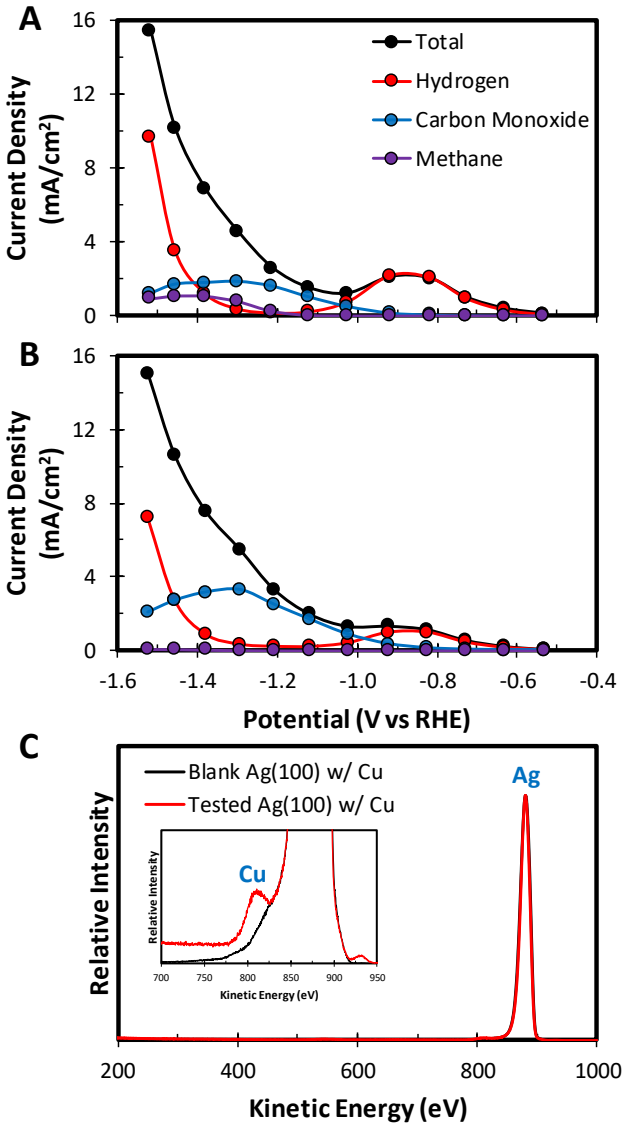

Figure S3.7 *– CO_2 reduction activity observed over Ag(100) thin films prepared using: (A) a Cu interlayer and (B) no Cu interlayer. ISS spectra of the Ag(100) thin films after experimentation. Note the presence of Cu on the surface of the Ag(100) thin film prepared using a Cu interlayer.*

3.6.8 Out-of-Plane and In-Plane X-Ray Diffraction of the Ag(hkl) Thin Films

Symmetric out-of-plane x-ray diffraction (XRD) measurements (θ/2θ) were conducted using Cu Kα radiation (40 kV, 40 mA) to determine the out-of-plane growth orientation of the Ag crystallites in the thin films. In-plane phi scans were conducted at Bragg conditions corresponding to both Si and Ag to determine the orientation of the Ag crystallites with respect to the Si substrate. Out-of-plane rocking curve scans were conducted at the Bragg condition corresponding to the out-of-plane growth orientation of thin films to determine the average degree of misorientation of the Ag crystallites.

The symmetric out-of-plane diffractogram of the Ag thin film deposited onto Si(111) only exhibited a Bragg reflection corresponding to Ag(111), as shown in Figure S3.8A. In-plane phi scans were then conducted at Bragg conditions corresponding to both Si(200) and Ag(200). The resulting diffractograms exhibited the 3-fold symmetry characteristic of the (111) plane. Furthermore, the Si and Ag reflections exhibited no offset. These results confirm the epitaxial nature of the Ag thin film on Si(111) with the relationship Si(111)‖Ag(111). Finally, an out-of-plane rocking curve scan was conducted at the Bragg condition corresponding to Ag(111) and exhibited a fwhm of 0.35°.

The symmetric out-of-plane diffractogram of the Ag thin film deposited onto Si(100) only exhibited a Bragg reflection corresponding to Ag(200), as shown in Figure S3.8B. In-plane phi scans were then conducted at Bragg conditions corresponding to both Si(111) and Ag(111). The resulting diffractograms exhibited the 4-fold symmetry characteristic of the (100) plane. Furthermore, the Si and Ag reflections exhibited no offset. These results confirm the epitaxial nature of the Ag thin film on Si(100) with the relationship Si(100)‖Ag(100). Finally, an out-of-plane rocking curve scan was conducted at the Bragg condition corresponding to Ag(200) and exhibited a fwhm of 1.41°.

The symmetric out-of-plane diffractogram of the Ag thin film deposited onto Si(110) only exhibited a Bragg reflection corresponding to Ag(220), as shown in Figure S3.8C. In-plane phi scans were then conducted at Bragg conditions corresponding to both Si(111) and Ag(111). The resulting diffractograms exhibited the 2-fold symmetry characteristic of the (110) plane. Furthermore, the Si and Ag reflections exhibited no offset. These results confirm the epitaxial nature of the Ag thin film on Si(110) with the relationship Si(110)‖Ag(110). Finally, an out-of-plane rocking curve scan was conducted at the Bragg condition corresponding to Ag(220) and exhibited a fwhm of 0.70°.

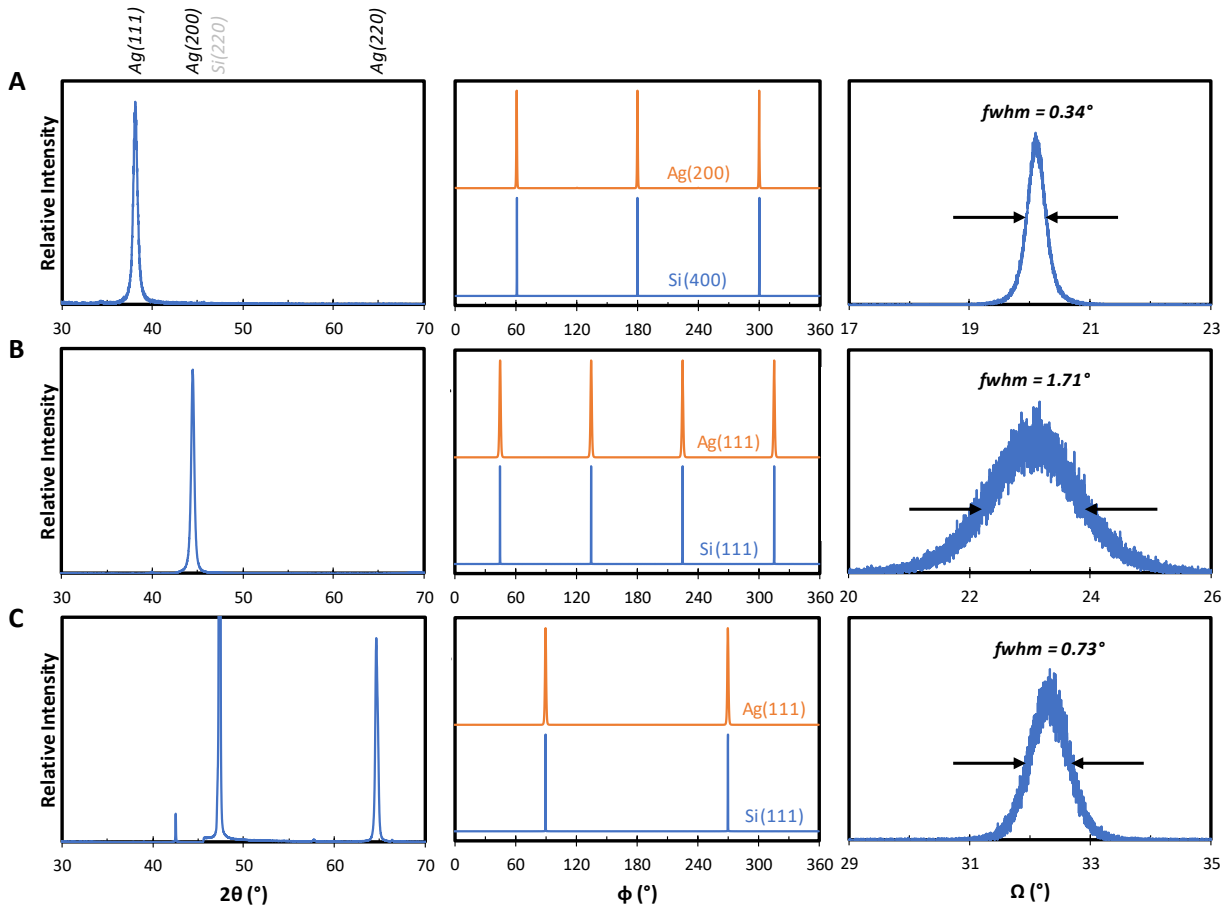

Figure S3.8 *– Symmetric out-of-plane scans, in-plane phi scans at Bragg conditions corresponding to Si and Ag, and rocking curve scans for (A) Ag(111), (B) Ag(100), and (C) Ag(110) thin films.*

3.6.9 Extended X-Ray Pole Figures of the Ag(110) Thin Film

Ag(111) and Ag(200) x-ray pole figures of the Ag thin film sputtered onto Si(110) are shown in Figures S3.9A and S3.9B, respectively. The 2-fold symmetry of the pole figures confirms the epitaxial nature of the Ag thin film sputtered onto Si(110) with the relationship Si(110)‖Ag(110).

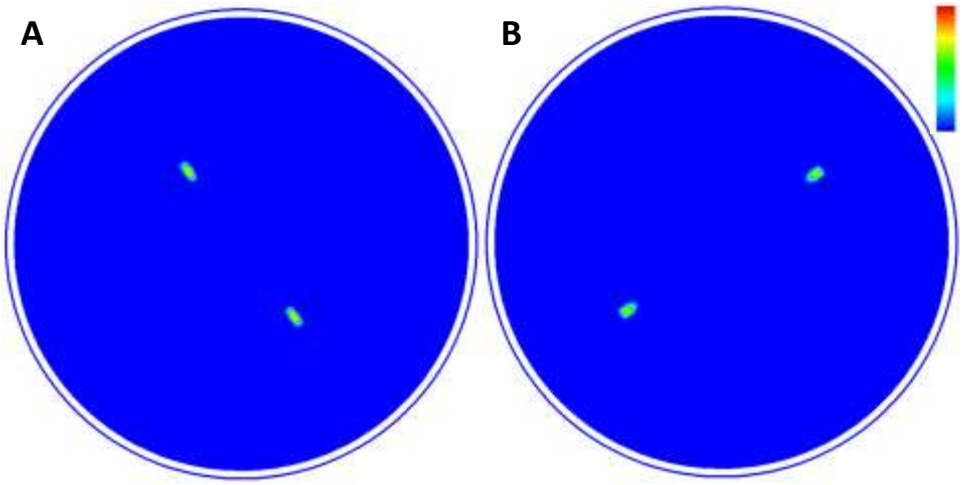

Figure S3.9 *– X-ray pole figures of the Ag thin film sputtered onto Si(110). (A) Ag(111) intensities shown. (B) Ag(200) intensities shown.*

3.6.10 Reversible Chloride Adsorption over the Ag(hkl) Thin Films

Reversible chloride adsorption was conducted over the Ag thin films during cyclic voltammetry from -0.5 to +0.4 V vs SHE at a scan rate of 500 mV/s in 0.01 M KCl saturated with N_2. The cyclic voltammetry was conducted continuously until a stable voltammogram was obtained, which occurred in approximately 10 cycles. The resulting stable cyclic voltammograms exhibited voltammetric waves centered at the reversible potentials for chloride adsorption reported over the corresponding Ag single crystals,[1] as shown in Figure S3.10. Thus, the majority of Ag surface sites are consistent with the bulk orientation of the Ag thin films.

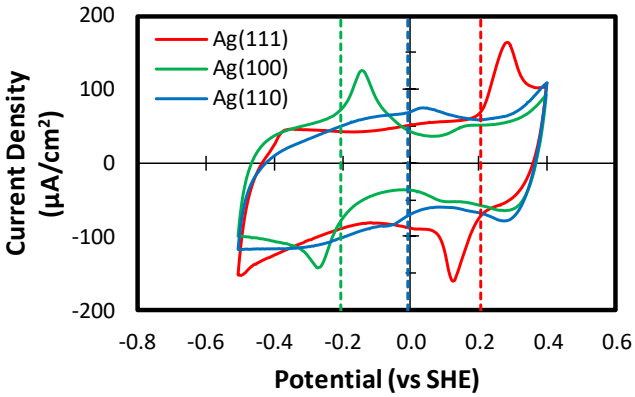

Figure S3.10 *– Reversible chloride adsorption over the Ag thin films measured during cyclic voltammetry at 500 mV/s in 0.01 M KCl. The dotted lines correspond to the reversible potentials of chloride adsorption over the corresponding Ag single crystals.*[1]

3.6.11 Calculation of the Contribution of Defects to the Observed Activity

The contribution of surface defects to the activity observed over an epitaxial thin film was calculated using:

$$\frac{\boldsymbol{j_{Defect}}}{\boldsymbol{j_{Total}}} = \frac{\boldsymbol{x_{Defect} * exp(-\Delta G^{\ddagger}_{Defect})}}{\boldsymbol{x_{Defect} * exp\left(-\Delta G^{\ddagger}_{Defect}\right) + (1 - x_{Defect}) * exp(-\Delta G^{\ddagger}_{Terrace})}}$$

Where:

$\frac{j_{Defect}}{j_{Total}}$	Fraction of observed activity due to surface defects
x_{Defect}	Surface site defect fraction
$\Delta G^{\ddagger}_{Defect}$	Activation barrier over surface defects
$\Delta G^{\ddagger}_{Terrace}$	Activation barrier over terrace sites

3.6.12 Hydrogen Evolution over the Ag(hkl) Thin Films

The H_2 evolution reaction (HER) activity of the Ag thin films was measured by conducting cyclic voltammetry at a scan rate of 20 mV/s in 0.1 M $KHCO_3$ in the absence of CO_2, as shown in Figure S3.11. While the HER activity of the Ag(100) and Ag(110) thin films were found be approximately equivalent, the Ag(111) thin film exhibited superior activity.

The reaction thermodynamics of HER were calculated over Ag(111), Ag(100), Ag(110), and Ag(211) surfaces, as shown in Figure S3.12. The Ag(211) surface was calculated as a representative step edge defect. Based on the calculated reaction thermodynamics, the Ag(110) thin film is expected to have a superior activity to both Ag(111) and Ag(100), which are predicted to have roughly equivalent activities. However, step edge defects are expected to exhibit similar activity as Ag(110).

The inconsistencies between the experimentally observed HER activities of the Ag thin films with what would be expected based on the calculated reaction thermodynamics can be rectified by considering the impact of film defects, such as step edges. Since step edges are expected to exhibit superior HER activity to either Ag(111) or Ag(100), their presence will significantly improve the HER activity observed over these surfaces. Conversely, since step edges are expected to exhibit approximately the same activity as Ag(110), their presence will have little effect on the HER activity observed over this surface. As a result, the presence of step edges more significantly improve the HER activity of Ag(111) and Ag(100) than Ag(110).

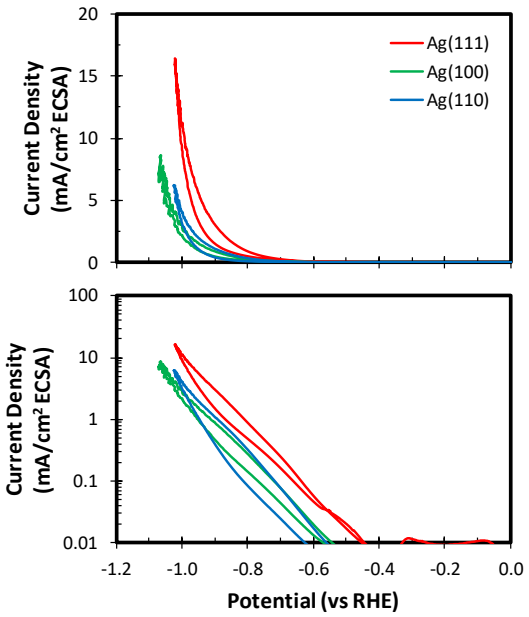

Figure S3.11 *– HER activity of the Ag thin films measured during cyclic voltammetry at a scan rate of 20 mV/s in 0.1 M $KHCO_3$ in the absence of CO_2.*

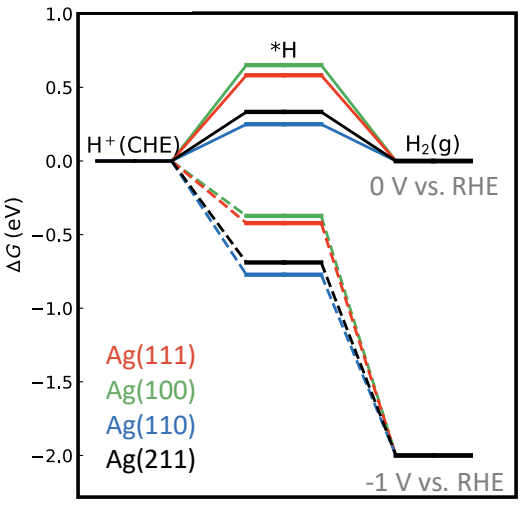

Figure S3.12 *– Homogeneous electric field corrected free energy diagram for CO evolution. A Stern capacitance of 25 $\mu F/cm^2$, a bulk dielectric permittivity of 2, and experimental (100, 111, 110) or theoretical (211) values for the PZCs were used to estimate the electric fields at specific applied potentials.*

3.6.13 Impact of CO_2 on Hydrogen Evolution over Polycrystalline Ag

The HER activity of polycrystalline Ag was measured during linear sweep voltammetry at a scan rate of 5 mV/s in 0.1 M $CsHCO_3$ with and without the presence of CO_2 using a differential electrochemical mass spectrometer reported elsewhere.[2] While the HER activity of polycrystalline Ag was observed to be unaffected by the presence of CO_2 at potentials anodic of -0.7 V vs RHE, the HER activity was substantially suppressed at more cathodic potentials, as shown in Figure S3.13A. Interestingly, this potential corresponds to the onset potential of CO evolution over polycrystalline Ag, as shown in Figure S3.13B. The HER activity did not resume Tafel kinetics until roughly -1 V vs RHE, which corresponds to the potential at which the CO evolution activity of polycrystalline Ag is inhibited by mass transfer limitations under the measurement conditions. These observations support the hypothesis that the evolution of CO inhibits the HER activity of polycrystalline Ag.

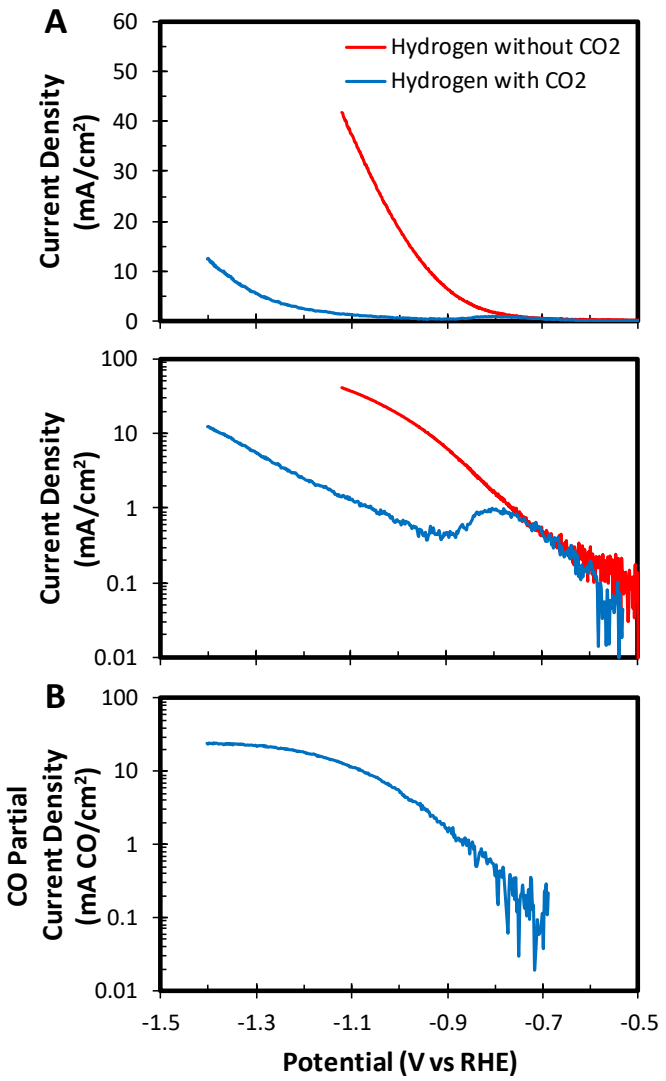

Figure S3.13 *– (A) HER activity observed over polycrystalline Ag during linear sweep voltammetry at a scan rate of 5 mV/s in 0.1 M $CsHCO_3$ with and without the presence of CO_2. (B) CO evolution activity observed over polycrystalline Ag during linear sweep voltammetry at a scan rate of 5 mV/s in 0.1 M $CsHCO_3$.*

3.6.14 Work Function Measurements of the Ag(hkl) Thin Films

The work functions of the Ag thin films were measured using a Kratos Axis Ultra DLD x-ray photoelectron spectrometer (XPS) using monochromatized Al Kα radiation (15 kV, 15 mA) and an accelerating voltage of 9 V. Prior to the measurement, Ar sputtering of the sample surface (5 kV) was briefly conducted to remove the native oxide layer. The work functions observed over the Ag thin films decrease with surface atom density and are in close agreement with what has been reported over Ag single crystals,[3] as shown in Figure S3.14.

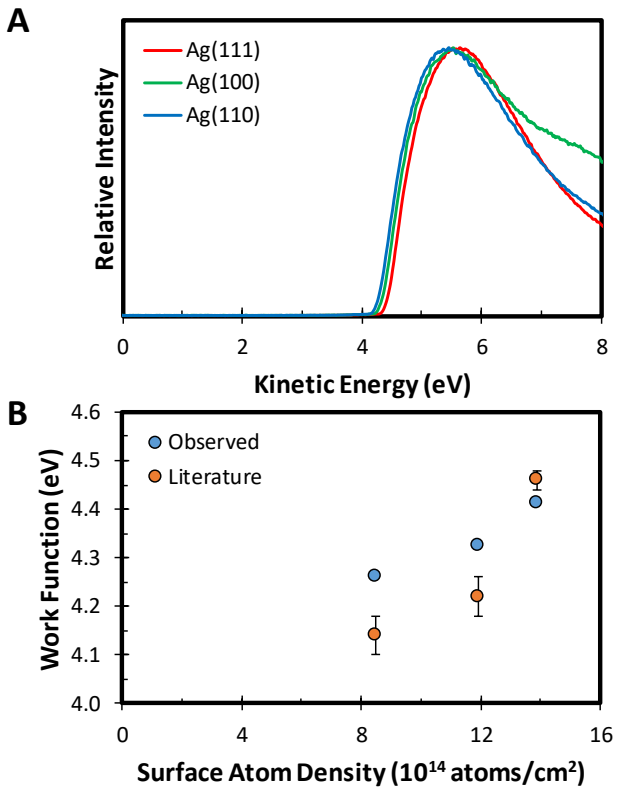

Figure S3.14 *– (A) XPS spectra of the Ag thin films in the low kinetic energy regime. (B) Observed work functions of the Ag thin films as a function of their surface atom density.*

3.6.15 Calculated Surface Charge Density over Ag(hkl)

Table S3.1 *– Experimentally and theoretically determined potentials of zero charge of Ag(111), Ag(100), and Ag(110) and their corresponding calculated surface charge densities at -1 V vs RHE*

	Experimental PZC (V vs SHE)	Calculated PZC (V vs SHE)	Calculated Surface Charge Density at -1 V vs RHE
Ag(111)	-0.45	-0.47	-0.057
Ag(100)	-0.62	-0.66	-0.062
Ag(110)	-0.73	-0.80	-0.073

3.6.16 Z-Component of the Electric Field Distribution over Ag(hkl)

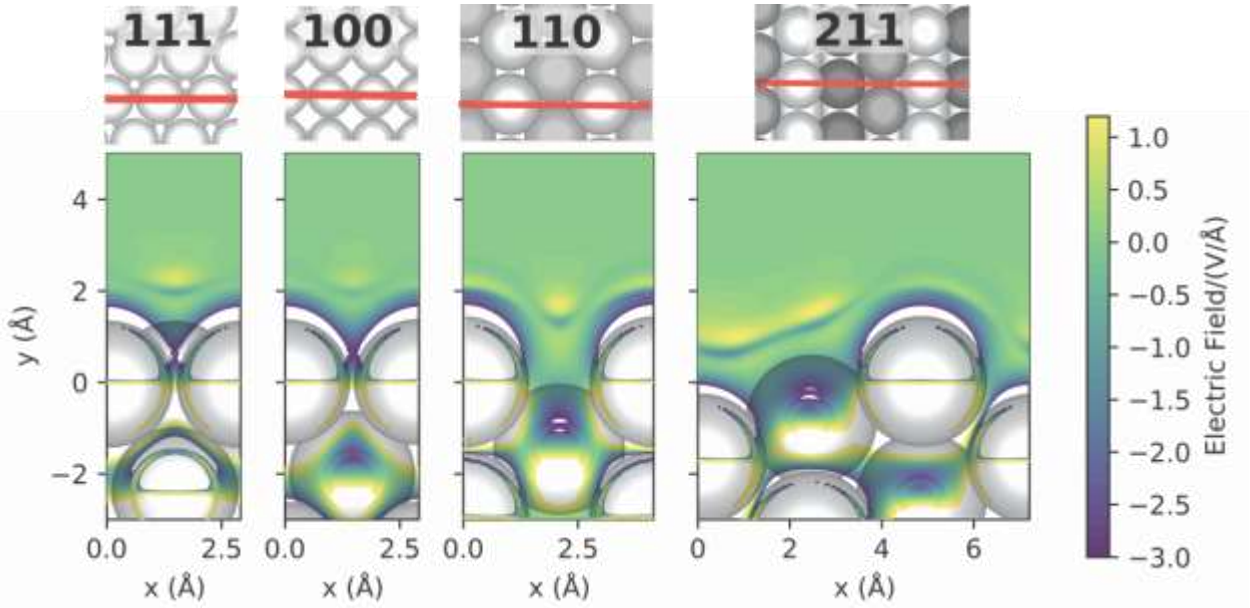

Figure S3.15 *– Magnitude of the z-component of the electric field distribution over Ag(111), Ag(100), Ag(110), and Ag(211) at an applied potential of -1 V vs RHE as obtained from DFT-LPB calculations using VASPsol. The electric field is plotted on an x-z cut through the 3D space as illustrated by the top views of the surfaces. Electric field magnitudes outside the limits of the color bar are represented in white.*

3.6.17 Supplementary Information References

(1) Hoshi, N.; Kato, M.; Hori, Y. Electrochemical Reduction of CO2 on Single Crystal Electrodes of Silver Ag(111), Ag(100), and Ag(110). *J. Electroanal. Chem.* **1997**, *440* (1–2), 283–286.

(2) Clark, E. L.; Bell, A. T. Direct Observation of the Local Reaction Environment during the Electrochemical Reduction of CO2. *J. Am. Chem. Soc.* **2018**, *140* (22), 7012–7020.

(3) Chelvayohan, M.; Mee, C. H. B. Work Function Measurements on (110), (100) and (111) Surfaces of Silver. *J. Phys. C Solid State Phys.* **1982**, *15* (10), 2305–2312.

Chapter 4

Online Quantification of the Products Produced during the Electrochemical Reduction of Carbon Dioxide via Differential Electrochemical Mass Spectrometry

Adapted from:
Clark, E. L.; Singh, M. R.; Kwon, Y.; Bell, A. T. *Anal. Chem.* **2015**, 87, 8013-8020.

Abstract

The discovery of electrocatalysts that can efficiently reduce CO_2 to fuels with high selectivity is a subject of contemporary interest. Currently, the available analytical methods for characterizing the products of CO_2 reduction require tens of hours to obtain the dependence of the product distribution on the applied potential. As a consequence, there is a need to develop novel analytical approaches that can reduce this analysis time down to about an hour. We report here the design, construction, and operation of a novel differential electrochemical mass spectrometer (DEMS) cell geometry that enables the partial current densities of volatile electrochemical reaction products to be quantified in real time. The capabilities of the novel DEMS cell design are demonstrated by carrying out the electrochemical reduction of CO_2 over polycrystalline copper. The reaction products are quantified in real time as a function of the applied potential during linear sweep voltammetry, enabling the product spectrum produced by a given electrocatalyst to be determined as a function of the applied potential on the timescale of roughly one hour.

4.1 Introduction

The prospect of utilizing solar energy to promote the electrochemical or photoelectrochemical reduction of CO_2 to transportation fuels has motivated extensive research aimed at identifying highly active and selective electrocatalysts for CO_2 reduction (CO_2R).[1–4] These efforts have revealed that copper is the only metallic electrocatalyst capable of reducing CO_2 to hydrocarbons and alcohols.[5–7] Unfortunately, the reaction requires an overpotential of approximately -1 V or more, resulting in a cathodic CO_2R energy efficiency of less than 25% (See 4.6.1).[8–11] It has also been

observed that metallic copper produces up to 16 different products depending on the surface morphology and the applied potential.[10,11] As a consequence, a great deal of attention is being devoted to the discovery of novel electrocatalysts that can reduce CO_2 to fuels with higher efficiency and a more narrowly defined product spectrum than can be achieved with metallic copper.

A combination of analytical techniques must be employed to fully characterize the products of CO_2R because the reaction produces both gaseous and liquid-phase products.[8,10] Gas chromatography has been used to quantify the gaseous products by periodically sampling the headspace of the electrochemical cell over the course of electrolysis. The liquid-phase products are analyzed after electrolysis using either high performance liquid chromatography (HPLC) or nuclear magnetic resonance (NMR).[8,10] While gas chromatography is sufficiently sensitive to quantify gaseous products from the effluent of an electrochemical cell, constant potential electrolysis must be performed for roughly one hour in order to reach the detection limits of HPLC or NMR because the Faradaic efficiencies of most liquid-phase products are less than 1%.[10] Due to the reliance on chromatography for product analysis, the dependence of the activity and selectivity of CO_2R electrocatalysts has not been studied extensively as a function of time. This is an issue because CO_2R has been reported to be highly sensitive to electrocatalyst deactivation.[12–18] Therefore, there is considerable interest in the development of an analytical technique capable of continuously quantifying the generation rates of the major reaction products in both phases in real time. The availability of such a technique would enable the potential dependence of the major reaction products to be determined rapidly by simply sweeping the applied potential and recording the product generation rates in real time. With this objective in mind, Koper *et al.* have developed a micron-sized sampling tip that can be placed close to an electrode surface in order to periodically collect liquid-phase reaction for *ex-situ* analysis using HPLC.[19] While this technique is well suited for detecting the presence of liquid-phase reaction products with a more rapid sampling rate, it cannot be used to quantify the Faradaic efficiencies of these products due to the low collection efficiency of the product.

Differential electrochemical mass spectrometry (DEMS) is an analytical technique that utilizes pervaporation to continuously separate and collect electrochemical reaction products.[20] Because the analysis time of mass spectrometry is on the order of a second, the generation rates of gaseous or volatile reaction products can be quantified in real time by recording the relevant mass ion currents and relating them to the partial current densities of the corresponding reaction products.[20] Koper *et al.* developed an online electrochemical mass spectrometer (OLEMS) capable of detecting the hydrocarbon products of CO_2R in real time using a sampling tip placed in close proximity with the electrode surface.[21] In related work, Mayrhofer *et al.* have recently reported the design of a novel DEMS cell capable of detecting the hydrocarbon products of CO_2R that can also be used to raster an electrode surface with varying composition in order to rapidly screen bimetallic CO_2R electrocatalysts.[22] While both approaches can be used to detect the presence of gaseous electrochemical reaction products in real time, neither approach is capable of quantification due to low and ill-defined product collection efficiencies. The collection efficiency of OLEMS is extremely low and highly sensitive to the distance

between the sampling tip and the electrode surface, whereas the thin-layer flow cell geometry employed by Mayrhofer *et al.* suffers from a low product collection efficiency under electrolyte convection.[23]

The capabilities of DEMS strongly depend on the design of the electrochemical cell, which must be capable of achieving both a rapid response time and a high product collection efficiency.[23,24] A number of additional design criteria must also be met to enable product quantification. The working and counter electrodes should be parallel to ensure a uniform potential distribution across the surface of the electrodes, and be separated by an ion-conducting membrane to prevent unwanted parasitic reactions, such as the oxidation of CO_2R products or the reduction of O_2. Electrolyte convection must be employed for two reasons: 1) to assure that the electrolyte does not become depleted of CO_2 and 2) to provide good mass transfer to and away from the cathode (see 4.6.2). It is also necessary to isolate the working electrode from the pervaporation membrane because significant CO_2 depletion will occur due to pervaporation through the collection membrane if it is in the vicinity of the working electrode. As a result, the electrolyte volume between the working electrode and the pervaporation membrane must be minimized so that an acceptable delay time between product generation and detection can be achieved without diluting the liquid-phase reaction products beyond the limits of detection. Finally, the surface area of the working electrode should be large so that the concentration of the liquid-phase products can be maximized.

DEMS cell designs described in the literature preclude product quantification primarily as a consequence of either poorly defined electrochemistry or low product collection efficiencies.[21,25] The dual thin-layer flow cell is capable of achieving liquid-phase product collection efficiencies as high as 40% by locating the working electrode and pervaporation membrane in separate chambers.[24] By minimizing the overall cell volume delay times of ~2 s were achieved. However, the design suffers from a non-parallel electrode configuration and a high cell resistance (~10 kΩ) due to the capillary tube connecting the working and counter electrode chambers.[23,24] The high cell resistance makes it impossible to drive CO_2R to hydrocarbons and alcohols using polycrystalline copper without first reaching the compliance voltage of modern potentiostats. To the best of the authors' knowledge, there have been no reports in the literature of using DEMS to detect the liquid-phase products of CO_2R or to quantify any reaction products in real time.[13,16,22,26–32] The objective of the work reported here was to design and construct a DEMS cell that meets all of the criteria noted above and to demonstrate its performance by conducting CO_2R using a polycrystalline copper cathode.

4.2 Experimental

4.2.1 Cell Design

A schematic of the DEMS cell is depicted in Figure 4.1. The catholyte enters the working electrode chamber through the center of a washer-shaped electrode with an exposed surface area of 1 cm^2. The catholyte rapidly reaches the ion-conducting

membrane, which is separated from the working electrode surface by a thin layer of electrolyte approximately 130 μm thick. The catholyte then flows radially outwards towards the four transfer capillaries, which connect the working electrode and collection chambers. Figure 4.2 shows the details of the working electrode chamber, which has a total catholyte volume of roughly 25 μL. The reference electrode intercepts the catholyte stream at the base of the working electrode mounting screw, which also serves as the electrolyte inlet to the working electrode chamber. By locating the reference electrode outside of the working electrode chamber the impact of gaseous product bubble formation on the potential referencing of the working electrode is minimized. A third chamber, located above the working electrode chamber, houses the counter electrode such that a parallel electrode configuration is achieved. The counter electrode is a mesh disc with an exposed surface area of roughly 2 cm^2. The electrolyte is pumped from a shared reservoir through both electrode chambers at the same flow rate using a set of identical syringe pumps. The surface area of the ion-conducting membrane separating the two electrode chambers is roughly 1.75 cm^2. As a result of these design decisions the DEMS cell has a low cell resistance (~50 Ω), robust electrode connectivity, and minimal overpotential at the counter electrode, which enables the potentials required to produce hydrocarbons and alcohols over polycrystalline copper to be experimentally accessible. Additional photographs of the DEMS cell and a table of specifications can be found in the supplementary information (see 4.6.3 and 4.6.4).

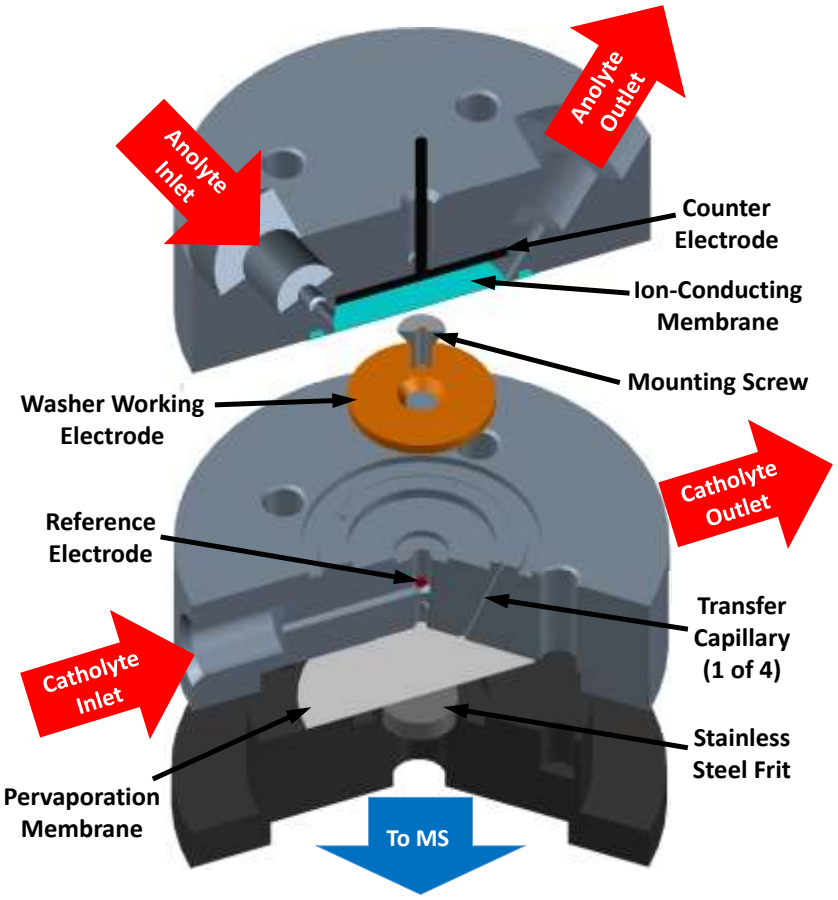

Figure 4.1 *– Schematic of the DEMS cell.*

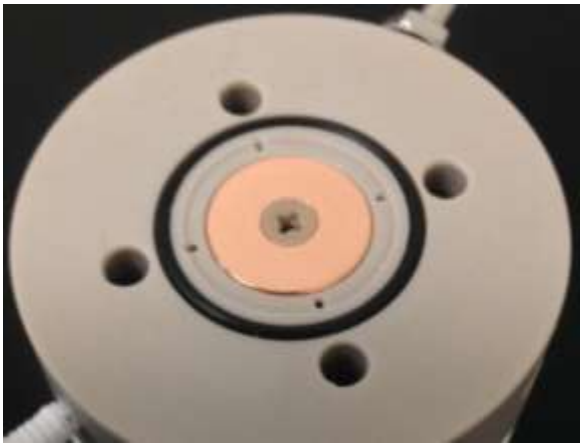

Figure 4.2 *– Photograph of the working electrode chamber.*

The working and counter electrode chambers were fabricated of polyether ether ketone (Professional Plastics) and polycarbonate (McMaster-Carr), respectively, and were fitted with Viton O-rings (McMaster-Carr). The cell was treated with UV-generated ozone to reduce the wetting angle of the electrolyte on the exposed surfaces of the cell, which reduces the holdup of gaseous product bubbles in the working electrode chamber (see 4.6.5). The working electrode was machined from a copper sheet (99.999% Sigma Aldrich). Prior to each experiment the copper surface was polished mechanically with a diamond polishing compound to a mirror-like finish (0.1 μm, Ted Pella Inc.). The counter electrode was a platinum gauze disc (100 mesh, 99.9% Sigma Aldrich) that was flame annealed prior to each experiment. A Ag/AgCl electrode was used as the reference (1 mm OD, Innovative Instruments Inc.). A proton-conducting membrane (Nafion 110, Ion Power Inc.) was used as the ion-conducting membrane. Attempts were made to use an anion-conducting membrane (Selemion AMV, AGC Inc.) but they were not successful due to gaseous product bubble holdup on the membrane surface that severely disrupted the electrochemical measurements. A PTFE sheet (20 nm pore size, Hangzhou Cobetter Filtration Equipment Co.) was used as the pervaporation membrane. A 0.05 M K_2CO_3 (99.995% Sigma Aldrich) solution prepared using 18.2 MΩ deionized water from a Millipore system was used as the electrolyte. After saturation with CO_2 (99.999% Praxair) at 25 °C the steady state pH of the electrolyte was 6.8, making it chemically equivalent to a 0.1 M $KHCO_3$ solution saturated with CO_2 at the same temperature (see 4.6.6).

4.2.2 Electrochemistry

Electrochemistry was performed using a Biologic VSP-300 potentiostat. All electrochemical data were recorded versus the reference electrode and converted to the RHE scale using the relationship $E_{RHE} = E_{Ag/AgCl} + 0.197 + 0.059 \times pH_{Bulk}$. A 5 Hz filter was used to eliminate noise from the working electrode potential measurement caused by the flow of electrolyte. Prior to each experiment the potential applied to the working electrode was swept from open circuit to -1 V vs RHE at 50 mV/s in order to reduce the native CuO_x layer. Potentiostatic electrochemical impedance spectroscopy (PEIS) was then used to determine the total uncompensated resistance (R_u) by applying frequencies from 10 Hz to 30 kHz at the open circuit potential (see 4.6.7). The potentiostat compensated for 85% of R_u *in-situ* and the last 15% was post-corrected to arrive at

accurate potentials. The potential applied to the working electrode was then swept from open circuit to -1.2 V vs RHE at 0.2 mV/s. This scan rate was determined experimentally to be optimal for reducing the impact of bubble noise on the recorded mass ion current trends (see 4.6.8). The linear potential sweep was repeated twice, and only the second scan was used for further analysis.

4.2.3 Mass Spectrometry

Mass spectra were acquired using a Hiden HPR40 dissolved-species mass spectrometer. An electron energy of 70 eV was used for the ionization of all species with an emission current of 500 μA. Hydrogen ions (m/z = 2) were accelerated using a voltage of 1.3 V to prevent detector saturation while methane (m/z = 15), ethene (m/z = 26), and ethanol/1-propanol (m/z = 31) ions were accelerated using a voltage of 3 V to maximize the detector response. All mass-selected product cations were detected using a secondary electron multiplier with a detector voltage of 1,200 V. These mass spectrometer settings were determined to be optimal for maximizing the signal to noise ratio of the liquid-phase products while not overloading the detector with H_2 (see 4.6.9). Using these settings a data point was recorded every 1.4 s. The data was averaged over 10 mV increments during linear sweep voltammetry and over 1 min intervals during chronoamperometry in order to minimize the influence of bubble noise on the recorded trends.

4.3 Results and Discussion

4.3.1 Electrolyte Flow Rate and Product Detectability

The flow pattern and the average residence time of the catholyte in the working electrode were found to influence the cell performance and the liquid-phase product detectability. First, the convection of the catholyte driven by either a positive pressure applied at the cell inlet or a negative pressure applied at the cell outlet was examined. In the first case, the formation of recirculation eddies led to an increase in the holdup of gaseous product bubbles in the working electrode chamber, which caused erratic current flow due to the partial blockage of catholyte access to the electrode surface. These difficulties were eliminated when electrolyte convection was driven by negative pressure applied at the cell outlet. To support these observations the electrolyte velocity field across the working electrode chamber was simulated for convection driven by both positive and negative pressure (see 4.6.10). As shown in Figure 4.3, the simulations confirm the existence of recirculation eddies in the case of electrolyte convection driven by positive pressure. However, these eddies do not form when electrolyte convection is driven by negative pressure. For this reason, negative pressure was employed to supply the electrolyte.

It is important that the average residence time of the electrolyte in the working electrode chamber be neither too short nor too long. Too short a residence time will lead to insufficient product accumulation in the electrolyte stream, thereby reducing the detectability of the products of interest. Conversely, too long a residence time will cause

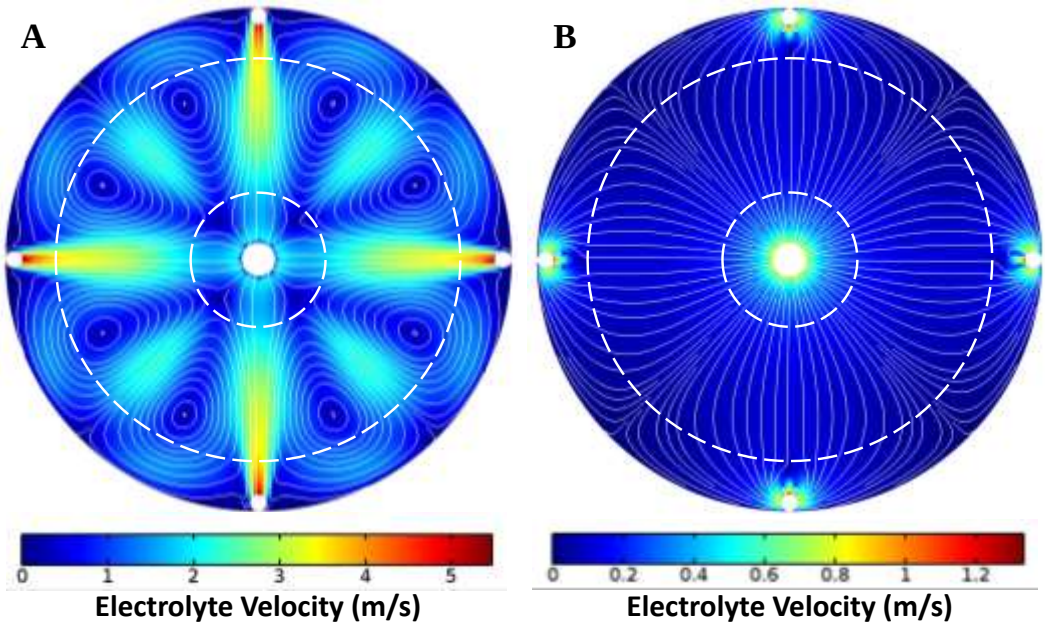

Figure 4.3 *– Catholyte flow field in the working electrode chamber at a flow rate of 1 mL/min for convection driven by (A) positive pressure applied at the inlet and (B) negative pressure applied at the outlet. The working electrode surface is denoted by the region between the dashed white lines.*

an accumulation of gaseous product bubbles in the working electrode chamber and a depletion of dissolved CO_2, which may result in mass transfer limitations. Ideally, the average residence time should be equivalent to the time interval over which mass spectrometry data will be acquired. To this end, the residence time distribution of the catholyte passing through the working electrode chamber and the transfer capillaries was calculated as a function of the flow rate by solving the Navier-Stokes and mass-balance equations in COMSOL Multiphysics v4.3b (see 4.6.10). As shown in Figure 4.4, the calculations indicate that a flow rate of at least 0.5 mL/min is required to achieve an average residence time on the order of the analysis time of the mass spectrometer (~1.5 s). However, there is a wide standard deviation in the residence time at this flow rate, as

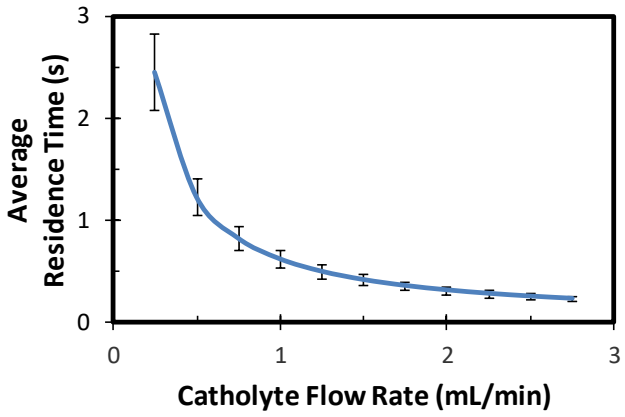

Figure 4.4 *– Average residence time and distribution (error bars) of the catholyte in the working electrode chamber as a function of the electrolyte flow rate.*

indicated by the error bars, which reduces the accuracy of the liquid-phase product quantification. To reduce this uncertainty a minimum flow rate of 1 mL/min was selected. The maximum volumetric generation rate of gaseous products produced using polycrystalline copper was calculated to be less than 100 µL/min at potentials positive of -1.2 V vs RHE (see 4.6.11). Thus, there should be no issues with gaseous product accumulation inside the cell chambers at the minimum flow rate selected.

All gaseous CO_2R products are detectable using DEMS except CO. CO is undetectable because its ionization produces the same mass fragments as CO_2, which is present in the electrolyte at a concentration at least three orders of magnitude higher than CO at the minimum electrolyte flow rate (see 4.6.12). To estimate the detection limit of the liquid-phase products, increasingly concentrated ethanol and 1-propanol solutions were fed into the cell at 1 mL/min. The limit of detection was defined as the concentration of these species that resulted in a mass ion current signal equal to the magnitude of the standard deviation of the baseline signal. By this means the liquid-phase product detection limit was determined to be ~5 µM (see 4.6.13). According to the current literature, the only liquid-phase products with generation rates high enough to reach this concentration at the minimum electrolyte flow rate are formic acid, ethanol, and 1-propanol (see 4.6.14). However, formic acid is undetectable since this species is fully dissociated, and hence cannot pervaporate into the mass spectrometer at the pH of the electrolyte. The inability to detect formic acid was verified experimentally using a formic acid solution two orders of magnitude more concentrated than expected to be observed during CO_2R at the minimum electrolyte flow rate (see 4.6.15).

Only signal from the primary ionization fragment of ethanol and 1-propanol (*m/z* = 31) was observable during CO_2R over polycrystalline copper at the minimum electrolyte flow rate. This is an issue because cations with this *m/z* ratio are also produced by methanol, glycolaldehyde, ethylene glycol, allyl alcohol, and propionaldehyde. However, based on previous literature reports only ethanol and 1-propanol will contribute significantly to the *m/z* = 31 signal, since the Faradaic efficiencies of the other products do not exceed 2% (see 4.6.16).[8,10] In principle, it should be possible to deconvolute the contributions to the *m/z* = 31 signal made by ethanol and 1-propanol using the mass ion currents associated with their secondary ionization fragments. However, the secondary ionization fragment produced by ethanol (*m/z* = 46) overlaps with that from $C^{12}O^{18}{}_2$, resulting in an erratic baseline that prevents clear trends from being observed (see 4.6.17). Furthermore, the concentration of 1-propanol expected to be formed by the reaction is insufficient to reach the detection limit of its secondary ionization fragment (*m/z* = 59) (see 4.6.17). In order to determine the contribution of ethanol and 1-propanol to the *m/z* = 31 signal their generation rates over polycrystalline copper were measured at a series of increasingly negative potentials in a conventional H-type cell. After electrolysis the composition of the catholyte was measured using HPLC and the relative concentration of ethanol to 1-propanol was plotted as a function of the applied potential (see 4.6.18). The linear relationship was then used to deconvolute the *m/z* = 31 signal as a function of potential so that the generation rates of both alcohols could be determined in real time, assuming that they are both uniformly distributed in the catholyte entering the collection chamber.

4.3.2 Product Quantifiability

Linear sweep voltammetry was conducted in a He-sparged electrolyte (pH = 11.3) so that the ion current for *m/z* = 2 could be related directly to the hydrogen generation rate. As shown in Figures 4.5A and 4.5B, the total current density and ion current for *m/z* = 2 track each other as a function of potential under these conditions. This clearly demonstrates that a recorded mass ion current can be related directly to the generation rate of the corresponding product.[20] As shown in Figures 4.5B and 4.5C, a discontinuity in the *m/z* = 2 signal response and a sudden increase in the standard deviation are observed at -0.6 V vs RHE. The current density corresponding to this potential was calculated to result in the saturation of the electrolyte with hydrogen (see 4.6.19). Thus, positive of -0.6 V vs RHE the hydrogen is entirely dissolved and hence no change is observed in the standard deviation of the ion current for *m/z* = 2 versus the baseline standard deviation. However, at potentials negative of -0.6 V vs RHE the hydrogen saturates the electrolyte and forms bubbles, causing the sudden increase in the standard

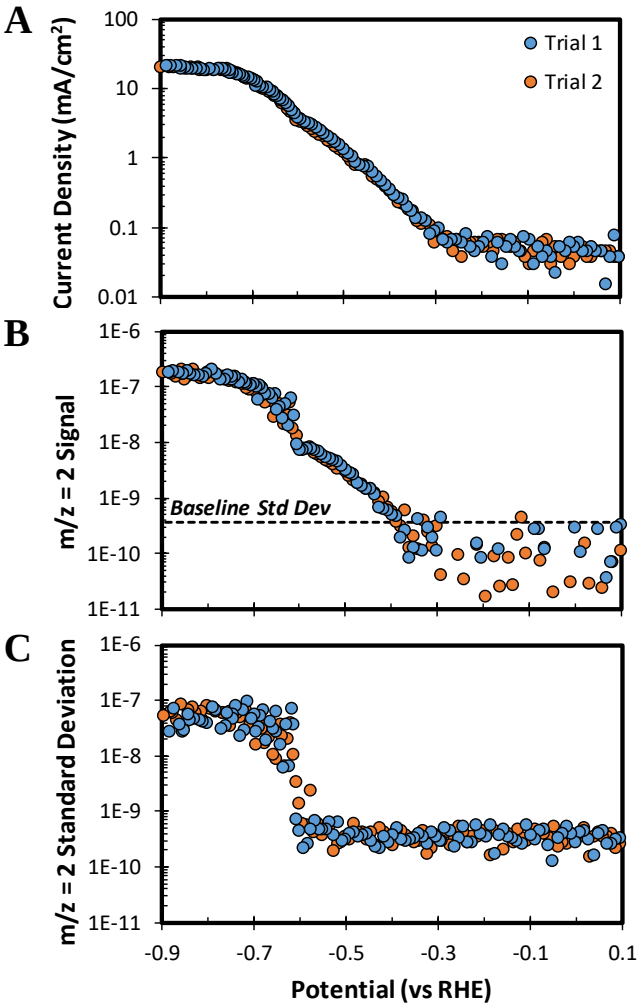

Figure 4.5 *– DEMS results obtained in a He-sparged 0.05 M K_2CO_3 electrolyte (pH = 11.3) using an electrolyte flow rate of 1 mL/min and a scan rate of 1 mV/s. (A) Current density. (B) m/z = 2 signal. (C) m/z = 2 standard deviation.*

deviation of the ion current for *m/z* = 2. Chronopotentiometry was conducted for 10 min at increasingly negative current densities in order to establish the *m/z* = 2 calibration curve for the case of He-sparged electrolyte. As shown in Figure 4.6, distinct calibration regimes were observed for dissolved and gaseous hydrogen. The signal response is greater for gaseous hydrogen because the collection efficiency of a gaseous product is higher than that of a dissolved product. Thus, it is imperative to use the standard deviation of the recorded mass ion currents to identify which phase the detected products are in so that accurate quantification can be performed.

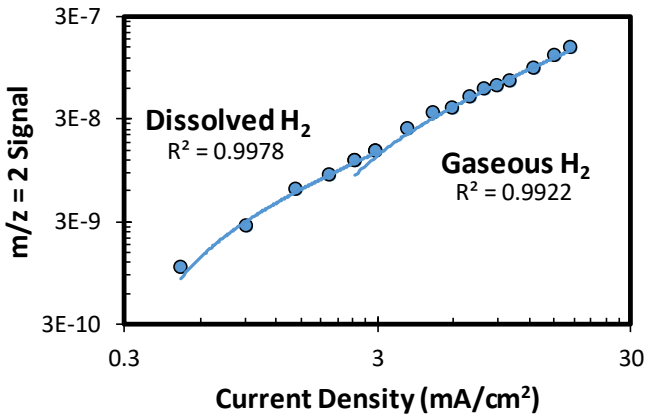

Figure 4.6 *– m/z = 2 calibration curve for the case of a He-sparged electrolyte.*

4.3.3 Rapid Electrocatalyst Screening via Linear Sweep Voltammetry

Linear sweep voltammetry was conducted in a CO_2-sparged electrolyte to demonstrate the ability of the DEMS cell to quantify the generation rates of multiple electrochemical reaction products in real time. The recorded voltammogram, shown in Figure 4.7, closely matches that reported by Jaramillo *et al.*[10] at potentials positive of -1.2 V vs RHE, indicating that the cell geometry does not significantly impact the electrochemistry up to this potential. At potentials more negative than -1.2 V vs RHE a suppression in the current density is observed that is a result of inadequate gaseous product bubble clearing from the working electrode surface. At the potentials of gaseous product detection onset the standard deviations of the corresponding ion currents increased versus the standard deviation of the baselines (see 4.6.20). This pattern, which was absent for *m/z* = 31, indicates that the detected gaseous products have phase segregated from the aqueous electrolyte at these potentials. Thus, the ion currents corresponding to the gaseous products were calibrated by introducing a standard gas containing hydrogen, methane, and ethene into the catholyte stream at a series of defined flow rates (see 4.6.21). This calibration methodology simulates the formation of gaseous product bubbles at the working electrode surface because the standard gas bubbles are completely removed from the catholyte stream in the collection chamber, enabling the mass ion current signals corresponding to the gaseous products to be directly related to the flux of the individual chemical species entering the collection chamber. The signal response for *m/z* = 2 obtained using this approach matched the gaseous hydrogen calibration curve obtained electrochemically in a He-sparged electrolyte, indicating that

this calibration methodology is accurate because it produces the same signal response that is observed electrochemically.

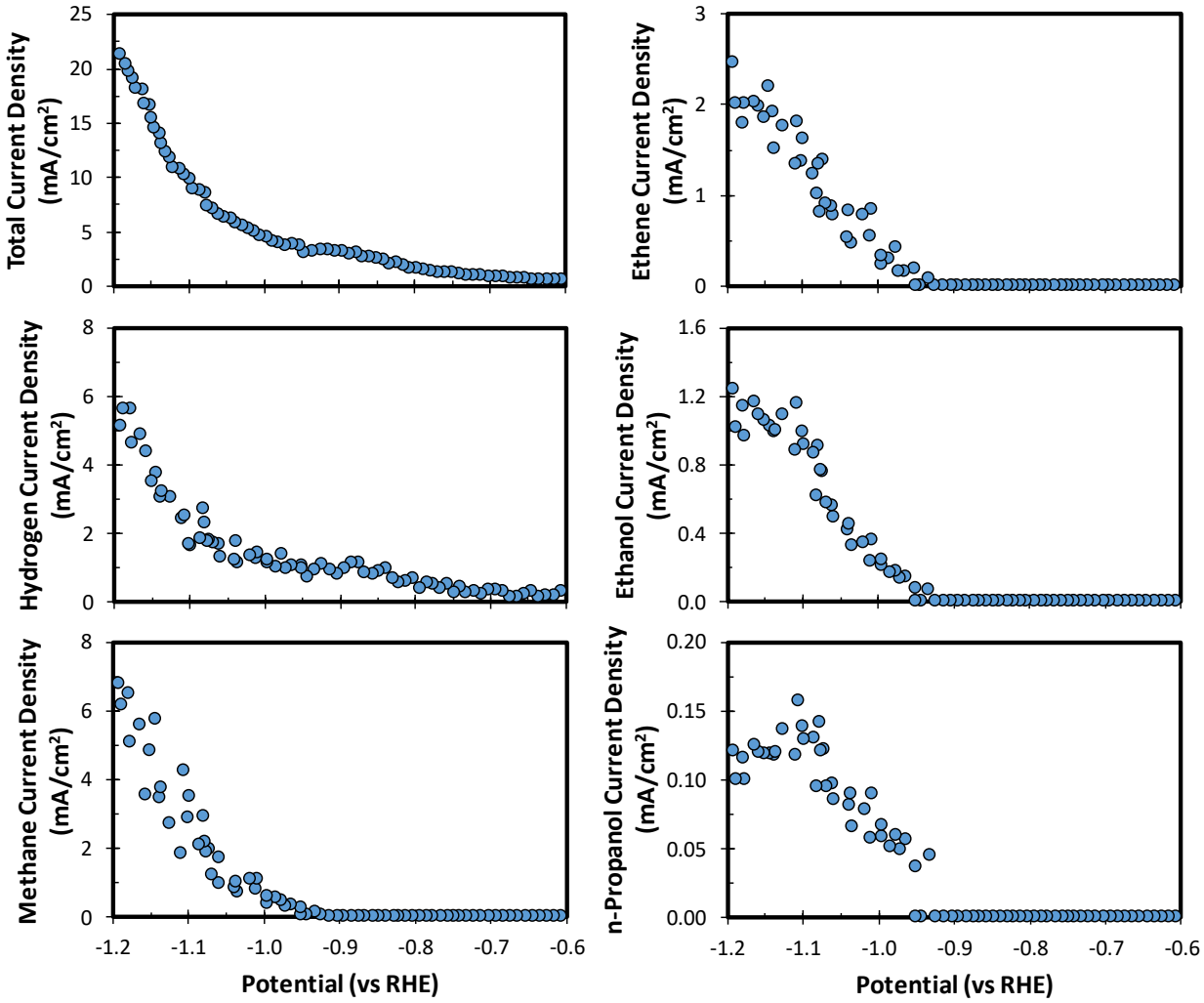

Figure 4.7 *– DEMS results obtained in a CO_2-sparged 0.05 M K_2CO_3 electrolyte (pH = 6.8) using an electrolyte flow rate of 1 mL/min and a scan rate of 0.2 mV/s.*

The partial current potential dependence of hydrogen, methane, ethene, ethanol, and 1-propanol recorded during the linear potential sweep are shown in Figure 4.7. While the recorded data exhibit trends similar to those previously reported[8,10,33] (see 4.6.22) two major discrepancies exist: (1) the total current density is higher at potentials positive of the onset of hydrocarbon and alcohol detection and (2) the partial current densities of the C_{2+} products do not decline at potentials negative of -1.1 V vs RHE. Both discrepancies can be explained by the use of electrolyte convection, which increases the CO_2 concentration and minimizes the CO_2R product concentrations in the vicinity of the cathode. The adsorption of CO onto the copper surface is known to result in potential-dependent deactivation.[8,34,35] By minimizing the concentration of CO in the vicinity of the cathode, a higher CO desorption rate is achieved, which reduces the extent of CO poisoning at potentials positive of the onset of hydrocarbons and alcohols. Recent modeling efforts suggest that a significant increase in the pH and a depletion of dissolved

CO_2 occur within the hydrodynamic boundary layer at the surface of a polycrystalline copper cathode at potentials negative of -1 V vs RHE despite vigorous electrolyte mixing.[36] These losses cause the measured electrocatalytic activity and selectivity to differ from those that would be observed in the absence of electrolyte polarization and mass-transfer limitations. The DEMS cell employed in this study minimizes these polarization and mass transfer effects by virtue of the continuous flow of electrolyte, which reduces the hydrodynamic boundary layer thickness and continuously supplies the electrode surface with CO_2. This is why the partial current densities of the C_{2+} products do not decline at potentials more negative than -1.1 V vs RHE. This hypothesis is further supported by the suppression of HER observed at these potentials using the DEMS cell. Thus, the DEMS cell described here is superior to conventional mixed electrolyte cells for measuring intrinsic electrocatalytic activities and selectivities at high current densities.

4.3.4 Measuring Transient Selectivity via Chronoamperometry

There have been no reports in the literature demonstrating changes in the selectivity of CO_2R to C_{2+} liquid-phase products as a function of time. This is an issue because the selectivity to C_{2+} products has been reported to be extremely sensitive to the presence of impurities in the electrolyte, such as iron and zinc, that quickly contaminate the copper surface at the potentials required to drive CO_2R to hydrocarbons and alcohols.[18,37] Currently, liquid product selectivity is quantified at the end of the reaction and it is assumed that no deactivation occurs over the course of ~1 h electrolysis. However, the validity of this assumption has not been substantiated experimentally due to the lack of an analytical technique capable of quantifying the transient generation rates of the C_{2+} liquid-phase products in real time. To fill this void chronoamperometry was conducted at -1.14 V vs RHE for 1 h. As shown in Figure 4.8, no substantial change in the ethanol or 1-propanol Faradaic efficiency was observed over the course of electrolysis. Furthermore, the Faradaic efficiencies of the other detectable reaction products were constant over the electrolysis period (see 4.6.23). These results suggest that deactivation of the copper electrode is not an issue as long as high purity reagents are used to prepare the electrolyte.

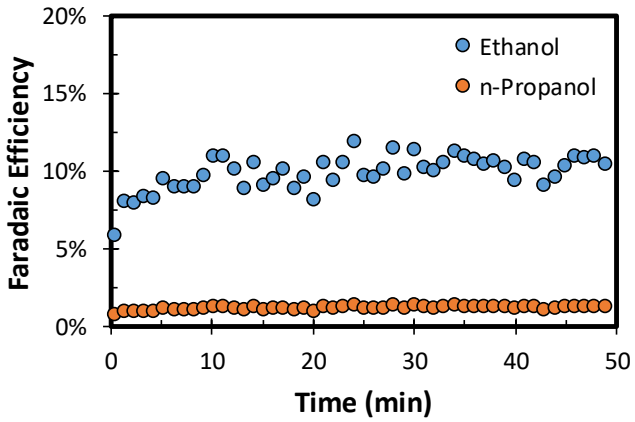

Figure 4.8 *– Transient ethanol and 1-propanol Faradaic efficiencies recorded during chronoamperometry at -1.14 V vs RHE in a CO_2-sparged 0.05 M K_2CO_3 electrolyte (pH = 6.8) using an electrolyte flow rate of 1 mL/min. The data represents a single experiment.*

4.4 Conclusions

In conclusion, a DEMS cell has been designed that satisfies all of the criteria required to achieve meaningful product quantification in real time. These criteria include a parallel electrode configuration, high product collection efficiencies, and a rapid response time. The efficacy of the cell was demonstrated by performing CO_2R over polycrystalline copper and quantifying the generation rates of both gaseous and liquid-phase products during a linear potential sweep and at a fixed potential as a function of time. To the best of our knowledge, this effort represents the first example of DEMS being used to quantify all major products of CO_2R, with the exception of CO and formic acid. The potential dependence of the partial current densities of the detectable reaction products matched the trends reported by other workers[8,10,33] but were obtained on the timescale of an hour rather than the tens of hours required using the conventional analytical approaches. It was also demonstrated that the copper electrocatalyst experiences no deactivation over the course of 1 h electrolysis at a fixed potential when pure reagents are used to prepare the electrolyte. This is the first time that the transient selectivity of CO_2R to C_{2+} liquid-phase products has been reported in the literature. The DEMS cell developed and described in this study is currently being used to screen the activity and selectivity of novel electrocatalysts as a function of potential and to investigate changes in their activity and selectivity over time.

4.5 References

(1) Jitaru, M.; Lowy, D. A.; Toma, M.; Toma, B. C.; Oniciu, L. Electrochemical Reduction of Carbon Dioxide on Flat Metallic Cathodes. *J. Appl. Electrochem.* **1997**, *27* (8), 875–889.

(2) Gattrell, M.; Gupta, N.; Co, A. A Review of the Aqueous Electrochemical Reduction of CO2 to Hydrocarbons at Copper. *J. Electroanal. Chem.* **2006**, *594* (1), 1–19.

(3) Hori, Y. Electrochemical CO2 Reduction on Metal Electrodes. In *Modern Aspects of Electrochemistry*; Vayenas, C. G., White, R. E., Gamboa-Aldeco, M. E., Eds.; Springer: New York, 2008; pp 89–189.

(4) Whipple, D. T.; Kenis, P. J. A. Prospects of CO2 Utilization via Direct Heterogeneous Electrochemical Reduction. *J. Phys. Chem. Lett.* **2010**, *1*, 3451–3458.

(5) Hori, Y.; Kikuchi, K.; Suzuki, S. Production of CO and CH4 in Electrochemical Reduction of CO2 at Metal Electrodes in Aqueous Hydrogencarbonate Solution. *Chem. Lett.* **1985**, *14* (11), 1695–1698.

(6) Noda, H.; Ikeda, S.; Oda, Y.; Imai, K.; Maeda, M.; Ito, K. Electrochemical Reduction of Carbon Dioxide at Various Metal Electrodes in Aqueous Potassium Hydrogen Carbonate Solution. *Bull. Chem. Soc. Jpn.* **1990**, *63* (9), 2459–2462.

(7) Hori, Y.; Wakebe, H.; Tsukamoto, T.; Koga, O. Electrocatalytic Process of CO Selectivity in Electrochemical Reduction of CO2 at Metal Electrodes in Aqueous Media. *Electrochim. Acta* **1994**, *39* (11–12), 1833–1839.

(8) Hori, Y.; Murata, A.; Takahashi, R. Formation of Hydrocarbons in the Electrochemical Reduction of Carbon Dioxide at a Copper Electrode in Aqueous Solution. *J. Chem. Soc. Faraday Trans. I* **1989**, *85* (8), 2309–2326.

(9) Peterson, A. A.; Abild-Pedersen, F.; Studt, F.; Rossmeisl, J.; Nørskov, J. K. How Copper Catalyzes the Electroreduction of Carbon Dioxide into Hydrocarbon Fuels. *Energy Environ. Sci.* **2010**, *3* (9), 1311.

(10) Kuhl, K. P.; Cave, E. R.; Abram, D. N.; Jaramillo, T. F. New Insights into the

Electrochemical Reduction of Carbon Dioxide on Metallic Copper Surfaces. *Energy Environ. Sci.* **2012**, *5* (5), 7050–7059.
(11) Tang, W.; Peterson, A. a; Varela, A. S.; Jovanov, Z. P.; Bech, L.; Durand, W. J.; Dahl, S.; Nørskov, J. K.; Chorkendorff, I. The Importance of Surface Morphology in Controlling the Selectivity of Polycrystalline Copper for CO2 Electroreduction. *Phys. Chem. Chem. Phys.* **2012**, *14* (1), 76–81.
(12) Dewulf, D. W.; Tuo, J.; Bard, A. J. Electrochemical and Surface Studies of Carbon Dioxide Reduction to Methane and Ethylene at Copper Electrodes in Aqueous Solutions. *J. Electrochem. Soc.* **1989**, *136* (6), 1686–1691.
(13) Wasmus, S.; Cataneo, E.; Vielstich, W. Reduction of Carbon Dioxide to Methane and Ethene-An On-Line MS Study with Rotating Electrodes. *Electrochim. Acta* **1990**, *35* (4), 711–715.
(14) Kyriacou, G.; Anagnostopoulos, A. Electroreduction of CO2 on Differently Prepared Copper Electrodes: The Influence of Electrode Treatment on the Current Efficiences. *J. Electroanal. Chem.* **1992**, *322*, 233–246.
(15) Shiratsuch, R.; Aikoh, Y.; Nogami, G. Pulsed Electroreduction of CO2 on Copper Electrodes. *J. Electrochem. Soc.* **1993**, *140* (12), 3479–3482.
(16) Friebe, P.; Bogdanoff, P.; Alonso-Vante, N.; Tributsch, H. A Real-Time Mass Spectroscopy Study of the (Electro)chemical Factors Affecting CO2 Reduction at Copper. *J. Catal.* **1997**, *168*, 374–385.
(17) Lee, J.; Tak, Y. Electrocatalytic Activity of Cu Electrode in Electroreduction of CO2. *Electrochim. Acta* **2001**, *46*, 3015–3022.
(18) Hori, Y.; Konishi, H.; Futamura, T.; Murata, A.; Koga, O.; Sakurai, H.; Oguma, K. “Deactivation of Copper Electrode” in Electrochemical Reduction of CO2. *Electrochim. Acta* **2005**, *50*, 5354–5369.
(19) Kwon, Y.; Koper, M. T. M. Combining Voltammetry with HPLC: Application to Electro-Oxidation of Glycerol. *Anal. Chem.* **2010**, *82* (13), 5420–5424.
(20) Wolter, O.; Heitbaum, J. Differential Electrochemical Mass Spectroscopy (DEMS) - a New Method for the Study of Electrode Processes. *Berichte der Bunsengesellschaft fur Phys. Chemie* **1984**, *88* (1), 2–6.
(21) Wonders, A. H.; Housmans, T. H. M.; Rosca, V.; Koper, M. T. M. On-Line Mass Spectrometry System for Measurements at Single-Crystal Electrodes in Hanging Meniscus Configuration. *J. Appl. Electrochem.* **2006**, *36* (11), 1215–1221.
(22) Grote, J.; Zeradjanin, A. R.; Cherevko, S.; Mayrhofer, K. J. J.; Grote, J.; Zeradjanin, A. R.; Cherevko, S.; Mayrhofer, K. J. J. Coupling of a Scanning Flow Cell with Online Electrochemical Mass Spectrometry for Screening of Reaction Selectivity. *Rev. Sci. Instrum.* **2014**, *85* (104101).
(23) Ashton, S. J. *Design, Construction and Research Application of a Differential Electrochemical Mass Spectrometer (DEMS)*; 2012; Vol. 8.
(24) Baltruschat, H. Differential Electrochemical Mass Spectrometry. *J. Am. Soc. Mass Spectrom.* **2004**, *15* (12), 1693–1706.
(25) Jusys, Z.; Massong, H.; Baltruschat, H. A New Approach for Simultaneous DEMS and EQCM: Electro-Oxidation of Adsorbed CO on Pt and Pt-Ru. *J. Electrochem. Soc.* **1999**, *146* (3), 1093–1098.
(26) Schouten, K. J. P.; Kwon, Y.; van der Ham, C. J. M.; Qin, Z.; Koper, M. T. M. A New Mechanism for the Selectivity to C1 and C2 Species in the Electrochemical Reduction of Carbon Dioxide on Copper Electrodes. *Chem. Sci.* **2011**, *2* (10), 1902–1909.
(27) Schouten, K. J. P.; Qin, Z.; Gallent, E. P.; Koper, M. T. M. Two Pathways for the Formation of Ethylene in CO Reduction on Single-Crystal Copper Electrodes. *J. Am. Chem. Soc.* **2012**, *134* (24), 9864–9867.
(28) Schouten, K. J. P.; Pe, E.; Koper, M. T. M. Structure Sensitivity of the Electrochemical

Reduction of Carbon Monoxide on Copper Single Crystals. *ACS Catal.* **2013**, *3*, 1292–1295.
(29) Schouten, K. J. P.; Pérez Gallent, E.; Koper, M. T. M. The Influence of pH on the Reduction of CO and CO2 to Hydrocarbons on Copper Electrodes. *J. Electroanal. Chem.* **2013**, *716*, 53–57.
(30) Kortlever, R.; Tan, K. H.; Kwon, Y.; Koper, M. T. M. Electrochemical Carbon Dioxide and Bicarbonate Reduction on Copper in Weakly Alkaline Media. *J. Solid State Electrochem.* **2013**, *17* (7), 1843–1849.
(31) Reske, R.; Duca, M.; Oezaslan, M.; Schouten, K. J. P.; Koper, M. T. M.; Strasser, P. Controlling Catalytic Selectivities during CO2 Electroreduction on Thin Cu Metal Overlayers. *J. Phys. Chem. Lett.* **2013**, *4* (15), 2410–2413.
(32) Kas, R.; Kortlever, R.; Milbrat, A.; Koper, M. T. M.; Mul, G.; Baltrusaitis, J. Electrochemical CO2 Reduction on Cu2O-Derived Copper Nanoparticles: Controlling the Catalytic Selectivity of Hydrocarbons. *Phys. Chem. Chem. Phys.* **2014**, *16* (24), 12194–12201.
(33) Noda, H.; Ikeda, S.; Oda, Y.; Ito, K. Potential Dependencies of the Products on Electrochemical Reduction of Carbon Dioxide at a Copper Electrode. *Chem. Lett.* **1989**, *2*, 289–292.
(34) Hori, Y.; Murata, A.; Yoshinami, Y. Adsorption of CO, Intermediately Formed in Electrochemical Reduction of CO2, at a Copper Electrode. *J. Chem. Soc. Faraday Trans.* **1991**, *87* (1), 125–128.
(35) Hori, Y.; Takahashi, R.; Yoshinami, Y.; Murata, A. Electrochemical Reduction of CO at a Copper Electrode. *J. Phys. Chem. B* **1997**, *101* (36), 7075–7081.
(36) Singh, M. R.; Clark, E. L.; Bell, A. T. Effects of Electrolyte, Catalyst, and Membrane Composition and Operating Conditions on the Performance of Solar-Driven Electrochemical Reduction of Carbon Dioxide. *Phys. Chem. Chem. Phys.* **2015**, No. Submitted.
(37) Hori, Y.; Kikuchi, K.; Murata, A.; Suzuki, S. Production of Methane and Ethylene in Electrochemical Reduction of Carbon Dioxide At Copper Electrode in Aqueous Hydrogencarbonate Solution. *Chem. Lett.* **1986**, *15* (6), 897–898.

4.6 Supplementary Information

4.6.1 Cathodic Energy Efficiency of CO_2R Using a Polycrystalline Copper Foil Cathode[1]

$$\eta = \frac{\sum FE_i(1.223 - E_{0,i})}{1.223 - E_{cathode}}$$

Where:

η	Cathodic Energy Efficiency
	Overall Cathodic Energy Efficiency includes H_2 and CO_2R products
	CO_2R Energy Efficiency includes CO_2R products only
FE_i	Faradaic Efficiency of Product i
$E_{0,i}$	Standard Reduction Potential of Product i
$E_{cathode}$	Potential Applied to Cathode

Unassigned Cathodic Current:

$$i_{\%\,unassigned} = (1 - \sum FE_i)$$

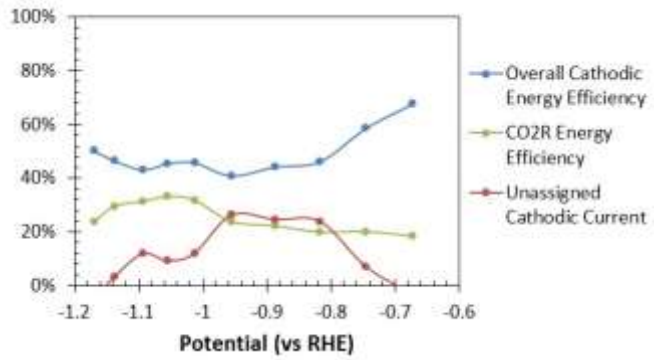

Figure S4.3 *– Cathodic energy efficiency of CO_2R as a function of the applied potential using a polycrystalline copper foil cathode in 0.1 M $KHCO_3$.*

4.6.2 Time Before CO_2 Depletion Occurs at the Surface of a Polycrystalline Copper Foil Cathode in a Stagnant Aqueous Electrolyte

Sand's equation can be used to estimate the time at which reactant depletion will occur at an electrode surface during galvanostatic electrolysis in a stagnant electrolyte. Using the data reported by Kuhl et al.[1] the time at which CO_2 depletion occurs at the cathode surface was estimated as a function of the applied current density, assuming that the reported reaction selectivities are constant despite the absence of electrolyte mixing.

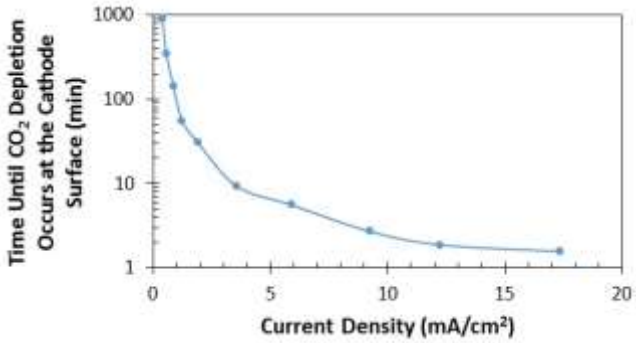

Figure S4.4 *– Time before CO_2 depletion occurs at the surface of a polycrystalline copper foil cathode as a function of the applied current density in a stagnant aqueous electrolyte.*

Sand's Equation:[2]

$$\tau = \frac{\pi D_{CO_2}}{4}\left(\frac{F C^*_{CO_2}}{\sum \frac{j_i m_i}{n_i}}\right)^2$$

Where:

τ	Time Until CO_2 Depletion at the Electrode Surface Occurs
D_{CO_2}	Diffusion Coefficient of CO_2 in H_2O = 1.92 x 10^{-5} cm^2/s @ 25 °C
F	Faraday's Constant
$C^*_{CO_2}$	Bulk Concentration of CO_2 = 33 mM @ 25 °C
j_i	Partial Current Density of Product i
m_i	mol CO_2 Consumed/mol Product i Generated
n_i	mol e^- Transferred/mol Product i Generated

4.6.3 Additional Photographs of the DEMS Cell

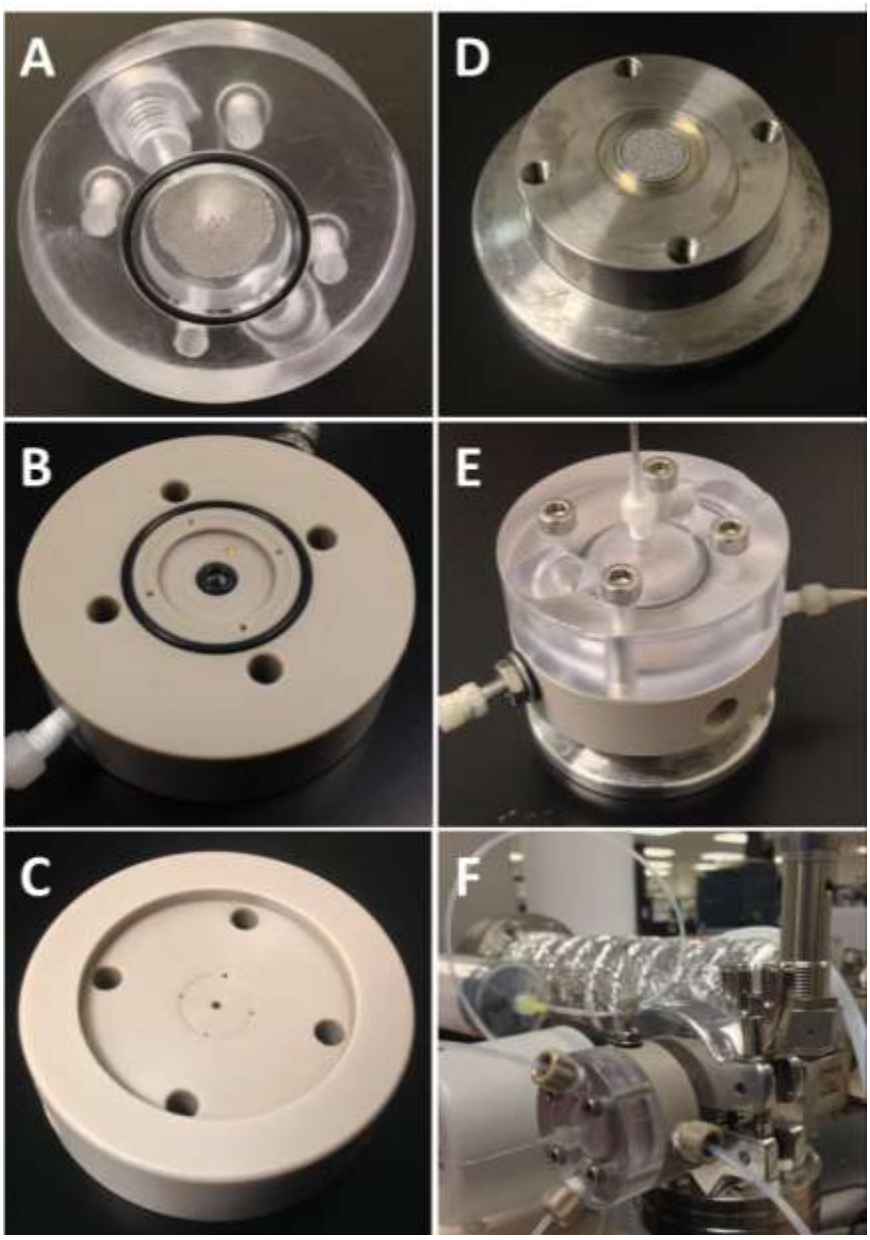

Figure S4.5 *– Additional photographs of the DEMS cell. (A) Anode chamber. (B) Cathode chamber with the working electrode removed. (C) Collection chamber. (D) Pervaporation membrane support. (E) Assembled DEMS cell. (F) DEMS cell mounted to the mass spectrometer.*

4.6.4 Table of Dimensional Specifications of the DEMS Cell

Table S4.1 *– Dimensional specifications of the DEMS cell.*

Metric	Measurement	Unit
Counter Electrode Chamber Diameter	15	mm
Counter Electrode Chamber Height	4	mm
Counter Electrode Chamber Volume	710	µL
Counter Electrode Surface Area	2	cm^2
Ion-Conducting Membrane Surface Area	1.75	cm^2
Working Electrode Chamber Diameter	15	mm
Working Electrode Chamber Height	130	µm
Working Electrode Chamber Volume	23	µL
Working Electrode Outer Diameter	12	mm
Working Electrode Inner Diameter	4	mm
Working Electrode Surface Area	1	cm^2
Working to Reference Electrode Spacing	5.5	mm
Transfer Capillary Diameter	0.5	mm
Transfer Capillary Length	1	mm
Total Transfer Capillary Volume	8	µL
Pervaporation Membrane Chamber Diameter	8	mm
Pervaporation Membrane Chamber Height	110	µm
Pervaporation Membrane Chamber Volume	5.5	µL
Pervaporation Membrane Surface Area	0.5	cm^2
Total Catholyte Volume	36.5	µL

4.6.5 UV-Generated Ozone Treatment of the DEMS Cell

The DEMS cell was exposed to UV-generated ozone until the contact angle of water on the surface of the cell body was measured to be less than 30°. As shown in Figure S4.5, a treatment time of ~20 min was required. Improving the wetting properties of the DEMS cell body was found to reduce the holdup of gaseous product bubbles inside the working electrode chamber.

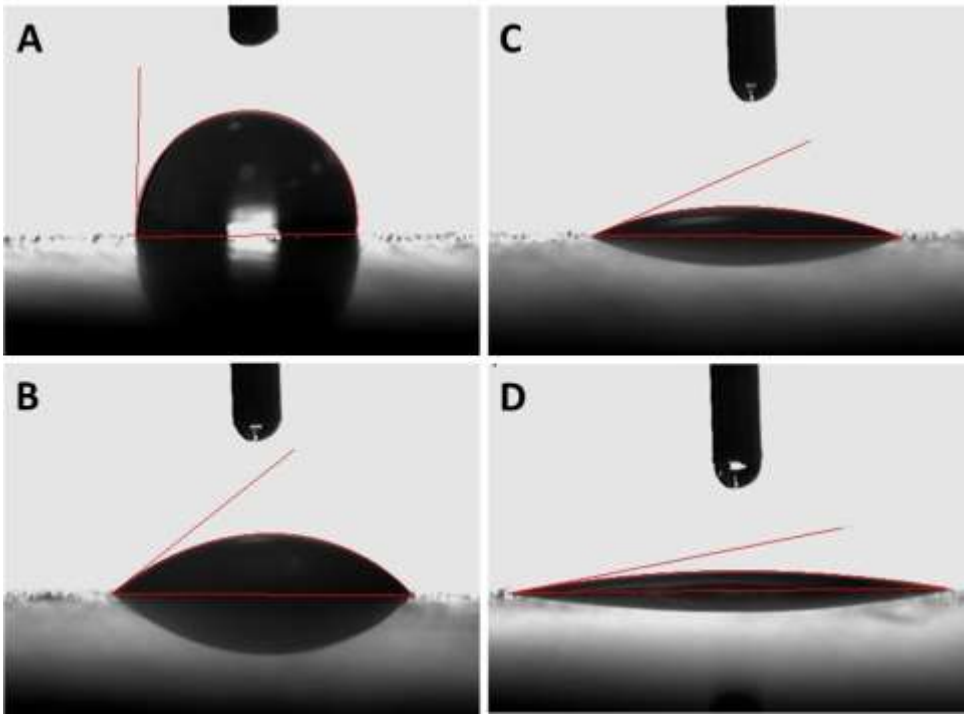

Figure S4.4 *– Wetting angle measurements on the surface of the DEMS cell after UV-generated ozone treatment for: (A) 0 min, (B) 10 min, (C) 20 min, and (D) 30 min.*

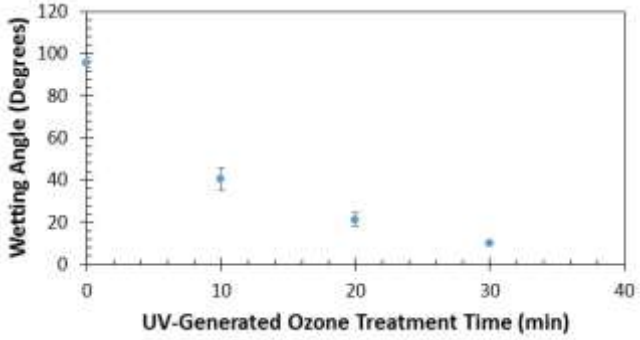

Figure S4.5 *– Wetting angle measurements on the DEMS cell body as a function of the UV-generated ozone treatment time.*

4.6.6 Chemical Composition of Potassium Bicarbonate and Potassium Carbonate Electrolytes in Equilibrium with 1 Atmosphere of CO_2 at Ambient Conditions

Electroneutrality:

$$\sum_i z_i[i] = 0$$

Where:

z_i	Charge of Species i
[i]	Concentration of Species i

$CO_{2\,(aq)} + H_2O \leftrightarrow H^+ + HCO_3^-$	$pK_a = 6.37$ Note: H_2O in Excess
$HCO_3^- \leftrightarrow H^+ + CO_3^{2-}$	$pK_a = 10.25$
$2H_2O \leftrightarrow OH^- + H_3O^+$	$pK_w = 14$

Table S4.2 *– Chemical composition of 0.1 M $KHCO_3$ and 0.05 M K_2CO_3 electrolytes in equilibrium with 1 atm of CO_2 at ambient conditions.*

Electrolyte	Potassium Bicarbonate ($KHCO_3$)	Potassium Carbonate (K_2CO_3)
Concentration (M)	0.1	0.05
$[K^+]$	0.1	0.1
$[CO_2]$	0.033	0.033
$[HCO_3^-]$	$9.99 * 10^{-2}$	$9.99 * 10^{-2}$
$[CO_3^{2-}]$	$3.18 * 10^{-5}$	$3.18 * 10^{-5}$
$[H^+]$	$1.47 * 10^{-7}$	$1.47 * 10^{-7}$
$[OH^-]$	$6.82 * 10^{-8}$	$6.82 * 10^{-8}$
pH	6.83	6.83

Note: The solubility of CO_2 in the electrolyte was assumed to be equivalent to that of water at 25 °C (33 mM). While the presence of salt in water is known to reduce the solubility of CO_2, neglecting this will not change the conclusions of the calculation since both solutions have identical salinity.

4.6.7 Determination of the Total Uncompensated Resistance of the DEMS Cell

Potentiostatic electrochemical impedance spectroscopy (PEIS) was conducted in order to determine the total uncompensated resistance (R_u) of the DEMS cell while a 0.05 M K_2CO_3 solution saturated with CO_2 was pumped through the cell at 1 mL/min. Potential waveforms with a sinus amplitude of 20 mV and frequencies of 10 Hz to 30 kHz were applied to the cell at the open circuit potential, with 10 different frequencies tested per decade. The average of 10 measurements at each frequency were used to construct the representative Nyquist plot shown in Figure S4.6.

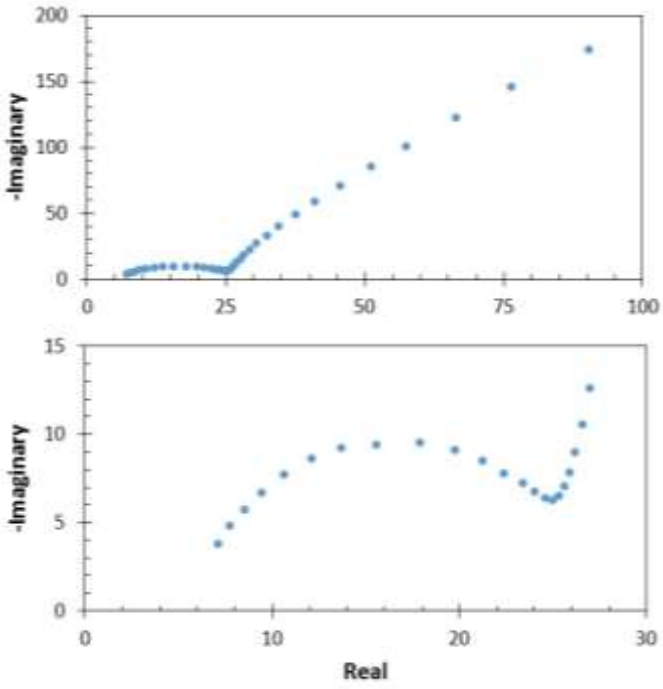

Figure S4.6 *– Nyquist impedance plot of the DEMS cell obtained at an electrolyte flow rate of 1 mL/min at the open circuit potential.*

The Nyquist plot obtained at the open circuit potential includes contributions from R_u as well as the working electrode-electrolyte interface. To determine which features of the Nyquist plot result from the working electrode-electrolyte interface the procedure above was repeated at a series of increasingly negative applied potentials. Since the charge transfer resistance at the working electrode-electrolyte interface decreases exponentially with the applied potential, the features of the Nyquist plot corresponding to R_u become clear, as shown in Figure S4.7.

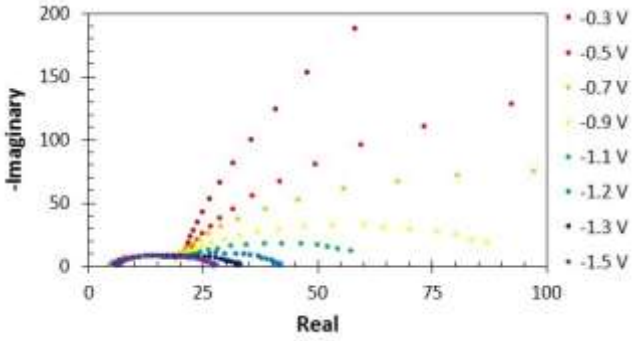

Figure S4.7 *– Nyquist impedance plots of the DEMS cell obtained at an electrolyte flow rate of 1 mL/min at a series of increasingly negative applied potentials.*

To accurately determine the value of R_u the Nyquist plot obtained at the open circuit potential was then fitted to an RRQRQ equivalent circuit using the EC-Lab software. The RRQRQ equivalent circuit is depicted in Figure S4.8, with the portions of the circuit attributed to the total uncompensated impedance (Z_u) and working electrode-electrolyte interface (Z_{WE}) labeled. Note that $R_u = R_1 + R_2$.

Q_2 was determined to be an artifact of the measurement parameters, which were narrowly confined due to the unconventional geometry of the DEMS cell reported in this study. At the open circuit potential the rising edge of the second arc of the Nyquist plot has a slope of ~60°, which does not agree with the 45° slope resulting from diffusional impedance (Warburg impedance). Furthermore, Figure S4.7 clearly demonstrates that the second arc corresponds to the electrode-electrolyte interface and that the sum of R_1 and R_2 is equivalent to R_u.

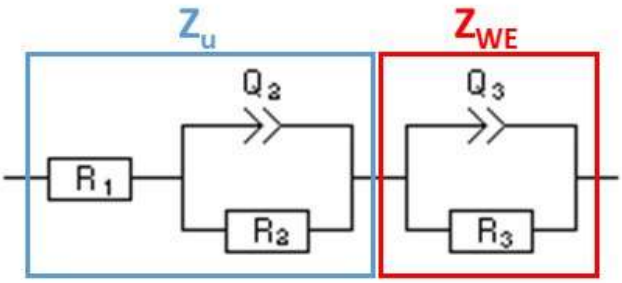

Figure S4.8 *– Circuit diagram of an RRQRQ equivalent circuit.*

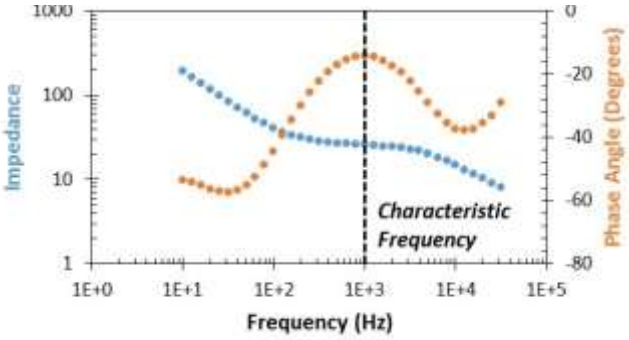

Figure S4.9 *– Bode impedance plot of the DEMS cell obtained using an electrolyte flow rate of 1 mL/min at the open circuit potential.*

To determine the characteristic frequency of the total uncompensated resistance a Bode impedance plot was constructed using the impedance data recorded at the open circuit potential. By this means, the characteristic frequency of Z_u was determined to be 1 kHz, as shown in Figure S4.9. To determine if R_u substantially increases as a result of bubble formation at the working electrode surface R_u was measured at a series of increasingly negative current densities using the current interrupt technique. To this end chronopotentiometry was conducted for 2 mins at each current density followed by 10 consecutive 50 ms current interruptions. The current interruptions allowed the voltage drop due to R_u to be measured since it instantaneously drops upon the interruption of current flow, whereas the voltage drop due to the working electrode-electrolyte interface decays with a time constant characteristic of the capacitance of electrochemical double layer. This procedure was repeated 3 times at each current density. By this means R_u was determined to be independent of the applied current density, as shown in Figure S4.10. Furthermore, the agreement between the fitted PEIS data and the current-interrupt technique reinforces that the sum of R_1 and R_2, as shown in Figure S4.8, is the true value of R_u.

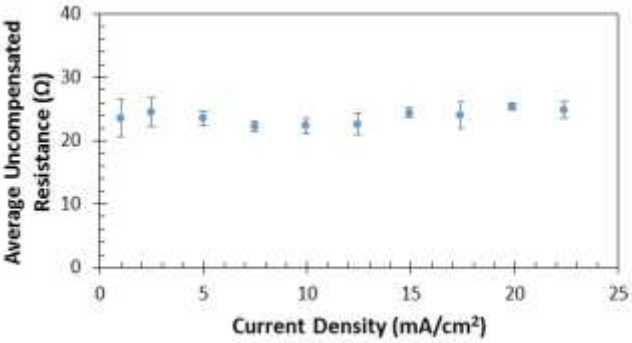

Figure S4.10 *– Average uncompensated resistance of the DEMS cell as a function of the applied current density measured using the current interrupt technique and an electrolyte flow rate of 1 mL/min.*

The negligible change in R_u with increasing current density is due to the location of the reference electrode, which intercepts the catholyte stream prior to the working electrode chamber inlet. As a result, the catholyte is constantly sweeping bubbles away from the portion of the working electrode where the potential referencing takes place. Thus, the solution resistance between the working and reference electrodes negligibly increases with the evolution of gaseous products. This is depicted in Figure S4.11.

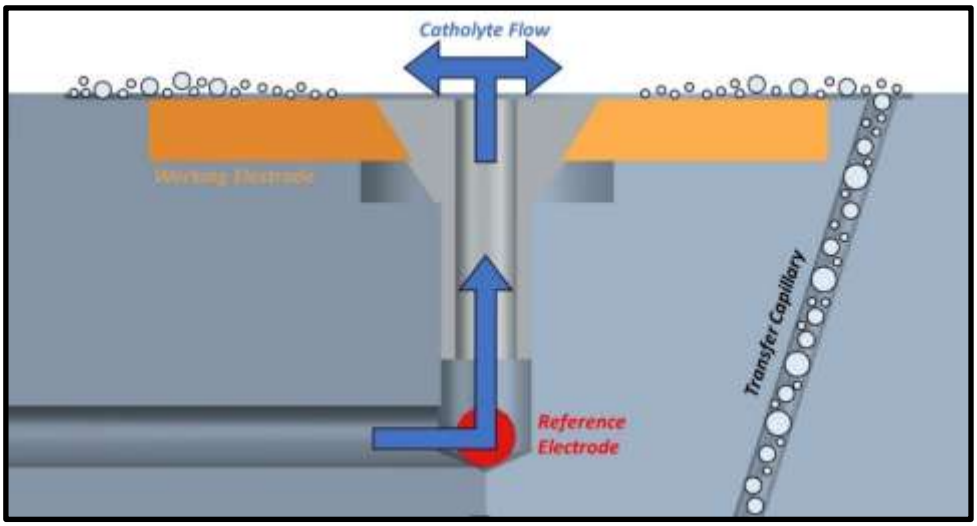

Figure S4.11 *– Depiction of gaseous product bubble clearing from the portion of the working electrode where potential referencing occurs as a result of electrolyte convection.*

4.6.8 Scan Rate Optimization

Linear sweep voltammetry was conducted at scan rates of 1, 0.5, and 0.2 mV/s using an electrolyte flow rate of 1 mL/min while the mass ion currents for *m/z* = 2, 15, 26, and 31 were recorded. The data was averaged over 10 mV increments and the trends of the mass ion currents vs potential were compared to determine the optimal scan rate. As can be seen in Figures S4.12 and S4.13, slower scan rates resulted in clearer mass ion current trends because more time was spent within each 10 mV increment, reducing the influence of bubble noise on the observed trends.

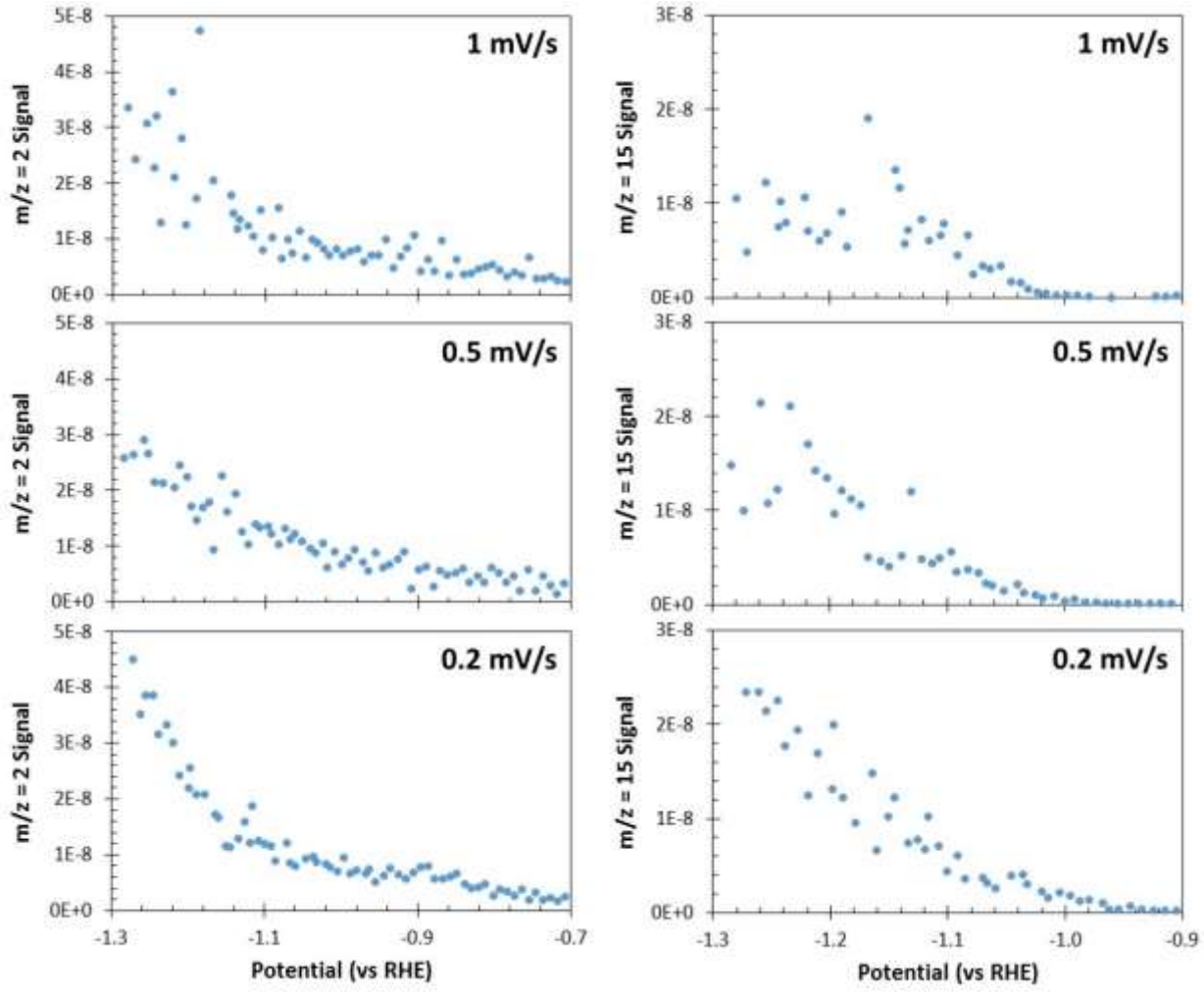

Figure S4.12 *– Ion currents for m/z = 2 and 15 recorded during linear sweep voltammetry in a CO_2 saturated 0.05 M K_2CO_3 electrolyte (pH = 6.8) flowing at 1 mL/min using scan rates of 1, 0.5, and 0.2 mV/s.*

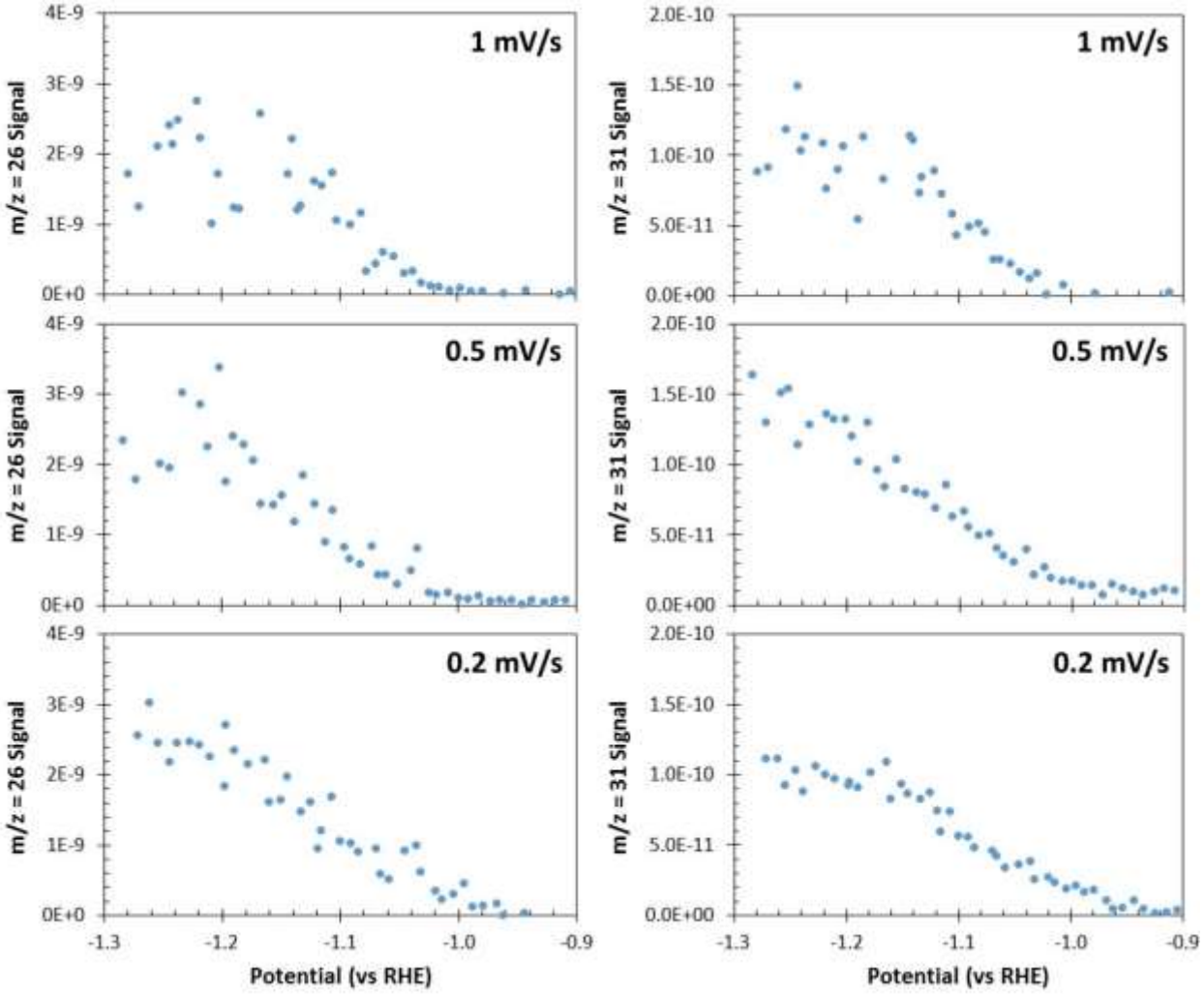

Figure S4.13 *– Ion currents for m/z = 26 and 31 recorded during linear sweep voltammetry in a CO_2 saturated 0.05 M K_2CO_3 electrolyte (pH = 6.8) flowing at 1 mL/min using scan rates of 1, 0.5, and 0.2 mV/s.*

4.6.9 Mass Spectrometry Optimization

In order to maximize the detectability of the liquid-phase products the emission current and scanning electron multiplier (SEM) voltage were adjusted to maximize the signal to noise ratio observed for a 30 μM ethanol standard. To this end, the ethanol standard was pumped through the DEMS cell at 1 mL/min for 10 mins while the *m/z* = 31 mass ion current signal was monitored. 18.2 MΩ deionized water from a Millipore system was pumped through the cell for 5 mins before and after the ethanol standard so that the background signal could be accurately subtracted. This process was repeated varying the emission current from 50 to 1,500 μA, as shown in Figure S4.14A. An emission current of 500 μA was selected because it resulted in a high signal to noise ratio but did not overload the SEM detector during the *in-situ* detection of H_2. The process was then repeated varying the SEM voltage from 750 to 1,500 V at an emission current of 500 μA, as shown in Figure S4.14B. The SEM voltage was found to negligibly affect the signal to noise ratio at voltages below 1,300 V. The sudden drop in the signal to noise ratio at SEM voltages >1,400 V is the result of the m/z = 31 mass ion current magnitude high enough to necessitate the use of the high gain amplifier, which substantially increases the noise of the baseline signal.

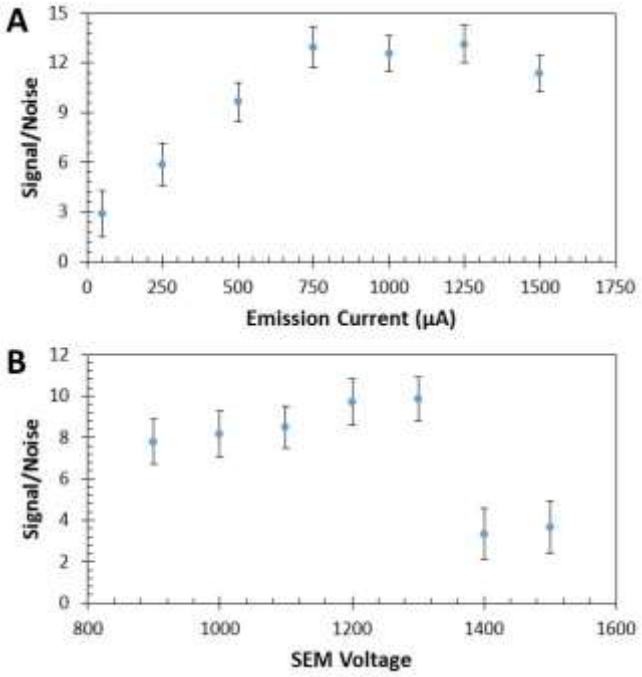

Figure S4.14 *– m/z = 31 signal to noise ratio recorded for a 30 μM ethanol standard as a function of (A) emission current and (B) scanning electron multiplier (SEM) voltage.*

4.6.10 Details of the COMSOL Model

4.6.10.1 Velocity Field Across the Working Electrode Chamber

The 2D flow field along the plane of the working electrode was simulated using COMSOL Multiphysics v4.3b. The plane of working electrode has four lines of reflection symmetry passing through the centers of the four outlet ports, which are offset by 45˚. Figure S4.16 shows a schematic of the plane of the working electrode chamber, which consists of eight symmetric segments.

Incompressible flow is assumed to occur through the DEMS cell. The velocity field is obtained by solving the equations of continuity and motion within a segment of symmetry. According to the equation of continuity the divergence of velocity is zero:

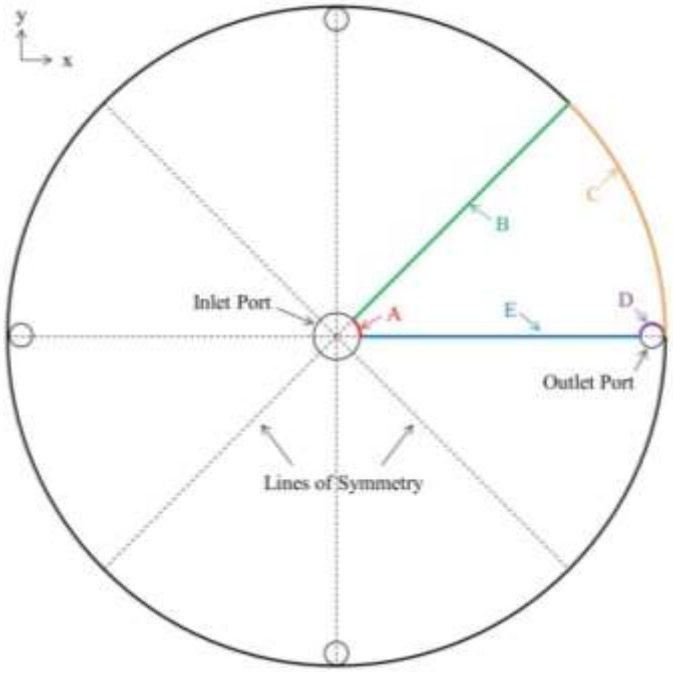

Figure S4.15 *– Plane of the working electrode chamber with eight symmetric segments. Each segment has five boundaries labeled A-E.*

$$\frac{\partial v_x}{\partial x} + \frac{\partial v_y}{\partial y} = 0$$

Where:

v_x	Component of Velocity Vector in the x Direction
v_y	Component of Velocity Vector in the y Direction

The equation of motion is given by:

$$\rho\left(\frac{\partial v_x}{\partial t} + v_x\frac{\partial v_x}{\partial x} + v_y\frac{\partial v_x}{\partial y}\right) = -\frac{\partial p}{\partial x} + \mu\left(\frac{\partial^2 v_x}{\partial x^2} + \frac{\partial^2 v_x}{\partial y^2}\right)$$
$$\rho\left(\frac{\partial v_y}{\partial t} + v_x\frac{\partial v_y}{\partial x} + v_y\frac{\partial v_y}{\partial y}\right) = -\frac{\partial p}{\partial y} + \mu\left(\frac{\partial^2 v_y}{\partial x^2} + \frac{\partial^2 v_y}{\partial y^2}\right)$$

Where:

ρ	Density of the Electrolyte = 1004.6 kg/m^3
μ	Viscosity of the Electrolyte = 1.015 mPa*s

p Pressure

The boundary conditions are as follows:

Boundary A: Inflow of Electrolyte

Positive Pressure Convection:

$$\boldsymbol{v} = -V_{in}\boldsymbol{n}$$

Negative Pressure Convection:

$$p = p_{in}\ and\ \mu(\nabla \boldsymbol{v} + \nabla \boldsymbol{v}^T)\boldsymbol{n} = 0$$

Where:

v	Velocity Vector
n	Normal Vector Pointing Outward form the Boundary
V_{in}	Inlet Velocity
p_{in}	Inlet Pressure = 1 atm

Boundaries B & E: Flow Symmetry

$$\boldsymbol{n}^T\boldsymbol{v} = 0$$

Boundary C: No Slip Condition

$$\boldsymbol{v} = 0$$

Boundary D: Outflow of Electrolyte

Positive Pressure Convection:

$$p = p_{out}\ and\ \mu(\nabla \boldsymbol{v} + \nabla \boldsymbol{v}^T)\boldsymbol{n} = 0$$

Negative Pressure Convection:

$$\boldsymbol{v} = V_{out}\boldsymbol{n}$$

Where:

P_{out}	Outlet Pressure = 1 atm
V_{out}	Outlet Velocity

The initial conditions are:

$$p = 1\ atm\ and\ \boldsymbol{v} = 0$$

4.6.10.2 Residence Time Distribution in the Working Electrode Chamber

The residence time distribution of the catholyte in the working electrode chamber was determined using a step-tracer experiment in COMSOL Multiphysics v4.3b. The equation of continuity for the tracer is given by:

$$\frac{\partial c}{\partial t} + v_x \frac{\partial c}{\partial x} + v_y \frac{\partial c}{\partial y} = D\left(\frac{\partial^2 c}{\partial x^2} + \frac{\partial^2 c}{\partial y^2}\right)$$

Where:

c	Concentration of the Tracer
D	Diffusion Coefficient of the Tracer = 10^{-9} m^2/s

The boundary conditions are as follows:

Boundary A: Inflow of Tracer

$$c = c_0 = 1\ mol/L$$

Boundaries B, C, and E: No Flux Condition

$$-\boldsymbol{n}^T \boldsymbol{N} = 0$$

Where:

N	Flux of Tracer = -D∇c + **v**c

Boundary D: Outflow of Tracer

$$-\boldsymbol{n}^T D \nabla c = 0$$

The initial condition is:

$$c = 0$$

The equations above are solved to calculate the concentration of the tracer at the outlet. The cumulative residence time can be calculated using:

$$F(t) = \frac{\bar{c}(t)}{c_0}$$

Where:

$\bar{c}$	Average Concentration of the Tracer at Boundary D

The average residence time $(\bar{t})$ and the standard deviation (σ) can be obtained as follows:

$$\bar{t} = \int_0^\infty [1 - F(t)]dt$$

$$\sigma^2 = 2\int_0^\infty t[1 - F(t)]dt - \bar{t}^2$$

4.6.11 Volumetric Generation Rate of Gaseous Products Using a Polycrystalline Copper Foil Cathode (Assuming No Dilution)[1]

$$V = \frac{A}{F}\sum \frac{j_i MW_i}{n_i \rho_i}$$

Where:

V	Total Volumetric Generation Rate of Gaseous Products
A	Electrode Surface Area
F	Faraday's Constant
j_i	Partial Current Density of Gaseous Product i
MW_i	Molecular Weight of Gaseous Product i
n_i	mol e^- Transferred/mol Gaseous Product i Generated
ρ_i	Density of Gaseous Product i @ 25 °C (g/L)

H_2	0.08235
CO	1.145
CH_4	0.6569
C_2H_4	1.153

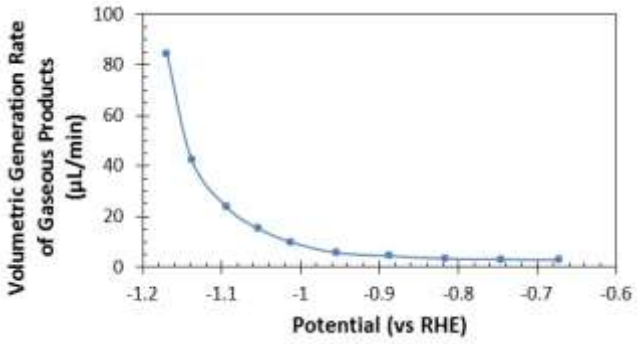

Figure S4.16 *– Volumetric generation rate of gaseous products produced as a function of the applied potential using a polycrystalline copper foil cathode assuming no dilution occurs.*

4.6.12 Relative Concentration of CO_2 to CO Entering the Collection Chamber Using a Polycrystalline Copper Foil Cathode[1]

$$[CO_2]/[CO] = \frac{QC^*_{CO_2} - \frac{A}{F}\sum\frac{j_i m_i}{n_i}}{\frac{A}{F}\sum\frac{j_{CO}}{n_{CO}}}$$

Where:

$[CO_2]/[CO]$	Relative Concentration of CO_2 to CO in the Catholyte
Q	Electrolyte Flow Rate = 1 mL/min
$C^*_{CO_2}$	Bulk Concentration of CO_2 = 33 mM @ 25 °C
A	Electrode Surface Area
F	Faraday's Constant
j_i	Partial Current Density of Product i
m_i	mol CO_2 Consumed/mol Product i Generated
n_i	mol e^- Transferred/mol Product i Generated

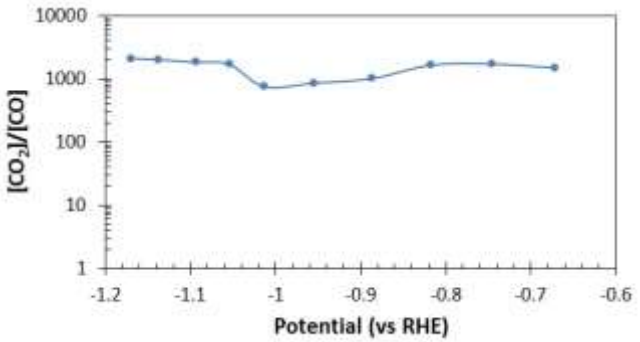

Figure S4.17 *– Relative concentration of CO_2 to CO in the catholyte entering the collection chamber as a function of the applied potential using a polycrystalline copper foil cathode and an electrolyte flow rate of 1 mL/min.*

4.6.13 Ethanol and 1-Propanol Calibration

A series of increasingly concentrated ethanol standards were pumped through the DEMS cell at 1 mL/min for 10 mins each while the mass ion current signals corresponding to the primary ionization fragments of ethanol were monitored (*m/z* = 31 and 46). 18.2 MΩ deionized water from a Millipore system was pumped through the cell for 5 mins before and after each ethanol standard so that the background signal could be accurately subtracted. The average signals recorded for each standard are plotted as a function of the ethanol concentration in Figure S4.19. The limit of detection was defined as the concentration of ethanol that produced a mass ion current signal equivalent to the standard deviation of the baseline signal, which was determined to be 5.5 x 10^{-12} for *m/z* = 31 over a 10 min period. Thus, the detection limit of ethanol was determined to be ~5 μM using *m/z* = 31, which corresponds to a partial current density of 0.13 mA/cm^2 at an electrolyte flow rate of 1 mL/min. Figure S4.20 depicts the results of the 1-propanol calibration conducted using an identical methodology, except that the signal response for *m/z* = 59 was monitored instead of *m/z* = 46. The 1-propanol detection limit was also determined to be ~5 μM. Since most liquid phase CO_2R products are as volatile as these alcohols the assumption was made that this detection limit would apply to all liquid phase products.

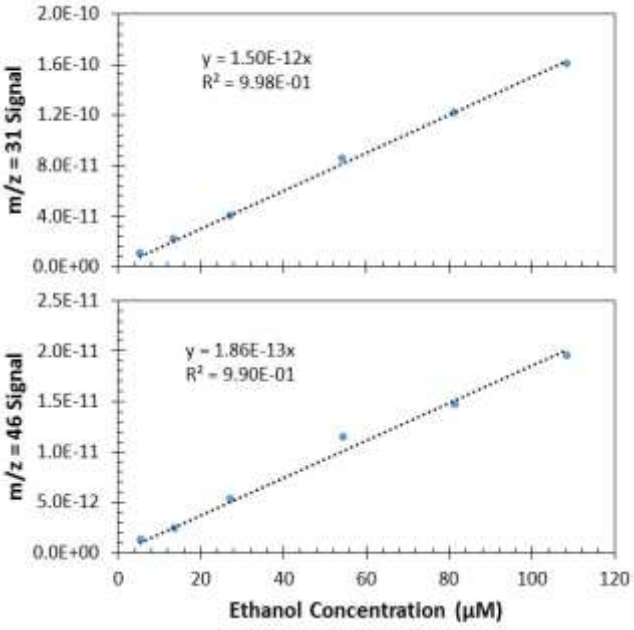

Figure S4.18 *– Ethanol calibration curves for m/z = 31 and 46 obtained at a flow rate of 1 mL/min.*

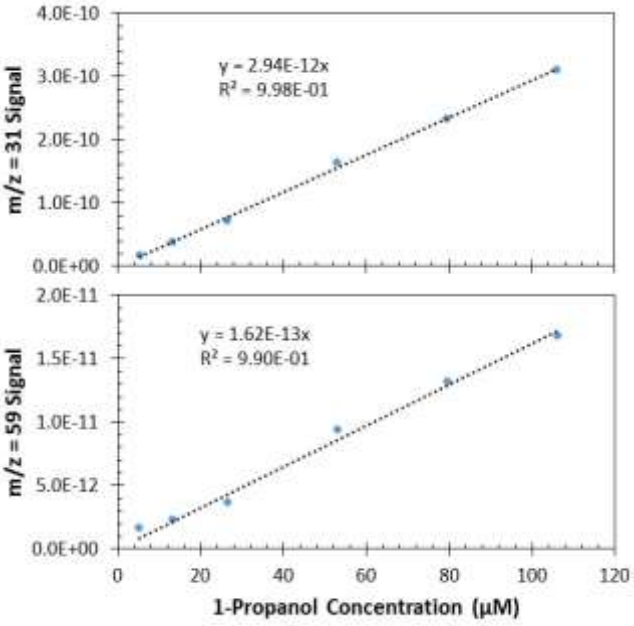

Figure S4.19 *– 1-propanol calibration curves for m/z = 31 and 59 obtained at a flow rate of 1 mL/min.*

4.6.14 Generation Rates of the Liquid Phase CO_2R Products Using a Polycrystalline Copper Foil Cathode[1]

$$\dot{n}_i = \frac{Aj_i}{Fn_i}$$

Where:

$\dot{n}_i$	Molar Generation Rate of Product i
A	Electrode Surface Area
j_i	Partial Current Density of Product i
F	Faraday's Constant
n_i	mol e^- Transferred/mol Product i Generated

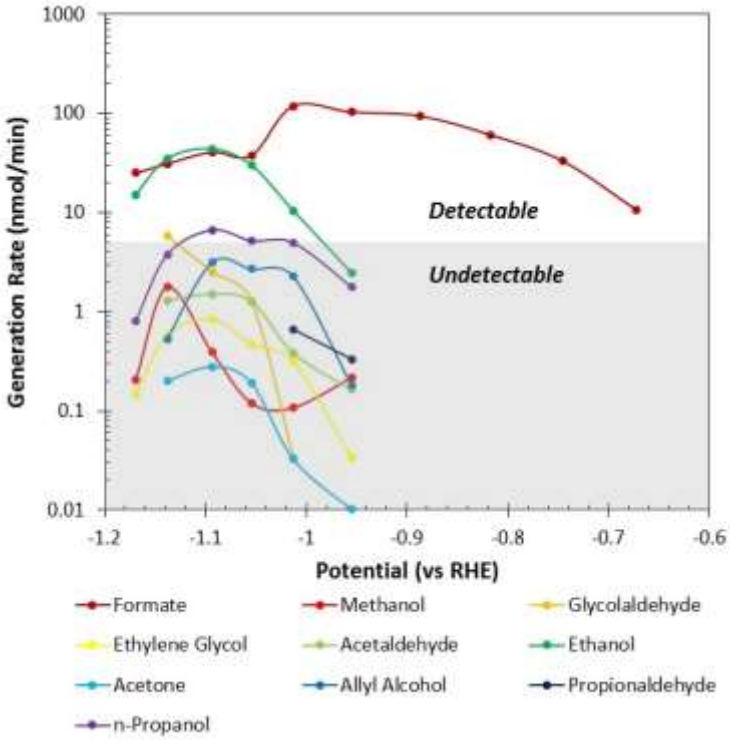

Figure S4.20 *– Molar generation rates of the liquid phase CO_2R products as a function of the applied potential using a polycrystalline copper foil cathode. The shaded region indicates generation rates that are insufficient to reach the detection limit of 5 μM at an electrolyte flow rate of 1 mL/min.*

4.6.15 Experimental Verification of the Undetectability of Formic Acid

$$[HCOO^-] = \frac{\dot{n_{HCOO^-}}}{Q}$$

Where:

$[HCOO^-]$	Concentration of Formate in the Catholyte
$\dot{n}_{HCOO^-}$	Molar Generation Rate of Formate
Q	Electrolyte Flow Rate = 1 mL/min

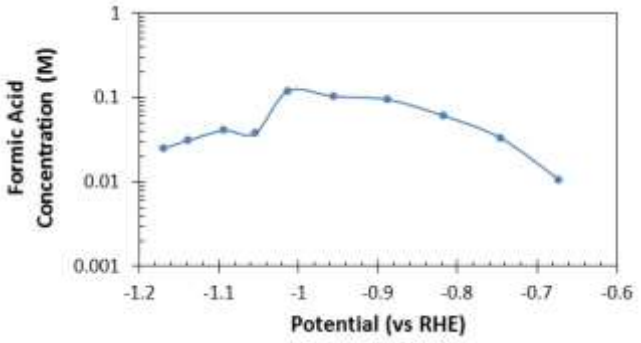

Figure S4.21 *– Expected formate concentration in the catholyte entering the collection chamber as a function of the applied potential using a polycrystalline copper foil cathode and an electrolyte flow rate of 1 mL/min.*

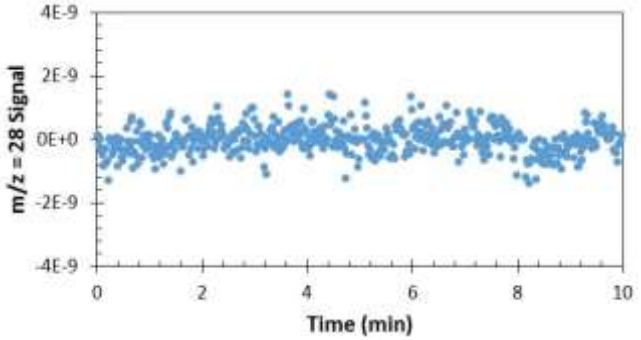

Figure S4.22 *– m/z = 28 signal response to a 0.05 M K_2CO_3 electrolyte saturated with CO_2 (pH = 6.8). After 5 min an identical solution containing 10 mM of formic acid was introduced. The lack of a recorded signal indicates that formic acid is undetectable.*

A 0.05 M K_2CO_3 solution saturated with CO_2 (pH = 6.8) was pumped through the DEMS cell at 1 mL/min while the mass ion currents of the four primary ionization fragments produced by formic acid were monitored (*m/z* = 28, 29, 45, and 46). After 5 mins had elapsed the solution was replaced with an identical solution containing formic acid at a concentration of 10 mM. The lack of a detector response is due to the low pKa of formic acid (3.77), which results in it being deprotonated at the conditions of the reaction and thus unable to pervaporate into the vacuum chamber and be detected.

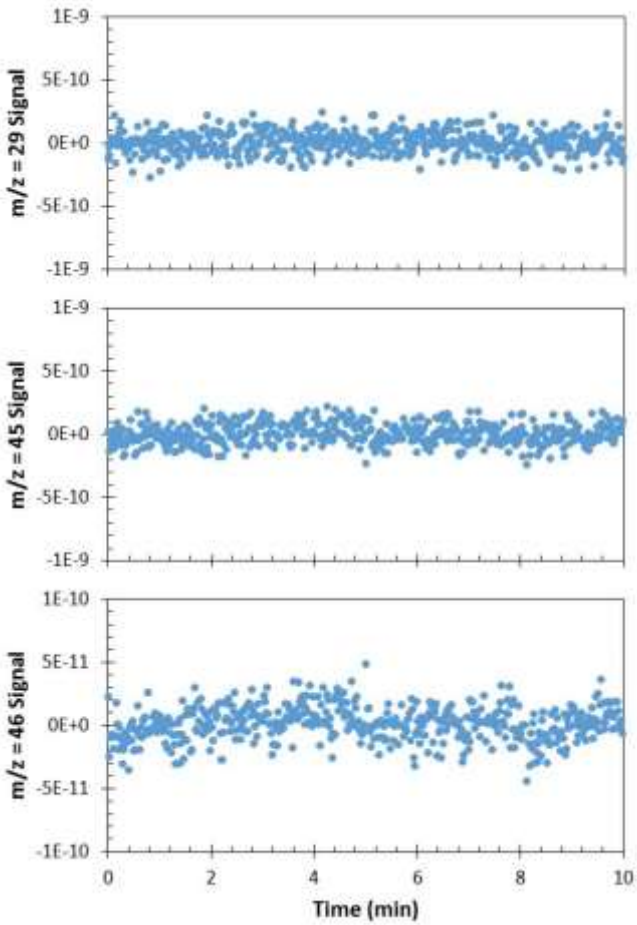

Figure S4.23 *– m/z = 29, 45, and 46 signal response to a 0.05 M K_2CO_3 electrolyte saturated with CO_2 (pH = 6.8). After 5 min an identical solution containing 10 mM of formic acid was introduced. The lack of a recorded signal indicates that formic acid is undetectable.*

4.6.16 Determination of the CO_2R Products that Significantly Contribute to the *m/z* = 31 Signal[1]

The mass spectra of the CO_2R products that produce the *m/z* = 31 fragment upon ionization are shown in Table S4.3.

Table S4.3 *– Mass spectra of the CO_2R products that produce the m/z = 31 fragment.*

m/z	Methanol	Glycolaldehyde	Ethylene Glycol	Ethanol	Allyl Alcohol	Propionaldehyde	1-Propanol
12	13						
13	25					11	
14	51					36	
15	274		179	66	27	76	13
17	15						
18	14				42		
19			30				10
26				98	99	31	21
27			58	224	269	205	102
28	50	80			142	65	54
29	512	280	174	298	477	991	101
30	70		28	81	193	999	15
31	999	610	1000	1000	417	83	999
32	737	100				42	22
33	16		286			10	11
37					31	28	
38					47	20	
39					266	52	32
40					88	14	
41					68	38	73
42		40	23	47		27	133
43		810	67	114	44	11	43
44		1000	25				
45		30		514			13
46		10		216			
53						16	
55					51	27	13
56					12		
57					999	223	29
58		20			201	787	
59		20			12	48	121
60							43

Since *m/z* = 31 is the primary ionization fragment of several liquid-phase CO_2R products it will be necessary to deconvolute the contributions that these products make to the overall m/z = 31 signal. The contribution percentage of these products to the overall m/z = 31 signal can be estimated using:[1]

$$Contribution\ to\ {}^{m}/_{z} = 31\ Signal = \frac{\dot{n}_i \frac{Im_{/z=31,i}}{\sum_j Im_{/z=j,i}}}{\sum_i \dot{n}_i \frac{Im_{/z=31,i}}{\sum_j Im_{/z=j,i}}}$$

Where:

$\dot{n}_i$ Generation Rate of Product i (nmol/min)

$Im_{/z=j,i}$ Relative Intensity of m/z = j for Product i

As shown in Figure S4.25, only ethanol and 1-propanol are expected to significantly contribute to the recorded *m/z* = 31 signal, enabling the contributions by the other CO_2R products to be neglected.

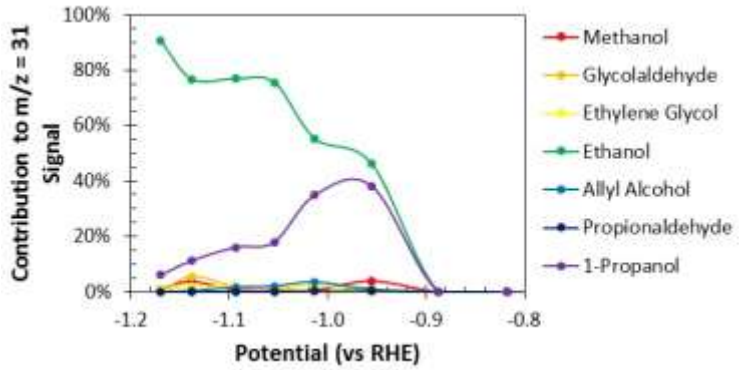

Figure S4.24 *– Estimated contributions of different CO_2R products to the overall m/z = 31 signal as a function of the applied potential using a polycrystalline copper foil cathode.*

4.6.17 Inability to Deconvolute the *m/z* = 31 Using Mass Spectrometry

Since ethanol and 1-propanol both contribute significantly to the *m/z* = 31 signal the fraction of the signal corresponding to each product must be determined so that accurate quantification can be conducted. To this end, a secondary ionization fragment that is selectively produced by either ethanol or 1-propanol in a sufficient abundance to be detected needs to be identified. The relative abundance of the ionization fragments produced by ethanol and 1-propanol are shown in Table S4.4. Fragments with a relative abundance >5% are promising secondary fragments for deconvoluting the *m/z* = 31 signal. The mass ion currents which meet this requirement are *m/z* = 27, 29, 42, 45, 46, and 59.

Table S4.4 *– Relative abundance of ionization fragments produced by ethanol and 1-propanol.*

m/z	Ethanol	1-Propanol
15	2.48%	0.70%
19		0.54%
26	3.69%	1.14%
27	8.43%	5.52%
28		2.92%
29	11.21%	5.47%
30	3.05%	0.81%
31	37.62%	54.06%
32		1.19%
33		0.60%
39		1.73%
41		3.95%
42	1.77%	7.20%
43	4.29%	2.33%
45	19.34%	0.70%
46	8.13%	
55		0.70%
57		1.57%
59		6.55%
60		2.33%

A mass ion current must have a background signal below 10^{-10} torr in order to have a high enough signal to noise ratio to be used to detect ethanol or 1-propanol at the concentrations expected to be formed using a polycrystalline copper foil cathode at an electrolyte flow rate of 1 mL/min. If this requirement is not met then the magnitude of the liquid phase product signal will be less than the magnitude of the standard deviation of the baseline signal, which will be erratic due to the necessity of using the high gain amplifier when recording mass ion current signals exceeding 10^{-10} torr. In order to identify which *m/z* ratios satisfy this requirement a profile scan was conducted at the open circuit potential while a 0.05 M K_2CO_3 electrolyte saturated with CO_2 was pumped through the DEMS cell at 1 mL/min. The results, shown in Figure S4.25, indicate that *m/z* = 29 and 45 have baseline signals which necessitate the use of the high gain amplifier, making them unsuitable for detecting the secondary ionization fragments of the liquid-phase reaction products.

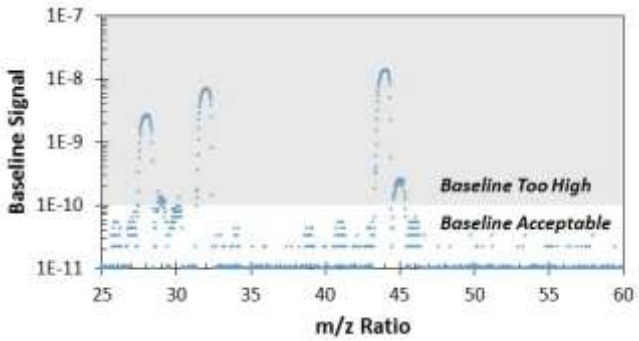

Figure S4.25 *– m/z baseline signals recorded using a CO_2-sparged 0.05 M K_2CO_3 electrolyte (pH = 6.8) at a flow rate of 1 mL/min. The shaded region indicates baseline signals that require the use of the high gain amplifier, which makes them unsuitable for detecting the secondary ionization fragments produced by the liquid-phase reaction products.*

Equation (26) was used to determine if any observed mass ion current signals corresponding to *m/z* = 27, 42, 46, and 59 could be attributed

solely to either ethanol or 1-propanol. The results indicate that only signals recorded for *m/z* = 46 and 59 can be can be attributed to the presence of either ethanol or 1-propanol, as shown in Figure S4.26.

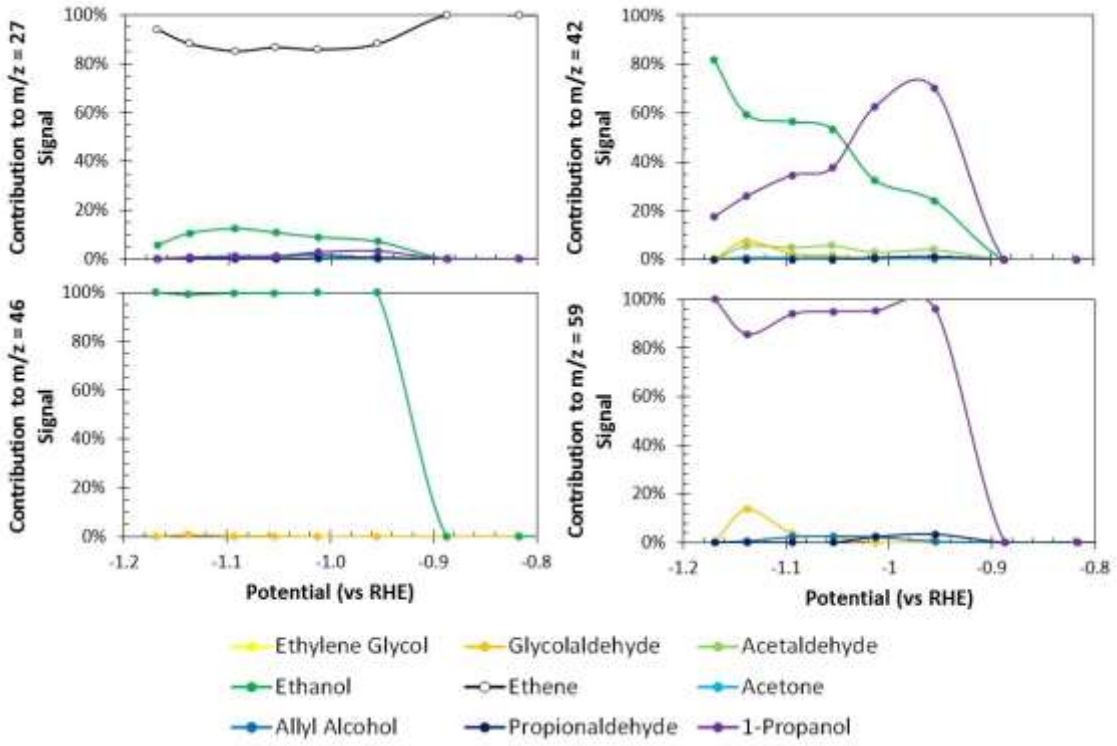

Figure S4.26 *– Estimated contributions of different CO_2R products to the overall m/z = 27, 42, 46, and 59 signals as a function of the applied potential using a polycrystalline copper foil cathode.*

However, CO_2 also produces a secondary ionization fragment with an *m/z* ratio of 46, resulting in an erratic *m/z* = 46 baseline signal that dramatically increases the ethanol concentration required to meet the conditions of detection. In fact, an ethanol concentration an order of magnitude higher than expected to be experimentally observed using polycrystalline copper and an electrolyte flow rate of 1 mL/min would be required to observe an *m/z* = 46 mass ion current signal greater than the standard deviation of the baseline noise due to the overlap with CO_2. Furthermore, the detection limit of *m/z* = 59 was determined to be roughly equivalent to the maximum expected concentration of 1-propanol produced using polycrystalline copper and an electrolyte flow rate of 1 mL/min. As a result, no signal was experimentally observed while monitoring the *m/z* = 59 mass ion current. Thus, deconvoluting the ethanol and 1-propanol contributions to the observed *m/z* = 31 signal using a secondary ionization fragment selectively produced by either alcohol is not possible when conducting CO_2R using $C^{13}O_2$.

4.6.18 Deconvoluting the *m/z* = 31 Signal Using Constant Potential Electrolysis and Liquid Chromatography

4.6.18.1 Cell Design and Construction

A custom air-tight electrochemical cell was machined out of a polycarbonate block (McMaster-Carr) and fitted with Viton O-rings (McMaster-Carr). The design of the cell was such that the working and counter electrodes were parallel and separated by an ion-conducting membrane. The geometric surface area of each electrode was 1.13 cm^2. The electrolyte volume of each electrode chamber was 1.3 mL. The electrode surface area to electrolyte volume ratio of this cell is higher than any previously reported in the literature by a factor of 2, which ensures good liquid-phase product detectability.

The working electrode was a copper sheet (0.1 mm thick 99.9999% Alfa Aesar) that was cut in 2 cm x 2 cm coupons. The working electrode coupons were initially cleaned by sonicating in acetone, followed by isopropanol, and finally deionized water for 30 min each. They were then electropolished at a potential of +2 V vs a Cu foil counter electrode for 5 min in concentrated phosphoric acid (85-87% J. T. Baker) to ensure a reproducible surface was obtained. The electrodes were then immediately rinsed with DI water and dried using compressed nitrogen. The counter electrode was a platinum foil (0.25 mm thick 99.9% Sigma Aldrich) that was flame annealed prior to each experiment. The working electrode potential was referenced against a Ag/AgCl electrode (1 mm OD, Innovative Instruments Inc.) that was calibrated against a homemade reversible hydrogen electrode. An anion-conducting membrane (Selemion AMV, AGC Inc.) was used as the ion-conducting membrane. A 0.05 M K_2CO_3 (99.995% Sigma Aldrich) solution prepared using 18.2 MΩ deionized (DI) water from a Millipore system was used as the electrolyte. The catholyte was sparged with CO_2 (99.999% Praxair) at a rate of 5 sccm for the duration of electrolysis to ensure saturation with CO_2 at all times.

4.6.18.2 Electrochemistry

Electrochemistry was performed using a Biologic VSP-300 potentiostat. All electrochemical data were recorded versus the reference electrode and converted to the RHE scale using the relationship $E_{RHE} = E_{Ag/AgCl} + 0.197 + 0.059 \times pH_{Bulk}$. Potentiostatic electrochemical impedance spectroscopy (PEIS) was used to determine the total uncompensated resistance (R_u) by applying frequencies from 10 Hz to 30 kHz at the open circuit potential. The potentiostat compensated for 85% of R_u *in-situ* and the last 15% was post-corrected to arrive at accurate potentials.

4.6.18.3 Liquid Phase Product Analysis via High Performance Liquid Chromatography

The electrolyte was collected from both the cathode and anode chambers after electrolysis and stored in air-tight vials inside of a refrigerated autosampler until analysis via high performance liquid chromatography (HPLC) could commence. The

concentrations of the liquid-phase CO_2R products contained in each electrolyte sample were determined using a Thermo Scientific UltiMate 3000 liquid chromatograph equipped with a refractive index detector (RID). The liquid-phase products contained in a 10 µM injection were separated using an Aminex HPX 87-H column (Bio-Rad) and a 1 mM sulfuric acid eluent. The column oven was maintained at 60 °C for the duration of the analysis. The signal response of the RID to each liquid-phase product was calibrated individually by analyzing solutions containing each product at a concentration of 1, 10, and 100 mM.

4.6.18.4 Deconvoluting the m/z = 31 Signal

The average total current densities and alcohol Faradaic efficiencies recorded after each chronoamperometric experiment are reported in Table S4.5 as a function of the applied potential. The data was used to create a plot of the relative concentration of ethanol to 1-propanol generated using polycrystalline copper at the potentials investigated. At the potentials where alcohols were formed by the reaction, the relative concentration of ethanol to 1-propanol was approximated using a linear trend line, as shown in Figure S4.27.

The percentage of the *m/z* = 31 signal attributed to ethanol can be approximated using this trend line and the following expression:

Table S4.5 *– Total current densities and alcohol Faradaic efficiencies recorded after chronoamperometry at a series of applied potentials.*

Potential (vs RHE)	Current Density (mA/cm²)	EtOH Faradaic Efficiency	1-PrOH Faradaic Efficiency
-0.76	0.93	0%	0%
-0.85	1.66	0%	0%
-0.95	2.06	0.02%	0.01%
-1.01	5.13	2.51%	0.83%
-1.08	7.97	4.55%	0.98%

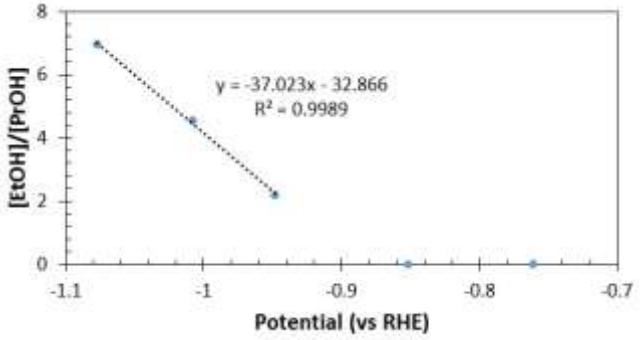

Figure S4.27 *– Relative concentration of ethanol to 1-propanol recorded after chronoamperometry at a series of applied potentials.*

$$Contribution\ of\ EtOH\ to\ {}^{m}/_{z} = 31\ Signal = \frac{[EtOH]\frac{Im_{/z=31,EtOH}}{\sum_j Im_{/z=j,EtOH}}}{[EtOH]\frac{Im_{/z=31,EtOH}}{\sum_j Im_{/z=j,EtOH}} + [PrOH]\frac{Im_{/z=31,PrOH}}{\sum_j Im_{/z=j,PrOH}}}$$

The result of this calculation is depicted in Figure S4.28, along with the estimation of the percentage of the *m/z* = 31 signal attributed to ethanol as calculated in 4.6.16 using data available in the current literature.[1] The good agreement between this methodology and that reported in the literature suggests that the measurements taken here are representative of polycrystalline copper. Thus, the trend line in Figure S4.27 and

Equation (27) were used to deconvolute the contributions made by each alcohol to the overall *m/z* = 31 signal.

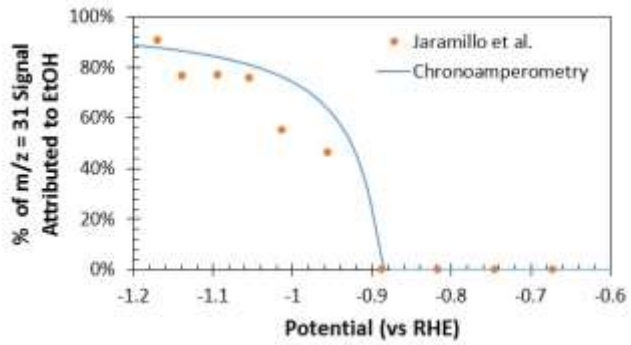

Figure S4.28 *– Percentage of the m/z = 31 signal attributed to ethanol as a function of the applied potential calculated using the trend line in Figure S27 and Equation (27). The ethanol contribution to the m/z = 31 signal calculated using data reported in the current literature is shown for comparison.*

4.6.19 Hydrogen Partial Current Density Required to Saturate the Electrolyte

$$j_{H_2\ Sat} = \frac{C_{H_2\ Sat} Q F n}{A}$$

Where:

$j_{H_2\ Sat}$	H_2 Partial Current that Results in Electrolyte Saturation = 2.52 mA/cm^2
$C_{H_2\ Sat}$	Solubility Limit of H_2 in H_2O = 0.782 mM @ 25 °C
Q	Electrolyte Flow Rate = 1 mL/min
F	Faraday's Constant
n	mol e^- Transferred/mol Product Generated
A	Electrode Surface Area

4.6.20 Mass Ion Currents Recorded During Linear Sweep Voltammetry Using a Polycrystalline Copper Cathode

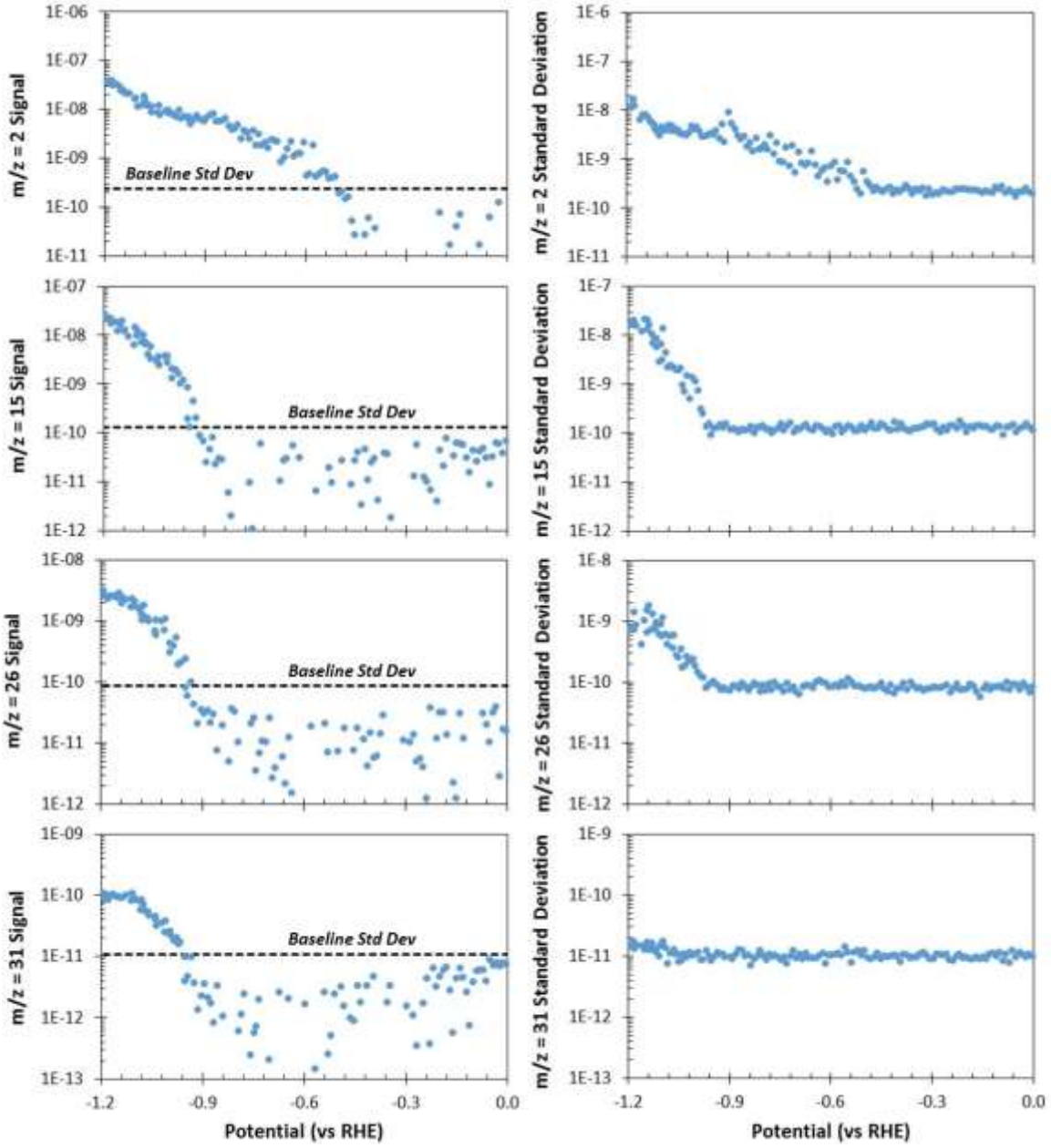

Figure S4.29 *– Signals (left column) and standard deviations (right column) of the mass ion currents recorded during linear sweep voltammetry at a scan rate of 0.2 mV/s using a polycrystalline copper cathode and an electrolyte flow rate of 1 mL/min. The electrolyte used was a CO_2 saturated 0.05 M K_2CO_3 solution (pH = 6.8). The data has been averaged over 10 mV increments.*

4.6.21 Hydrocarbon Product Calibration

In order to calibrate the mass ion currents corresponding to the hydrocarbon products a standard gas containing 1000 ppm of hydrogen, methane, and ethene (balanced in helium) was introduced into the catholyte stream prior to entering the DEMS cell at a series of defined flow rates. The standard gas was introduced at each flow rate for 10 mins and the average signal responses of the mass ion currents corresponding to *m/z* = 2, 15, and 26 were plotted as a function of the flux of the corresponding species into the DEMS cell. Standard gas flow rates which resulted in the emergence of the standard gas from the collection chamber were omitted, since the gaseous product collection efficiency must be 100% for this calibration methodology to be valid. By converting the fluxes into partial current densities the calibration curves in Figure S4.30 were constructed. The standard deviations of the mass ion current baselines corresponding to *m/z* = 2, 15, and 26 were then determined over a 10 min period in order

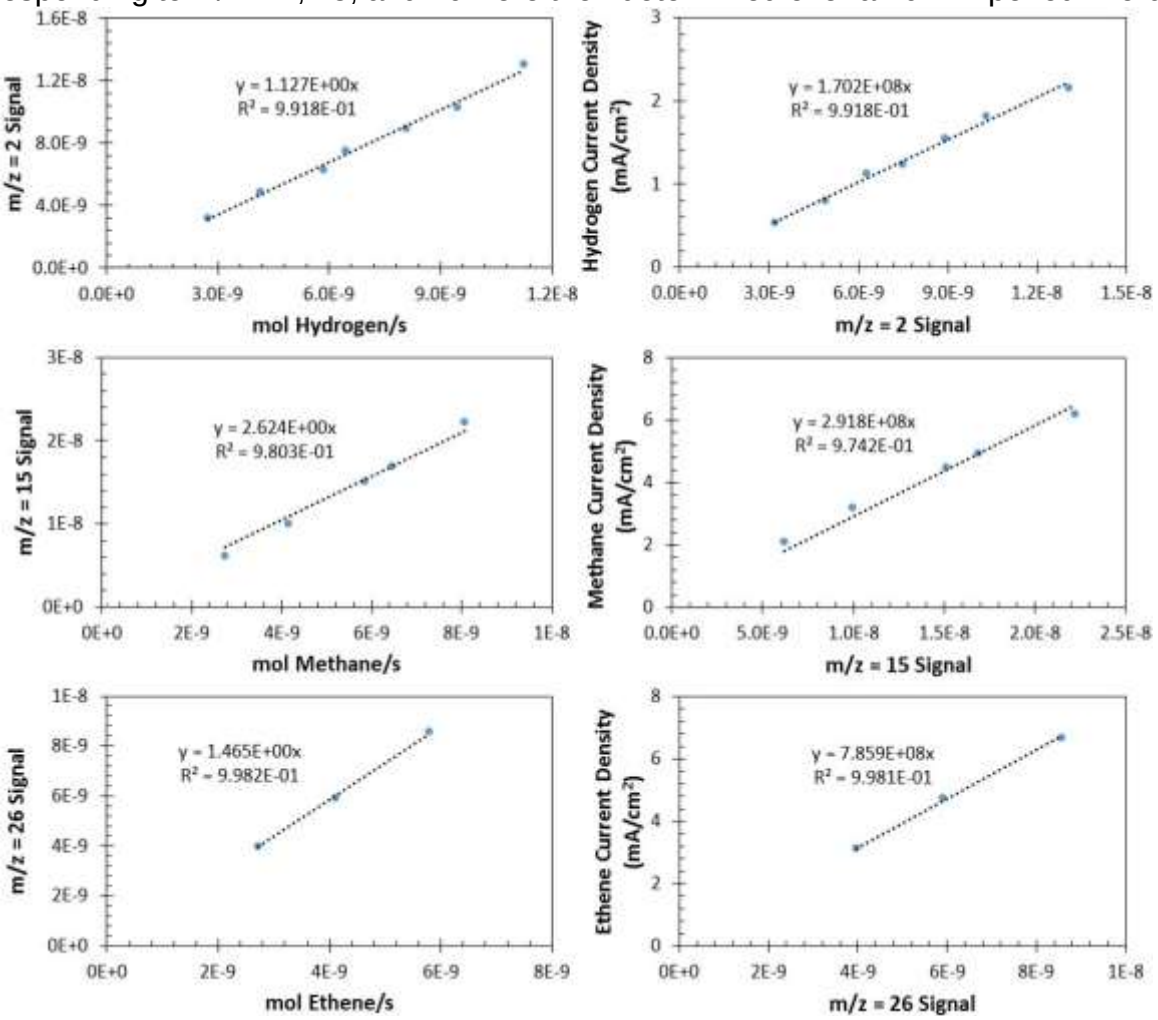

Figure S4.30 *– Signal responses of the mass ion currents corresponding to m/z = 2, 15, and 26 recorded by introducing a standard gas containing 1000 ppm of H_2, CH_4, and C_2H_4 balanced in He into the electrolyte stream at a series of defined flow rates (left column). The fluxes of the gaseous products were converted into partial current densities to construct the final gaseous product calibration curves (right column).*

to calculate the detection limits of the gaseous products. The detection limits were calculated to be 0.03, 0.04, and 0.05 mA/cm^2 for hydrogen, methane, and ethene, respectively.

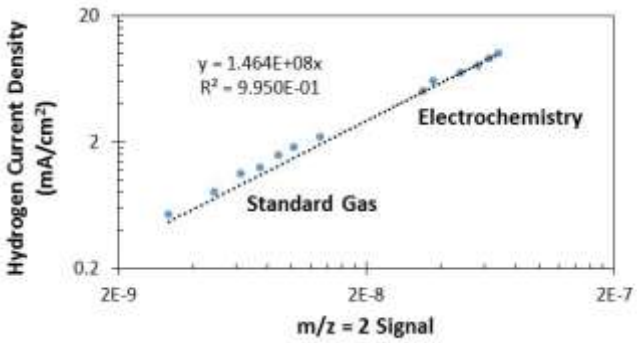

Figure S4.31 *– Comparison of the m/z = 2 calibration curve corresponding to gaseous H_2 obtained electrochemically by applying a series of fixed current densities in a helium-sparged electrolyte to that obtained by introducing a standard gas containing H_2 into the catholyte stream at a series of define flow rates.*

In order to prove the validity of this calibration methodology the results obtained for the *m/z* = 2 mass ion current were compared to the gaseous hydrogen calibration curve obtained electrochemically in a helium-sparged electrolyte. The results obtained using the standard gas fell along the calibration curve for gaseous hydrogen obtained electrochemically, as shown in Figure S4.31. This proves the validity of this calibration approach and also demonstrates that the signal response of a given product is not affected by the presence of other reaction products simultaneously entering the ionization chamber.

4.6.22 Comparison of the Partial Current Densities Recorded During Linear Sweep Voltammetry Using DEMS with Those Reported by Jaramillo *et al.* Using the Conventional Analytical Approach[1]

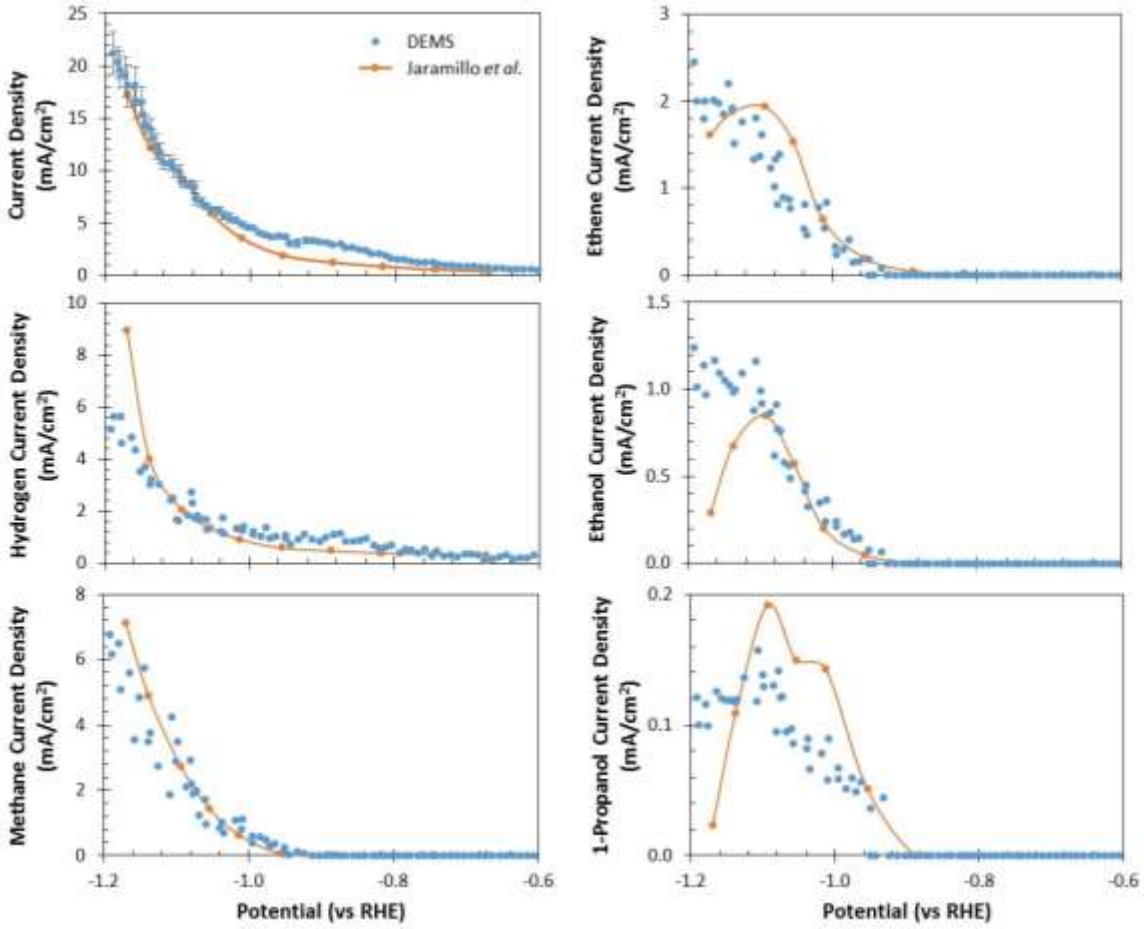

Figure S4.32 *– Comparison of the CO_2R voltammogram and product partial current densities recorded during linear sweep voltammetry using DEMS (blue dots) to those reported by Jaramillo et al. recorded during chronoamperometry at a series of applied potentials using a combination of GC and NMR (orange trace).*

4.6.23 Extended Chronoamperometry Results

The drop in the hydrogen Faradaic efficiency over time is due to issues with accurate background subtraction. After chronoamperometry was conducted the base pressure of the system had increased, indicating the presence of residual water in the ionization chamber. This water will increase the magnitude of the *m/z* = 2 mass ion current baseline, making accurate baseline subtraction difficult.

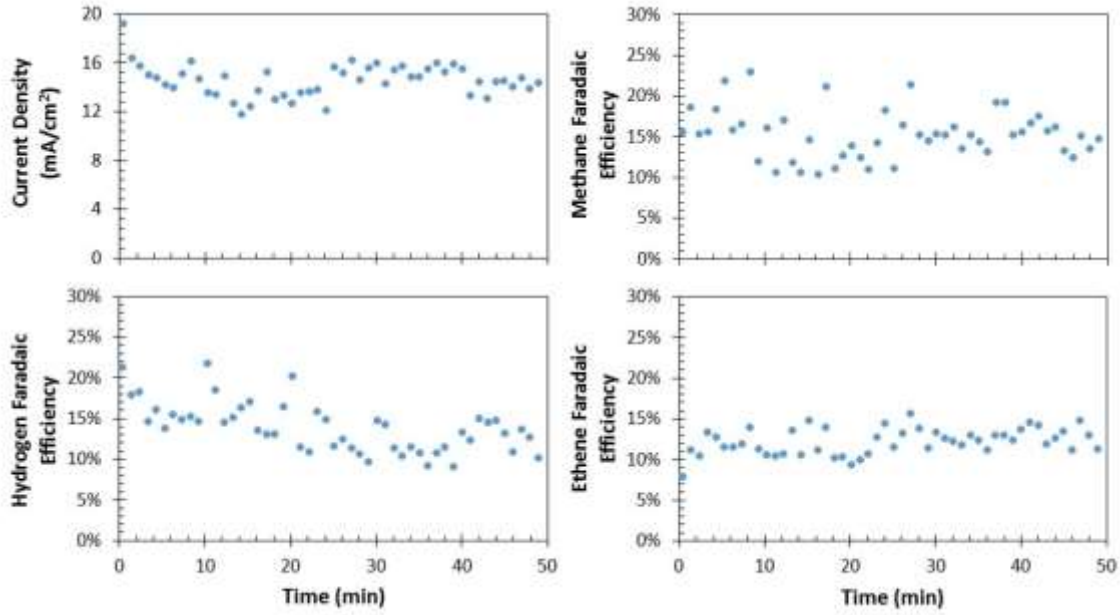

Figure S4.33 *– Total current density and gaseous product partial current densities recorded during chronoamperometry at -1.14 V vs RHE using a polycrystalline copper cathode and an electrolyte flow rate of 1 mL/min. The electrolyte used was a CO_2 saturated 0.05 M K_2CO_3 solution (pH = 6.8). The data has been averaged over 60 s increments.*

4.6.24 Supplementary Information References

(1) Kuhl, K. P.; Cave, E. R.; Abram, D. N.; Jaramillo, T. F. *Energy Environ. Sci.* **2012**, *5*, 7050–7059.
(2) Bard, A.; Faulkner, L. *Electrochemical Methods: Fundamentals and Applications*; 2nd ed.; John Wiley & Sons, Inc., 2002.

Chapter 5

Direct Observation of the Local Reaction Environment during the Electrochemical Reduction of Carbon Dioxide

Adapted from:
Clark, E. L.; Bell, A. T. *J. Am. Chem. Soc.* **2018**, 140, 7012-7020.

Abstract

The electrochemical reduction of carbon dioxide is sensitive to electrolyte polarization, which causes gradients in pH and the concentration of carbon dioxide to form near the cathode surface. Since the intrinsic kinetics of carbon dioxide reduction depend on the composition of the local reaction environment it is desirable to measure the concentration of reaction-relevant species in the immediate vicinity of the cathode. Meeting this objective has proven difficult, since conventional analytical methods only sample products from the bulk electrolyte. In this study, we describe the use of differential electrochemical mass spectrometry to measure the concentration of carbon dioxide and reaction products in the immediate vicinity of the cathode surface. This capability is achieved by coating the electrocatalyst directly onto the pervaporation membrane used to transfer volatile species into the mass spectrometer, thereby enabling species to be sampled directly from the electrode-electrolyte interface. This approach has been used to investigate hydrogen evolution and carbon dioxide reduction over Ag and Cu. We find that the measured CO_2 reduction activity of Ag agrees well with what is measured by gas chromatography of the effluent from an H-cell operated with the same catalyst and electrolyte. A distinct advantage of our approach is that it enables observation of the depletion of carbon dioxide near the cathode surface due to reaction with hydroxide anions evolved at the cathode surface, something that cannot be done using conventional analytical techniques. We also demonstrate that the influence of this relatively slow chemical reaction can be minimized by evaluating electrocatalytic activity during a rapid potential sweep; thereby enabling measurement of the intrinsic kinetics. For CO_2 reduction over Cu, nine products can be observed simultaneously in real time. A notable finding is that the abundance of aldehydes relative to alcohols near the cathode surface is much higher than that observed in the bulk electrolyte. It is also observed that for increasingly cathodic potentials the relative abundance of ethanol increases at the expense of propionaldehyde. These finding suggest that acetaldehyde is a precursor to ethanol and propionaldehyde and that propionaldehyde is a precursor to n-propanol.

5.1 Introduction

Fuels and commodity chemicals can potentially be produced by the electrochemical reduction of carbon dioxide (CO_2).[1–3] The product distribution obtained is highly dependent on the composition of both the metal used as the cathode and the reaction environment in the immediate vicinity of its surface. For example, silver (Ag) produces carbon monoxide (CO) almost exclusively, while copper (Cu) is the only known electrocatalyst capable of reducing CO_2 to hydrocarbons and alcohols with high Faradaic efficiency.[4,5] Recent theoretical studies have shown that as the current density increases, electrolyte polarization occurs due to inadequate mass transfer to and from the electrode surface. As a result, the pH and CO_2 concentration near the cathode surface deviate significantly from those in the bulk of the electrolyte.[6,7] Determining the extent to which the observed electrocatalytic activity is influenced by concentration polarization is difficult because conventional analytical techniques sample species from the gas-phase effluent and the bulk electrolyte. Additionally, there is currently little experimental evidence to support any of the proposed mechanisms by which CO_2 is reduced to multi-carbon products over Cu. For example, it has been hypothesized that aldehydes are intermediates to the corresponding alcohols.[8] While this hypothesis is supported by the observation that the acetaldehyde concentration quickly saturates during prolonged electrolysis and that the electrochemical reduction of these aldehydes yields the corresponding alcohols,[9,10] these data are not sufficient to conclude that aldehydes are intermediates in the reduction of CO_2 to either ethanol or n-propanol over Cu. Therefore, the ability to quantify the composition of the local reaction environment would enable activity trends to be directly related to the catalytically relevant reactant concentration under different operating conditions. Furthermore, it could potentially enable transient intermediate reaction products to be observed, providing insight into the selectivity-determining steps of multi-carbon product formation. A promising approach for addressing these issues is differential electrochemical mass spectrometry (DEMS). This analytical technique utilizes pervaporation to continuously collect volatile electrochemical reaction products in real time.[11,12] Unfortunately, DEMS cells for CO_2 reduction are typically configured such that volatile species are sampled form the bulk electrolyte.[9,13] However, by coating the pervaporation membrane with the electrocatalyst, volatile species at the electrode-electrolyte interface can be sampled.[11,12] Furthermore, by co-locating the electrocatalyst and the point of product sampling, the delay time between product generation and detection is minimized and the liquid-phase product collection efficiency is maximized.[11,12]

Here, we report the merits of investigating CO_2 reduction with a DEMS cell that enables reactant and product concentrations to be probed in the immediate vicinity of the cathode. This capability has enabled us to observe the acid-base reaction of CO_2 with hydroxide anions evolved at the cathode surface and demonstrate that the influence of this relatively slow chemical reaction on the measured activity of Ag can be minimized by conducting product analysis during a rapid potential sweep. Furthermore, we have been able to probe the effects of electrolyte hydrodynamics on the electrocatalytic activity of Ag and relate the observed changes to differences in the composition of the local reaction environment. We demonstrate a method of signal deconvolution over Cu that enables the

continuous observation of nine different reaction products and observe a potential-dependent hysteresis of the product distribution that favors multi-carbon product generation during the anodic sweep. Finally, we have discovered that aldehydes are much more abundant than the corresponding alcohols in the immediate vicinity of the Cu cathode, supporting the hypothesis that they are intermediates to more reduced products.

5.2 Experimental

5.2.1 Electrochemical Cell

Figure 5.1 illustrates the DEMS setup. It consists of an electrochemical cell, a set of electrolyte reservoirs, and a peristaltic pump. The electrochemical cell was machined from PEEK and was cleaned by sonication in 20 wt. % nitric acid prior to each experiment. The working and counter electrodes are parallel and separated by an anion-conducting membrane (Selemion AMV AGC Inc.). The exposed geometric surface area of the cathode is ~0.5 cm^2. The anode is a platinum gauze disc (100 mesh, 99.9% Sigma Aldrich) with an exposed surface area of roughly 2 cm^2. The working electrode potential was referenced against an Ag/AgCl electrode (Innovative Instruments Inc.) that was calibrated against a homemade standard hydrogen electrode. A 0.05 M Cs_2CO_3 (99.995% Sigma Aldrich) solution prepared using 18.2 MΩ DI water was used as the electrolyte. This electrolyte was selected because it has been shown to enhance the C_{2+} product selectivity obtained over polycrystalline Cu.[14–16] Metallic impurities in the as-prepared electrolyte were removed before electrolysis by chelating them with Chelex 100

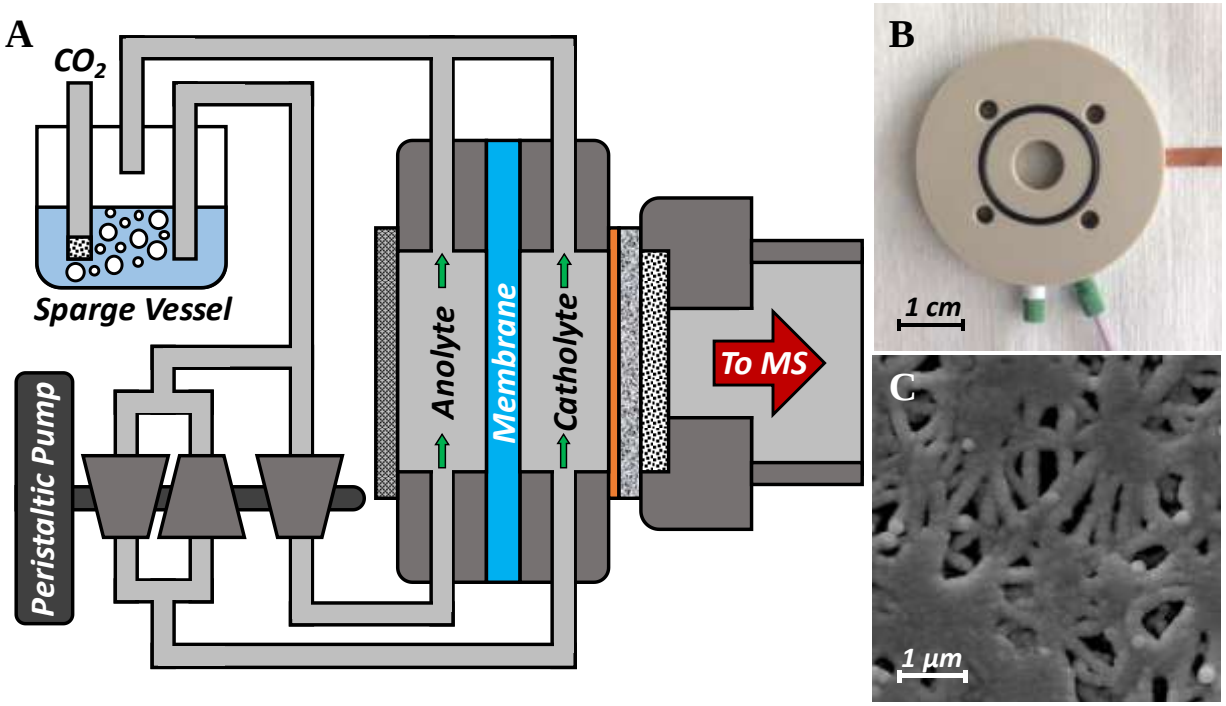

Figure 5.1 *– (A) Schematic of the DEMS setup with only one electrolyte reservoir shown for simplicity. (B) Photograph of the cathode chamber of the DEMS cell. (C) SEM image of the nanoporous PTFE membrane coated with Ag.*

(Na form Sigma Aldrich).[17] Each electrode chamber had an associated electrolyte vessel that was sparged with CO_2 (99.999% Praxair Inc.) for 30 min prior to and throughout the duration of all electrochemical measurements. Upon saturation with CO_2 the pH of the electrolyte was 6.8, which was maintained throughout the duration of each experiment. The electrolyte from these reservoirs was continuously pumped through the chambers of the electrochemical cell and recycled using a peristaltic pump. The catholyte was pumped using a parallel set of pump cartridges with opposing polarities, which resulted in constant pressure flow. Constant pressure flow was only employed for the catholyte since it was critical to obtaining stable mass-ion currents.

5.2.2 Electrode Preparation

A nanoporous PTFE membrane (20 nm pore size, Hangzhou Cobetter Filtration Equipment Co.) was used as the pervaporation membrane and electrocatalyst support. The nanoporous PTFE membrane was sonicated in acetone for 30 min, sonicated in methanol for 30 min, rinsed with DI water, dried over N_2, and exposed to UV generated ozone for 5 min to clean the surface prior to sputter deposition. Cu and Ag thin films were deposited onto the nanoporous PTFE membrane using an AJA ATC Orion-5 magnetron sputtering system. Cu (99.999% Kurt J. Lesker) and Ag (99.999% Kurt J. Lesker) were deposited at a rate of 1 Å/s to an effective thickness of 400 nm under Ar. This thickness was determined to maximize the CO mass-ion current signal during linear sweep voltammetry over Ag (see 5.6.1). A scanning electron micrograph of the nanoporous PTFE membrane coated with Ag is shown in Figure 5.1C.

5.2.3 Electrode Characterization

The bulk crystal structure of the Cu and Ag thin films deposited onto the nanoporous PTFE membrane were analyzed using a Rigaku Smartlab x-ray diffractometer (XRD). The symmetric out-of-plane diffractograms were acquired using Cu Kα radiation (40 kV, 40 mA). The average crystallite size of the particles comprising the thin films was calculated using the Scherrer equation. Scanning electron micrographs of the Cu and Ag thin films were acquired using an FEI Quanta FEG 250 scanning electron microscope (SEM). The micrographs were acquired using an electron beam energy of 15 kV and a spot size of 3.0 nm.

The near-surface composition of the Cu and Ag thin films were measured before and after electrolysis using a Kratos Axis Ultra DLD x-ray photoelectron spectrometer (XPS). All spectra were acquired using monochromatized Al Kα radiation (15 kV, 15 mA). Ar sputtering of the sample surface was avoided to prevent the removal of surface contaminants. The kinetic energy scale of the measured spectra were calibrated by setting the C 1s binding energy to 284.8 eV. The same instrument was also used to measure the surface composition of the Cu and Ag thin films before and after electrolysis by ion scattering spectroscopy (ISS). All spectra were acquired using a focused He ion beam (1 kV). No impurities were detected on the electrode surface before or after electrolysis by either XPS or ISS (see 5.6.2).

5.2.4 Electrochemistry

Electrochemistry was performed using a Biologic VSP-300 potentiostat. All electrochemical measurements were recorded versus the reference electrode and converted to the RHE scale. The working electrode was conditioned prior to experimentation by conducting chronopotentiometry at -20 mA/cm^2 for 30 min. Potentiostatic electrochemical impedance spectroscopy (PEIS) and current interrupt (CI) were used to determine the uncompensated resistance (R_u) of the electrochemical cell (see 5.6.3). While the potentiostat compensated for 85% of R_u *in-situ*, the last 15% was not corrected since this would result in a potential scale that does not vary linearly with time, making the accurate alignment of the electrochemistry and mass spectrometry erroneous.

The roughness factor of the Ag films deposited onto the nanoporous PTFE membrane were determined relative to an identical film deposited onto a polished Si wafer by taking the ratio of their double layer capacitances. The double layer capacitance of each electrode was measured by conducting cyclic voltammetry in a potential range where no Faradaic processes occur at a series of increasingly rapid scan rates (see 5.6.4).

5.2.5 Mass Spectrometry

Mass spectra were acquired using a Hiden HPR40 dissolved-species mass spectrometer. An electron energy of 70 eV was used for the ionization of all species with an emission current of 500 μA. All mass-selected product cations were accelerated using a voltage of 3 V and were detected using a secondary electron multiplier with a detector voltage of 1,350 V. The mass spectra of relevant species were measured so that accurate deconvolution of the observed mass spectrum could be conducted (see 5.6.5).

5.3 Results and Discussion

5.3.1 Hydrogen Evolution over Ag

Hydrogen evolution was investigated over Ag in the absence of CO_2 to confirm that the measured mass-ion currents are directly proportional to the rates of products generation by electrochemical reaction. To this end, a chronopotentiometry staircase was conducted imposed while monitoring the *m/z* = 2 mass-ion current (see 5.6.6). The linear correlation between the *m/z* = 2 mass-ion current signal and the total current density confirms the quantitative nature of the observed mass-ion currents and demonstrates that the product collection efficiency is independent of the absolute current density. Furthermore, the reproducibility of the H_2 calibration curve indicates that the product collection efficiency does not vary with extended operation. By comparing the slope of the H_2 calibration curve to that observed under stagnant electrolyte conditions the product collection efficiency was estimated to be ~80% at an electrolyte flow rate of 85 mL/min, assuming complete product collection under stagnant conditions. Thus, product collection

efficiencies remain high despite that electrolyte convection enhances the flux of electrochemical reaction products away from the electrode surface and into the bulk of the electrolyte. The H_2 detection limit, defined as the partial current density that results in a mass-ion current signal greater than the standard deviation of the baseline, was determined to be ~40 μA/cm^2 at this flow rate.

The temporal accuracy of product quantification was evaluated by conducting linear sweep voltammetry at rates of 5 to 100 mV/s while monitoring the *m/z* = 2 mass-ion current. The observed *m/z* = 2 signal was converted into the corresponding H_2 partial current density using the calibration curve described above and is shown in Figure 5.2A. As the scan rate increased, higher current densities were observed at a given potential. The increase in the observed current density at a given potential due to the variation of the scan rate was roughly 3 orders of magnitude higher than the current associated with charging the electrochemical double layer (see 5.6.4). Thus, the increase in the observed current density is hypothesized to be the result of the suppressed depletion of bicarbonate anions near the cathode surface as the scan rate is increased. The depletion of the bicarbonate anions near the cathode is suppressed at higher scan rates because fewer hydroxide anions are evolved over the course of the linear potential sweep as the scan rate is increased. Recent work has shown that HCO_3^- anions can serve as a source of adsorbed H atoms (H*) via the reaction: $HCO_3^- + e^- \rightarrow H^* + CO_3^{2-}$. The reason that HCO_3^- anions are an effective source of absorbed H* is that the pKa of HCO_3^- anions is 3.7 pKa units lower than that of water (10.3 vs 14), which means that despite the lower concentration of HCO_3^- anions (0.1 M) relative to that of water (55 M), HCO_3^- anions can compete with water as a source of H*.[18]

The difference between the total current density and the observed H_2 partial current density was calculated to determine the scan rate dependence of the quantification error, as shown in Figure 5.2B. The total fraction of charge passed during the linear potential sweep accounted for by detected H_2 only decreases marginally with scan rate (see 5.6.7). However, a greater fraction of the H_2 is detected after the scan ends as the scan rate is increased due to the finite time between product generation and detection. This ultimately results in product detection after the terminal potential is reached. However, the observed mass-ion current signal accurately reproduces the voltammogram for scan rates below ~10 mV/s. The exponential decay of the *m/z* = 2 signal is thought to be caused by the diffusion of H_2 into the electrolyte and then back toward the pervaporation membrane once the scan has ended. It is notable that this behavior was not observed for other reaction products, which diffuse through water at much slower rates than H_2 (see 5.6.7).

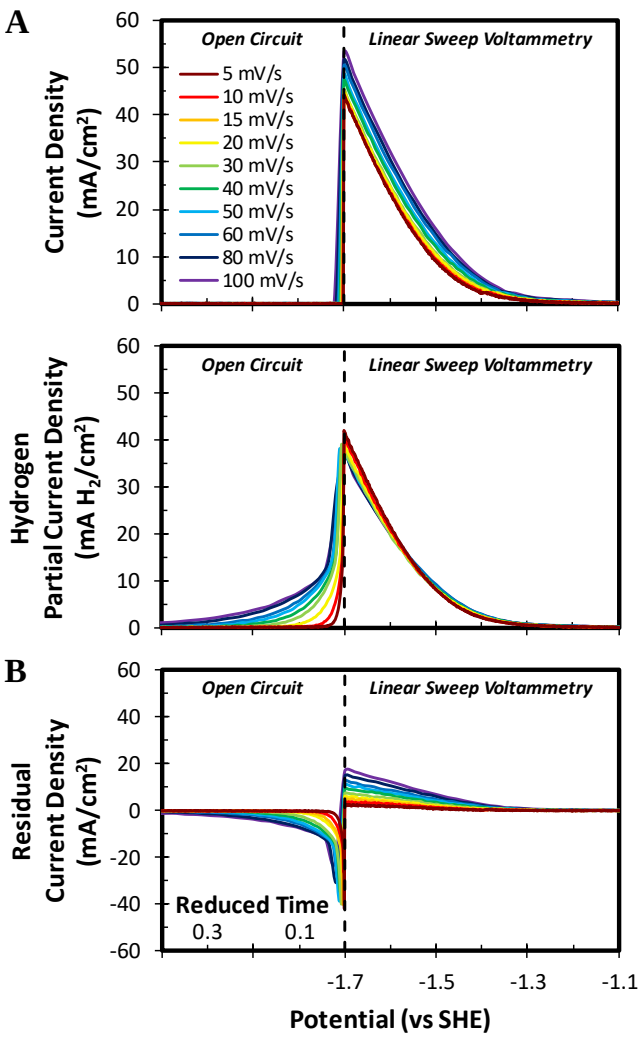

Figure 5.2 *– (A) H_2 evolution activity of Ag measured during linear sweep voltammetry at a series of increasingly rapid scan rates in 0.1 M $CsHCO_3$ saturated with N_2 at a flow rate of 85 mL/min. (B) Difference between the total current density and the observed H_2 partial current density. Reduced time is defined as the time elapsed after the terminal potential of the potential scan is reached normalized by the time required to scan through a 1 mV potential window.*

5.3.2 CO_2 Reduction over Ag

CO_2 reduction was conducted over Ag to validate that the electrocatalytic activity measured by DEMS accurately reproduces what is measured by gas chromatography (GC). Ag is an ideal electrocatalyst for this purpose because it predominately produces H_2 and CO at all applied potentials.[19,20] The ionization of CO produces some of the same mass fragments as the ionization of CO_2, necessitating deconvolution of the contributions of CO and CO_2 to the observed mass spectrum (see 5.6.8). CO calibration was conducted in an analogous way as H_2 calibration, except that the mass-ion currents for *m/z* = 2, 28, and 44 were all monitored during the chronopotentiometry staircase (see 5.6.9). The CO partial current density was assumed to be equivalent to the difference between the total current density and the H_2 partial current density, which was determined using the

observed *m/z* = 2 mass-ion current and the H_2 calibration curve. The contribution of CO_2 to the observed *m/z* = 28 signal was accounted for using the observed *m/z* = 44 mass-ion current and the measured mass spectrum of CO_2. The resulting linear correlation between the deconvoluted *m/z* = 28 mass-ion current signal and the calculated CO partial current density validates the assumption that the only products evolved at the cathode surface in appreciable quantities under these conditions are H_2 and CO (see 5.6.9).

Linear sweep voltammetry was conducted at a scan rate of 5 mV/s while monitoring the mass-ion currents for *m/z* = 2, 28, and 44. The results obtained were analyzed in an analogous fashion and compared to those obtained by analyzing the effluent of an H-cell using gas chromatograph while performing a chronoamperometry staircase over a polycrystalline Ag thin film. As shown in Figure 5.3A and 5.3B, the ECSA-

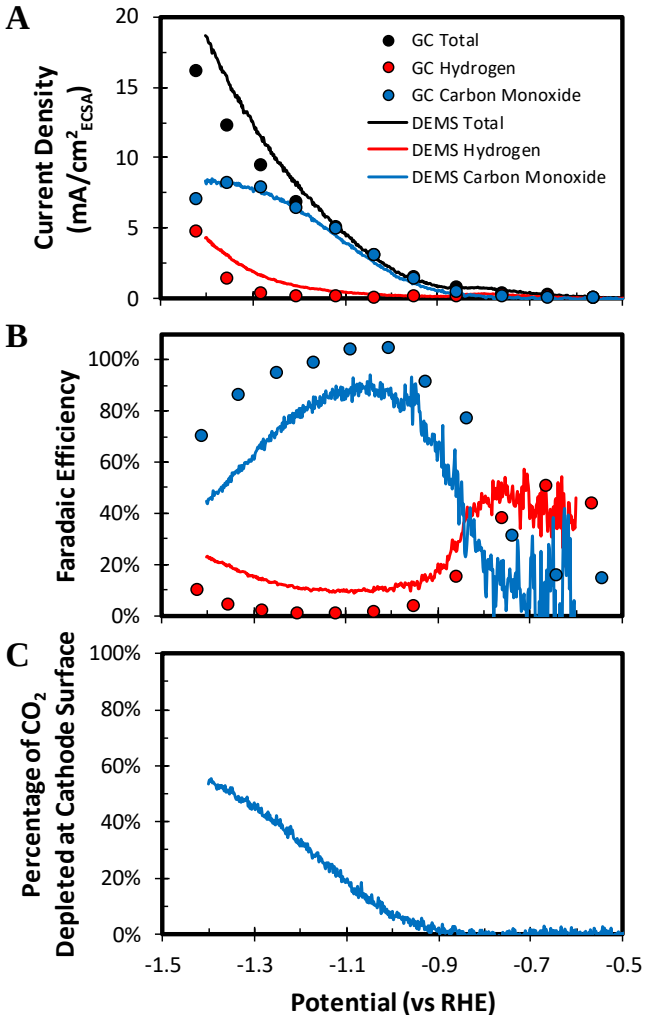

Figure 5.3 *– Comparison of the CO_2 reduction activity of Ag measured via GC and DEMS in 0.1 M $CsHCO_3$: (A) ECSA-normalized partial current densities and (B) Faradaic efficiencies. GC measurements were conducted during a chronoamperometry staircase in a traditional H-cell with a CO_2 flow rate of 20 sccm. DEMS measurements were conducted during linear sweep voltammetry at a scan rate of 5 mV/s with an electrolyte flow rate of 85 mL/min. (C) Fraction of CO_2 depleted at the cathode surface as measured by DEMS during linear sweep voltammetry.*

normalized partial current densities and Faradaic efficiencies observed via DEMS and GC match exceptionally well, notwithstanding the fact that the DEMS approach acquires the data nearly two orders of magnitude faster than the conventional approach. Furthermore, the DEMS approach enables the extent of CO_2 depletion near the cathode surface to be measured experimentally, as shown in Figure 5.3C. Thus, the technique can be used to relate changes in the observed electrocatalytic activity to the composition of the local reaction environment.

To determine if the scan rate impacts the observed electrocatalytic activity and local reaction environment over Ag, linear sweep voltammetry was conducted at increasingly rapid scan rates (see 5.6.10). As shown in Figure 5.4A, as the scan rate is increased the small bump in the H_2 partial current density at roughly -0.8 V vs RHE shifts to more cathodic potentials. This feature is likely caused by the poisoning of surface sites by adsorbed intermediates associated with the reduction of CO_2 to CO. This hypothesis is corroborated by the observation that the H_2 partial current density declines at the onset potential of CO evolution and that spectroscopic studies in the published literature have observed IR absorption bands associated with COOH over polarized Ag cathodes during CO_2 reduction.[21] The maximum in the H_2 partial current bump shifts to more cathodic potentials as the scan rate is increased because these intermediates take a finite time to accumulate on the Ag surface, enabling more cathodic potentials to be reached before they accumulate to a significant extent as the scan rate is increased. Furthermore, as the scan rate is increased from 5 to 20 mV/s the observed H_2 partial current density decreases, while the observed CO partial current density increases at potentials cathodic of -1 V vs RHE. However, scan rates faster than 20 mV/s do not exhibit any additional changes. The origin of this scan rate dependence was determined by plotting the mass-ion current signal associated with CO_2 as a function of the deconvoluted mass-ion current signal associated with CO measured during each linear potential sweep, as shown in Figure 5.4B. A linear correlation is observed at low CO generation rates regardless of the scan rate employed, suggesting that a molecule of CO is generated for every molecule of CO_2 consumed. However, at higher rates of CO generation the local CO_2 concentration is depleted to a greater degree than expected based on the rate of CO generation alone. Furthermore, the magnitude of this excessive depletion increases at a fixed CO generation rate as the scan rate drops below 20 mV/s. These trends cannot be explained in terms of differences in the rates of mass transfer of CO and CO_2 from the electrode surface into the mass spectrometer since both species diffuse through aqueous solutions at nearly identical rates, with diffusion coefficients of 1.92 and 2.03 x 10^{-5} cm^2/s, respectively. Conversely, these observations suggest that there is a second mode of CO_2 depletion that becomes relevant at scan rates below 20 mV/s. This additional mode of CO_2 depletion is hypothesized to be the reaction of CO_2 with hydroxide anions evolved at the cathode surface, which produces bicarbonate anions and depletes the local CO_2 concentration.[6,7] The extent to which this reaction depletes the local CO_2 concentration scales with the concentration of hydroxide anions produced at the cathode surface during the linear potential sweep, which decreases as the scan rate increases. It is important to realize that the intrinsic electrocatalytic activity can only be measured if the extent of concentration polarization is minimized. The DEMS approach accomplishes this by sampling products directly at the electrode-electrolyte interface, thereby enabling product

analysis to be conducted continuously during a rapid potential sweep, reducing the depletion of CO_2 by limiting the evolution of hydroxide anions at the cathode surface.

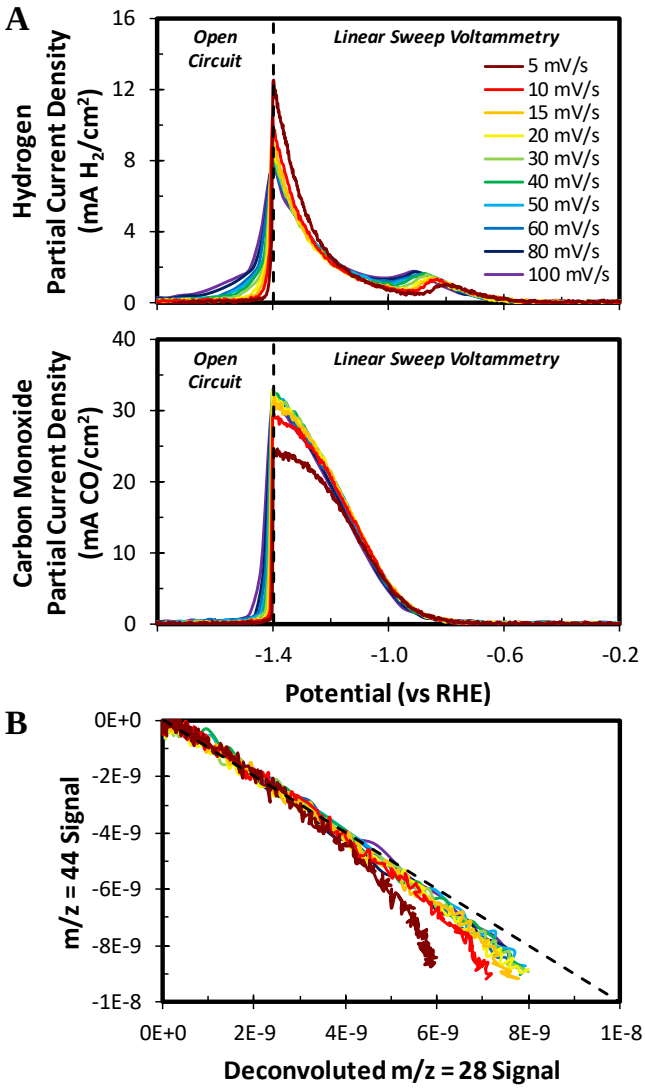

Figure 5.4 *– (A) CO_2 reduction activity of Ag measured during linear sweep voltammetry at a series of increasingly rapid scan rates in 0.1 M $CsHCO_3$ at a flow rate of 85 mL/min. (B) CO_2 signal (m/z = 44) vs CO signal (deconvoluted m/z = 28) observed during linear sweep voltammetry over Ag at a series of increasingly rapid scan rates. The dotted line depicts the relationship expected if CO_2 depletion occurs only by the evolution of CO.*

To demonstrate the impact that the rate of mass transfer to the cathode surface has on the observed electrocatalytic activity and local reaction environment over Ag, linear sweep voltammetry was conducted at a series of increasingly rapid electrolyte flow rates. As the electrolyte flow rate is increased, the thickness of the hydrodynamic and mass-transfer boundary layers at the cathode surface decreases, which, in turn, increases the flux of CO_2 to the cathode surface. As a result, the *m/z* = 44 mass-ion current signal increases with electrolyte flow rate (see 5.6.11). As the hydrodynamic boundary layer thickness is reduced, the H_2 partial current density decreases and the CO partial current density increases at a given potential, as shown in Figure 5.5A (see 5.6.12).

Similar trends are observed over polycrystalline Ag thin films in a traditional H-cell when the products are quantified by GC (see 5.6.13). As the hydrodynamic boundary layer thickness increases the local pH should increase at a given current density, leading to CO_2 depletion by acid-base reaction at more anodic potentials.[7] To validate this hypothesis, the mass-ion current signal associated with CO_2 was plotted as a function of the deconvoluted mass-ion current signal associated with CO for each linear potential sweep performed. Figure 5.5B shows that as the electrolyte flow rate is increased the point at which the CO_2 signal rapidly declines shifts to higher CO evolution rates, which correspond to increasingly cathodic potentials. These results demonstrate the ability of the DEMS approach to explain observed activity trends based on the composition of the local reaction environment in the immediate vicinity of the cathode.

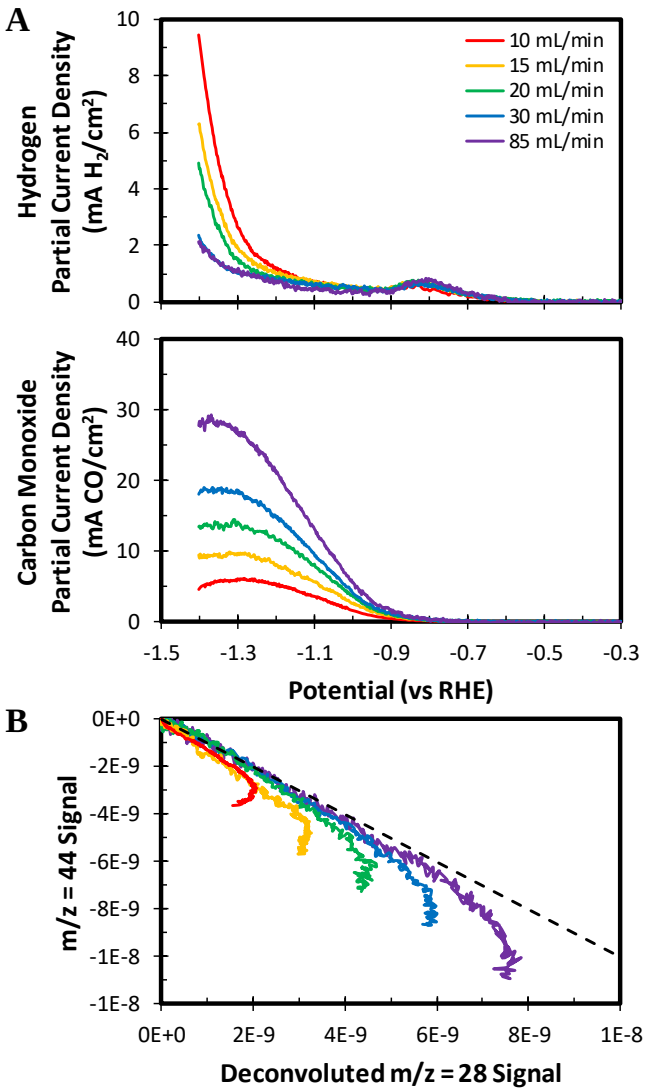

Figure 5.5 *– (A) CO_2 reduction activity of Ag measured during linear sweep voltammetry at a scan rate of 5 mV/s in 0.1 M $CsHCO_3$ at different flow rates. (B) CO_2 signal (m/z = 44) vs CO signal (deconvoluted m/z = 28) observed during linear sweep voltammetry over Ag at different electrolyte flow rates. The dotted line depicts the relationship expected if CO_2 depletion occurs only by the evolution of CO.*

5.3.3 CO_2 Reduction over Cu

Carbon dioxide (*m/z* = 44), hydrogen (*m/z* = 2), methane (*m/z* = 15), and ethene (*m/z* = 26) are the only reaction products produced over Cu that generate a unique mass fragment upon ionization (see 5.6.14). Formic acid is undetectable because it does not pervaporate. However, carbon monoxide can be detected after deconvoluting the mass-ion current for *m/z* = 28, which also contains contributions from CO_2 and ethene. The primary C_3 products produced over Cu are allyl alcohol, propionaldehyde, and n-propanol each of which generate a series of unique mass fragments at *m/z* = 57, 58, and 59 upon ionization. As a result, the extent to which each of these products contributes to the observed mass spectrum can be calculated by solving a system of linear equations (see 5.6.15). Once this is accomplished, the contribution of the C_3 products to the remaining mass-ion currents can be accounted for. Acetaldehyde and ethanol produce a series of mass fragments upon ionization at *m/z* = 31 and 43 that are also unique once the contributions of the C_3 products have been accounted for. Thus, the contributions of acetaldehyde and ethanol to the observed mass spectrum can also be calculated by solving a system of linear equations. Using this approach, the complete deconvolution of the observed mass spectrum can be conducted, enabling 10 different relevant species to be detected in real time during cyclic voltammetry, as shown in Figure 5.6. While the deconvoluted mass-ion current signals are directly proportional to the generation rates of the corresponding reaction products, quantifying the partial current densities of these products based on the deconvoluted signal is not possible due to the lack of a calibration protocol analogous to the method employed over Ag. Furthermore, alternative calibration protocols, such as flowing a standard gas mixture into the mass spectrometer, would not be accurate, since the observed mass-ion currents are dependent on the flux of each product into the mass spectrometer, which is a convolution of the generation rate and collection efficiency for each species.

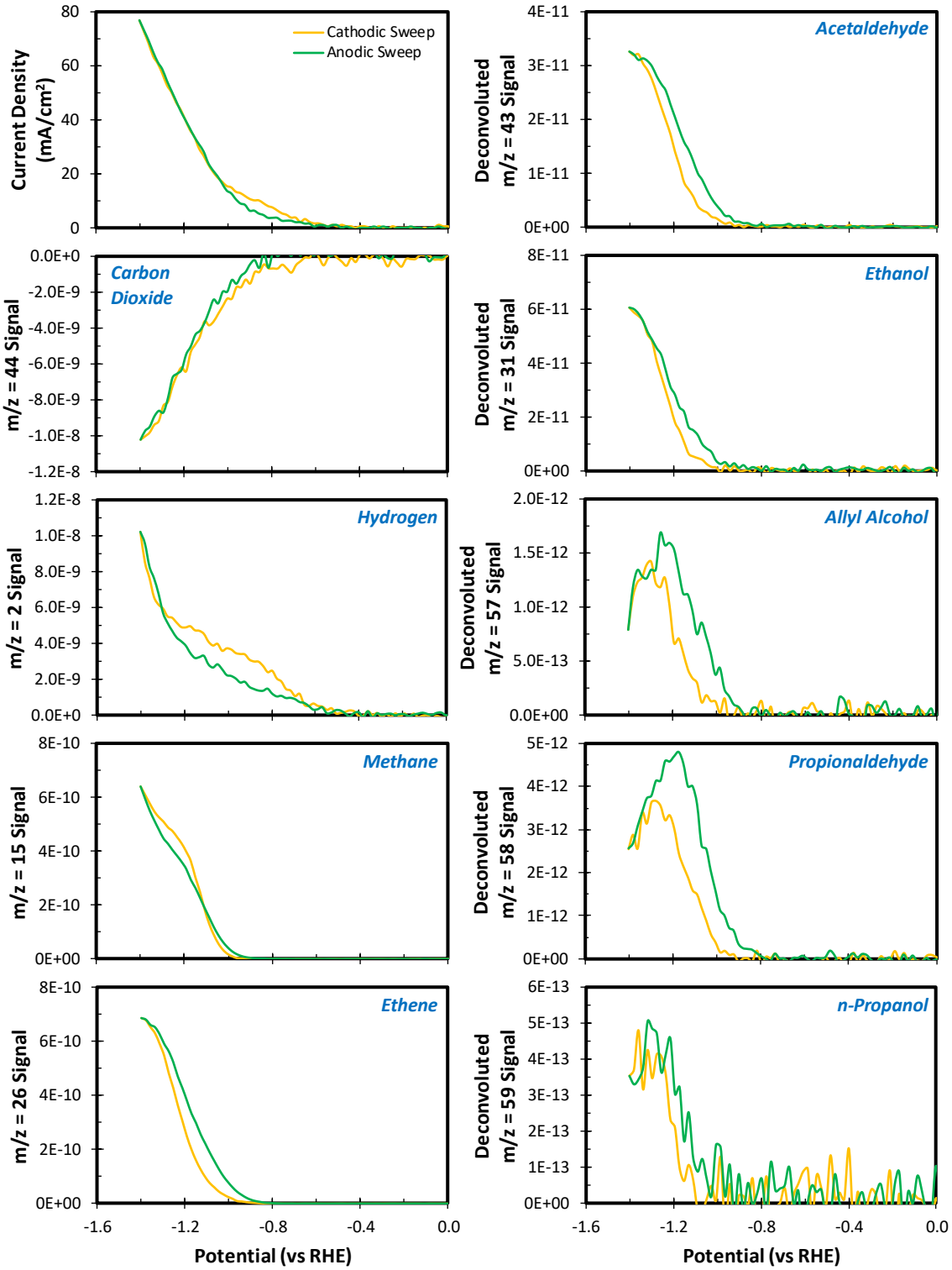

Figure 5.6 *– CO_2 reduction activity of Cu measured during cyclic voltammetry at a scan rate of 1 mV/s in 0.1 M $CsHCO_3$ at a flow rate of 85 mL/min. Signals shown in the right-hand panels have been obtained by deconvoluting the total mass-ion current so that only the signal of the primary contributing product is displayed.*

It is notable that the product distribution observed over Cu during cyclic voltammetry displays hysteresis between the cathodic and anodic sweeps. This hysteresis is characterized by an enhanced generation rate of multi-carbon products at the expense of hydrogen and methane during the anodic sweep. The hysteresis cannot be attributed to discrepancies in the local CO_2 concentration as the CO_2 signal is identical in both scan directions. To determine whether the hysteresis is potential dependent, cyclic voltammetry was conducted to a series of increasingly cathodic vertex potentials while monitoring the *m/z* = 2 mass-ion current. As shown in Figure 5.7A, hysteresis only occurs upon polarization to potentials more cathodic than -0.8 V vs RHE. As shown in Figure 5.7B, this potential agrees well with the potential at which CO is first observed by mass spectrometry. Furthermore, the hysteresis saturates at -1 V vs RHE, where the rate of CO evolution over Cu is observed to plateau. It has been proposed previously that

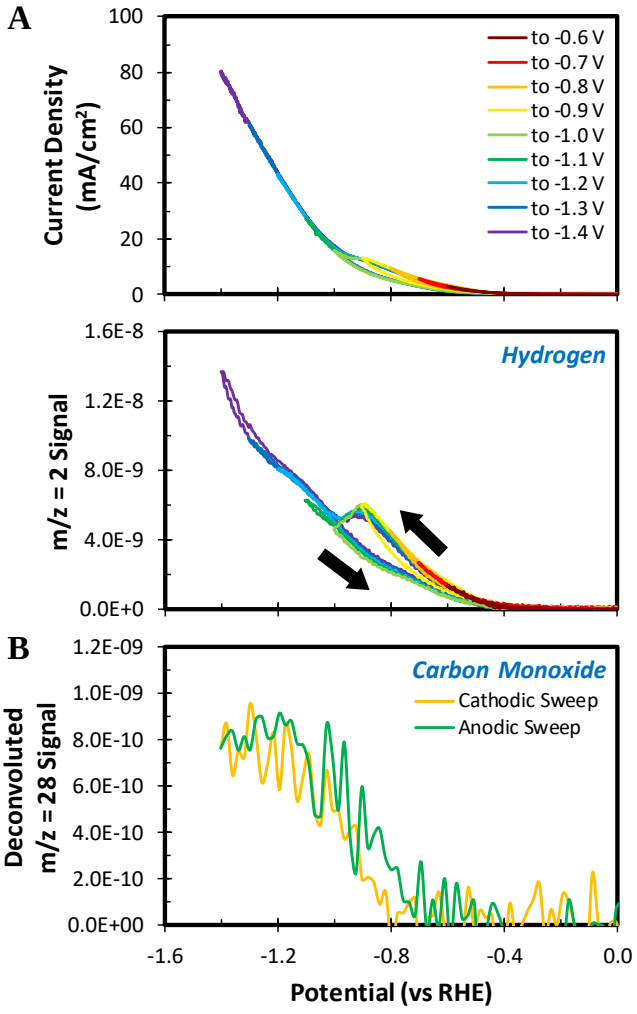

Figure 5.7 *– (A) H_2 evolution activity of Cu during CO_2 reduction measured during cyclic voltammetry to a series of increasingly cathodic vertex potentials at a scan rate of 20 mV/s in 0.1 M $CsHCO_3$ at a flow rate of 85 mL/min. The black arrows indicate the scan direction. (B) CO evolution activity of Cu measured during cyclic voltammetry at a scan rate of 1 mV/s in 0.1 M $CsHCO_3$ at a flow rate of 85 mL/min. Note that the onset and plateau of CO evolution correspond to the onset and saturation point, respectively, of the observed hysteresis in the rate of H_2 evolution over Cu during CO_2 reduction.*

hysteresis of the voltammogram is a result of CO accumulation on the Cu surface.[22,23] While the product distribution hysteresis observed over Cu during cyclic voltammetry has not been reported previously, the results obtained here are in agreement with the hypothesis that the hysteresis is caused by the accumulation of CO on the Cu surface. The rate of multi-carbon product formation is higher during the anodic sweep because polarization to more cathodic potentials results in an elevated coverage of CO on the Cu surface that persists long enough to significantly impact the activity of Cu during the anodic sweep. To confirm this hypothesis, the transient activity of Cu was measured at -1 V vs RHE before and after polarization to -1.4 V vs RHE (see 5.6.16). After polarization to -1.4 V vs RHE the ethene signal (*m/z* = 26) observed at -1 V vs RHE was ~20% higher than before the brief cathodic polarization. Furthermore, the enhanced activity took over 5 min to decay back to the value observed before the brief cathodic polarization to -1.4 V vs RHE. Thus, it seems likely that the observed product distribution hysteresis is caused by the accumulation of CO on the Cu surface, which takes several minutes to reach steady state once the extent of cathodic polarization is reduced.

To determine the relative generation rates of the liquid-phase products, the differences in their relative volatilities must be accounted for. This can be accomplished by normalizing the deconvoluted signal for each product by the signal observed upon analysis of a standard solution with a fixed concentration. As shown in Figure 5.8, the relative abundance of the liquid-phase products observed by DEMS is significantly

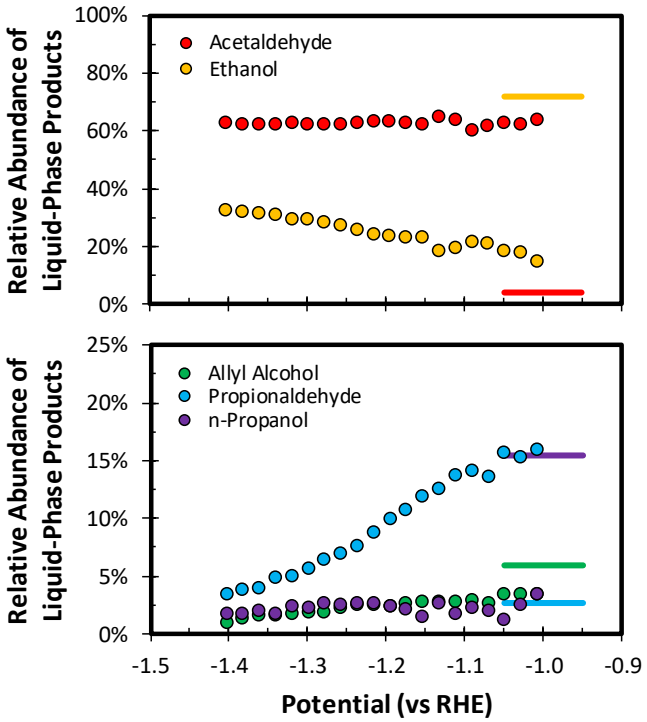

Figure 5.8 *– Observed relative abundance of the liquid-phase products produced over Cu during cyclic voltammetry at a scan rate of 1 mV/s in 0.1 M $CsHCO_3$ at a flow rate of 85 mL/min. The solid lines represent the relative molar abundances of the liquid phase-products produced over Cu during chronoamperometry at -1 V vs RHE in a traditional H-cell when analyzing the bulk electrolyte.*

different from what is typically observed over Cu when the liquid-phase products are sampled from the bulk electrolyte. Acetaldehyde and propionaldehyde are produced with a 2-4 times higher abundance than ethanol or n-propanol. Conversely, the ethanol and n-propanol are typically produced with a molar abundance roughly an order of magnitude higher than the corresponding aldehydes.[22,24] While it has been demonstrated that the electrochemical reduction of these aldehydes produces the corresponding alcohols,[9,25] this is not sufficient evidence to conclude that they are transiently produced during CO_2 reduction over Cu. However, by collecting products at the electrode-electrolyte interface these extremely volatile intermediate reaction products can be observed, suggesting that these aldehydes are relatively abundant within the local reaction environment but are typically reduced further to the corresponding primary alcohols before diffusing into the bulk electrolyte. To confirm that the pervaporate contains a high concentration of aldehydes relative to alcohols, chronoamperometry was conducted at -1.3 V vs RHE for 200 min while the pervaporate was passed through a condenser cooled with liquid N_2. The condensate was collected and analyzed by HPLC, which confirmed the high concentration of aldehydes relative to alcohols in the pervaporate (see 5.6.17). The concentration of aldehydes and alcohols in the recirculated catholyte was found to be negligible, confirming the high collection efficiency for the liquid-phase products. Interestingly, the relative abundance of ethanol increases at the expense of propionaldehyde at more cathodic potentials, as shown in Figure 5.9A. This novel observation suggests that ethanol and propionaldehyde share a common intermediate, such as acetaldehyde. This proposed mechanism is shown in Figure 5.9B. As the potential becomes increasingly cathodic the electrochemical reduction of acetaldehyde to ethanol is expected to become increasingly exergonic relative to the chemical C-C coupling between acetaldehyde and CO, which is hypothesized to lead to propionaldehyde formation.[8,26] Thus, the observed liquid phase product selectivity potential dependence can be rationalized based on both reaction products being derived from an acetaldehyde intermediate.

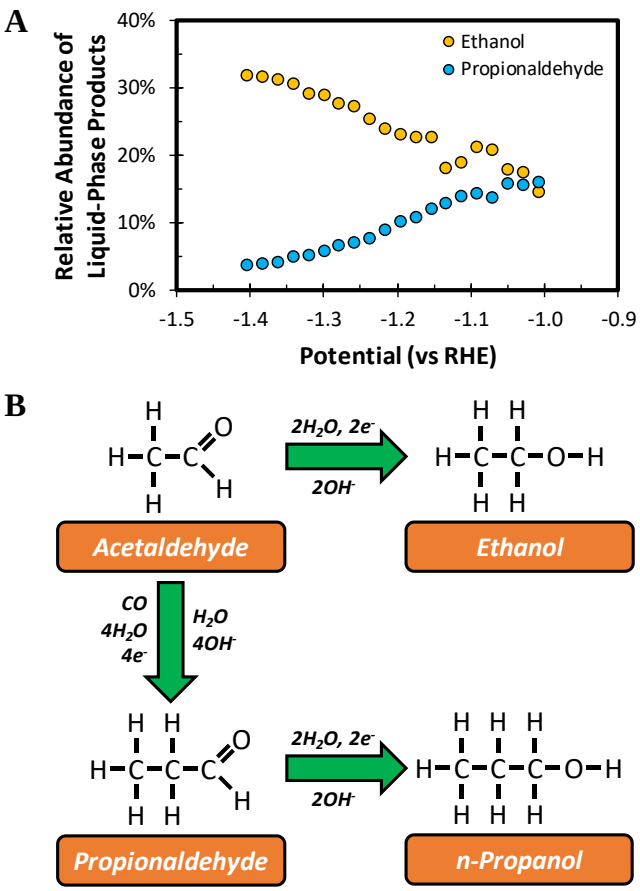

Figure 5.9 *– (A) Enhanced relative abundance of ethanol at the expense of propionaldehyde observed over Cu during cyclic voltammetry at a scan rate of 1 mV/s in 0.1 M $CsHCO_3$ at a flow rate of 85 mL/min. (B) Proposed mechanism of C_2 and C_3 primary alcohol formation over Cu from an acetaldehyde intermediate.*

5.4 Conclusions

In conclusion, we have demonstrated that the local reaction environment during the electrochemical reduction of CO_2 can be observed and quantified using a DEMS cell in which the catalyst is deposited directly onto the pervaporation membrane. We have shown that for CO_2 reduction over Ag, the amounts of H_2 and CO generated agree very well with what is observed by gas chromatographic analysis of the effluent from an H-cell operated with the same catalyst and electrolyte. Furthermore, we have observed the reaction of CO_2 with hydroxide anions evolved at the cathode surface and have demonstrated that the influence of this relatively slow chemical reaction on the measured electrocatalytic activity of Ag can be minimized by conducting product analysis during a rapid potential sweep. We have also shown how mass transfer to and from the catalyst influences the composition of the local reaction environment and measured electrocatalytic activity of Ag. For the electrochemical reduction of CO_2 over Cu, we have detected nine products continuously during cyclic voltammetry, which led to the observation of a potential-dependent hysteresis of the product distribution that favors

multi-carbon product generation during the anodic sweep. Finally, we have discovered that the electrolyte in contact with the cathode has a much higher concentration of aldehydes (acetaldehyde and propionaldehyde) than the corresponding alcohols (ethanol and n-propanol). We have also observed that at more cathodic potentials the concentration of ethanol near the cathode increases as the expense of propionaldehyde. These observations suggest acetaldehyde is a precursor to ethanol and propionaldehyde, and that the latter is precursor to n-propanol.

5.5 References

(1) Jitaru, M.; Lowy, D. A.; Toma, M.; Toma, B. C.; Oniciu, L. Electrochemical Reduction of Carbon Dioxide on Flat Metallic Cathodes. *J. Appl. Electrochem.* **1997**, *27* (8), 875–889.

(2) Gattrell, M.; Gupta, N.; Co, A. A Review of the Aqueous Electrochemical Reduction of CO2 to Hydrocarbons at Copper. *J. Electroanal. Chem.* **2006**, *594* (1), 1–19.

(3) Hori, Y. Electrochemical CO2 Reduction on Metal Electrodes. In *Modern Aspects of Electrochemistry*; Vayenas, C. G., White, R. E., Gamboa-Aldeco, M. E., Eds.; Springer: New York, 2008; pp 89–189.

(4) Hori, Y.; Kikuchi, K.; Suzuki, S. Production of CO and CH4 in Electrochemical Reduction of CO2 at Metal Electrodes in Aqueous Hydrogencarbonate Solution. *Chem. Lett.* **1985**, *14* (11), 1695–1698.

(5) Noda, H.; Ikeda, S.; Oda, Y.; Imai, K.; Maeda, M.; Ito, K.; Ideka, S.; Oda, Y.; Imai, K.; Maeda, M.; et al. Electrochemical Reduction of Carbon Dioxide at Various Metal Electodes in Aqueous Potassium Hydrogen Carbonate Solution. *Bull. Chem. Soc. Jpn.* **1990**, *63* (9), 2459–2462.

(6) Gupta, N.; Gattrell, M.; MacDougall, B. Calculation for the Cathode Surface Concentrations in the Electrochemical Reduction of CO2 in KHCO3 Solutions. *J. Appl. Electrochem.* **2006**, *36* (2), 161–172.

(7) Singh, M. R.; Clark, E. L.; Bell, A. T. Effects of Electrolyte, Catalyst, and Membrane Composition and Operating Conditions on the Performance of Solar-Driven Electrochemical Reduction of Carbon Dioxide. *Phys. Chem. Chem. Phys.* **2015**, *17* (29), 18924–18936.

(8) Garza, A.; Bell, A. T.; Head-Gordon, M. On the Mechanism of CO2 Reduction at Copper Surfaces: Pathways to C2 Products. *ACS Catal.* **2018**, *8*, 1490–1499.

(9) Schouten, K. J. P.; Kwon, Y.; van der Ham, C. J. M.; Qin, Z.; Koper, M. T. M. A New Mechanism for the Selectivity to C1 and C2 Species in the Electrochemical Reduction of Carbon Dioxide on Copper Electrodes. *Chem. Sci.* **2011**, *2* (10), 1902–1909.

(10) Bertheussen, E.; Verdaguer-Casadevall, A.; Ravasio, D.; Montoya, J. H.; Trimarco, D. B.; Roy, C.; Meier, S.; Wendland, J.; Nørskov, J. K.; Stephens, I. E. L.; et al. Acetaldehyde as an Intermediate in the Electroreduction of Carbon Monoxide to Ethanol on Oxide-Derived Copper. *Angew. Chemie - Int. Ed.* **2016**, *55* (4), 1450–1454.

(11) Wolter, O.; Heitbaum, J. Differential Electrochemical Mass Spectroscopy (DEMS) - a New Method for the Study of Electrode Processes. *Berichte der Bunsengesellschaft fur Phys. Chemie* **1984**, *88* (1), 2–6.

(12) Baltruschat, H. Differential Electrochemical Mass Spectrometry. *J. Am. Soc. Mass Spectrom.* **2004**, *15* (12), 1693–1706.

(13) Clark, E. L.; Singh, M. R.; Kwon, Y.; Bell, A. T. Differential Electrochemical Mass Spectrometer Cell Design for Online Quantification of Products Produced during Electrochemical Reduction of CO2. *Anal. Chem.* **2015**, *87* (15), 8013–8020.

(14) Murata, A.; Hori, Y. Product Selectivity Affected by Cationic Species in Electrochemical

Reduction of CO2 and CO at a Cu Electrode. *Bull. Chem. Soc. Jpn.* **1991**, *64*, 123–127.
(15) Kyriacou, G. Z.; Anagnostopoulos, A. K. Influence CO2 Partial Pressure and the Supporting Electrolyte Cation on the Product Distribution in CO2 Electroreduction. *J. Appl. Electrochem.* **1993**, *23* (5), 483–486.
(16) Singh, M. R.; Kwon, Y.; Lum, Y.; Ager, J. W.; Bell, A. T. Hydrolysis of Electrolyte Cations Enhances the Electrochemical Reduction of CO2 over Ag and Cu. *J. Am. Chem. Soc.* **2016**, *138* (39), 13006–13012.
(17) Wuttig, A.; Surendranath, Y. Impurity Ion Complexation Enhances Carbon Dioxide Reduction Catalysis. *ACS Catal.* **2015**, *5* (7), 4479–4484.
(18) Resasco, J.; Lum, Y.; Clark, E. L.; Zeledon, J.; Bell, A. T. Effects of Anion Identity and Concentration on the Electrochemical Reduction of CO2. *ChemElectroChem* **2018**, *5*, 1–10.
(19) Hoshi, N.; Kato, M.; Hori, Y. Electrochemical Reduction of CO2 on Single Crystal Electrodes of Silver Ag(111), Ag(100), and Ag(110). *J. Electroanal. Chem.* **1997**, *440* (1–2), 283–286.
(20) Hatsukade, T.; Kuhl, K. P.; Cave, E. R.; Abram, D. N.; Jaramillo, T. F. Insights into the Electrocatalytic Reduction of CO2 on Metallic Silver Surfaces. *Phys. Chem. Chem. Phys.* **2014**, *16* (27), 13814–13819.
(21) Firet, N. J.; Smith, W. A. Probing the Reaction Mechanism of CO2 Electroreduction over Ag Films via Operando Infrared Spectroscopy. *ACS Catal.* **2017**, *7* (1), 606–612.
(22) Hori, Y.; Murata, A.; Takahashi, R. Formation of Hydrocarbons in the Electrochemical Reduction of Carbon Dioxide at a Copper Electrode in Aqueous Solution. *J. Chem. Soc. Faraday Trans. I* **1989**, *85* (8), 2309–2326.
(23) Hori, Y.; Murata, A.; Yoshinami, Y. Adsorption of CO, Intermediately Formed in Electrochemical Reduction of CO2, at a Copper Electrode. *J. Chem. Soc. Faraday Trans.* **1991**, *87* (1), 125–128.
(24) Kuhl, K. P.; Cave, E. R.; Abram, D. N.; Jaramillo, T. F. New Insights into the Electrochemical Reduction of Carbon Dioxide on Metallic Copper Surfaces. *Energy Environ. Sci.* **2012**, *5* (5), 7050–7059.
(25) Hori, Y.; Takahashi, R.; Yoshinami, Y.; Murata, A. Electrochemical Reduction of CO at a Copper Electrode. *J. Phys. Chem. B* **1997**, *101* (36), 7075–7081.
(26) Goodpaster, J. D.; Bell, A. T.; Head-Gordon, M. Identification of Possible Pathways for C-C Bond Formation during Electrochemical Reduction of CO2: New Theoretical Insights from an Improved Electrochemical Model. *J. Phys. Chem. Lett.* **2016**, *7* (8), 1471–1477.

5.6 Supplementary Information

5.6.1 Optimization of the Metallic Thin Film Thickness

Ag thin films were deposited onto the nanoporous PTFE membrane to effective thicknesses of 100 to 600 nm. X-ray diffractograms of each Ag thin film were measured, as shown in Figure S5.1A. The diffractograms were utilized to calculate the average crystallite size using the Scherrer equation, as shown in Figure S5.1B. Scanning electron micrographs were recorded for each thin film, as shown in Figure S5.2. Ag thin films with low effective thicknesses result in minimal coating of the PTFE fibers, which could compromise the electrical continuity of the electrocatalyst layer. Conversely, Ag thin films with high effective thicknesses begin to block the nanopores in the PTFE membrane, which will compromise the efficiency of product collection. Thus, the optimal film thickness was determined by measuring the slope of the H_2 calibration curve and the maximum CO signal (*m/z* = 28) during linear sweep voltammetry. As shown in Figure S5.3A, Ag thin films with effective thicknesses greater than 400 nm resulted in a reduced sensitivity to H_2, presumably due to a reduced collection efficiency

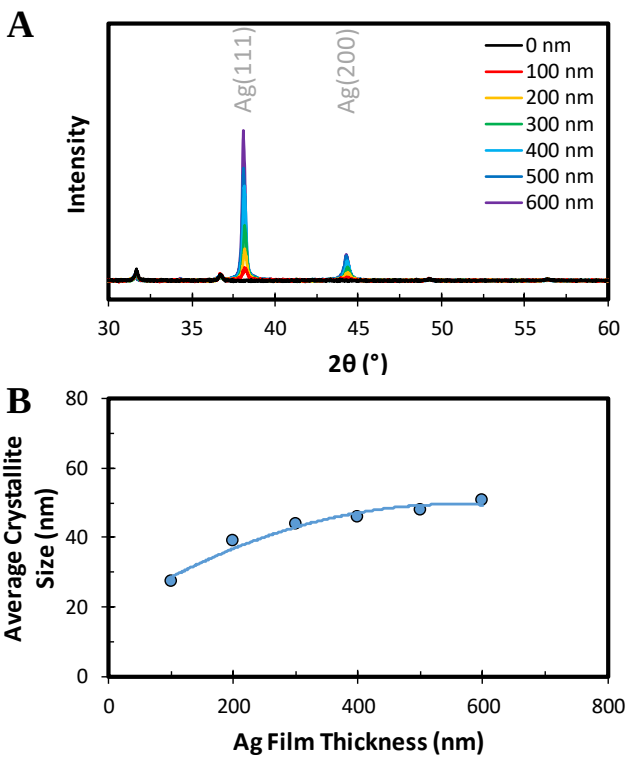

Figure S5.1 *– (A) X-ray diffractograms of the Ag thin film on the nanoporous PTFE membrane as a function of the effective thickness. (B) Average crystallite size of the Ag thin films deposited on the nanoporous PTFE membrane, as calculated using the Scherrer equation.*

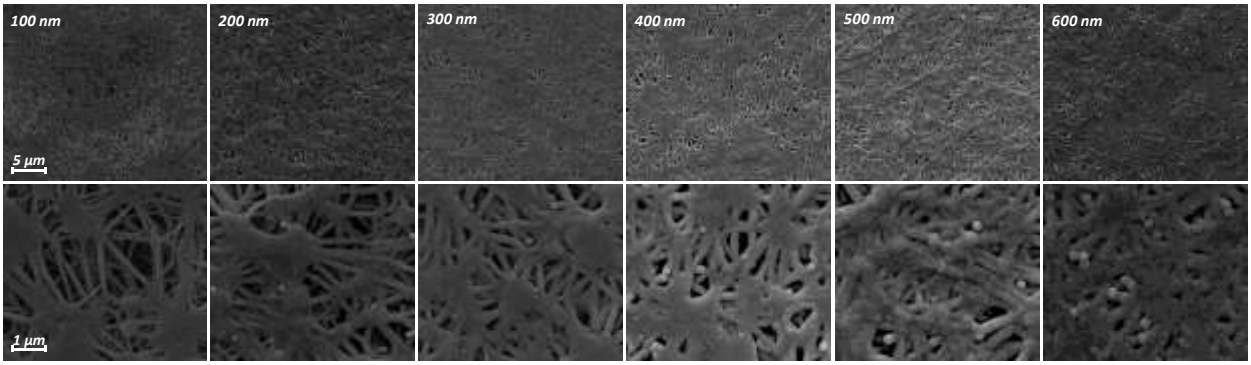

Figure S5.2 *– Scanning electron micrographs of the Ag thin films deposited onto the nanoporous PTFE membrane to different effective thicknesses.*

resulting from the blocking of the nanopores in the PTFE membrane. As shown in Figure S5.3B, the CO signal was maximized over Ag thin films with an effective thickness of 400 nm. The CO signal at lower and higher thicknesses decreases presumable due to the excessive depletion of CO_2 due to pervaporation and the reduced product collection efficiency, respectively.

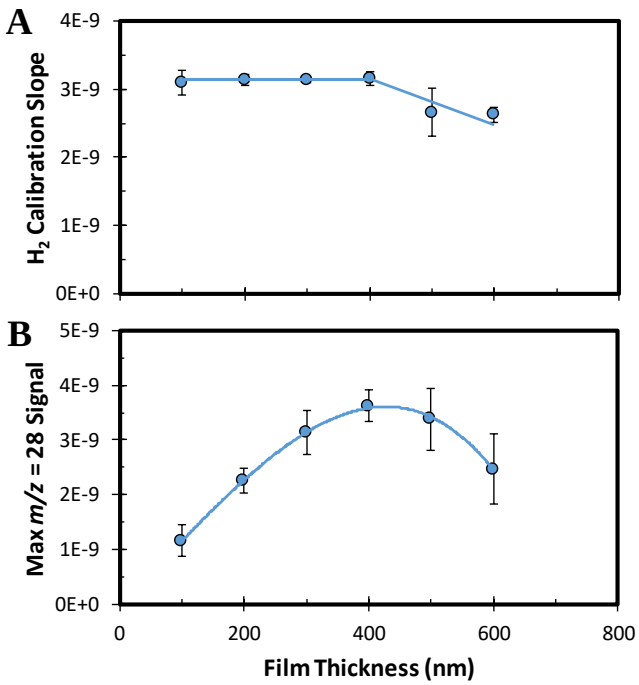

Figure S5.3 *– Impact of Ag film thickness on: (A) H_2 calibration curve slope and (B) maximum CO signal (m/z = 28) observed during linear sweep voltammetry.*

5.6.2 Validating Surface Purity by X-Ray Photoelectron and Ion-Scattering Spectroscopies

The purity of the working electrode surface was validated before and after experimentation using x-ray photoelectron (XPS) and ion scattering spectroscopies (ISS). As shown in Figure S5.4, no impurities were detected before or after experimentation by either analytical technique over a representative Ag thin film deposited onto the nanoporous PTFE membrane.

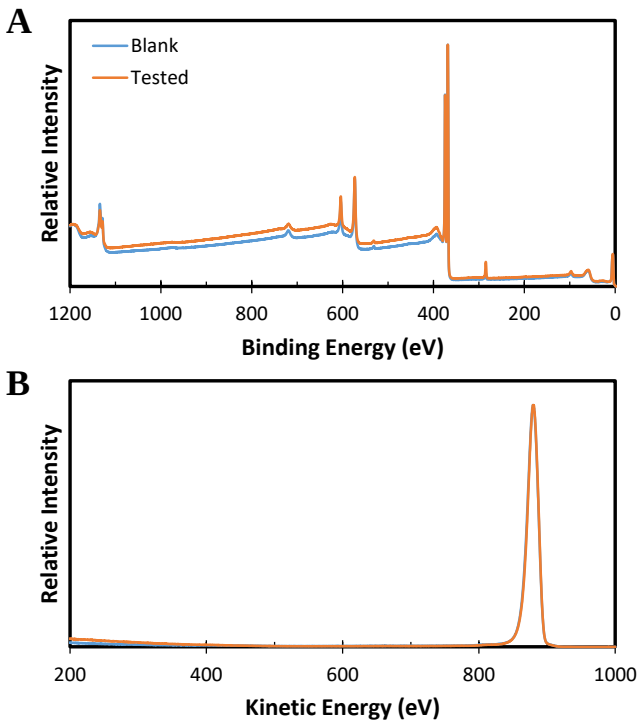

Figure S5.4 *– Analysis of a representative Ag thin film deposited on the nanoporous PTFE membrane before and after experimentation by: (A) XPS and (B) ISS.*

5.6.3 Quantifying the Uncompensated Resistance of the DEMS Cell

The uncompensated resistance of the electrochemical cell was determined by potentiostatic electrochemical impedance spectroscopy. The uncompensated resistance was found to be ~60 Ω at electrolyte flow rates of 0 to 85 mL/min when the voltage waveforms were centered at the open circuit potential, as shown in Figure S5.5A. Furthermore, the uncompensated resistance was found to be ~60 Ω when the voltage waveforms were centered at increasingly cathodic potentials using an electrolyte flow rate of 85 mL/min, as shown in Figure S5.5B.

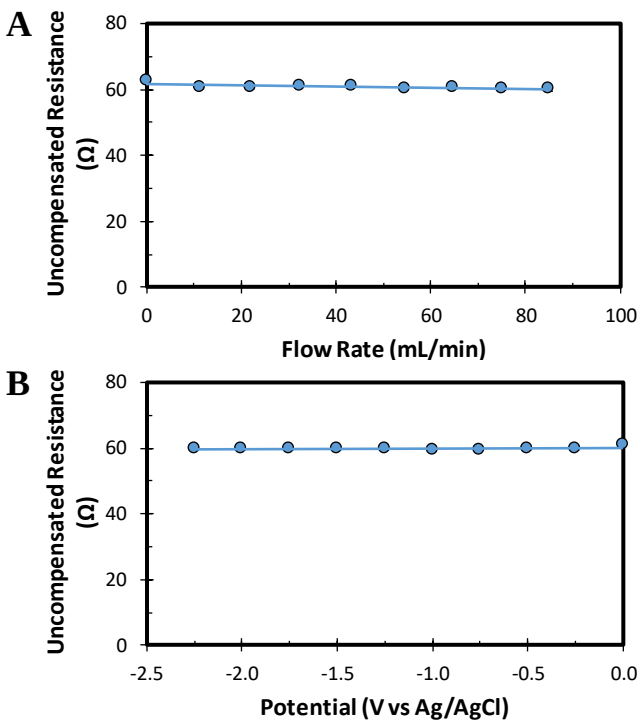

Figure S5.5 *– Uncompensated resistance of the electrochemical cell as determined using potentiostatic electrochemical impedance spectroscopy: (A) as a function of flow rate with voltage waveforms centered at the open circuit potential and (B) with voltage waveforms centered at increasingly cathodic potentials at a flow rate of 85 mL/min.*

The uncompensated resistance of the electrochemical cell was also determined using the current interrupt technique. The uncompensated resistance was found to be ~65 Ω at electrolyte flow rates of 0 to 85 mL/min when the interrupted current density was 40 mA/cm^2, as shown in Figure S5.6A. Furthermore, the uncompensated resistance was also found to be ~65 Ω when the interrupted current density was increasingly cathodic using an electrolyte flow rate of 85 mL/min, as shown in Figure S5.6B.

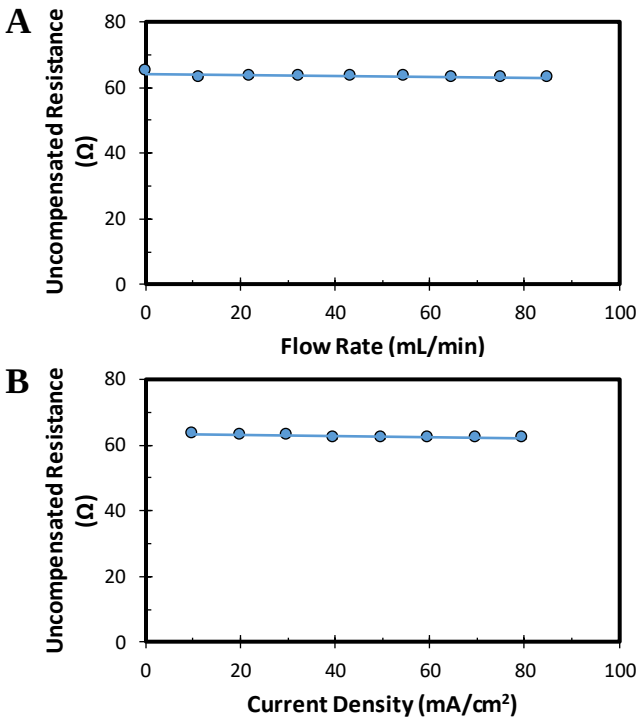

Figure S5.6 *– Uncompensated resistance of the electrochemical cell as determined using the current interrupt technique: (A) as a function of flow rate using an interrupted current density of 20 mA/cm^2 and (B) with an increasingly cathodic interrupted current density at a flow rate of 85 mL/min.*

5.6.4 Quantifying the Relative Electrochemical Surface Area of the DEMS Electrode

The roughness factor of the DEMS electrode was compared to an analogous thin film deposited on a polished Si wafer by taking the ratio of their double layer capacitances. The double layer capacitance of each electrode was determined by measuring the charging current in a potential range where no Faradaic processes occur at a series of increasingly rapid scan rates, as shown in Figure S5.7A. As shown in Figure S5.7B, the DEMS electrode had a roughness factor of ~2.9 relative to the thin film deposited on a polished Si wafer.

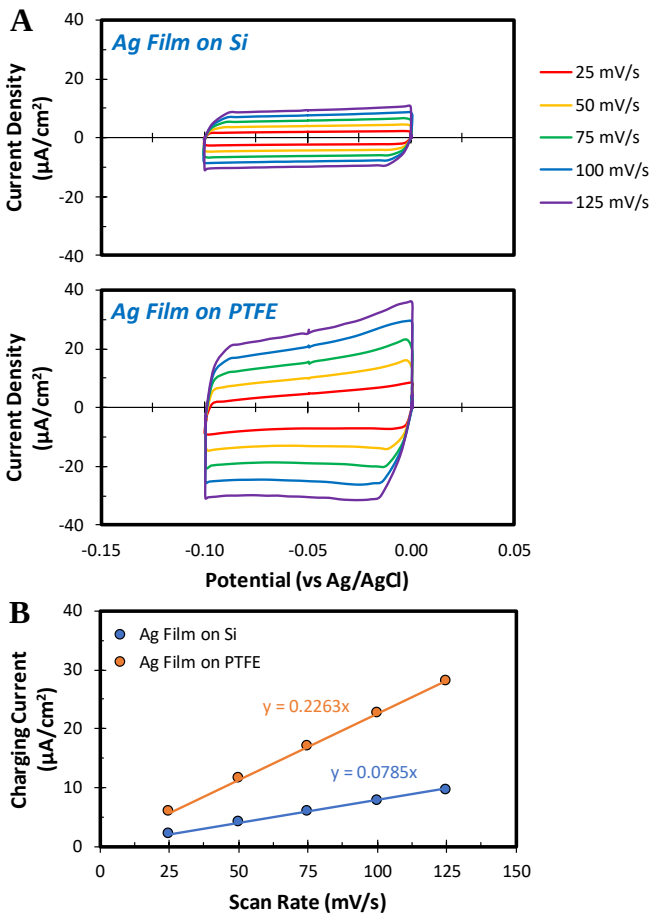

Figure S5.7 *– (A) Cyclic voltammetry in a potential range where no Faradaic processes occur at a series of increasingly rapid scan rates over Ag thin films deposited onto a polished Si wafer and the nanoporous PTFE membrane. (B) Comparison of the double layer capacitances of the Ag thin films deposited onto a polished Si wafer and the nanoporous PTFE membrane.*

5.6.5 Mass Spectra of Reactants and Products

The mass spectra of CO_2, CO, and ethene were measured by feeding a standard gas into the mass spectrometer to enable accurate deconvolution of the *m/z* = 28 mass-ion current, as shown in Figure S5.8. The mass spectra of acetaldehyde, ethanol, allyl alcohol, propionaldehyde, and n-propanol were measured by analyzing 50 mM solutions of each species to enable accurate deconvolution of the *m/z* = 31, 43, 57, 58, and 59 mass-ion currents, as shown in Figure S5.9.

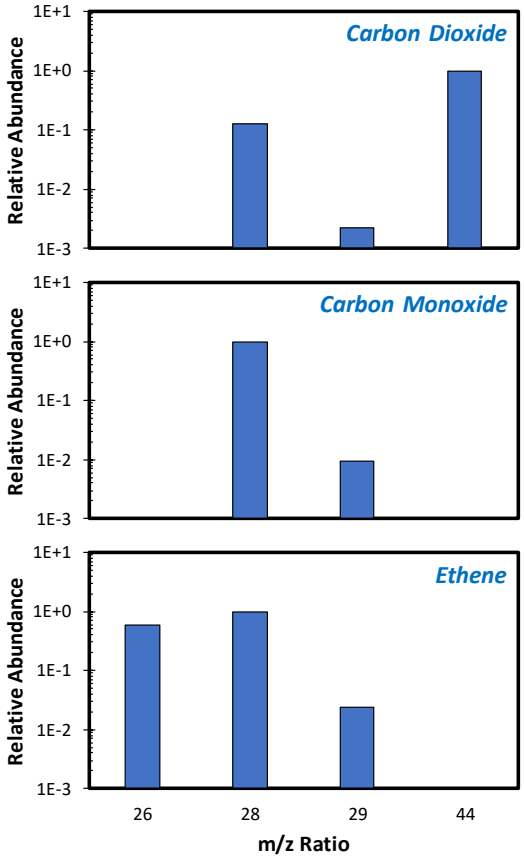

Figure S5.8 *– Mass spectra of gas phase species that produce the m/z = 28 fragment upon ionization.*

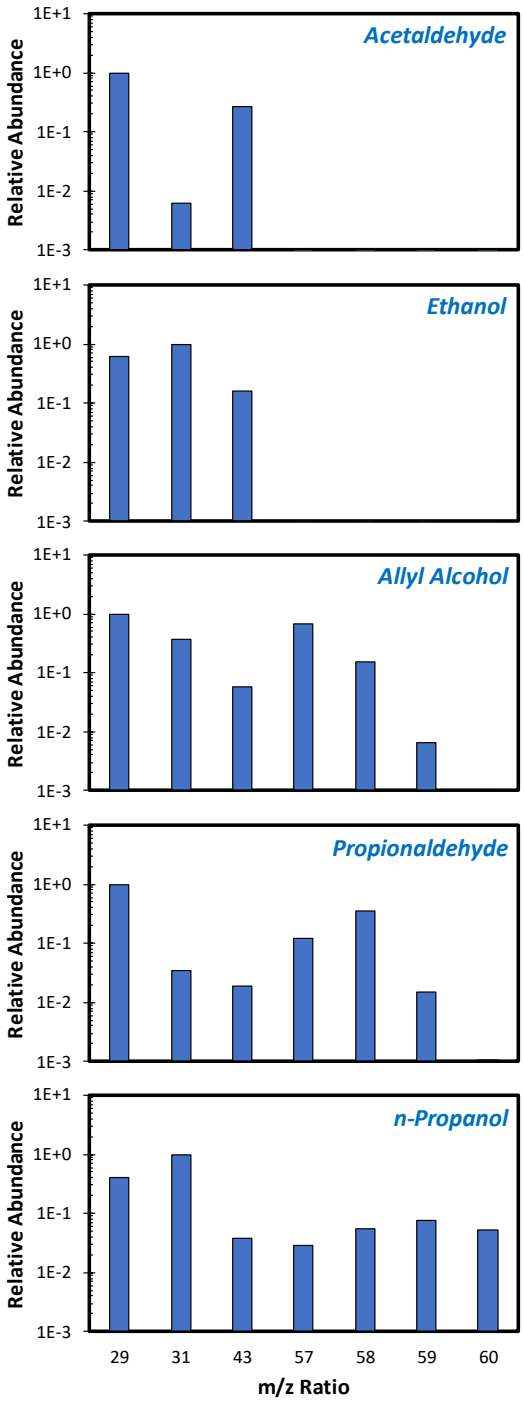

Figure S5.9 *– Mass spectra of the primary liquid phase products produced over Cu as measured by analyzing 50 mM standard solutions of each product.*

5.6.6 H_2 Calibration Procedure

The signal response of the mass spectrometer to the evolution of H_2 was calibrated by conducting a chronopotentiometry staircase from 2 to 40 mA/cm^2 with a step length of 10 s while monitoring the *m/z* = 2 mass-ion current, as shown in Figure S5.10A. As shown in Figure S5.10B, a linear correlation between the *m/z* = 2 mass-ion current signal and the total current density was observed. The chronopotentiometry staircase was repeated several times to demonstrate the reproducibility of the H_2 calibration curve, which indicates that the product collection efficiency does not vary with extended operation, as shown in Figure S5.11. Finally, the chronopotentiometry staircase was conducted at increasingly rapid electrolyte flow rates to determine the impact that electrolyte convection has on the efficiency of product collection. The collection efficiency was assumed to be 100% under stagnant electrolyte conditions. As shown in Figure S5.12, the collection efficiency was found to decrease linearly with flow rate but was still greater than 80% at the maximum flow rate employed in the study.

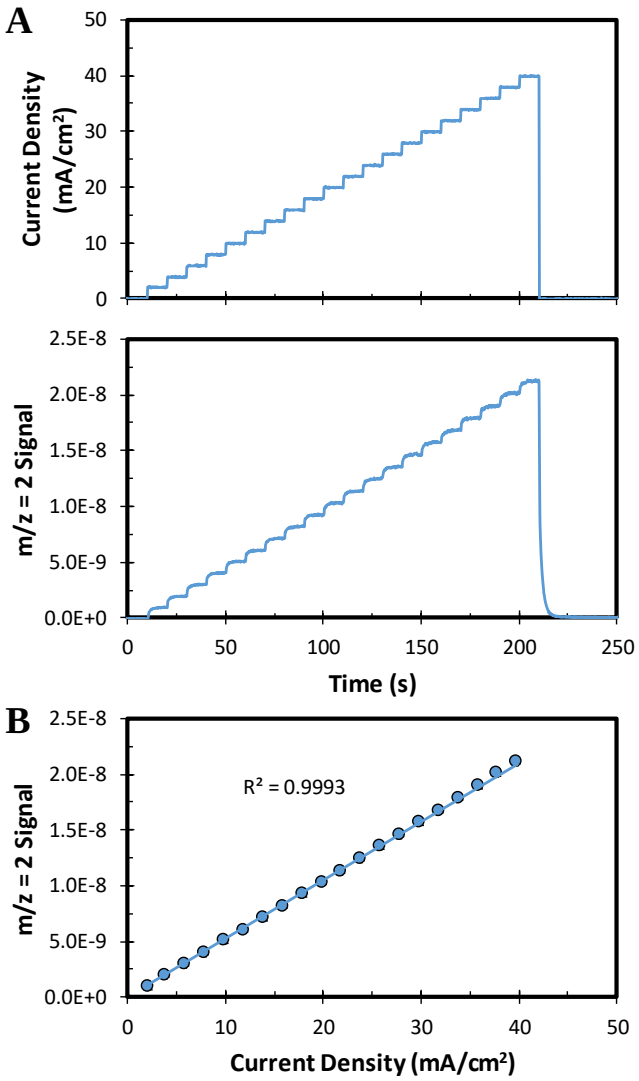

Figure S5.10 *– H_2 calibration protocol: (A) chronopotentiometry staircase. (B) H_2 calibration curve.*

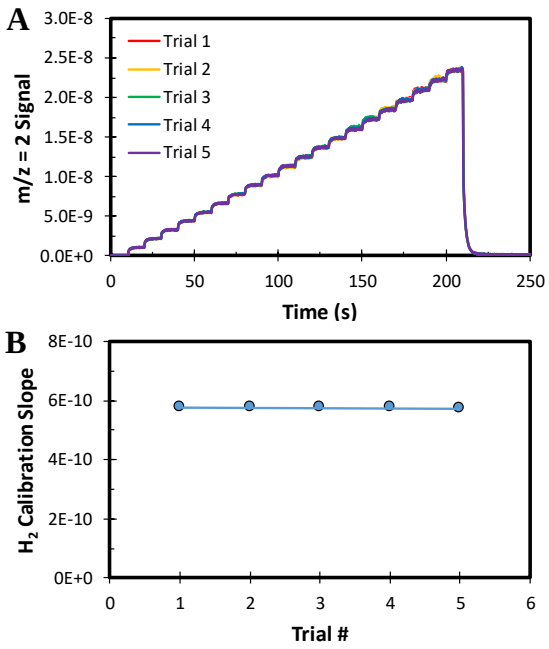

Figure S5.11 *– (A) m/z = 2 signal observed during 5 successive chronopotentiometry staircases. (B) Slope of H_2 calibration curve as a function of the trial number.*

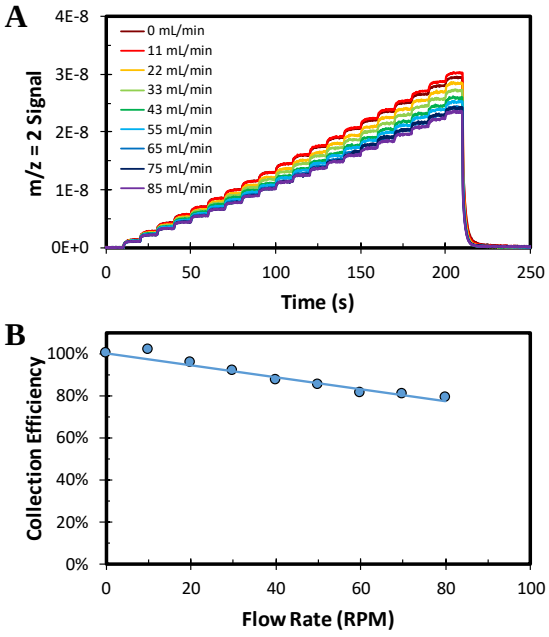

Figure S5.12 *– (A) m/z = 2 signal observed during chronopotentiometry staircases at increasingly rapid electrolyte flow rates.* (B) H_2 collection efficiency vs flow rate calculated assuming complete collection under stagnant conditions.

5.6.7 H_2 Evolution Linear Sweep Voltammetry over Ag vs Scan Rate

The total fraction of H_2 generated during linear sweep voltammetry that was detected by mass spectrometry is shown in Figure S5.13. It is apparent that the total amount of H_2 generated during the scan that is detected by mass spectrometry begins to decline slightly at scan rates faster than 50 mV/s. However, a greater fraction of this H_2 is detected after the scan ends due to the finite time associated with mass transfer from the electrode surface into the mass spectrometer. This issue was compounded by the fact that products generated at the electrode surface can either pervaporate into the mass spectrometer or diffuse into the bulk of the electrolyte, as shown in Figure S5.14. Once the scan ends and the product concentration near the electrode surface is rapidly diminished by pervaporation, causing products that diffused away from the electrode surface to diffuse back and pervaporate, causing an exponential decline in the mass-ion current signals after Faradaic charge transfer ceases. This phenomenon was only significant for H_2 because it diffuses much more rapidly into the electrolyte than other reaction products.

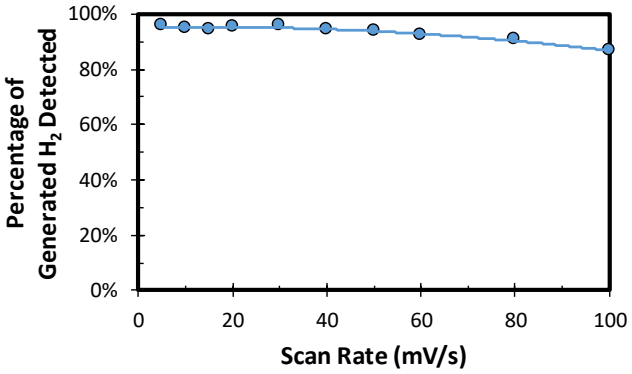

Figure S5.13 *– Total percentage of generated H_2 that is detected by mass spectrometry during linear sweep voltammetry as a function of the scan rate.*

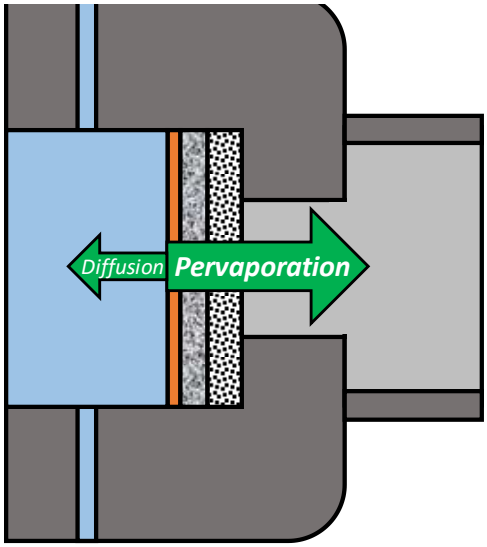

Figure S5.14 *– Directions of product flux at the surface of the DEMS electrode. Arrow sizes indicate relative magnitudes.*

5.6.8 Calculated Signal Contributions over Ag

The contributions of different species to the expected mass spectrum over Ag at an applied potential of -1 V vs RHE were calculated to determine which mass-ion currents should be monitored using:

$$Contribution\ of\ species\ i\ to\ {}^{m}/_{z} = j\ Signal = \frac{\dot{n}_i \frac{I{}^{m}/_{z=j,i}}{\sum_j I{}^{m}/_{z=j,i}}}{\sum_i \dot{n}_i \frac{I{}^{m}/_{z=j,i}}{\sum_j I{}^{m}/_{z=j,i}}}$$

Where:

$\dot{n}_i$	Flux of species i at the electrode surface (nmol/min)
$I{}^{m}/_{z=j,i}$	Relative intensity of *m/z* = j for species i

The results of this calculation are shown in Table S5.1. There is no mass-ion current that is solely produced by the ionization of CO, necessitating the contributions of CO_2 to the observed mass spectrum to be deconvoluted to obtain a mass-ion current signal that is directly proportional to the generation rate of CO.

Table S5.1 *– Calculated contributions of reactants and products to the expected mass spectrum over Ag at -1 V vs RHE.*

m/z Ratio	Primary Contributor	Calculated Contribution	Other Contributors
2	H_2	100.00%	N/A
28	CO	91.34%	CO_2 (8.66%)
44	CO_2	100.00%	N/A

5.6.9 CO Calibration Procedure

CO calibration was conducted in an analogous way as H_2 calibration, except that the mass-ion currents for *m/z* = 2, 28, and 44 were all monitored during the chronopotentiometry staircase, as shown in Figure S5.15. Furthermore, the chonopotentiometry staircase was conducted from high current density to low current density during CO calibration. This was done because the rate of CO evolution exhibited transient changes at low current density, which compromised accurate quantification. However, if high current densities were applied before the application of low current densities then the CO partial current density did not exhibit transient changes at low current density. Thus, CO calibration was accomplish using chronopotentiometry staircases from high current density to low current density to improve the accuracy of CO quantification.

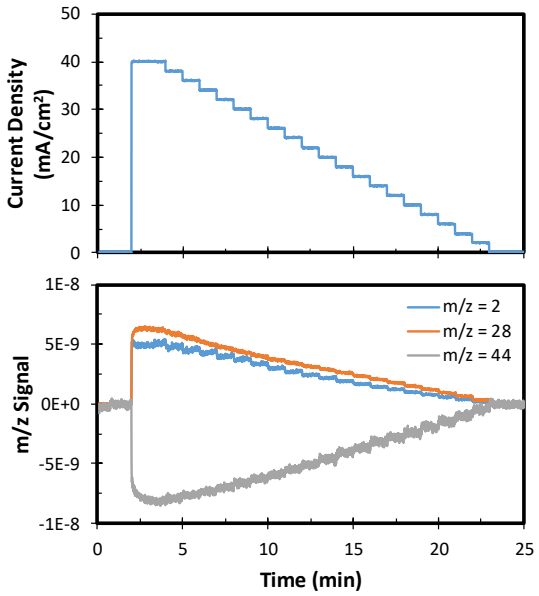

Figure S5.15 *– CO calibration chronopotentiometry staircase.*

The CO partial current density was assumed to be equivalent to the difference between the total current density and the H_2 partial current density, which was determined using the observed *m/z* = 2 mass-ion current and the H_2 calibration curve. The contribution of CO_2 to the observed *m/z* = 28 signal was accounted for using the observed *m/z* = 44 mass-ion current and the measured mass spectrum of CO_2. The results of this analysis are shown in Figure S5.16A. A linear correlation between the deconvoluted *m/z* = 28 mass-ion current signal and the calculated CO partial current density was obtained, as shown in Figure S5.16B.

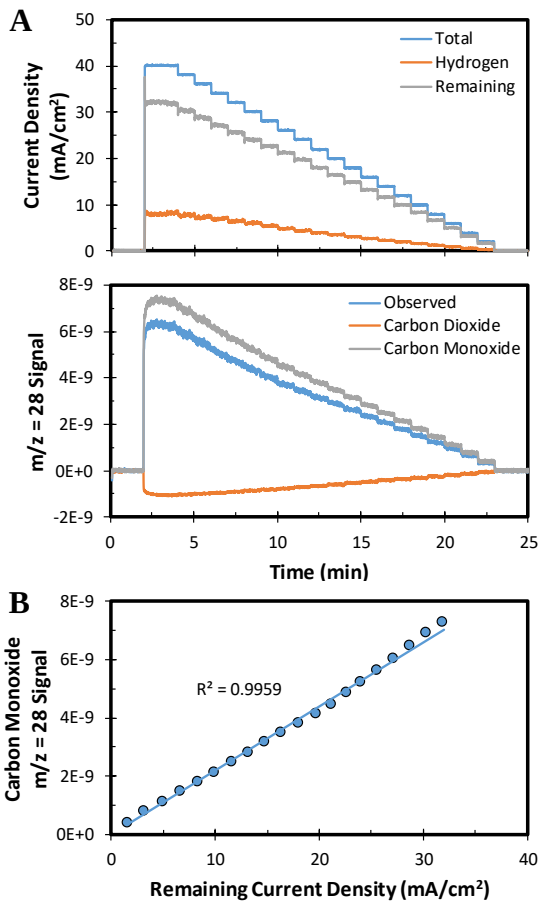

Figure S5.16 *– (A) Calculation of the CO partial current density and m/z = 28 signal due to the ionization of CO during the chronopotentiometry staircase. (B) CO calibration curve.*

5.6.10 Linear Sweep Voltammetry over Ag vs Scan Rate

Linear sweep voltammetry was conducted over Ag at different scan rates. As shown in Figure S5.17, the overall current evolved at a given potential was found to be independent of the scan rate employed. However, the H_2 partial current density decreased and the CO partial current density increased at a fixed potential as the scan rate was increased from 5 to 20 mV/s. However, the H_2 and CO partial current densities did not change further when scan rates faster than 20 mV/s were employed. These changes resulted in a reduced H_2 Faradaic efficiency and an enhanced CO Faradaic efficiency at a fixed potential as the scan rate was increased from 5 to 20 mV/s, with no additional changes for scan rates faster than 20 mV/s.

To understand the origin of these activity trends the scan rate dependence of the local CO_2 concentration was investigated. As shown in Figure S5.18, the local CO_2 concentration was found to be independent of the scan rate at a given potential, despite the differences in the rates of CO evolution for scan rates below 20 mV/s. This suggests

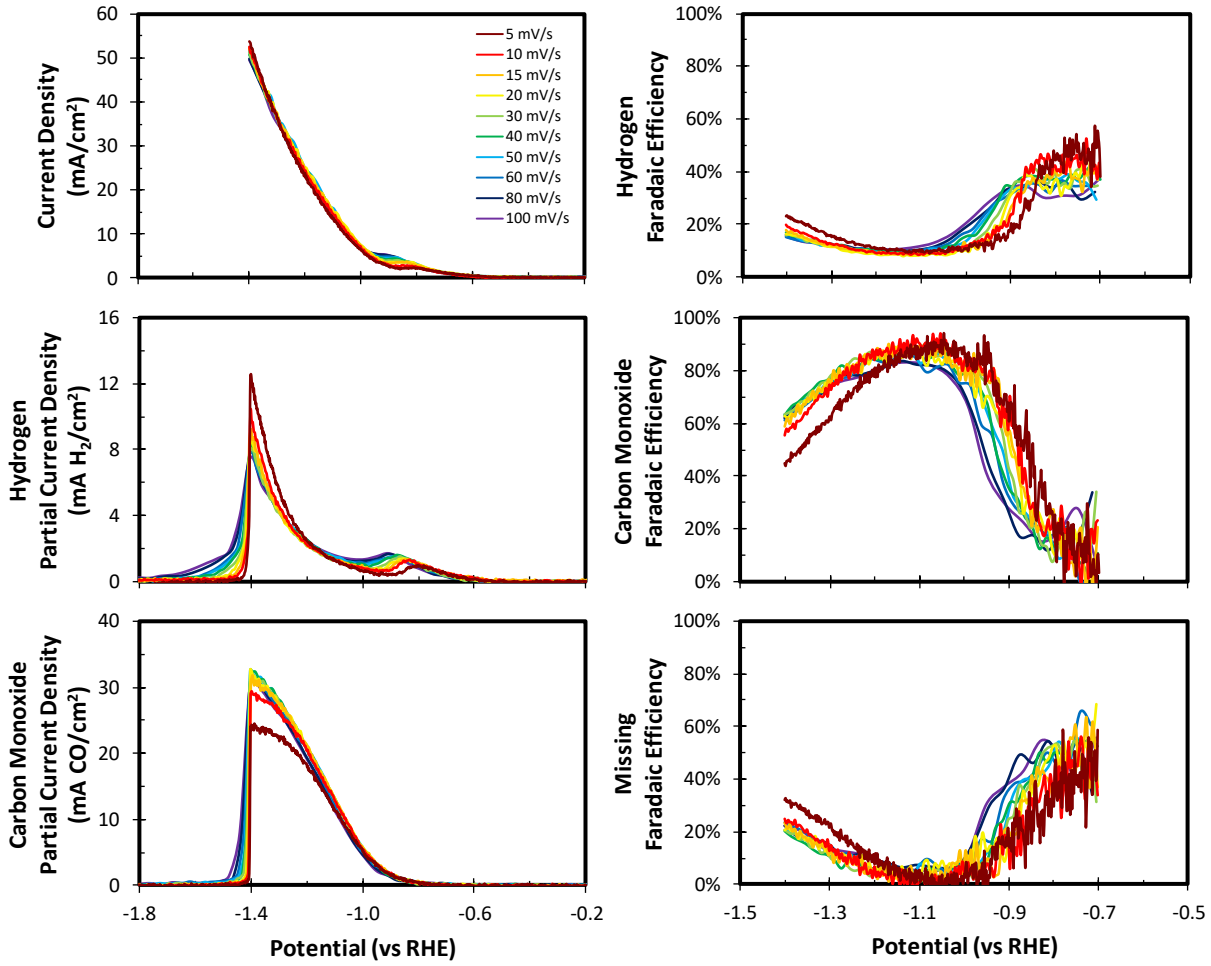

Figure S5.17 *– CO_2 reduction activity of Ag measured during linear sweep voltammetry at a series of increasingly rapid scan rates in 0.1 M $CsHCO_3$ at a flow rate of 85 mL/min.*

that there is a second mode of CO_2 depletion that is responsible for depleting a greater fraction of the local CO_2 concentration as the scan rate drops below 20 mV/s.

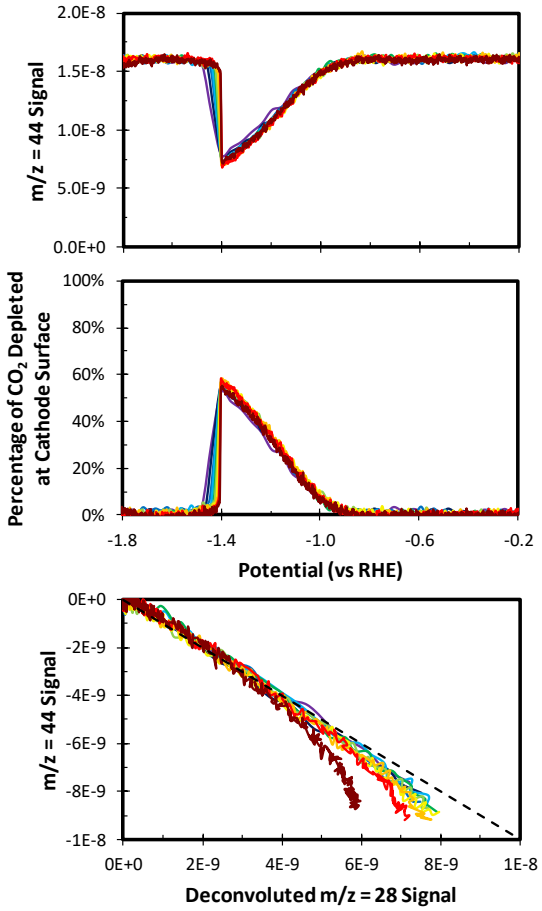

Figure S5.18 *– Local CO_2 concentration observed over Ag during linear sweep voltammetry at a series of increasingly rapid scan rates in 0.1 M $CsHCO_3$ at a flow rate of 85 mL/min.*

5.6.11 CO_2 Signal vs Flow Rate

The steady state *m/z* = 44 signal was monitored as a function of the electrolyte flow rate to determine the impact that the flow rate has on the flux of CO_2 to the cathode surface. As shown on Figure S5.19, as the electrolyte flow rate increases the rate of CO_2 supply to the cathode increases, as reflected by the increased *m/z* = 44 mass-ion current signal. This occurs because higher electrolyte flow rates result in a reduced hydrodynamic and mass transfer boundary layer thickness at the cathode surface. However, the flux of CO_2 to the cathode surface begins to plateau at electrolyte flow rates faster than 70 mL/min.

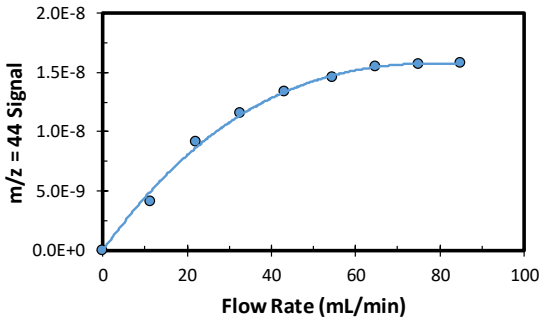

Figure S5.19 *– Dependence of the CO_2 signal (m/z = 44) on the electrolyte flow rate.*

5.6.12 Linear Sweep Voltammetry over Ag vs Flow Rate

Linear sweep voltammetry was conducted over Ag at a scan rate of 5 mV/s using different electrolyte flow rates. As shown in Figure S5.20, the overall current evolved at a given potential increased with the electrolyte flow rate. Furthermore, the H_2 partial current density decreased and the CO partial current density increased at a fixed potential as the electrolyte flow rate was increased. These changes resulted in a reduced H_2 Faradaic efficiency and an enhanced CO Faradaic efficiency at a fixed potential as the as the electrolyte flow rate was increased.

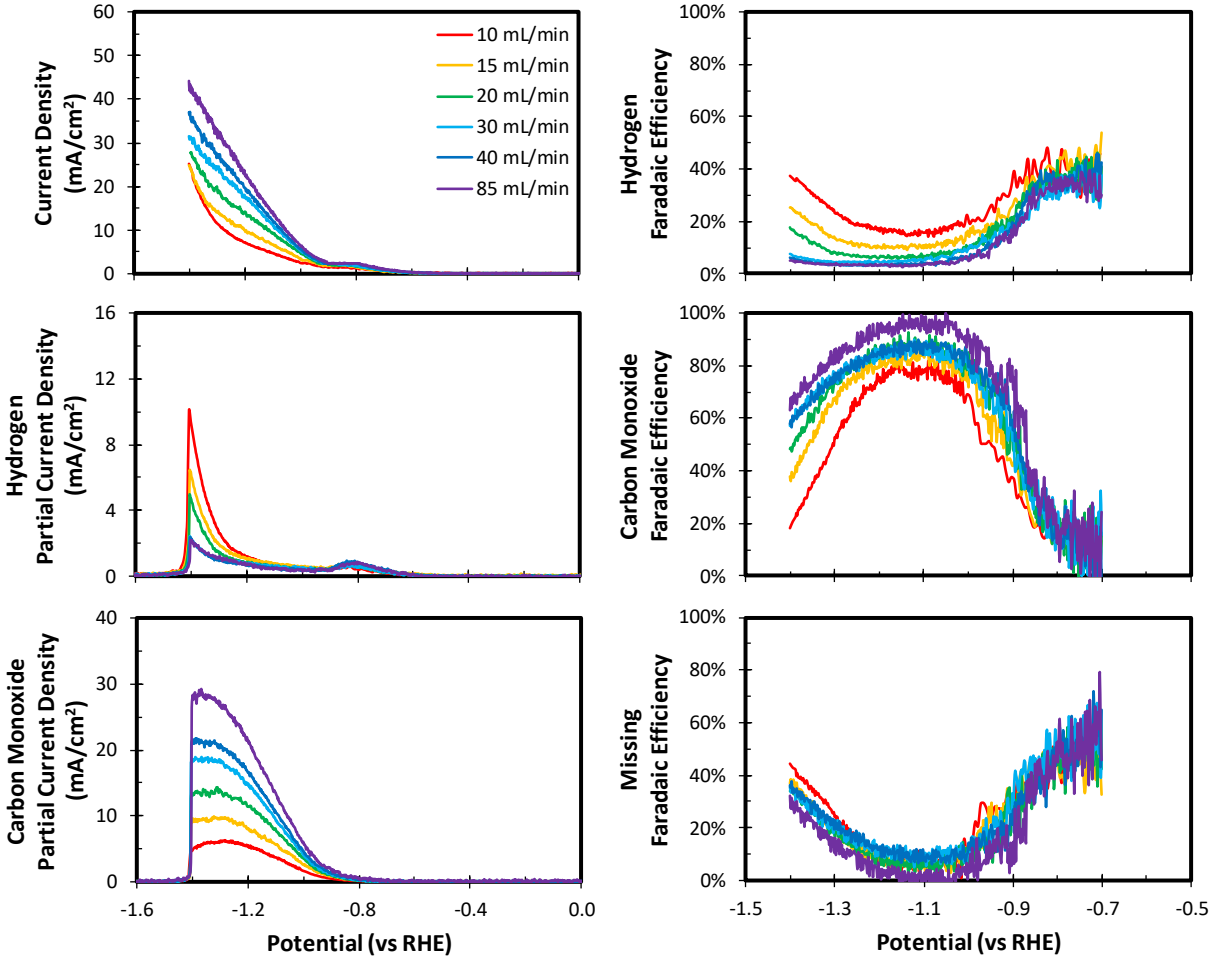

Figure S5.20 *– CO_2 reduction activity of Ag measured during linear sweep voltammetry at a scan rate of 5 mV/s in 0.1 M $CsHCO_3$ using a series of increasingly rapid electrolyte flow rates.*

To understand the origin of these activity trends the flow rate dependence of the local CO_2 concentration was investigated. As shown in Figure S5.21, as the flow rate increases the CO_2 signal increases in the absence of Faradaic current, as explained in section 5.6.11. At the terminal potential of the linear potential sweep there is also a higher concentration of CO_2 near the cathode surface, as evidenced by the increased signal with flow rate. While more CO_2 is consumed by the evolution of CO as the electrolyte flow rate increases, the fractional depletion of CO_2 at the cathode surface decreases as the electrolyte flow rate increases. This is a result of an earlier onset of CO_2 depletion by

reaction with hydroxyl anions evolved at the cathode surface as the electrolyte flow rate decreases.

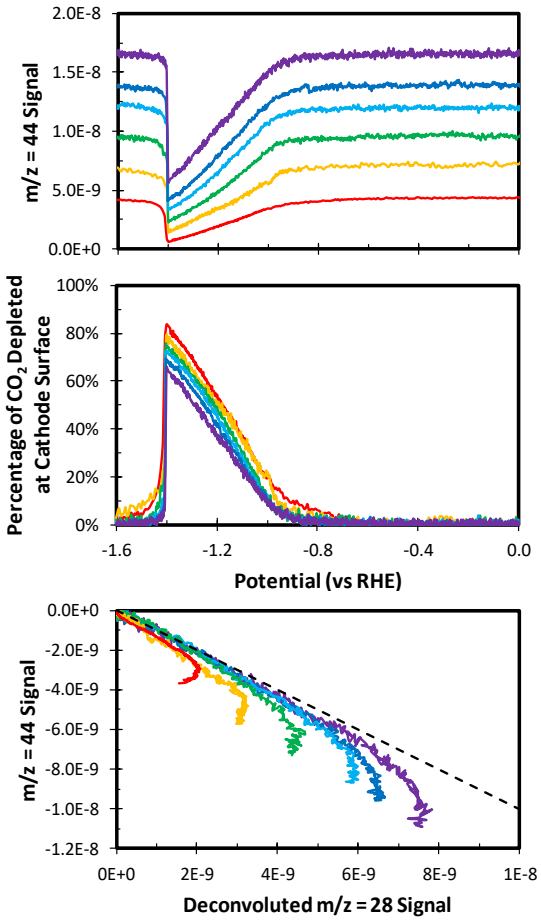

Figure S5.21 *– Local CO_2 concentration observed over Ag during linear sweep voltammetry at a scan rate of 5 mV/s in 0.1 M $CsHCO_3$ using a series of increasingly rapid electrolyte flow rates.*

5.6.13 Chronoamperometry Staircase over Ag vs CO_2 Flow Rate in an H-Cell

Chronoamperometry staircases were conducted over a polycrystalline Ag film deposited onto a polished Si wafer from -0.5 to -1.5 V vs RHE at increasingly rapid CO_2 flow rates in a traditional H-cell. The electrochemical cell was mixed only by the column of CO_2 bubbles. Thus, as the CO_2 flow rate is increased the hydrodynamic and mass transfer boundary layers at the cathode surface become narrower, improving the rate of CO_2 supply to the cathode. As a result, less H_2 and more CO are generated at a given protentional as the CO_2 flow rate is increased, as shown in Figure S5.22. This results in a reduced H_2 Faradaic efficiency and an enhanced CO Faradaic efficiency at a fixed potential as the CO_2 flow rate is increased. These trends qualitatively reproduce the trends observed in the DEMS cell at increasingly rapid electrolyte flow rates.

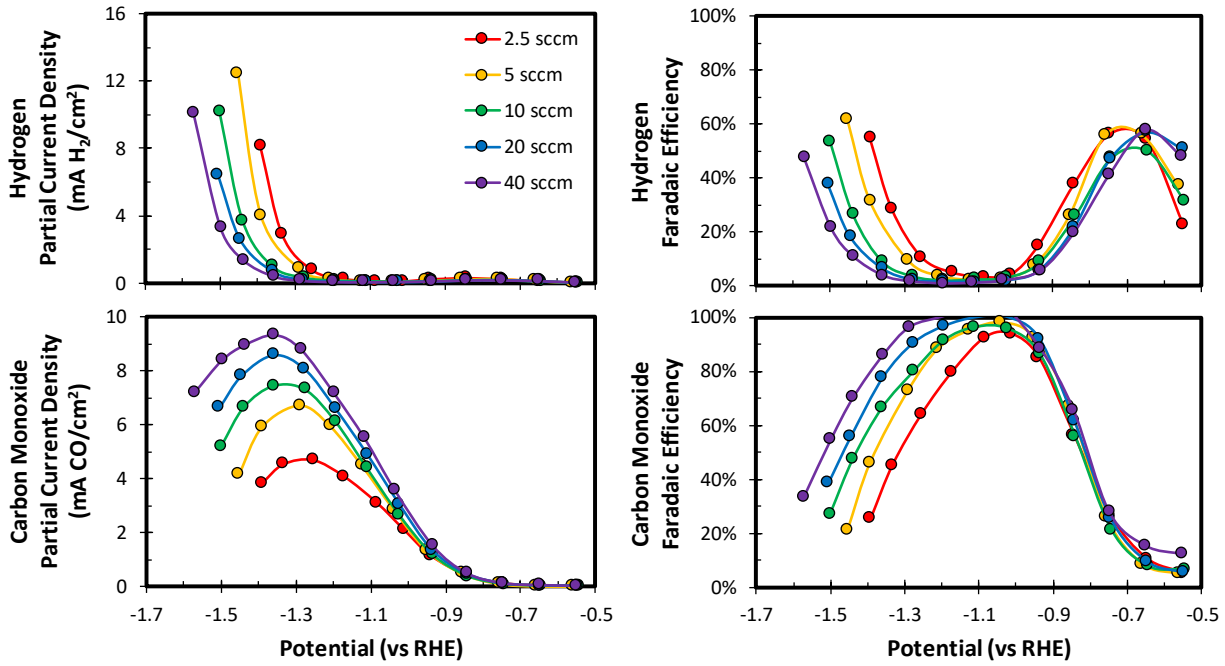

Figure S5.22 *– CO_2 reduction activity of Ag measured during a chronoamperometry staircase in a traditional H-cell in 0.1 M $CsHCO_3$ at a series of increasingly rapid CO_2 flow rates.*

5.6.14 Calculated Signal Contributions over Cu

The contributions of different species to the expected mass spectrum over Cu at an applied potential of -1.05 V vs RHE were calculated to determine which mass-ion currents should be monitored using:

$$Contribution\ of\ species\ i\ to\ {}^{m}/_{z} = j\ Signal = \frac{\dot{n}_i \frac{I{}^{m}/_{z=j,i}}{\sum_j I{}^{m}/_{z=j,i}}}{\sum_i \dot{n}_i \frac{I{}^{m}/_{z=j,i}}{\sum_j I{}^{m}/_{z=j,i}}}$$

Where:

$\dot{n}_i$ Flux of species i at the electrode surface (nmol/min)

$I{}^{m}/_{z=j,i}$ Relative intensity of m/z = j for species i

The results of this calculation are shown in Table S5.2. Carbon dioxide (*m/z* = 44), hydrogen (*m/z* = 2), methane (*m/z* = 15), and ethene (*m/z* = 26) are the only species that generate a unique mass fragment upon ionization. The deconvolution strategy for the remaining mass fragments is discussed in 5.6.15.

Table S5.2 *– Calculated contributions of reactants and products to the expected mass spectrum over Cu at -1.05 V vs RHE.*

m/z Ratio	Primary Contributor	Calculated Contribution	Other Contributors
2	H_2	99.21%	Negligible
15	CH_4	98.22%	Negligible
26	C_2H_4	93.12%	CH_3CH_2OH (5.71%)
28	CO_2	48.33%	C_2H_4 (36.05%) CO (15.22%)
31	CH_3CH_2OH	74.67%	$CH_3CH_2CH_2OH$ (23.19%) CH_2CHCH_2OH (1.97%)
43	CH_3CH_2OH	76.18%	CH_3CHO (12.83%) $CH_3CH_2CH_2OH$ (8.93%) CH_2CHCH_2OH (1.86%)
44	CO_2	99.89%	Negligible
57	CH_2CHCH_2OH	80.95%	$CH_3CH_2CH_2OH$ (11.52%) CH_3CH_2CHO (7.53%)
58	CH_3CH_2CHO	62.01%	CH_2CHCH_2OH (37.99%)
59	$CH_3CH_2CH_2OH$	94.88%	CH_3CH_2CHO (3.20%) CH_2CHCH_2OH (1.92%)

5.6.15 Deconvolution of the Mass-Ion Currents Observed over Cu

The primary C_3 products produced over Cu are allyl alcohol, propionaldehyde, and n-propanol each of which generate a series of unique mass fragments at *m/z* = 57, 58, and 59 upon ionization. As a result, the extent to which each of these products contributes to the observed mass spectrum can be calculated by solving a system of linear equations:

$$Im_{/z=58,Propion} = \frac{Im_{/z=59} - Im_{/z=58}\frac{Im_{/z=59}}{Im_{/z=58}{}_{n-PrOH}} - (Im_{/z=57} - Im_{/z=58}\frac{Im_{/z=57}}{Im_{/z=58}{}_{n-PrOH}})\frac{(\frac{Im_{/z=59}}{Im_{/z=58}{}_{Allyl}} - \frac{Im_{/z=59}}{Im_{/z=58}{}_{n-PrOH}})}{(\frac{Im_{/z=57}}{Im_{/z=58}{}_{Allyl}} - \frac{Im_{/z=57}}{Im_{/z=58}{}_{n-PrOH}})}}{(\frac{Im_{/z=59}}{Im_{/z=58}{}_{Propion}} - \frac{Im_{/z=59}}{Im_{/z=58}{}_{n-PrOH}}) - (\frac{Im_{/z=57}}{Im_{/z=58}{}_{Propion}} - \frac{Im_{/z=57}}{Im_{/z=58}{}_{n-PrOH}})\frac{(\frac{Im_{/z=59}}{Im_{/z=58}{}_{Propion}} - \frac{Im_{/z=59}}{Im_{/z=58}{}_{n-PrOH}})}{(\frac{Im_{/z=57}}{Im_{/z=58}{}_{Allyl}} - \frac{Im_{/z=57}}{Im_{/z=58}{}_{n-PrOH}})}}$$

$$Im_{/z=58,Allyl} = \frac{Im_{/z=57} - Im_{/z=58}\frac{Im_{/z=57}}{Im_{/z=58}{}_{n-PrOH}} - Im_{/z=58,Propion}(\frac{Im_{/z=57}}{Im_{/z=58}{}_{Propion}} - \frac{Im_{/z=57}}{Im_{/z=58}{}_{n-PrOH}})}{(\frac{Im_{/z=57}}{Im_{/z=58}{}_{Allyl}} - \frac{Im_{/z=57}}{Im_{/z=58}{}_{n-PrOH}})}$$

$$Im_{/z=58,n-PrOH} = Im_{/z=58} - Im_{/z=58,Propion} - Im_{/z=58,Allyl}$$

Where:

$Im_{/z=j}$	Mass-ion current signal for *m/z* = j
$Im_{/z=j,i}$	Mass-ion current signal for *m/z* = j corresponding to product i
$\frac{Im_{/z=j}}{Im_{/z=k}{}_{Product\ i}}$	Intensity of *m/z* = j signal relative to *m/z* = k signal for product i

Once the contributions of the C_3 products to *m/z* = 58 have been analytically calculated their contribution to the other observed mass-ion currents can be calculated using:

$$Im_{/z=j,i} = Im_{/z=k,i}\frac{Im_{/z=j}}{Im_{/z=k}{}_{Product\ i}}$$

Acetaldehyde and ethanol produce a series of mass fragments upon ionization at *m/z* = 31 and 43 that are also unique once the contributions of the C_3 products have been accounted for. Thus, the contributions of acetaldehyde and ethanol to the observed mass spectrum can also be calculated by solving another system of linear equations:

$$Im_{/z=43,Remaining} = Im_{/z=43} - Im_{/z=43,Allyl} - Im_{/z=43,Propion} - Im_{/z=43,n-PrOH}$$

$$Im_{/z=43,Me-CHO} = \frac{Im_{/z=31,Remaining} - Im_{/z=43,Remaining}\frac{Im_{/z=31}}{Im_{/z=43}{}_{EtOH}}}{\left(\frac{Im_{/z=31}}{Im_{/z=43}{}_{Me-CHO}} - \frac{Im_{/z=31}}{Im_{/z=43}{}_{EtOH}}\right)}$$

$$Im_{/z=43,EtOH} = Im_{/z=43,Remaining} - Im_{/z=43,Me-CHO}$$

The results of this deconvolution protocol are shown in Figure S5.23, which displays the observed mass-ion currents for m/z = 31, 43, 57, 58, and 59 along with the calculated percent that acetaldehyde, ethanol, allyl alcohol, propionaldehyde, and n-propanol are contributing to each signal.

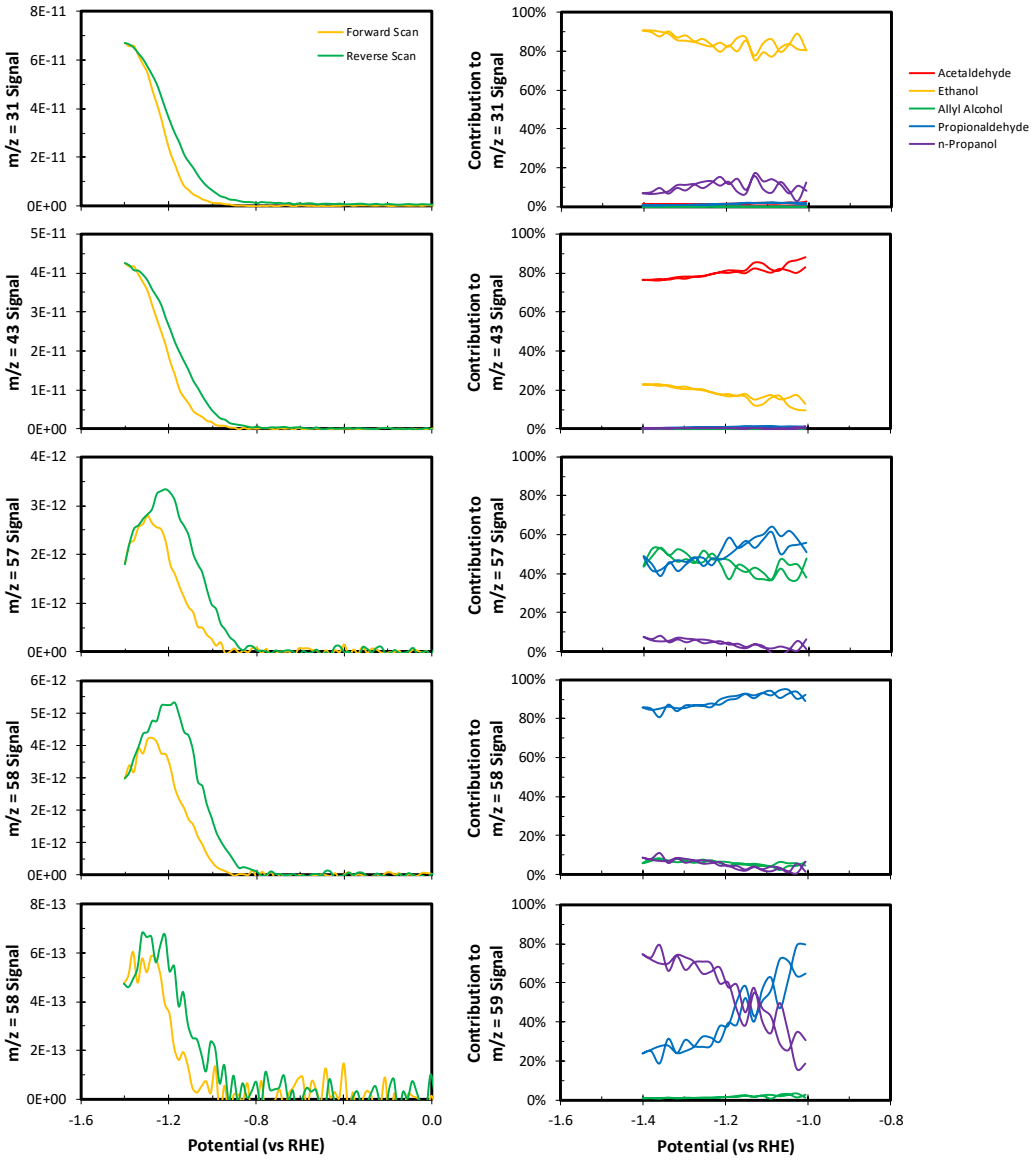

Figure S5.23 *– Deconvolution of the m/z = 31, 43, 57, 58, and 59 mass-ion current signals observed over Cu during cyclic voltammetry at a scan rate of 1 mV/s in 0.1 M $CsHCO_3$ at a flow rate of 85 mL/min.*

5.6.16 Transient Ethene Generation Rate Before and After Cathodic Polarization

The transient activity of Cu for producing ethene (*m/z* = 26) was monitored at -1 V vs RHE before and after a brief cathodic polarization at -1.4 V vs RHE. As shown in Figure S5.24, the ethene partial current density was elevated after the brief cathodic polarization took ~5 min to decay back to the initial value. This suggests that the prior history of Cu can influence its transient activity for several minutes until steady state activity is reached.

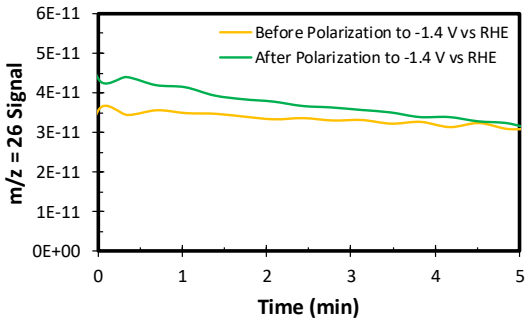

Figure S5.24 *– Transient ethene (m/z = 26) generation rate over Cu at an applied potential of -1 V vs RHE before and after a brief cathodic polarization to -1.4 V vs RHE in 0.1 M $CsHCO_3$ at a flow rate of 85 mL/min.*

5.6.17 Analysis of the Pervaporate Collected over Cu by Liquid Chromatography

The relative abundance of the multi-carbon liquid-phase products produced over Cu as measured in a traditional H-cell using HPLC, the DEMS cell using MS, and the condensed DEMS cell pervaporate using HPLC are shown in Table S5.3. This data was utilized to calculate the molar ratio of aldehydes to the corresponding alcohols observed in each case. As shown in Table S5.4, the pervaporate of the DEMS cell had a higher abundance of aldehydes relative to alcohols when quantified by mass spectrometry or when condensed and analyzed by liquid chromatography. The aldehyde to alcohol ratio of the DEMS cell pervaporate was lower when condensed and quantified by HPLC than when quantified by MS, presumably due to the loss of aldehydes by evaporation when collecting the condensed pervaporate. This hypothesis is corroborated by the greater discrepancy of the aldehyde to alcohol ratio of the DEMS cell pervaporate as quantified by MS and HPLC for the C_2 products than the C_3 products, which occurs due to the higher volatility of acetaldehyde than propionaldehyde.

Table S5.3 *– Relative abundance of the liquid-phase products produced over Cu as measured in a traditional H-cell via HPLC, the DEMS cell pervaporate by MS, and the condensed DEMS cell pervaporate by HPLC.*

	H-Cell	DEMS	Condensed Pervaporate
Acetaldehyde	4.04%	61.85%	37.02%
Ethanol	71.75%	28.04%	59.65%
Allyl Alcohol	5.97%	1.72%	0.06%
Propionaldehyde	2.74%	5.86%	1.63%
n-Propanol	15.50%	2.53%	1.64%

Table S5.4 *– Abundance of aldehydes relative to the corresponding alcohols observed over Cu as measured in a traditional H-cell via HPLC, the DEMS cell pervaporate by MS, and the condensed DEMS cell pervaporate by HPLC.*

	H-Cell	DEMS	Condensed Pervaporate
Acetaldehyde/Ethanol	0.056	2.200	0.621
Propionaldehyde/n-Propanol	0.177	2.300	0.993

Chapter 6

Electrochemical Reduction of Carbon Dioxide over Compressively Strained CuAg Surface Alloys with Enhanced Multi-Carbon Oxygenate Selectivity

Adapted from:
Clark, E. L.; Hahn. C.; Jaramillo, T. F.; Bell, A. T. *J. Am. Chem. Soc.* **2017**, 139, 15848-15857.

Abstract

The electrochemical reduction of carbon dioxide using renewably generated electricity offers a potential means for producing fuels and chemicals in a sustainable manner. To date, copper has been found to be the most effective catalyst for electrochemically reducing carbon dioxide to products such as methane, ethene, and ethanol. Unfortunately, the current efficiency of the process is limited by competition with the relatively facile hydrogen evolution reaction. Since multi-carbon products are more valuable precursors to chemicals and fuels than methane, there is considerable interest in modifying copper to enhance the multi-carbon product selectivity. Here, we report our investigations of electrochemical carbon dioxide reduction over CuAg bimetallic electrodes and surface alloys, which we find to be more selective for the formation of multi-carbon products than pure Cu. This selectivity enhancement is a result of the selective suppression of hydrogen evolution, which occurs due to compressive strain induced by the formation of a CuAg surface alloy. Furthermore, we report that these bimetallic electrocatalysts exhibit an unusually high selectivity for the formation of multi-carbon carbonyl-containing products, which we hypothesize to be the consequence of a reduced coverage of adsorbed hydrogen and the reduced oxophilicity of the compressively strained Cu. Thus, we show that promoting Cu surface with small amounts of Ag is a promising means for improving the selectivity of Cu to multi-carbon oxygenated products formed by the CO_2RR.

6.1 Introduction

Carbon dioxide (CO_2) is a potential source of renewable carbon for the production of fuels and chemicals. For this process to be sustainable, the hydrogen required for CO_2

reduction must be derived from water and the necessary energy must be supplied by a renewable source, such as solar radiation. One approach to this goal is utilization of electrical energy generated by photovoltaics to drive the electrochemical CO_2 reduction reaction (CO_2RR).[1–3] Previous research has shown that the overall rate of the CO_2RR and the distribution of products formed depend primarily on the electrocatalyst used as the cathode. Copper (Cu) is the only monometallic electrocatalyst capable of reducing CO_2 into potential fuels or multi-carbon chemicals with a total Faradaic efficiency (FE) in excess of 1%.[4,5] Experimental and theoretical studies have demonstrated that carbon monoxide (CO) reduction is the overpotential-determining step in the reduction of CO_2 to hydrocarbons and alcohols over Cu.[6–11] The principal products formed by the reduction of CO are methane (CH_4), ethene (C_2H_4), and ethanol (C_2H_5OH).[7,12] However, a variety of other multi-carbon alcohols, aldehydes, and carboxylic acids are also produced, albeit in trace quantities.[7,12] Since multi-carbon products are more valuable precursors to chemicals and fuels than CH_4, there is considerable interest in modifying Cu to enhance the multi-carbon product selectivity (see 6.6.1). Unfortunately, the FE of multi-carbon product generation over Cu is limited by parasitic loss of total current density to the relatively facile hydrogen evolution reaction (HER). Thus, recent studies have focused on suppressing HER and enhancing the multi-carbon product selectivity. These studies have revealed that the applied potential,[7,12,13] surface morphology,[14–18] cation identity,[19–21] and buffer concentration[22–24] influence the product distribution obtained over Cu. While alloying is another means for tuning the product distribution,[25] no multi-metallic electrocatalyst has been discovered with a multi-carbon product selectivity superior to pure Cu.[26–29] In fact, it has been shown that the multi-carbon product selectivity observed over Cu-based alloys decreases systematically with the Cu content, suggesting that neighboring Cu atom ensembles are required for efficient C-C coupling.[29]

Under the conditions of CO_2RR a substantial portion of the Cu surface is covered by adsorbed CO, which suppresses HER by both reducing the effective number of electrocatalytically active surface sites and by weakening the H adsorption energy of the remaining open sites.[7,30–32] As a result, the surface coverage of CO influences the rate of HER as well as the distribution of products derived from CO, with higher CO coverages presumably inhibiting HER and enhancing the multi-carbon product selectivity. Consistent with this interpretation, the ratio of CH_4 to C_2H_4 has been observed to scale directly with the FE for H_2.[22,33,34] At potentials cathodic of -1 V vs RHE the FEs for H_2 and CH_4 increase rapidly at the expense of C_{2+} products over Cu.[12] The onset potential of this selectivity shift corresponds to the potential at which Cu reduces nearly all of the CO that it produces into hydrocarbons or alcohols (see 6.6.2), suggesting that this selectivity shift is caused by a reduced coverage of adsorbed CO. Thus, we hypothesized that supplying additional CO to Cu by co-locating domains of Cu with those of a CO-generating metal would enhance the C_{2+} products selectivity because the elevated CO concentration in the vicinity of the cathode will result in a higher steady-state coverage adsorbed on Cu (see 6.6.3).[35] To this end, we identified the Cu-Ag system as the optimal bimetallic system to probe this hypothesis because Ag produces more CO than Cu at a given potential and because Cu and Ag are virtually immiscible in the bulk at all compositions at room temperature (see 6.6.4).[36,37] As a result, effects of alloying should minimally impact the steady state electrocatalytic activity of this bimetallic system.

In the balance of this paper, we report the results of our investigation of CO_2RR over CuAg bimetallic electrodes and surface alloys. While we have observed evidence of synergy between Cu and Ag, the data do not support our original hypothesis that this is a result of CO spillover. Instead, we have discovered that Ag promotes the Cu surface by the formation of a CuAg surface alloy that induces compressive strain in the Cu surface atoms. The compressive strain in the Cu surface results in an observable shift in the valence band structure of Cu to deeper levels. This modification weakens the adsorption energy of H, resulting in a 60-75% reduction in the HER activity of Cu during CO_2RR. Interestingly, the inhibition of HER does not impact the ability of Cu to produce products derived from CO, leading to a 10-15% boost in the total FE for C_{2+} products. Furthermore, the distribution of products derived from CO changes in favor of multi-carbon carbonyl-containing products at the expense of hydrocarbons. This product selectivity modification is attributed to reduced rates of C-O bond scission resulting from the suppression of HER and the reduced oxophilicity of the compressively strained Cu, which presumably inhibits the ability of Cu to reduce these carbonyl-containing intermediate products further.

6.2 Experimental

6.2.1 Electrode Preparation

All CuAg bimetallic electrodes were prepared by melting physical mixtures of Cu (99.999%) and Ag (99.999%) in the desired atomic ratios under Ar in a vacuum arc furnace. The molten mixtures were rapidly quenched in deionized (DI) water and cold-rolled into foils. The bimetallic foils were then polished with a series of sandpapers (600, 1200, and 2500 grit 3M) and sonicated in DI water for 30 min before any characterization or electrochemical testing was performed.

Cu(100) thin films were prepared using an AJA ATC Orion-5 magnetron sputtering system. Polished Si(100) wafers (1-10 Ω*cm Virginia Semiconductor) were utilized as substrates and were etched immediately before deposition using 10 wt. % HF.[38,39] Cu (99.999% Kurt J. Lesker) was then sputtered onto the etched wafers at a rate of 1 Å/s to a thickness of 100 nm under Ar. The Cu films were then exposed to a deaerated solution of $AgNO_3$ at 50°C for 5 min in order to galvanically exchange Ag into the Cu surface. The surface Ag content was controlled by adjusting the $AgNO_3$ concentration in the galvanic exchange solution.

6.2.2 Electrode Characterization

The crystal structure of the bimetallic electrodes and epitaxial Cu films was analyzed with a Rigaku Smartlab x-ray diffractometer (XRD) using Cu Kα radiation (40 kV, 40 mA). The diffractometer was equipped with parallel beam optics and a 0.5° parallel slit analyzer in order to mitigate measurement errors arising from the surface curvature of the bimetallic foils. The bulk crystal structure was analyzed by conducting symmetric measurements while the near-surface crystal structure was analyzed by conducting asymmetric measurements with the incident radiation beam fixed at a grazing angle of 0.5°. The compositions of the observed phases were calculated using Vegard's law and

their average crystallite sizes were calculated using the Scherrer equation. The orientation of the Cu crystallites with respect to the Si substrate were determined by conducting symmetric in-plane φ scans at the Bragg reflections corresponding to both Si(111) and Cu(111). The degree of preferred orientation in the epitaxial Cu thin films was determined by conducting symmetric out-of-plane Ω scans, or rocking curves, at the Bragg condition corresponding to Cu(200).

The bulk composition of the bimetallic electrodes was measured using an FEI Quanta FEG 250 scanning electron microscope (SEM) equipped with a Bruker Quantax energy dispersive spectrometer (EDS). Elemental quantification was conducted by measuring the x-ray emission from the Cu K and the Ag L levels upon excitation by an electron beam (15 kV). Each electrode was analyzed at 10 distinct positions in order to assess the spatial uniformity of the measured bulk composition. The standard deviation of the measured bulk composition was found to be <1 at. % for all bimetallic electrodes, indicating that they are compositionally uniform at the micron length scale.

The near-surface composition and valence band structure of the bimetallic electrodes and surface alloys were measured using a Kratos Axis Ultra DLD x-ray photoelectron spectrometer (XPS). All spectra were acquired using monochromatized Al Kα radiation (15 kV, 15 mA). Ar sputtering of the sample surface was avoided in order to prevent surface composition changes resulting from the nonequivalent sputtering rates of Cu and Ag unless explicitly stated otherwise. Where applicable, Ar sputtering of the sample surface was conducted using a focused Ar ion beam (5 kV). The kinetic energy scale of the measured core level spectra was calibrated by setting the C 1s binding energy to 284.8 eV. Elemental quantification was conducted by measuring the photoelectron emission from the Cu 2p and Ag 3d orbitals using a Shirley background and normalizing their integrated areas by an internally calibrated relative sensitivity factor. The Cu 2p spectral features were fit to three individual components (Cu^0, Cu^{1+}, and Cu^{2+}) using the CasaXPS software. The kinetic energy scale of the measured valence band spectra was calibrated by setting the maximum rate of signal loss to 0 eV. Angle-resolved XPS (ARXPS) was conducted by measuring photoelectrons ejected at an angle of 30° from the sample surface, which results in twice the surface sensitivity compared to photoelectrons collected normal to the sample surface. The surface composition of the bimetallic electrodes and surface alloys were measured by ion scattering spectroscopy (ISS) using the same instrument. All ISS spectra were acquired using a focused He ion beam (1 kV). Elemental quantification was conducted by integrating the Cu and Ag spectral features using a linear background and normalizing their integrated areas by an internally calibrated relative sensitivity factor.

6.2.3 Electrochemistry

All electrochemical measurements were conducted in a custom gas-tight electrochemical cell machined from PEEK.[40] The cell was sonicated in 20 wt. % nitric acid and thoroughly rinsed with DI water prior to all experimentation. The working and counter electrodes were parallel and separated by an anion-conducting membrane (Selemion AMV AGC Inc.). Gas dispersion frits were incorporated into both electrode chambers in

order to provide ample electrolyte mixing. The exposed geometric surface area of each electrode was 1 cm^2 and the electrolyte volume of each electrode chamber was 1.8 mL. The counter electrode was a glassy carbon plate (Type 2 Alfa Aesar) that was also sonicated in 20 wt. % nitric acid prior to all experimentation. Platinum was not used as the anode due to the possibility of contaminating the cathode.[41] The working electrode potential was referenced against a Ag/AgCl electrode (Innovative Instruments Inc.) that was calibrated against a homemade standard hydrogen electrode. A 0.05 M Cs_2CO_3 (99.995% Sigma Aldrich) solution prepared using 18.2 MΩ DI water was used as the electrolyte. This electrolyte was selected because it has been shown to enhance the C_{2+} product selectivity obtained over polycrystalline Cu.[19–21] Metallic impurities in the as-prepared electrolyte were removed before electrolysis by chelating them with Chelex 100 (Na form Sigma Aldrich).[42] Both electrode chambers were sparged with CO_2 (99.999% Praxair Inc.) at a rate of 5 sccm for 30 min prior to and throughout the duration of all electrochemical measurements. Upon saturation with CO_2 the pH of the electrolyte was 6.8, which was maintained throughout the duration of chronoamperometry.

Electrochemistry was performed using a Biologic VSP-300 potentiostat. All electrochemical measurements were recorded versus the reference electrode and converted to the RHE scale. Potentiostatic electrochemical impedance spectroscopy (PEIS) was used to determine the uncompensated resistance (R_u) of the electrochemical cell by applying voltage waveforms about the open circuit potential with an amplitude of 20 mV and frequencies ranging from 50 Hz to 500 kHz (see 6.6.5). The potentiostat compensated for 85% of R_u *in-situ* and the last 15% was post-corrected to arrive at accurate potentials. The redox properties of the bimetallic electrodes were assessed by performing cycling voltammetry from -0.3 to +1.1 V vs RHE at a scan rate of 10 mV/s until a stable voltammogram was obtained, which occurred in less than 10 cycles. The electrocatalytic activity of each bimetallic electrode and surface alloy was assessed by conducting chronoamperometry at -1.05 and -1.00 V vs RHE, respectively, for 70 min. Each electrode was tested at least three times in order to ensure the statistical relevance of the observed trends.

6.2.4 Product Analysis

The effluent from the electrochemical cell was introduced directly into the sampling loop of an Agilent 7890B gas chromatograph (GC) equipped with a pulsed-discharge helium ionization detector (PDHID). The effluent was sampled after the first 10 min of chronoamperometry and every 14 min thereafter. The constituents of the gaseous sample were separated in He (99.9999% Praxair Inc.) using a Hayesep-Q capillary column (Agilent) in series with a packed ShinCarbon ST column (Restek Co.). After sampling the reaction effluent the column oven was maintained at 50 °C for 1 min followed by a temperature ramp at 30 °C/min to 250 °C, which was maintained for the duration of the analysis. The signal response of the PDHID was calibrated by analyzing a series of NIST-traceable standard gas mixtures (Airgas Inc.) (see 6.6.6).

The electrolyte from both electrode chambers was collected after electrolysis and analyzed using a Thermo Scientific UltiMate 3000 liquid chromatograph (HPLC) equipped

with a refractive index detector (RID). The electrolyte samples were stored in a refrigerated autosampler until analyzed in order to minimize the evaporation of volatile liquid-phase reaction products. The liquid-phase products contained in a 10 μL aliquot were separated using a series of two Aminex HPX 87-H columns (Bio-Rad Inc.) and a 1 mM sulfuric acid eluent (99.999% Sigma Aldrich). The column oven was maintained at 60 °C for the duration of the analysis. The signal response of the RID was calibrated by analyzing standard solutions of each product at a concentration of 1, 10, and 50 mM (see 6.6.7).

6.3 Results and Discussion

6.3.1 Characterization of the As-Prepared Bimetallic Electrodes

XRD and GIXRD measurements were carried out to determine the bulk and near-surface crystal structures, respectively, of the bimetallic electrodes (see 6.6.8 and 6.6.9). Figure 6.1 shows the asymmetric GIXRD patterns of the bimetallic electrodes. The presence of diffraction peaks associated with Cu-rich and Ag-rich phases and the absence of any diffraction peaks associated with a substantially alloyed CuAg phase confirms the complete phase-segregated nature of the electrodes. Furthermore, the minimal shift of the Cu and Ag diffraction peak positions indicates that the Cu and Ag phases have undergone minimal alloying (<3 at. % on average as calculated by Vegard's law). The near-surface Cu and Ag crystallites were calculated to be 10-15 nm in size and were observed to be preferentially oriented in the (111) direction, despite that GIXRD does not probe lattice planes parallel to the electrode surface. Moreover, the relative intensities of the Cu and Ag diffraction peaks in the near-surface region were found to be independent of the bulk composition (see 6.6.10).

The bulk compositions of the as-prepared bimetallic electrodes were quantified by EDS (see 6.6.11), the near-surface compositions were quantified by XPS (see 6.6.12), and the surface compositions were quantified by ISS (see 6.6.13). Both XPS and ISS yielded results that were completely consistent with EDS, as shown in Figure 6.2A. Thus, the average composition of the as-prepared bimetallic electrodes was determined to be independent of depth from the surface.

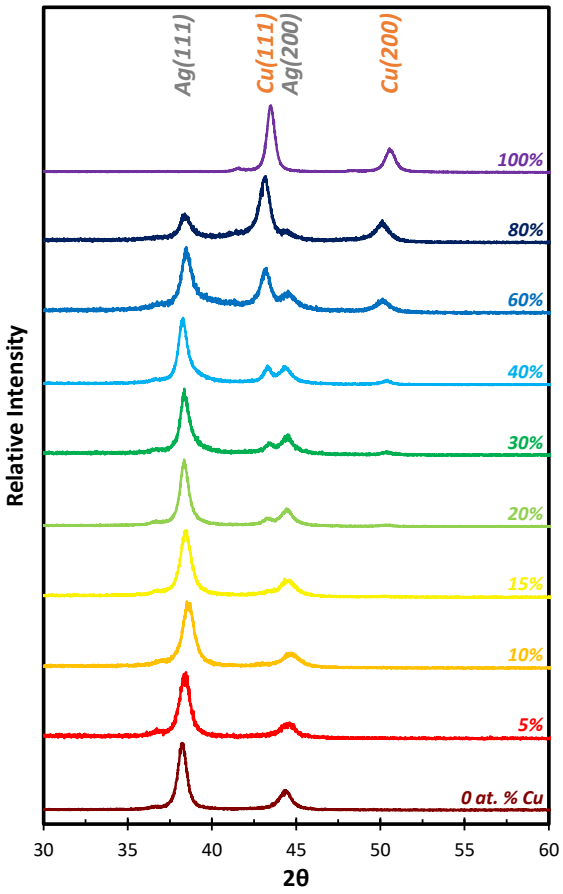

Figure 6.1 *– Asymmetric GIXRD patterns of the CuAg bimetallic electrodes.*

6.3.2 Transient Reaction Selectivity of the Bimetallic Electrodes

The FEs of the gaseous products produced over the CuAg bimetallic electrodes were monitored with time during CO_2RR at -1.05 V vs RHE in order to determine the stability of the electrodes. While the FEs of the gaseous products were constant over pure Cu and Ag, all of the bimetallic electrodes exhibited changes in the product distribution over the first 20 min of electrolysis. These changes were most significant for the Ag-rich bimetallic electrodes and were characterized by a drop in the FE of CO and an increase in the total FE of products derived from CO, as shown in Figure 6.2B. These observations suggest that the surface of the bimetallic electrodes undergo Cu enrichment during this transient period. To confirm this hypothesis the near-surface and surface compositions of the bimetallic electrodes were measured by XPS and ISS after chronoamperometry. As shown in Figure 6.2A, the XPS and ISS measurements taken after chronoamperometry confirm that Cu surface enrichment occurs over the course of electrolysis. Furthermore, the magnitude of the reaction selectivity changes over the transient period scale with the magnitude of the observed Cu surface enrichment, confirming that the transient reaction selectivity is caused by the segregation of Cu to the electrode surface (see 6.6.14). However, no change in the average crystallite size or extent of alloying was observed by GIXRD after electrolysis, potentially due the inadequate surface sensitivity of the

measurement. Interestingly, the Ag-rich bimetallic electrodes undergo more Cu surface enrichment than those that are Cu-rich. This suggests that Cu initially dissolved in the Ag phase segregates to the surface, since the fraction of Cu present in the bimetallic electrodes that is dissolved in the Ag phase increases with the bulk Ag content. The consistency of the measured near-surface and surface compositions suggests that the segregation of Cu to the surface of the Ag phase forms a Cu-rich skin with a thickness ≥1 nm. The driving force for the segregation of Cu to the surface of the Ag phase is hypothesized to be the stronger interaction of CO with Cu than Ag.[9,10]

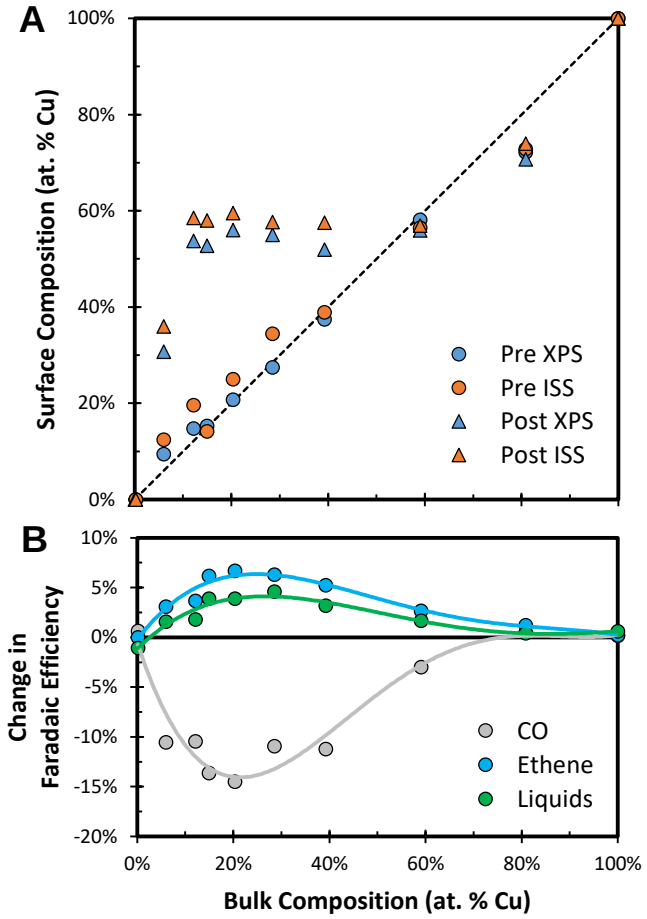

Figure 6.2 *– (A) Near-surface (XPS) and surface (ISS) compositions of the CuAg bimetallic electrodes before and after CO_2RR. (B) Transient changes in the reaction selectivity observed over the CuAg bimetallic electrodes during the first 20 min of electrolysis at -1.05 V vs RHE.*

6.3.3 Steady State Selectivity of the Bimetallic Electrodes

The steady state CO_2 consumption rate observed over all of the bimetallic electrodes was lower than the diffusion limited consumption rate observed over polycrystalline Ag, ensuring that the trends reported herein are not excessively affected by mass transfer effects (see 6.6.15). Since the bimetallic electrodes with bulk compositions of 10-60 at.% Cu enrich to roughly the same surface composition at steady state, the results obtained over all of these electrocatalysts were averaged together. The

H_2 FE observed over the bimetallic electrodes was significantly lower than that observed over polycrystalline Cu, with the nominal bimetallic electrodes exhibiting H_2 FEs ~30% lower than observed over pure Cu (see 6.6.16). A large fraction of this current is instead utilized to produce CO, which is produced with an average FE of ~20% over the nominal bimetallic electrodes. However, a portion of this current is also utilized to produce products derived from CO, with a total FE ~10% higher observed over the nominal bimetallic electrodes than pure Cu. Interestingly, the bimetallic electrodes are also unusually selective for the formation of multi-carbon oxygenates, producing a maximum FE of ~35%, which is more than double the total oxygenate FE observed over pure Cu. Acetate and acetaldehyde account for a substantial portion of the multi-carbon oxygenate selectivity, reaching a combined FE of ~15%, which is significant because neither of these products is produced over pure Cu with a FE above 1%.

6.3.4 Steady State Activity of the Bimetallic Electrodes

The steady state partial current densities of the major reaction products are plotted as a function of the steady state near-surface composition of the CuAg bimetallic electrodes in Figure 6.3. The steady state activity of the bimetallic electrodes did not display any dependence on the extent of alloying observed in the individual phases by XRD or GIXRD. However, it is apparent that the HER activity is suppressed compared to what would be expected if the bimetallic electrodes behaved as a linear combination of Cu and Ag, with the nominal bimetallic electrodes producing ~75% less H_2 than pure Cu. Conversely, the total partial current density to products derived from CO scales linearly with the surface Cu content, meaning that the suppression of HER does not inhibit the ability of Cu to produce products derived from CO. Thus, the enhanced selectivity to multi-carbon products observed over the bimetallic electrodes is a consequence of the suppression of HER and not the enhancement of CO_2RR. The suppression of HER could

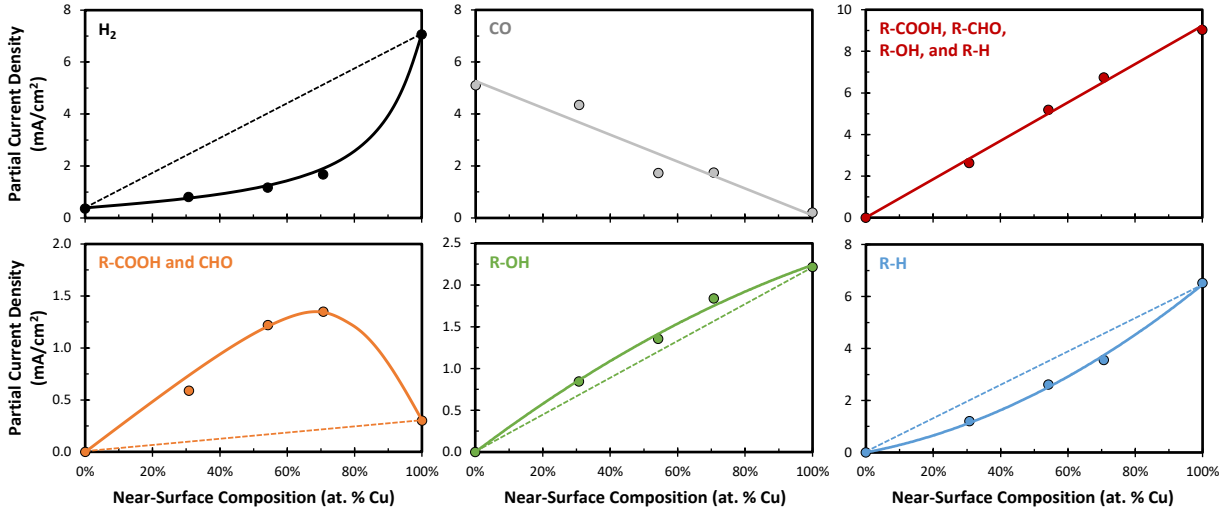

Figure 6.3 *– Steady state partial current densities observed over the CuAg bimetallic electrodes at an applied potential of -1.05 V vs RHE as a function of the steady state near-surface composition, as quantified by XPS after electrolysis. The solid line is meant to guide the eye while the dotted line displays what was expected to be observed had the CuAg bimetallic electrodes behaved as a linear combination of Cu and Ag.*

be explained in terms of an enhanced coverage of CO adsorbed on Cu due to spillover from Ag. However, if significant CO spillover occurred, the observed CO partial current density would be lower than expected for a linear combination of Cu and Ag. Conversely, the CO generation rate scales linearly with the surface Ag content of the bimetallic electrodes. Therefore, the absence of missing CO does not support our initial hypothesis that CO generated over Ag is consumed over Cu. As mentioned previously, the distribution of products derived from CO is modified compared to what is typically observed over pure Cu, with a ~400% enhancement of the generation rate of multi-carbon carbonyl-containing products compared to pure Cu. This activity boost is accompanied by a concomitant suppression of the hydrocarbon partial current density, which is predominately ethene. Additional experiments conducted over a Ag mesh backed by a Cu foil confirmed that an elevated local CO concentration does not significantly impact the distribution of products obtained over Cu, confirming that CO spillover is not the cause of the modified product distribution observed over the bimetallic electrodes (see 6.6.17).

The total partial current densities to products produced over Cu were normalized by the steady state near-surface Cu content and plotted as a function of the steady state near-surface composition in order to gain insight into the dependence of the activity of the Cu phase in the bimetallic electrodes on the near-surface composition. As shown in Figure 6.4, the addition of Ag into Cu suppresses the HER activity of the Cu phase by ~75% during CO_2RR. Conversely, the addition of Ag into Cu does not impact the total partial current density to products derived from CO, as previously stated. However, the distribution of products derived from CO does change, with the generation rate of carbonyl-containing products being enhanced at the expense of hydrocarbons. Interestingly, the activity of the Cu phase in the bimetallic electrodes is independent of the near-surface composition, suggesting that Ag may act as a surface promoter of Cu. However, this promoter effect saturates before a bulk Ag phase forms, which is why the Cu phase is identical in electrocatalytic activity in all the bimetallic electrodes studied here. Thus, the Cu phase in the bimetallic electrodes is expected to have a surface atomic arrangement that is independent of the bulk composition. In the next section, we explore the possibility that small amounts of Ag can promote the Cu surface and shift the product distribution to favor multi-carbon oxygenates at the expense of H_2 and hydrocarbons.

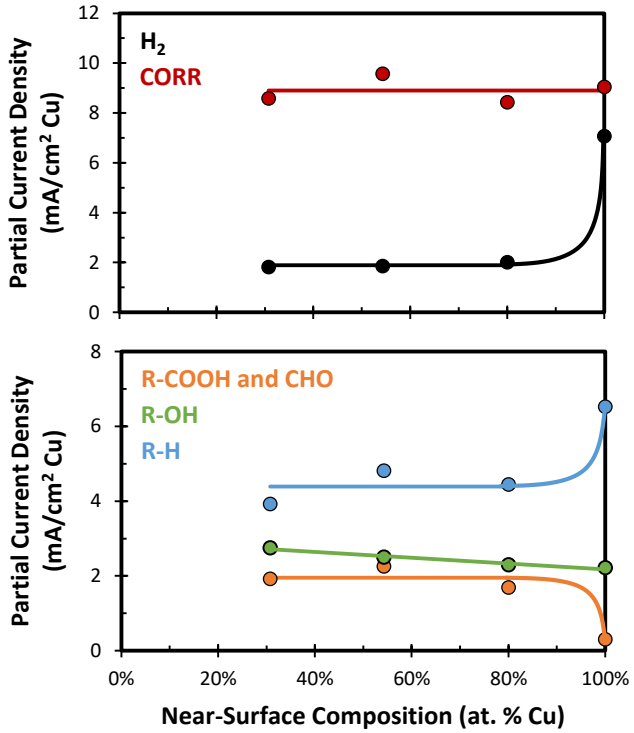

Figure 6.4 *– Steady state activity of the Cu phase in the bimetallic electrodes at an applied potential of -1.05 V vs RHE as a function of the steady state near-surface Cu content.*

6.3.5 Cu(100)+Ag Surface Alloys

Epitaxial Cu(100) thin films have been observed to exhibit surface adlattices upon electrochemical reduction that are identical to their bulk structure,[43] which makes them a well-defined foundation for a systematic study of the effect of Ag surface promotion on the electrocatalytic activity of Cu. Accordingly, Cu(100)+Ag electrodes were prepared by epitaxial growth of Cu on Si(100) followed by galvanic exchange with Ag. As shown in Figure 6.5A, Cu(111) x-ray pole figures of the Cu(100) thin films exhibit the 4-fold symmetry characteristic of Cu(100), confirming the epitaxial nature of the Cu thin films (see 6.6.18). The Ag loading on the Cu(100) thin films was quantified by XPS after galvanic exchange and was found to scale with the concentration of $AgNO_3$ in the galvanic exchange solution (See 6.6.19). As shown in Figure 6.5B, ion scattering spectroscopy confirmed that the Ag was incorporated into the Cu(100) surface. The direct correlation between the integrated area of the Ag ISS peak with the near-surface Ag composition, as quantified by XPS, suggests that all of the exchanged Ag atoms are located at the electrode surface (see 6.6.20).

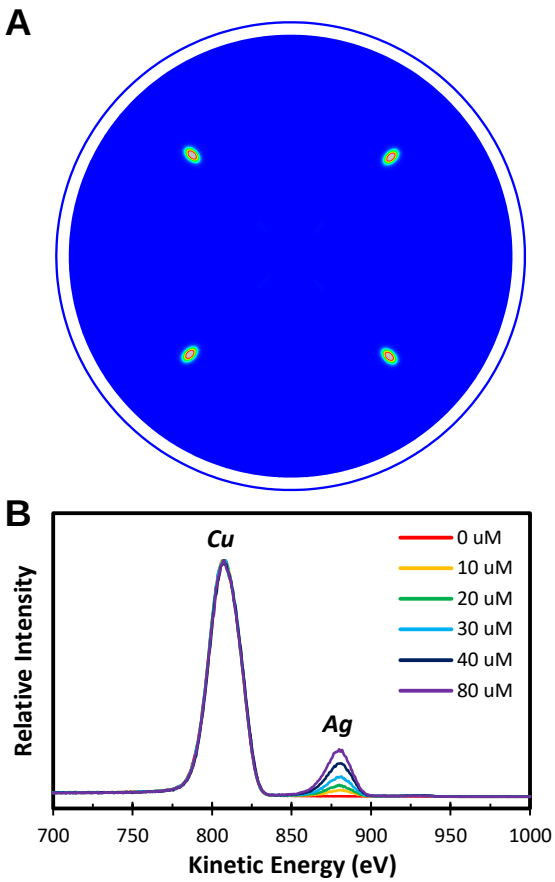

Figure 6.5 *– (A) Cu(111) x-ray pole figure of the epitaxial Cu(100) thin film deposited on Si(100). (B) ISS spectra of the Cu(100)+Ag electrodes.*

The electrocatalytic activity of the Cu(100)+Ag electrodes was measured under conditions similar to those utilized to assess the CuAg bimetallic electrodes. Unlike the bimetallic electrodes, the Cu(100)+Ag electrodes did not display significant changes in reaction selectivity with time, suggesting that the surface structure and composition are stable throughout the duration of electrolysis (see 6.6.21). This stability is expected because the immiscibility of Cu and Ag prevents Ag from diffusing into the bulk of the Cu thin film during electrolysis. As the near-surface Ag content of the Cu(100)+Ag electrodes increased, the steady state activity more closely resembled that observed over the Cu phase in the bimetallic electrodes, as shown in Figure 6.6. In fact, the HER activity of the Cu(100) thin films decreased by ~60% by the incorporation of ~3 at. % Ag into the near-surface region. Furthermore, the suppression of HER had a negligible impact on the ability of Cu to reduce CO, resulting in a 10% boost in the multi-carbon product FE compared to pure Cu(100). Furthermore, the addition of Ag into Cu(100) resulted in an enhanced production rate of carbonyl-containing products at the expense of ethene. Thus, the activity trends observed over the Cu phase in the bimetallic electrodes were qualitatively reproduced by adding <3 at. % Ag into the near-surface region of Cu(100), confirming the role of Ag as a surface promoter of Cu.

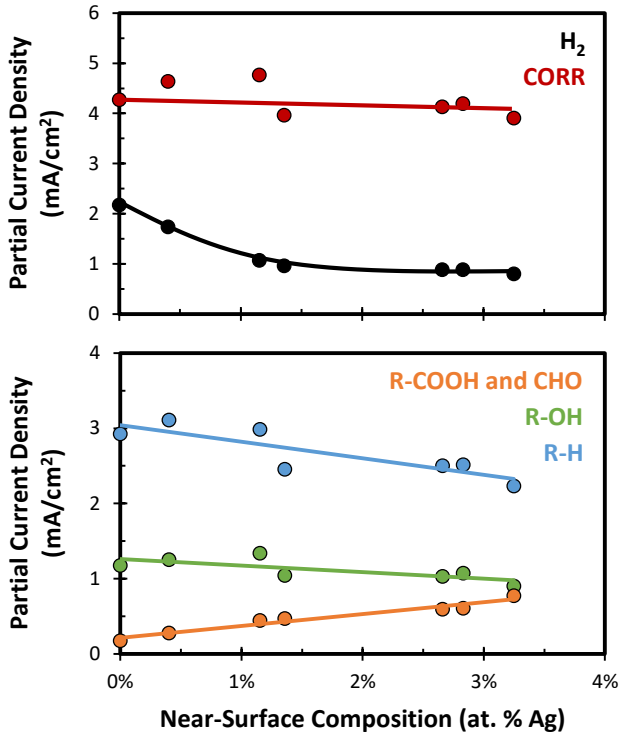

Figure 6.6 *– Steady state activity of the Cu(100)+Ag electrodes at an applied potential of -1 V vs RHE as a function of the near-surface composition, as measured by XPS.*

6.3.6 Electronic Modifications of Cu Induced by Compressive Strain

While Cu and Ag are immiscible in the bulk at room temperature,[37] surface science studies have revealed that they exhibit limited surface miscibility.[44] In fact, the addition of Ag adatoms onto Cu(100) single crystals was found to spontaneously result in the formation of a random substitutional surface alloy at room temperature with a maximum Ag content of ~16 at. % in the top layer of atoms.[44] Since the penetration depth of XPS is ~10 atomic layers, a Ag-saturated Cu(100)+Ag surface alloy would have a near-surface composition of ~1.6 at. % Ag, which we have found to be the optimal near-surface composition for the suppression of HER. Interestingly, surface scientists have observed that the Ag atoms incorporated into the Cu(100) surface have fewer Ag nearest neighbors than would be expected for an ideal solution. This occurs because the substitution of larger Ag atoms into the Cu surface induces compressive strain in the surrounding Cu atoms, which causes the incorporated Ag atoms to repel one another.[44,45] Thus, the incorporation of a relatively small amount of Ag into the Cu surface will result in compressive strain in the majority of Cu surface atoms.

Strain has been identified both theoretically and experimentally as a means of modifying the electrocatalytic activity of transition metals.[46–48] This electrocatalytic activity modification arises due to changes in the valence band structure of the strained metal, with compressive strain inducing a shift of the valence band density of states to higher binding energies.[49] Since the interaction of the valence orbitals of a transition metal with the electronic orbitals of the adsorbate is what determines the adsorption energy, these

strain-induced electronic modifications are accompanied by a concomitant shift in the adsorption energy of reactive chemical species.[46,50,51] The magnitude of these adsorption energy shifts scale with the magnitude of the lateral surface strain, with the adsorption energy of O being roughly 5 times more sensitive to strain effects than CO.[52,53] As the valence band density of states shifts to higher binding energies there is generally less interaction with the electronic orbitals of adsorbates, resulting in the population of the anti-bonding orbital and a weak adsorption energy.[54,55]

To provide evidence for the presence of electronic modifications in the CuAg bimetallic electrodes and surface alloys consistent with compressive strain, the valence band density of states of the bimetallic electrodes were measured and compared to what would be expected if they behaved as a linear combination of Cu and Ag (see 6.6.22). As shown in Figure 6.7, the valence band density of states of the CuAg bimetallic electrodes behave largely as a linear combination of Cu and Ag. However, subtle differences in the observed valence band at binding energies below 3.5 eV suggest that the valence band density of states of the Cu phase in the bimetallic electrodes has shifted to higher binding

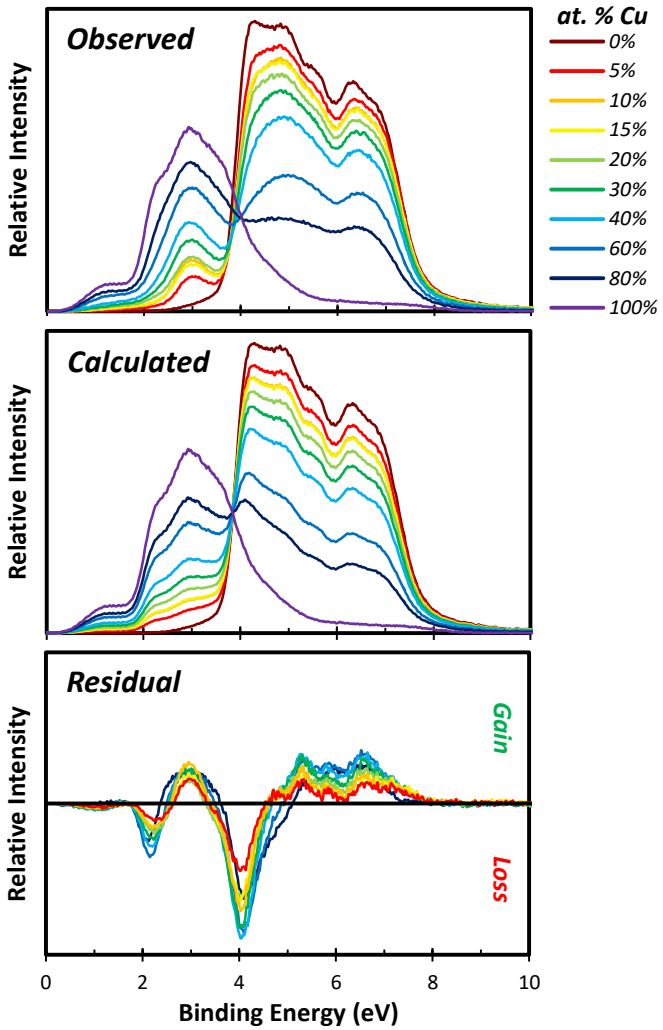

Figure 6.7 *– Valence band spectra of the CuAg bimetallic electrodes.*

energies. Furthermore, the magnitude of the shift is nearly independent of the bulk composition of the bimetallic electrodes, consistent with the notion that the surface of the Cu phase in the bimetallic electrodes consists of a CuAg surface alloy with a saturated Ag content. It is important to note that such valence band modifications can also arise due to ligand effects, wherein a formal electron transfer between the constituent metals occurs.[55] However, the driving force for such an electron transfer is either a difference in the electronegativity of the constituent metals or a difference in the fraction of their valence bands that are populated by electrons.[56–59] Since Cu and Ag have equally filled valence bands, and possess nearly identical electronegativities, there is no driving force for an electron transfer between the Cu and Ag. This hypothesis was confirmed by the lack of a shift in the binding energies of the Cu 2p or Ag 3d core level spectra in the bimetallic electrodes, which would be expected if an electron transfer between the constituent metals occurred (see 6.6.23).

As previously stated, the binding energy of O is roughly 5 times more sensitive to strain effects than CO.[53] Conveniently, the oxophilicity of transition metals is highly correlated with their standard reduction potentials (see 6.6.24). Thus, cyclic voltammetry can be utilized to determine if the compressive strain induced by the incorporation of Ag atoms into the Cu surface results in an observable reduction of the oxophilicity of Cu (see 6.6.25). As shown in Figure 6.8, the Cu^{2+}/Cu^{+} reduction wave is shifted to more anodic

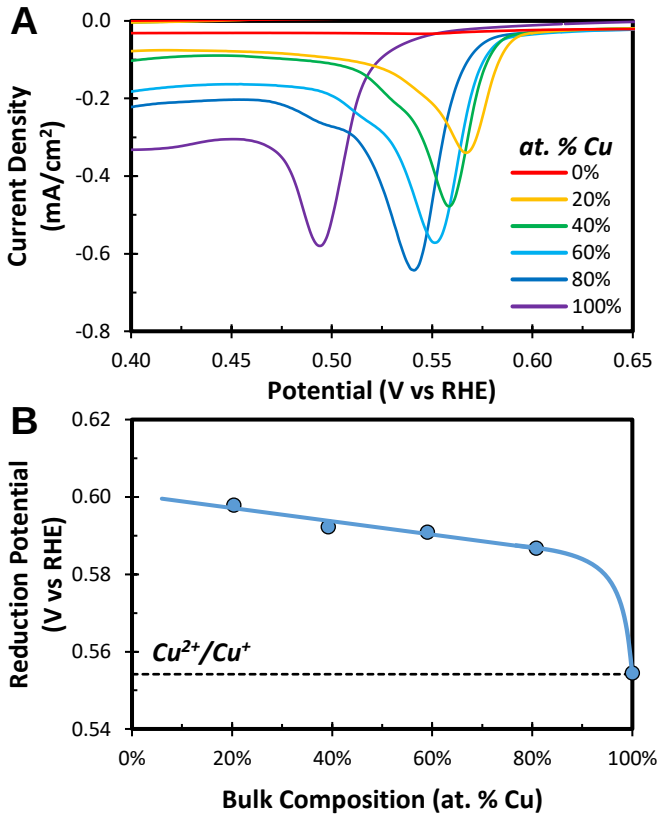

Figure 6.8 *– (A) Cu^{2+}/Cu^{+} reduction waves observed during cyclic voltammetry over the CuAg bimetallic electrodes. (B) Onset potential of the Cu^{2+}/Cu^{+} reduction wave observed during cyclic voltammetry over the CuAg bimetallic electrodes.*

potentials over the bimetallic electrodes compared to pure Cu, consistent with the notion that the Cu surface is compressively strained by surface alloying with Ag.

6.3.7 Impact of Compressive Strain on the Reaction Kinetics and Product Selectivity

The activity descriptor for HER over transition metals has been shown theoretically to be the H adsorption energy.[60–62] Since monometallic Cu has a suboptimal H adsorption energy, the adsorption of H is the rate-determining step of HER over Cu.[60] Thus, weakening the H adsorption energy by compressive strain should reduce the HER activity of Cu further by reducing the fraction of the surface covered by adsorbed hydrogen atoms. Conversely, the activity descriptor of CO_2RR has been proposed to be the CO adsorption energy since the reduction of CO is the rate-determining step in the reduction of CO_2 to hydrocarbons and alcohols over Cu.[7–10,63] Thus, one would expect the rates of CO_2RR over Cu to be influenced by compressive strain, in contrast to what is observed in the present work. To reconcile this apparent inconsistency one must consider the differences in the site of adsorption for H and CO. While it is difficult to observe adsorbed H spectroscopically, theory has found that H adsorbs in the hollow site on both the Cu(111) and Cu(100) surfaces.[64] Conversely, the infrared absorption studies have found that CO adsorbs on the ontop site on Cu surfaces under electrochemical conditions.[65–67] Thus, H and CO adsorb on different surface sites, the electronic properties of which are modified by different magnitudes by surface strain. A recent theoretical study of Cu-based surface alloys found that H adsorbed in the hollow site was more significantly destabilized by compressive strain than CO adsorbed on the ontop site.[68] Thus, compressive strain results in a greater reduction of the adsorption energy of H relative to CO, leading to an enhanced selectivity for the production of products derived from CO by selective suppression of HER.

Theoretical studies have found that the lowest energy pathway to C-C coupling at potentials cathodic of -1 V vs RHE over Cu(100) involves the reaction of CO with CHO to form CO-CHO.[69] This intermediate could be reduced to glyoxal, the simplest C_2 product produced by CO_2RR over Cu.[12] Furthermore, it has been shown that glyoxal reduction produces acetaldehyde over pure Cu and that at more cathodic potentials acetaldehyde can be reduced further to yield ethanol.[8,70,71] The reduction of glyoxal is relatively facile in comparison to CO_2RR unlike the reduction of acetaldehyde, which requires a slightly lower overpotential than the reduction of CO.[70] This observation suggests that acetaldehyde has a relatively weak binding energy to the Cu surface compared to other carbonyl-containing intermediate reaction products. Thus, the enhanced production of acetaldehyde may be a result of the reduced oxophilicity of the compressively strained Cu, which presumably reduces the acetaldehyde adsorption energy to the extent that it desorbs from the Cu surface as it is produced. Once desorbed, acetaldehyde may then be susceptible to “Cannizzaro-type” disproportionation in the relatively alkaline conditions found within the hydrodynamic boundary layer at the cathode surface, producing ethanol and acetate.[72] This would explain the correlation between the generation rates of acetate and acetaldehyde observed here and reported elsewhere.[73] Interestingly, the molar ratio of acetate to acetaldehyde was observed to be constant in all experiments performed

despite nearly an order of magnitude variation in their absolute generation rates (see 6.6.26). The observed acetate to acetaldehyde molar ratio is equivalent to the equilibrium constant of acetaldehyde hydration in water, suggesting that the formation of 1,1-ethanediol by hydration of acetaldehyde may initiate the "Cannizzaro-type" disproportionation.

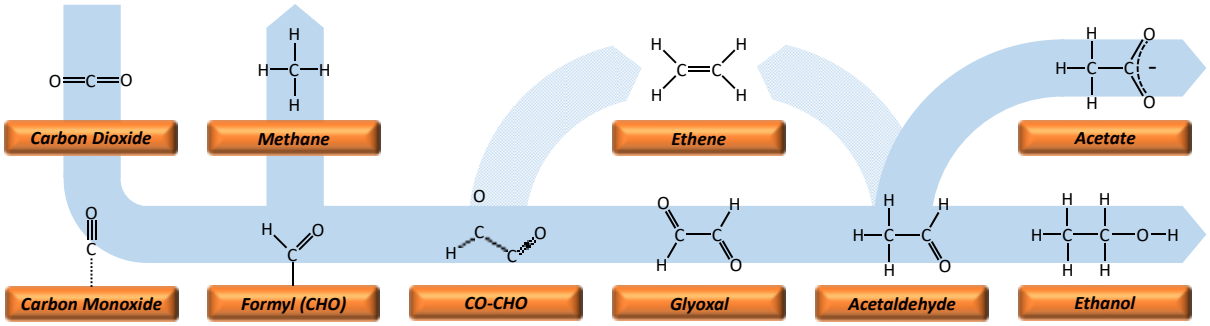

Scheme 6.1 *– Proposed reaction mechanisms to C_1 and C_2 products. Light blue arrows denote potential pathways to ethene.*

It is difficult to explain why the enhanced production rate of carbonyl-containing products comes at the expense of ethene because little is known about the mechanism leading to ethene formation from CO. One potential explanation is that acetaldehyde intermediates are present on the electrode surface as vinyl alcohol, the keto form of acetaldehyde, and that this species can be reduced to ethene.[12] An alternative mechanism is that the ethene pathway diverges from the ethanol pathway before the formation of glyoxal. These potential routes are summarized in Scheme 6.1. Interestingly, a recent theoretical study has concluded that surface adsorbed water plays a critical role in determining the hydrocarbon selectivity observed over Cu by initiating C-O bond scission.[74] Thus, the enhanced formation of carbonyl-containing products at the expense of ethene may be a result of the suppression of HER, which also reduces the rate of C-O bond scission by reducing the surface coverage of HER intermediates. This hypothesis is supported by the inverse correlation between the oxygenate selectivity, defined as the fraction of the current going toward the production of products derived from CO that are oxygenates, and the HER activity observed over the Cu(100)+Ag surface alloys, as shown in Figure 6.9. Thus, the addition of Ag into the Cu surface enhances the oxygenate selectivity observed during CO_2RR by selectively titrating HER active surface sites.

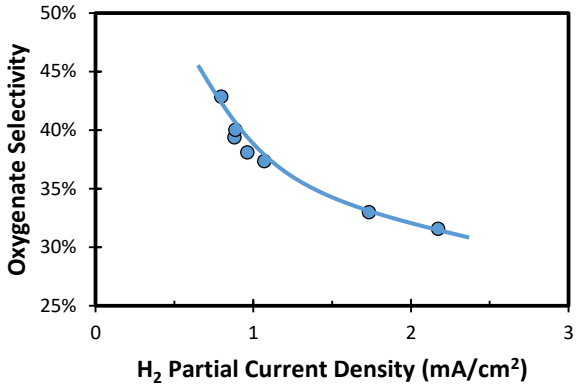

Figure 6.9 *– Oxygenate selectivity as a function of the HER activity of the Cu(100)+Ag surface alloys measured at an applied potential of -1 V vs RHE.*

6.4 Conclusions

As-prepared CuAg bimetallic electrodes consist of Cu-rich and Ag-rich crystallites with a surface composition equivalent to that of the bulk. However, during CO_2RR the Ag-rich bimetallic electrodes undergo Cu surface enrichment due to CO adsorbate-induced segregation of the Cu initially dissolved in the Ag phase. The distribution of products produced over stable CuAg bimetallic electrodes indicate that CO is primarily produced on the surface of the Ag domains, whereas CO reduction occurs exclusively on the surface of the Cu domains. However, the distribution of products observed over the Cu domains is altered compared to pure Cu, with H_2 production being suppressed by ~75%. While the suppression of HER does not inhibit the ability of the Cu domains to produce products derived from CO, the distribution of products shifts to favor carbonyl-containing products at the expense of hydrocarbons. This activity modification was found to be independent of the near-surface composition of the bimetallic electrodes, suggesting that the Cu phase is modified by a small amount of Ag. The surface promotion occurs due to compressive strain induced by the formation of a Cu+Ag surface alloy, which induces a shift in the valence band density of states of Cu to deeper levels. Furthermore, this interpretation is strongly supported by observations over Cu+Ag surface alloys prepared by Galvanic exchange of Ag into Cu(100) thin films, which display a shift in product selectivity by the addition of <3 at. % Ag into the near-surface region that is in good agreement with those observed over the Cu phase in the bimetallic electrodes.

Thus, the incorporation of Ag atoms into the Cu surface results in compressive strain in the neighboring Cu atoms, which induces an observable shift in the valence band density of states of Cu to deeper levels. This electronic structure modification reduces the binding energies of H and O relative to CO, leading to an enhanced selectivity for the production of products derived from CO due to the selective suppression of HER. These strain effects also result in an enhanced selectivity to multi-carbon carbonyl-containing products at the expense of ethene due to the reduced coverage of adsorbed H and the reduced oxophilicity of the compressively strained Cu. These insights provide a rational means for modifying the activity of CO_2RR electrocatalysts to favor the formation of oxygenated products.

6.5 References

(1) Jitaru, M.; Lowy, D. A.; Toma, M.; Toma, B. C.; Oniciu, L. Electrochemical Reduction of Carbon Dioxide on Flat Metallic Cathodes. *J. Appl. Electrochem.* **1997**, *27* (8), 875–889.

(2) Gattrell, M.; Gupta, N.; Co, A. A Review of the Aqueous Electrochemical Reduction of CO2 to Hydrocarbons at Copper. *J. Electroanal. Chem.* **2006**, *594* (1), 1–19.

(3) Hori, Y. Electrochemical CO2 Reduction on Metal Electrodes. In *Modern Aspects of Electrochemistry*; Vayenas, C. G., White, R. E., Gamboa-Aldeco, M. E., Eds.; Springer: New York, 2008; pp 89–189.

(4) Hori, Y.; Kikuchi, K.; Suzuki, S. Production of CO and CH4 in Electrochemical Reduction of CO2 at Metal Electrodes in Aqueous Hydrogencarbonate Solution. *Chem. Lett.* **1985**, *14* (11), 1695–1698.

(5) Noda, H.; Ikeda, S.; Oda, Y.; Imai, K.; Maeda, M.; Ito, K. Electrochemical Reduction of

Carbon Dioxide at Various Metal Electrodes in Aqueous Potassium Hydrogen Carbonate Solution. *Bull. Chem. Soc. Jpn.* **1990**, *63* (9), 2459–2462.
(6) Hori, Y.; Murata, A.; Takahashi, R.; Suzuki, S. Electrochemical Reduction of Carbon Monoxide to Hydrocarbons at Various Metal Electrodes in Aqueous Solution. *Chem. Lett.* **1987**, *16* (8), 1665–1668.
(7) Hori, Y.; Murata, A.; Takahashi, R. Formation of Hydrocarbons in the Electrochemical Reduction of Carbon Dioxide at a Copper Electrode in Aqueous Solution. *J. Chem. Soc. Faraday Trans. I* **1989**, *85* (8), 2309–2326.
(8) Hori, Y.; Takahashi, R.; Yoshinami, Y.; Murata, A. Electrochemical Reduction of CO at a Copper Electrode. *J. Phys. Chem. B* **1997**, *101* (36), 7075–7081.
(9) Peterson, A. A.; Abild-Pedersen, F.; Studt, F.; Rossmeisl, J.; Nørskov, J. K. How Copper Catalyzes the Electroreduction of Carbon Dioxide into Hydrocarbon Fuels. *Energy Environ. Sci.* **2010**, *3* (9), 1311.
(10) Peterson, A. A.; Nørskov, J. K. Activity Descriptors for CO2 Electroreduction to Methane on Transition-Metal Catalysts. *J. Phys. Chem. Lett.* **2012**, *3*, 251–258.
(11) Nie, X.; Esopi, M. R.; Janik, M. J.; Asthagiri, A. Selectivity of CO2 Reduction on Copper Electrodes: The Role of the Kinetics of Elementary Steps. *Angew. Chemie - Int. Ed.* **2013**, *52* (9), 2459–2462.
(12) Kuhl, K. P.; Cave, E. R.; Abram, D. N.; Jaramillo, T. F. New Insights into the Electrochemical Reduction of Carbon Dioxide on Metallic Copper Surfaces. *Energy Environ. Sci.* **2012**, *5* (5), 7050–7059.
(13) Noda, H.; Ikeda, S.; Oda, Y.; Ito, K. Potential Dependencies of the Products on Electrochemical Reduction of Carbon Dioxide at a Copper Electrode. *Chem. Lett.* **1989**, *2*, 289–292.
(14) Li, C. W.; Kanan, M. W. CO2 Reduction at Low Overpotential on Cu Electrodes Resulting from the Reduction of Thick Cu2O Films. *J. Am. Chem. Soc.* **2012**, *134* (17), 7231–7234.
(15) Tang, W.; Peterson, A. a; Varela, A. S.; Jovanov, Z. P.; Bech, L.; Durand, W. J.; Dahl, S.; Nørskov, J. K.; Chorkendorff, I. The Importance of Surface Morphology in Controlling the Selectivity of Polycrystalline Copper for CO2 Electroreduction. *Phys. Chem. Chem. Phys.* **2012**, *14* (1), 76–81.
(16) Manthiram, K.; Beberwyck, B. J.; Alivisatos, A. P. Enhanced Electrochemical Methanation of Carbon Dioxide with a Dispersible Nanoscale Copper Catalyst. *J. Am. Chem. Soc.* **2014**, *136* (38), 13319–13325.
(17) Roberts, F. S.; Kuhl, K. P.; Nilsson, A. High Selectivity for Ethylene from Carbon Dioxide Reduction over Copper Nanocube Electrocatalysts. *Angew. Chemie - Int. Ed.* **2015**, *54* (17), 5179–5182.
(18) Feng, X.; Jiang, K.; Fan, S.; Kanan, M. W. A Direct Grain-Boundary-Activity Correlation for CO Electroreduction on Cu Nanoparticles. *ACS Cent. Sci.* **2016**, *2* (3), 169–174.
(19) Murata, A.; Hori, Y. Product Selectivity Affected by Cationic Species in Electrochemical Reduction of CO2 and CO at a Cu Electrode. *Bull. Chem. Soc. Jpn.* **1991**, *64*, 123–127.
(20) Kyriacou, G. Z.; Anagnostopoulos, A. K. Influence CO2 Partial Pressure and the Supporting Electrolyte Cation on the Product Distribution in CO2 Electroreduction. *J. Appl. Electrochem.* **1993**, *23* (5), 483–486.
(21) Singh, M. R.; Kwon, Y.; Lum, Y.; Ager, J. W.; Bell, A. T. Hydrolysis of Electrolyte Cations Enhances the Electrochemical Reduction of CO2 over Ag and Cu. *J. Am. Chem. Soc.* **2016**, *138* (39), 13006–13012.
(22) Hori, Y.; Murata, A.; Takahashi, R.; Suzuki, S. Enhanced Formation of Ethylene and Alcohols at Ambient Temperature and Pressure in Electrochemical Reduction of Carbon Dioxide at a Copper Electrode. *J. Am. Chem. Soc. Chem. Commun.* **1988**, *1*, 17–19.
(23) Kas, R.; Kortlever, R.; Yilmaz, H.; Koper, M. T. M.; Mul, G. Manipulating the Hydrocarbon Selectivity of Copper Nanoparticles in CO2 Electroreduction by Process Conditions.

ChemElectroChem **2015**, *2* (3), 354–358.
(24) Varela, A. S.; Kroschel, M.; Reier, T.; Strasser, P. Controlling the Selectivity of CO 2 Electroreduction on Copper: The Effect of the Electrolyte Concentration and the Importance of the Local pH. *Catal. Today* **2016**, *260*, 8–13.
(25) Hansen, H. A.; Shi, C.; Lausche, A.; Peterson, A.; Nørskov, J. K. Bifunctional Alloys for the Electroreduction of CO2 and CO. *Phys. Chem. Chem. Phys.* **2016**, *18* (111), 9194–9201.
(26) Hahn, C.; Abram, D. N.; Hansen, H. A.; Hatsukade, T.; Jackson, A.; Johnson, N. C.; Hellstern, T. R.; Kuhl, K. P.; Cave, E. R.; Feaster, J. T.; et al. Synthesis of Thin Film AuPd Alloys and Their Investigation for Electrocatalytic CO2 Reduction. *J. Mater. Chem. A* **2015**, *3*, 20185–20194.
(27) Ren, D.; Ang, B. S. H.; Yeo, B. S. Tuning the Selectivity of Carbon Dioxide Electroreduction toward Ethanol on Oxide-Derived CuxZn Catalysts. *ACS Catal.* **2016**, *6* (12), 8239–8247.
(28) Torelli, D. A.; Francis, S. A.; Crompton, J. C.; Javier, A.; Thompson, J. R.; Brunschwig, B. S.; Soriaga, M. P.; Lewis, N. S. Nickel–Gallium-Catalyzed Electrochemical Reduction of CO2 to Highly Reduced Products at Low Overpotentials. *ACS Catal.* **2016**, *6*, 2100–2104.
(29) Ma, S.; Sadakiyo, M.; Heim, M.; Luo, R.; Haasch, R. T.; Gold, J. I.; Yamauchi, M.; Kenis, P. J. A. Electroreduction of Carbon Dioxide to Hydrocarbons Using Bimetallic Cu-Pd Catalysts with Different Mixing Patterns. *J. Am. Chem. Soc.* **2017**, *139* (1), 47–50.
(30) Hori, Y.; Murata, A.; Yoshinami, Y. Adsorption of CO, Intermediately Formed in Electrochemical Reduction of CO2, at a Copper Electrode. *J. Chem. Soc. Faraday Trans.* **1991**, *87* (1), 125–128.
(31) Hori, Y.; Koga, O.; Yamazaki, H.; Matsuo, T. Infrared Spectroscopy of Adsorbed CO and Intermediate Species in Electrochemical Reduction of CO2 to Hydrocarbons on a Cu Electrode. *Electrochim. Acta* **1995**, *40* (16), 2617–2622.
(32) Zhang, Y.-J.; Sethuraman, V.; Michalsky, R.; Peterson, A. a. Competition between CO2 Reduction and H2 Evolution on Transition-Metal Electrocatalysts. *ACS Catal.* **2014**, *4*, 3742–3748.
(33) Hori, Y.; Murata, A.; Ito, S.-Y. Nickel and Iron Modified Copper Electrode for Electroreduction of CO2 by In-Situ Electrodeposition. *Chem. Lett.* **1989**, No. 9, 1567–1570.
(34) Monzo, F. J.; Malewski, Y.; Kortlever, R.; Vidal-Iglesias, F. J.; Solla-Gullon, J.; Koper, M. T. .; Rodriguez, P. Enhanced Electrocatalytic Activity of Au@Cu Core@Shell Nanoparticles Towards CO2 Reduction. *J. Mater. Chem. A* **2015**, *3*, 23690–23698.
(35) Wuttig, A.; Liu, C.; Peng, Q.; Yaguchi, M.; Hendon, C. H.; Motobayashi, K.; Ye, S.; Osawa, M.; Surendranath, Y. Tracking a Common Surface-Bound Intermediate during CO_2-to-Fuels Catalysis. *ACS Cent. Sci.* **2016**, *2* (8), 522–528.
(36) Hatsukade, T.; Kuhl, K. P.; Cave, E. R.; Abram, D. N.; Jaramillo, T. F. Insights into the Electrocatalytic Reduction of CO2 on Metallic Silver Surfaces. *Phys. Chem. Chem. Phys.* **2014**, *16* (27), 13814–13819.
(37) Subramanian, P. R.; Perepesko, J. H. The Copper-Silver System. *J. Phase Equilibria* **1993**, *14* (1), 62–63.
(38) Krastev, E. T.; Voice, L. D.; Tobin, R. G. Surface Morphology and Electric Conductivity of Epitaxial Cu(100) Films Grown on H-Terminated Si(100). *J. Appl. Phys.* **1996**, *79* (9), 6865–6871.
(39) Jiang, H.; Klemmer, T. J.; Barnard, J. A.; Payzant, E. A. Epitaxial Growth of Cu on Si by Magnetron Sputtering. *J. Vac. Sci. Technol. B* **1998**, *16* (6), 3376–3383.
(40) Lobaccaro, P.; Singh, M. R.; Clark, E. L.; Kwon, Y.; Bell, A. T.; Ager, J. W. Effects of Temperature and Gas-Liquid Mass Transfer on the Operation of Small Electrochemical Cells for the Quantitative Evaluation of CO2 Reduction Electrocatalysts. *Phys. Chem. Chem. Phys.* **2016**, *18* (38), 26777–26785.
(41) Dunwell, M.; Lu, Q.; Heyes, J. M.; Rosen, J.; Chen, J. G.; Yan, Y.; Jiao, F.; Xu, B. The Central Role of Bicarbonate in the Electrochemical Reduction of Carbon Dioxide on Gold.

J. Am. Chem. Soc. **2017**, *139* (10), 3774–3783.
(42) Wuttig, A.; Surendranath, Y. Impurity Ion Complexation Enhances Carbon Dioxide Reduction Catalysis. *ACS Catal.* **2015**, *5* (7), 4479–4484.
(43) Hahn, C.; Hatsukade, T.; Kim, Y.; Vailionis, A.; Baricuatro, J. H.; Higgins, D. C. Engineering Cu Surfaces for the Electrocatalytic Conversion of CO2 : Controlling Selectivity toward Oxygenates and Hydrocarbons. *Proc. Natl. Acad. Sci.* **2017**, *114* (23), 5918–5923.
(44) Sprunger, P. T.; Lægsgaard, E.; Besenbacher, F. Growth of Ag on Cu(100) Studied by STM: From Surface Alloying to Ag Superstructures. *Phys. Rev. B* **1996**, *54* (11), 8163–8171.
(45) Christensen, A.; Ruban, A. V.; Stoltze, P.; Jacobsen, K. W.; Skriver, H. L.; Nørskov, J. K.; Besenbacher, F. Phase Diagrams for Surface Alloys. *Phys. Rev. B* **1997**, *56* (10), 5822–5834.
(46) Hammer, B.; Morikawa, Y.; Nørskov, J. K. CO Chemisorption at Metal Surfaces and Overlayers. *Phys. Rev. Lett.* **1996**, *76* (12), 2141–2144.
(47) Kibler, L. A.; El-Aziz, A. M.; Hoyer, R.; Kolb, D. M. Tuning Reaction Rates by Lateral Strain in a Palladium Monolayer. *Angew. Chemie - Int. Ed.* **2005**, *44* (14), 2080–2084.
(48) Sandberg, R. B.; Montoya, J. H.; Chan, K.; Nørskov, J. K. CO-CO Coupling on Cu Facets: Coverage, Strain and Field Effects. *Surf. Sci.* **2016**, *654*, 56–62.
(49) Ruban, A.; Hammer, B.; Stoltze, P.; Skriver, H. L.; Nørskov, J. K. Surface Electronic Structure and Reactivity of Transition and Noble Metals. *J. Mol. Catal. A Chem.* **1997**, *115* (3), 421–429.
(50) Nilsson, A.; Pettersson, L. G. M.; Hammer, B.; Bligaard, T.; Christensen, C. H.; Nørskov, J. K. The Electronic Structure Effect in Heterogeneous Catalysis. *Catal. Letters* **2005**, *100* (3–4), 111–114.
(51) Xin, H.; Vojvodic, A.; Voss, J.; Nørskov, J. K.; Abild-Pedersen, F. Effects of D -Band Shape on the Surface Reactivity of Transition-Metal Alloys. *Phys. Rev. B - Condens. Matter Mater. Phys.* **2014**, *89* (11), 1–5.
(52) Kampshoff, E.; Hahn, E.; Kern, K. Correlation between Surface Stress and the Vibrational Shift of CO Chemisorbed on Cu Surfaces. *Phys. Rev. Lett.* **1994**, *73* (5), 704–707.
(53) Mavrikakis, M.; Hammer, B.; Nørskov, J. K. Effect of Strain on the Reactivity of Metal Surfaces. *Phys. Rev. Lett.* **1998**, *81* (13), 2819–2822.
(54) Hammer, B.; Nørskov, J. K. Electronic Factors Determining the Reactivity of Metal Surfaces. *Surf. Sci.* **1995**, *343* (3), 211–220.
(55) Bligaard, T.; Nørskov, J. K. Ligand Effects in Heterogeneous Catalysis and Electrochemistry. *Electrochim. Acta* **2007**, *52* (18), 5512–5516.
(56) Rodriguez, J. A.; Campbell, R. A.; Goodman, D. W. Electronic Interactions in Bimetallic Systems: An X-Ray Photoelectron Spectroscopic Study. *J. Phys. Chem.* **1990**, *94* (21), 6936–6939.
(57) Rodriguez, J. A.; Campbell, R. A.; Goodman, D. W. Electron Donor-Electron Acceptor Interactions in Bimetallic Surfaces: Theory and XPS Studies. *J. Phys. Chem.* **1991**, *95* (May), 5716–5719.
(58) Rodriguez, J. A.; Goodman, D. W. The Nature of the Metal-Metal Bond in Bimetallic Surfaces. *Science* **1992**, *257* (5072), 897–903.
(59) Rodriguez, J. A.; Campbell, R. A.; Goodman, D. W. The Nature of Metal-Metal Bonding at Bimetallic Interfaces. *Surf. Sci.* **1994**, *307–309*, 377–383.
(60) Nørskov, J. K.; Bligaard, T.; Logadottir, A.; Kitchin, J. R.; Chen, J. G.; Pandelov, S.; Stimming, U. Trends in the Exchange Current for Hydrogen Evolution. *J. Electrochem. Soc.* **2005**, *152* (3), J23–J26.
(61) Sheng, W.; Zhuang, Z.; Gao, M.; Zheng, J.; Chen, J. G.; Yan, Y. Correlating Hydrogen Oxidation and Evolution Activity on Platinum at Different pH with Measured Hydrogen Binding Energy. *Nat. Commun.* **2015**, *6*, 1–6.

(62) Zheng, J.; Sheng, W.; Zhuang, Z.; Xu, B.; Yan, Y. Universal Dependence of Hydrogen Oxidation and Evolution Reaction Activity of Platinum-Group Metals on pH and Hydrogen Binding Energy. *Sci. Adv.* **2016**, *2* (e1501602), 1–8.
(63) Kuhl, K. P.; Hatsukade, T.; Cave, E. R.; Abram, D. N.; Kibsgaard, J.; Jaramillo, T. F. Electrocatalytic Conversion of Carbon Dioxide to Methane and Methanol on Transition Metal Surfaces. *J. Am. Chem. Soc.* **2014**, *136* (40), 14107–14113.
(64) Kratzer, P.; Hammer, B.; Nørskov, J. . Geometric and Electronic Factors Determining the Differences in Reactivity of H2 on Cu(100) and Cu(111). *Surf. Sci.* **1996**, *359* (1–3), 45–53.
(65) Miyake, H.; Osawa, M. Surface-Enhanced Infrared Spectrum of CO Adsorbed on Cu Electrodes in Solution. *Chem. Lett.* **2004**, *33* (3), 278–279.
(66) Wang, H. F.; Yan, Y. G.; Huo, S. J.; Cai, W. Bin; Xu, Q. J.; Osawa, M. Seeded Growth Fabrication of Cu-on-Si Electrodes for in Situ ATR-SEIRAS Applications. *Electrochim. Acta* **2007**, *52* (19), 5950–5957.
(67) Heyes, J.; Dunwell, M.; Xu, B. CO2 Reduction on Cu at Low Overpotentials with Surface-Enhanced in Situ Spectroscopy. *J. Phys. Chem. C* **2016**, *120* (31), 17334–17341.
(68) Sarfraz, S.; Garcia-Esparza, A. T.; Jedidi, A.; Cavallo, L.; Takanabe, K. Cu-Sn Bimetallic Catalyst for Selective Aqueous Electroreduction of CO2to CO. *ACS Catal.* **2016**, *6* (5), 2842–2851.
(69) Goodpaster, J. D.; Bell, A. T.; Head-Gordon, M. Identification of Possible Pathways for C-C Bond Formation during Electrochemical Reduction of CO2: New Theoretical Insights from an Improved Electrochemical Model. *J. Phys. Chem. Lett.* **2016**, *7* (8), 1471–1477.
(70) Schouten, K. J. P.; Kwon, Y.; van der Ham, C. J. M.; Qin, Z.; Koper, M. T. M. A New Mechanism for the Selectivity to C1 and C2 Species in the Electrochemical Reduction of Carbon Dioxide on Copper Electrodes. *Chem. Sci.* **2011**, *2* (10), 1902–1909.
(71) Bertheussen, E.; Verdaguer-Casadevall, A.; Ravasio, D.; Montoya, J. H.; Trimarco, D. B.; Roy, C.; Meier, S.; Wendland, J.; Nørskov, J. K.; Stephens, I. E. L.; et al. Acetaldehyde as an Intermediate in the Electroreduction of Carbon Monoxide to Ethanol on Oxide-Derived Copper. *Angew. Chem. Int. Ed.* **2016**, *55*, 1450–1454.
(72) Birdja, Y. Y.; Koper, M. T. M. The Importance of Cannizzaro-Type Reactions during Electrocatalytic Reduction of Carbon Dioxide. *J. Am. Chem. Soc.* **2017**, *139* (5), 2030–2034.
(73) Hori, Y.; Takahashi, I.; Koga, O.; Hoshi, N. Electrochemical Reduction of Carbon Dioxide at Various Series of Copper Single Crystal Electrodes. *J. Mol. Catal. A Chem.* **2003**, *199*, 39–47.
(74) Xiao, H.; Cheng, T.; Goddard, W. A. Atomistic Mechanisms Underlying Selectivities in C1 and C2 Products from Electrochemical Reduction of CO on Cu(111). *J. Am. Chem. Soc.* **2017**, *139* (1), 130–136.

6.6 Supplementary Information

6.6.1 Profitability Analysis of CO_2RR Products

The profitability of different CO_2RR products were calculated and compared to the lifecycle cost of electricity generated by solar photovoltaics in order to determine which products should be targeted from an economic perspective. Each product was assumed to be produced with a current efficiency of 100% and a voltage efficiency of 75%, based on the calculated thermoneutral cell potential required to produce each product. Chemical pricing was obtained from ICIS Chemical Business. The value of generated products were calculated using:

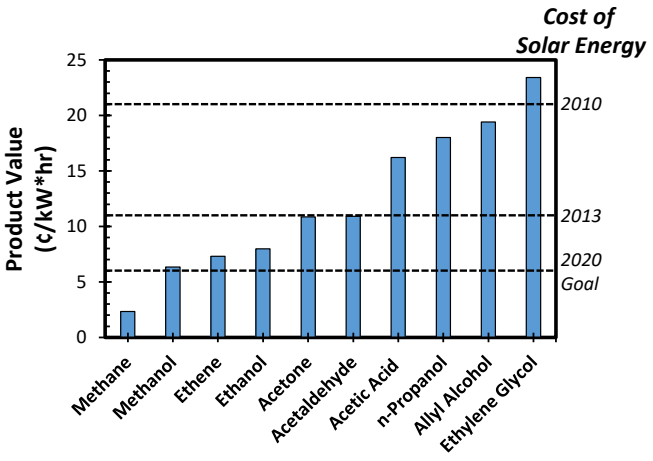

Figure S6.1 *– Profitability analysis of known CO_2RR products compared to the lifecycle cost of electricity derived from photovoltaics.*

$$V_i = \frac{0.75 * C_i}{nFV_{Th}}$$

Where:

V_i	Value of Product i (¢/kW*hr)
C_i	Value of Product i (¢/mol Product i)
n	mol e^-/mol Product i
F	Faraday's Constant
V_{Th}	Thermoneutral Cell Potential

The results of the calculation, shown in Figure S6.1, suggest that multi-carbon products are the most profitable. In fact, if the assumptions of the calculation are satisfied several multi-carbon products could be profitably produced from solar electricity today, whereas significant reductions in the lifecycle cost of solar electricity would be required to make methane production profitable. Furthermore, multi-carbon oxygenates are more profitable than multi-carbon hydrocarbons. Finally, the use of saturated salt electrolytes has been shown to result in the spontaneous separation of some liquid-phase products from the electrolyte, mitigating the need for an expensive post-reaction separation.[1] Thus, electrocatalysts should be developed that can produce multi-carbon oxygenates selectively at low overpotential.

6.6.2 Analysis of Polycrystalline Cu

The typical product distribution observed over polycrystalline Cu is shown in Figure S6.2A as a function of the applied potential.[2] It is apparent that there is a sudden shift in the product distribution at an applied potential of -1.05 V vs RHE that is characterized by an increased selectivity to H_2 and CH_4 at the expense of C_{2+} products. In order to understand what is driving this sudden selectivity shift, the fraction of CO that is produced over polycrystalline Cu that is reduced further to hydrocarbons and alcohols was calculated:

$$\%\ CO\ Reduced = \frac{\sum FE_i \frac{m_i}{n_i}}{\sum FE_i \frac{m_i}{n_i} + \frac{1}{2} FE_{CO}}$$

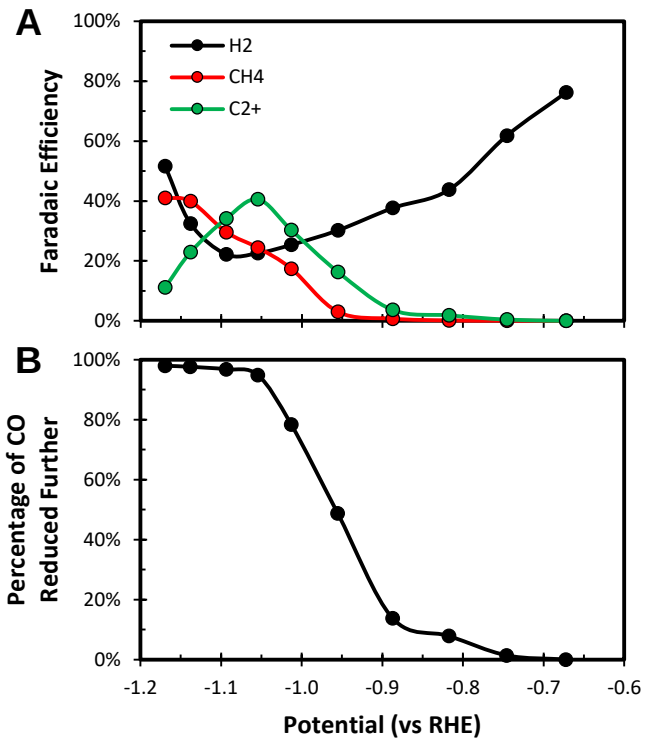

Figure S6.2 *– (A) Product distribution observed over polycrystalline Cu as a function of the applied potential. (B) Fraction of CO generated over polycrystalline Cu that is reduced further to hydrocarbons and alcohols.*

Where:

FE_i	Faradaic Efficiency for CO-Derived Product i
m_i	mol CO/mol Product i
n_i	mol e^-/mol Product i
FE_{CO}	Faradaic Efficiency for CO

As shown in Figure S6.2B, at applied potentials cathodic of -1.05 V vs RHE >95% of the CO generated over polycrystalline Cu is reduced further. This suggests that in this potential regime the availability of CO is impacting the product distribution and is inhibiting the ability of Cu to produce C_{2+} products.

6.6.3 Supplying Additional CO to Cu by Spillover

By co-locating domains of Cu with those of a CO generating metal additional CO can be supplied to Cu by spillover, as shown in Figure S6.3. CO spillover can occur via surface diffusion over short length scales or by increasing the local CO concentration in the electrolyte, which will result in a higher coverage of adsorbed CO on Cu. The metal selected to supply additional CO to Cu by spillover should produce more CO than Cu at a given applied potential. As shown in Figure S6.4, only Au and Ag produce more CO than Cu at a fixed potential.[3] Thus, these are the only metals expected to increase the supply of CO to Cu by spillover.

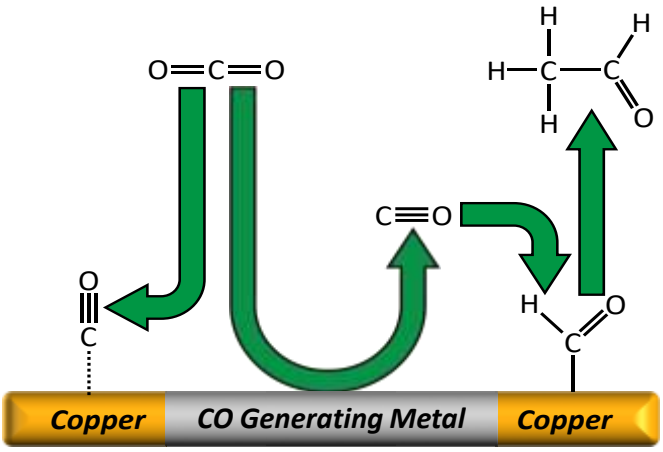

Figure S6.3 *– CO spillover from domains of a CO generating metal to co-located domains of Cu.*

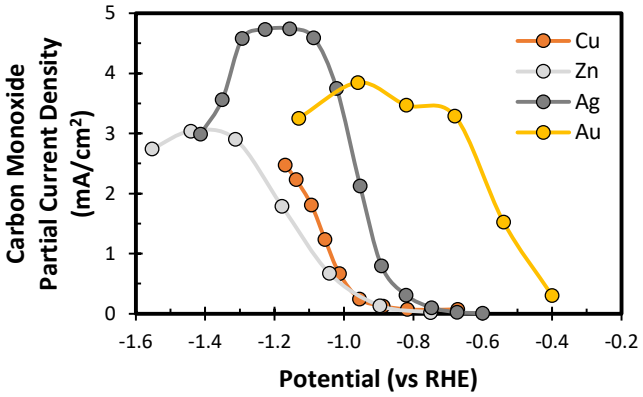

Figure S6.4 *– Intrinsic CO partial current densities observed over monometallic transition metal electrocatalysts.*

6.6.4 Cu-Ag Phase Diagram

Cu and Ag are totally immiscible at temperatures below 200 °C, as depicted in Figure S6.5.[4] Thus, the Cu-Ag system is the ideal system to probe the CO spillover hypothesis because the extent of alloying should be negligible.

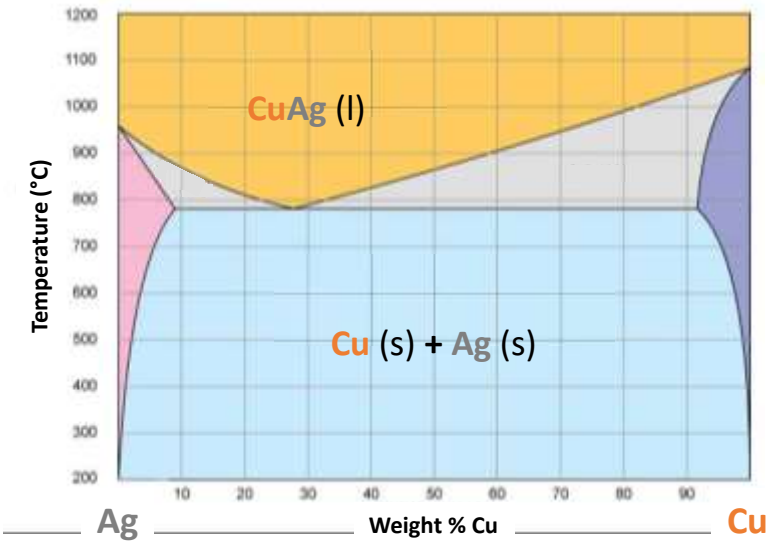

Figure S6.5 *– Cu-Ag phase diagram.*

6.6.5 Potentiostatic Electrochemical Impedance Spectroscopy

Potentiostatic electrochemical impedance spectroscopy (PEIS) was conducted in order to determine the total uncompensated resistance (R_u) of the electrochemical cell. Potential waveforms, centered at the open circuit potential, were applied to the electrochemical cell with a sinus amplitude of 20 mV and frequencies ranging from 50 Hz to 500 kHz, with 10 different frequencies tested per decade. The average of 10 measurements at each frequency were used to construct a Bode plot, as shown in Figure S6.6A. Using the Bode plot, the characteristic frequency and uncompensated resistance of the electrochemical cell were determined to be ~6 kHz and ~50 Ω, respectively.

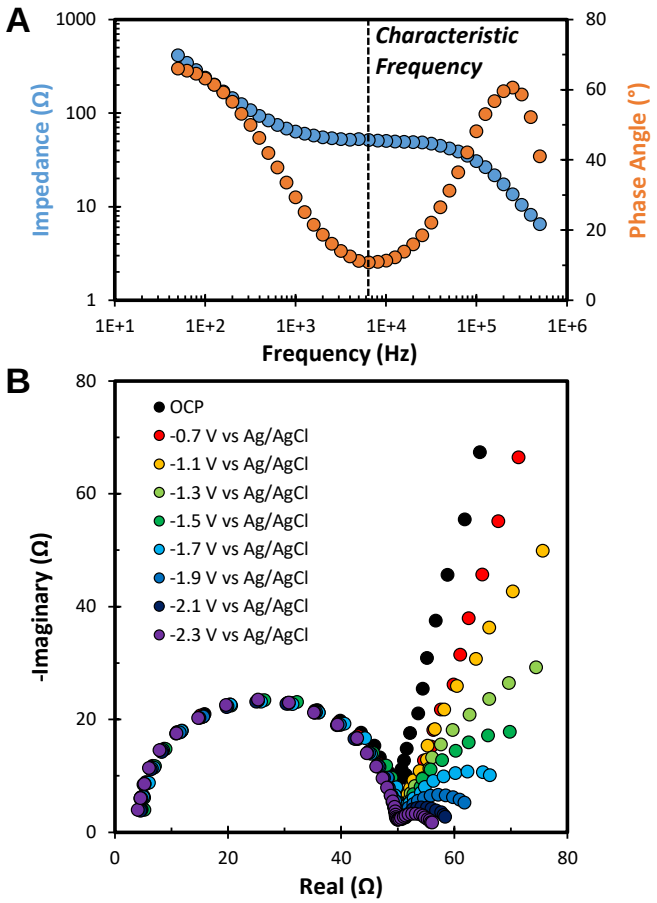

Figure S6.6 *– (A) Bode diagram obtained by applying voltage waveforms with the potential centered at the open circuit potential. (B) Nyquist plot obtained by applying voltage waveforms with the applied potential centered increasingly negative values.*

The Bode plot obtained with the applied potential centered at the open circuit potential includes contributions from the uncompensated resistance as well as the working electrode-electrolyte interface. In order to confirm the value of the uncompensated resistance the PEIS measurements were repeated with the voltage waveforms centered at increasingly negative applied potentials. The resulting Nyquist plot, shown in Figure S6.6B, corroborates the conclusion that the correct value of the uncompensated resistance is ~50 Ω.

6.6.6 Gas Chromatography

Gas chromatography (GC) was utilized to quantify the concentration of reaction products in the electrochemical cell effluent, which was sampled after the first 10 min of electrolysis and every 14 min thereafter. A typical gas chromatogram is depicted in Figure S6.7A. This chromatogram was obtained by analyzing a standard gas mixture containing 1000 ppm of H_2, CO, CH_4, C_2H_4, and C_2H_6 balanced in He. The signal response of the PDHID was calibrated by analyzing a series of standard gas mixtures. The resulting calibration curves are depicted in Figure S6.7B.

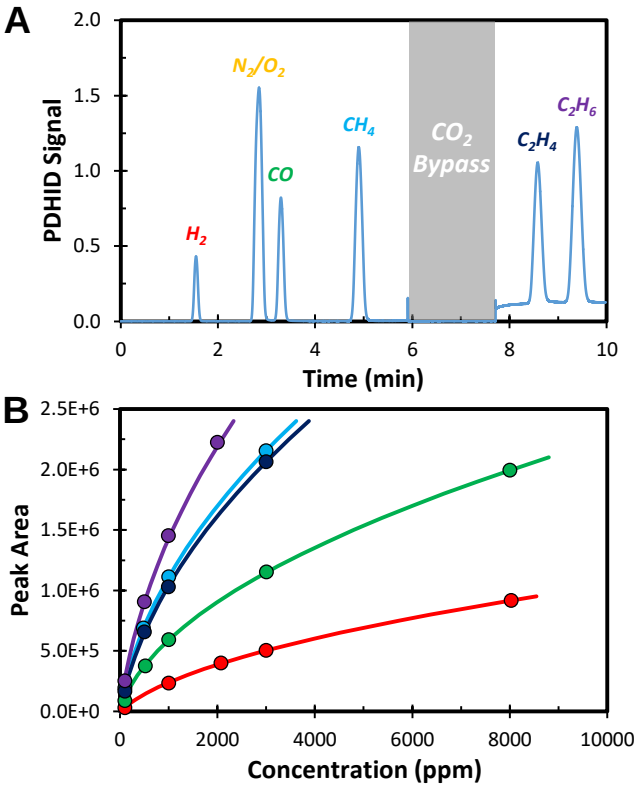

Figure S6.7 *– (A) Representative gas chromatogram containing all of the gaseous products expected during CO_2RR. (B) Calibration curves of all the gaseous products expected during CO_2RR.*

6.6.7 High Performance Liquid Chromatography

High performance liquid chromatography (HPLC) was utilized to quantify the reaction products dissolved in the electrolyte. The electrolyte samples collected after chronoamperometry were stored in a refrigerated autosampler until analyzed in order to minimize the evaporation of volatile liquid-phase reaction products. A typical liquid chromatogram is depicted in Figure S6.8A. This chromatogram was obtained by analyzing a standard solution containing ~10 mM of every liquid-phase product expected during CO_2RR. The signal response of the RID was calibrated by analyzing standard solutions of each product at a concentration of 1, 10, and 50 mM. The resulting calibration curves are depicted in Figure S6.8B.

It is apparent from Figure S6.8A that all of the liquid-phase products are well resolved with the exception of allyl alcohol, ethanol, and propionaldehyde. To determine if peak overlap between these products compromises accurate quantification, standard solutions of these products were prepared at the maximum concentrations expected to be observed in the catholyte after conducting CO_2RR for 70 min. As shown in Figure S6.8C, these products can be resolved by dividing the signal response into three distinct regions.

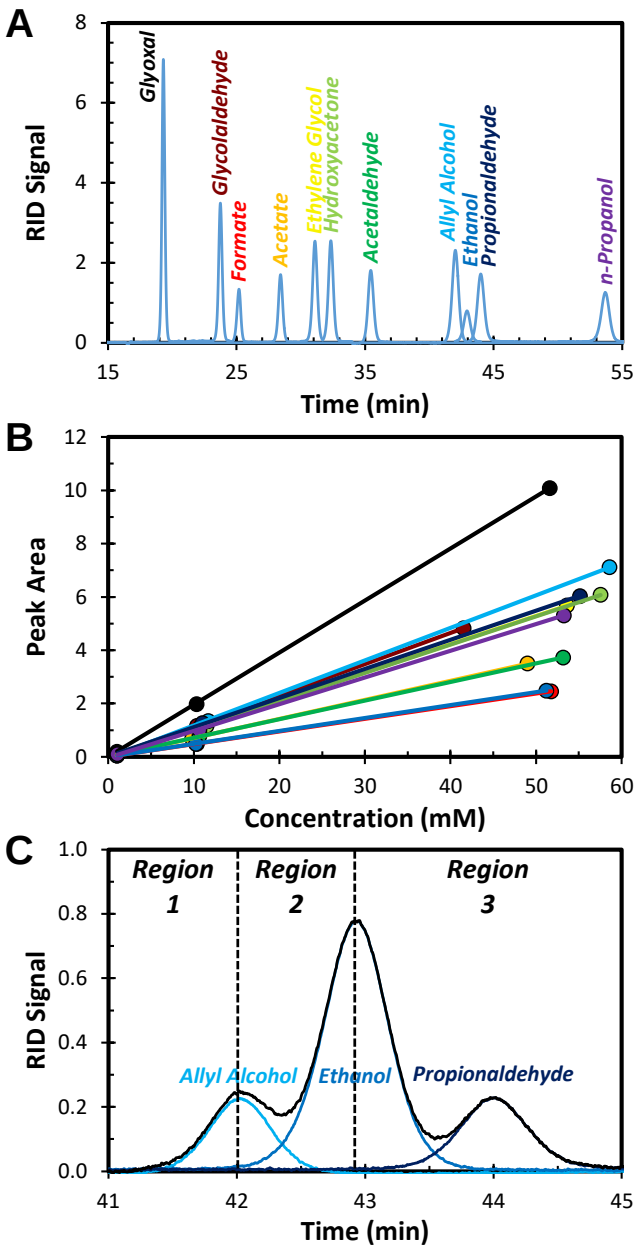

Figure S6.8 *– (A) Liquid chromatogram obtained by analyzing a standard solution containing ~10 mM of all liquid-phase products expected during CO_2RR. (B) Liquid-phase product calibration curves. (C) Deconvolution of the RID signal corresponding to allyl alcohol, ethanol, and propionaldehyde.*

6.6.8 Symmetric X-Ray Diffraction of the Bimetallic Electrodes

Symmetric x-ray diffraction (XRD) measurements (θ/2θ) were conducted using Cu Kα radiation (40 kV, 40 mA) in order to analyze the bulk crystal structure of the CuAg bimetallic electrodes. The diffractometer was equipped with parallel beam optics and a 0.5° parallel slit analyzer in order to mitigate measurement errors arising from the surface curvature of the bimetallic foils. The resulting diffractograms are depicted in Figure S6.9. The composition and average crystallite size of the observed phases were calculated using Vegard's law and the Scherrer equation, respectively. The results, summarized in Table S6.1, suggest that the extent of alloying is limited to 3 at. % on average, with the Cu phase undergoing slightly more alloying than the Ag phase.

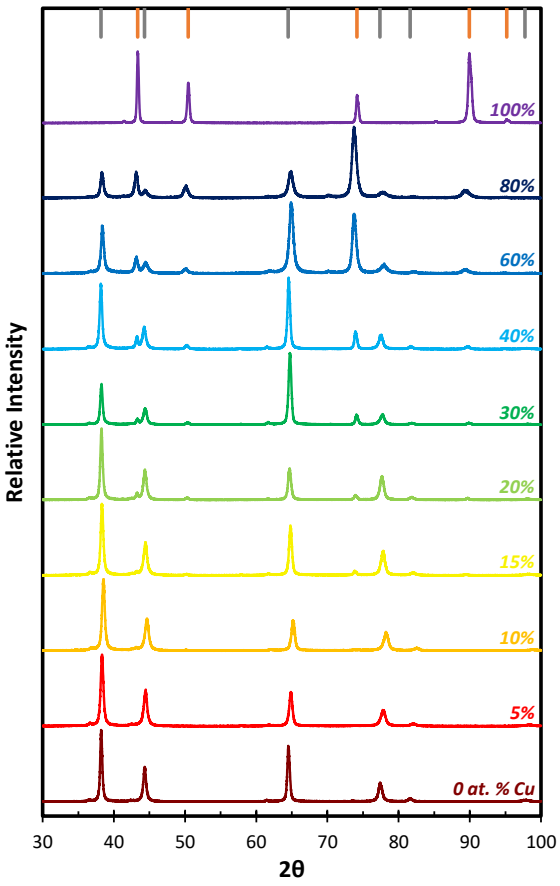

Figure S6.9 *– Symmetric x-ray diffractograms of the CuAg bimetallic electrodes.*

Table S6.1 *– Average composition and crystallite size of the Cu and Ag phases present in the bulk of the CuAg bimetallic electrodes.*

	Cu Phase	*Ag Phase*
Composition (at. %)	96.8% ± 1.9%	97.7% ± 1.9%
Size (nm)	25.7 ± 6.6	21.8 ± 4.0

6.6.9 Asymmetric X-Ray Diffraction of the Bimetallic Electrodes

Asymmetric grazing incidence x-ray diffraction (GIXRD) measurements (2θ) were conducted using Cu Kα radiation (40 kV, 40 mA) with an incident angle of 0.5° in order to analyze the near-surface crystal structure of the CuAg bimetallic electrodes. The diffractometer was equipped with parallel beam optics and a 0.5° parallel slit analyzer in order to mitigate measurement errors arising from the surface curvature of the bimetallic foils. The resulting diffractograms are depicted in Figure S6.10. The composition and average crystallite size of the observed phases were calculated using Vegard's law and the Scherrer equation, respectively. The results, summarized in Table S6.2, suggest that the extent of alloying is limited to 3 at. % on average, with the Cu phase undergoing slightly more alloying than the Ag phase. The results suggest that the extent of alloying near the electrode surface is consistent with what is observed in the bulk.

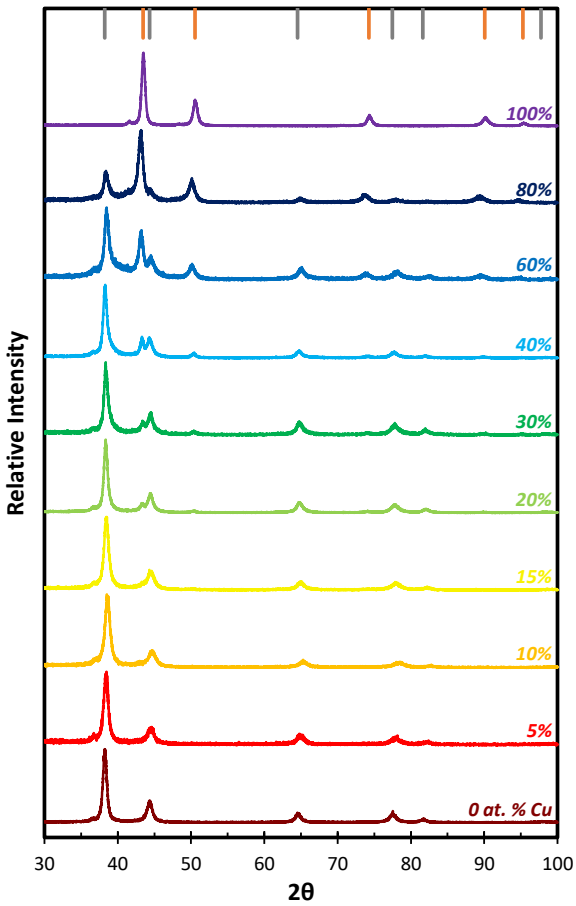

Figure S6.10 *– Asymmetric grazing incidence x-ray diffractograms of the CuAg bimetallic electrodes.*

Table S6.2 *– Average composition and crystallite size of the Cu and Ag phases present near the surface of the CuAg bimetallic electrodes.*

	Cu Phase	*Ag Phase*
Composition (at. %)	96.9% ± 2.5%	97.9% ± 1.2%
Size (nm)	13.2 ± 2.8	11.6 ± 1.2

6.6.10 Near-Surface Crystallite Orientation vs Bulk Composition of the Bimetallic Electrodes

The relative intensities of the diffraction peaks associated with the Cu and Ag phases near the electrode surface, as measured by GIXRD, are depicted in Figures S6.11A and S6.11B, respectively, as a function of the bulk composition of the bimetallic electrodes. It is apparent that the crystallites in both phases are preferentially oriented in the (111) direction near the electrode surface and that this preferential orientation is independent of the bulk composition of the bimetallic electrodes. Preferential orientation of the crystallites in the (111) direction near the surface is expected due to the low surface energy of this facet termination.

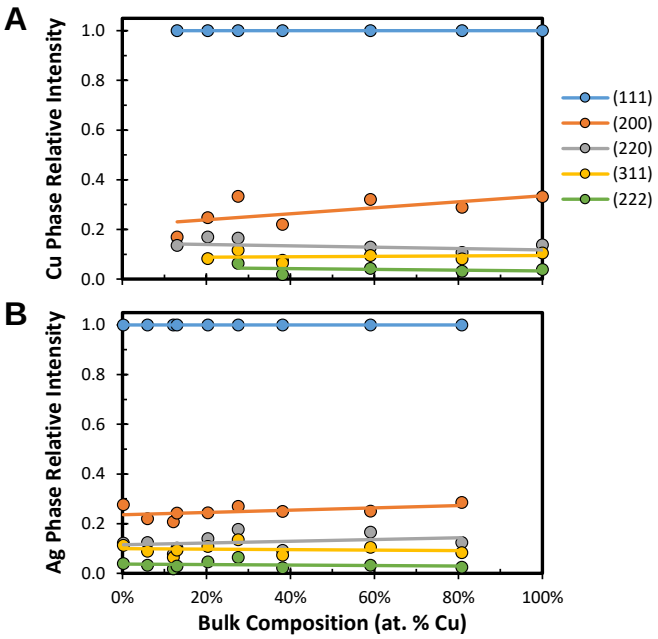

Figure S6.11 *– Relative intensity of the GIXRD peaks associated with: (A) the Cu phase and (B) the Ag phase.*

6.6.11 Energy Dispersive Spectroscopy of the Bimetallic Electrodes

Energy dispersive spectroscopy (EDS) was conducted in order to quantify the bulk composition of the CuAg bimetallic electrodes. Elemental quantification was conducted by measuring the x-ray emission from the Cu K and the Ag L levels upon excitation with an electron beam (15 kV). The observed EDS spectra are depicted in Figure S6.12A. The measured bulk compositions were in good agreement with what was intended, as shown in Figure S6.12B. Furthermore, each bimetallic electrode was analyzed at 10 distinct positions in order to assess the spatial uniformity of the bulk composition. The standard deviation of the measured composition was <1 at. % for all the bimetallic electrodes, indicating that they are compositionally uniform at the micron length scale.

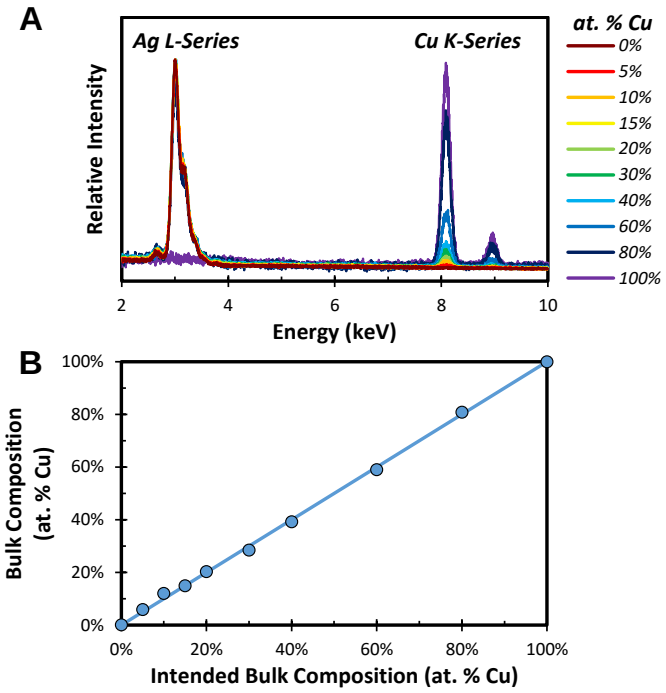

Figure S6.12 *– (A) Energy dispersive spectra of the CuAg bimetallic electrodes. (B) Correlation between the measured and the intended bulk composition of the CuAg bimetallic electrodes.*

6.6.12 X-Ray Photoelectron Spectroscopy of the Bimetallic Electrodes

X-ray photoelectron spectroscopy (XPS) was conducted in order to quantify the near-surface composition of the CuAg bimetallic electrodes. All spectra were acquired using monochromatized Al Kα radiation (15 kV, 15 mA). Ar sputtering of the sample surface was avoided in order to prevent composition changes resulting from the nonequivalent sputtering rates of Cu and Ag. The energy scale of the measured core level spectra were calibrated by setting the observed C 1s binding energy to 284.8 eV. The resulting Cu 2p and Ag 3d spectra are depicted in Figures S6.13A and S6.13B, respectively. Elemental quantification was conducted by integrating the Cu 2p and Ag 3d spectral features using a Shirley background and normalizing their integrated areas by an internally calibrated relative sensitivity factor:

$$RSF = \frac{A_{Cu\ 2p,x=100\%}}{A_{Ag\ 3d,x=0\%}}$$

$$x_{Cu} = \frac{\frac{A_{Cu\ 2p}}{RSF}}{\frac{A_{Cu\ 2p}}{RSF} + A_{Ag\ 3d}}$$

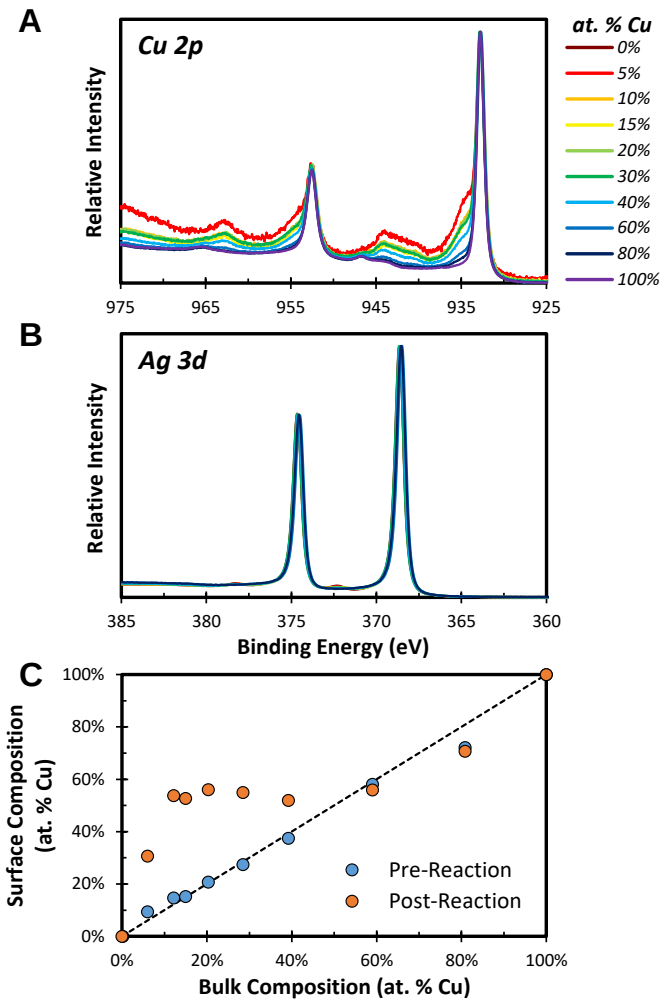

Figure S6.13 *– XPS spectra of the CuAg bimetallic electrodes corresponding to: (A) Cu 2p and (B) Ag 3d. (C) Correlation between the near-surface and bulk compositions of the CuAg bimetallic electrodes before and after chronoamperometry.*

Where:

RSF	Relative Sensitivity Factor
$A_{Cu\ 2p,\ x\ =\ 100\%}$	Cu 2p Area Observed over Pure Cu
$A_{Ag\ 3d,\ x\ =\ 0\%}$	Ag 3d Area Observed over Pure Ag
x_{Cu}	Near-Surface Cu Composition
$A_{Cu\ 2p}$	Observed Cu 2p Area
$A_{Ag\ 3d}$	Observed Ag 3d Area

The near-surface compositions of the as-prepared CuAg bimetallic electrodes were determined to be completely consistent with the bulk composition before

chronoamperometry, as depicted in Figure S6.13C. However, after chronoamperometry the Ag-rich bimetallic electrodes were determined to have a higher near-surface Cu content. Thus, it was concluded that the bimetallic electrodes undergo Cu surface enrichment over the course of electrolysis.

6.6.13 Ion Scattering Spectroscopy of the Bimetallic Electrodes

Ion scattering spectroscopy (ISS) was conducted in order to quantify the surface composition of the CuAg bimetallic electrodes. All spectra were acquired using a focused He ion beam (1 kV). The resulting spectra are depicted in Figure S6.14A. Elemental quantification was conducted by integrating the Cu and Ag spectral features using a linear background and normalizing their integrated areas by an internally calibrated relative sensitivity factor. Since ISS is a line-of-sight technique accurate quantification must take into account changes in the fraction of the surface atoms that are oxidized as the composition changes. This was done by creating an oxygen-dependent relative sensitivity factor and assuming that the fraction of Ag surface atoms that are oxidized is independent of the bulk composition. The validity of this assumption is confirmed by the consistency of the normalized Ag 3d core level spectra shown in Figure S6.13B. The relevant equations are as follows:

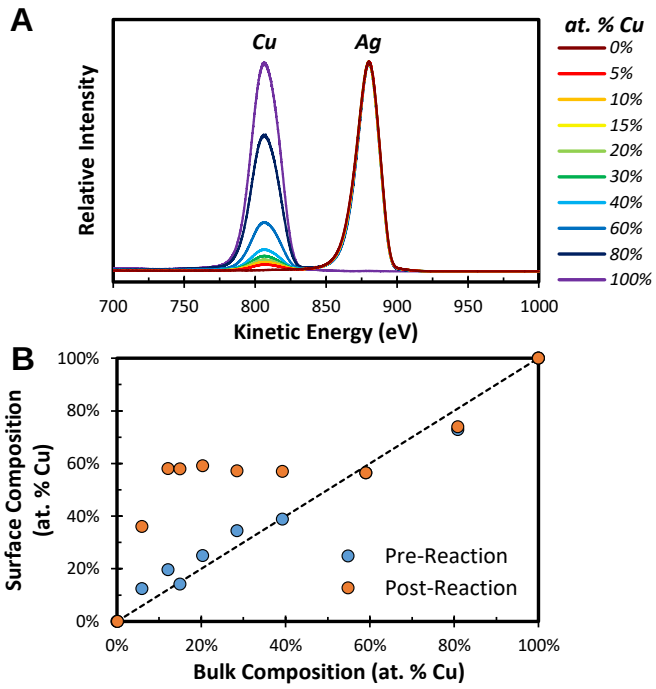

Figure S6.14 *– (A) ISS spectra of the CuAg bimetallic electrodes. (B) Correlation between the surface and bulk compositions of the CuAg bimetallic electrodes before and after chronoamperometery.*

$$RSF = \frac{A_{Cu}A_{O,x=100\%}}{A_O A_{Ag,x=0\%} - A_{Ag}A_{O,x=0\%}}$$

$$x_{Cu} = \frac{\frac{A_{Cu}}{RSF}}{\frac{A_{Cu}}{RSF} + A_{Ag}}$$

Where:

RSF	Relative Sensitivity Factor
A_{Cu}	Observed Cu Area
$A_{O,\ x\ =\ 100\%}$	O Area Observed over Pure Cu
A_O	Observed O Area
$A_{Ag,\ x\ =\ 0\%}$	Ag Area Observed over Pure Ag
A_{Ag}	Observed Ag Area
$A_{O,\ x\ =\ 0\%}$	O Area Observed over Pure Ag
x_{Cu}	Surface Cu Composition

The surface composition of the as-prepared CuAg bimetallic electrodes was determined to be completely consistent with the bulk composition before chronoamperometry, as depicted in Figure S6.14B. However, after chronoamperometry the Ag-rich bimetallic electrodes were determined to have a higher surface Cu content, as shown in Figure S6.14B. Thus, it was concluded that the bimetallic electrodes undergo Cu surface enrichment over the course of electrolysis.

6.6.14 Transient Reaction Selectivity of the Bimetallic Electrodes

Unlike pure Cu and Ag, all of the bimetallic electrodes displayed changes in reaction selectivity with time, as shown in Figure S6.15A. These transient changes were characterized by a decreased selectivity for CO and an enhanced selectivity for products derived from CO over time and were more significant for the Ag-rich bimetallic electrodes. As shown in Figure S6.15B, the Ag-rich bimetallic electrodes undergo significant Cu surface enrichment over the course of electrolysis. The correlation between the magnitudes of the transient selectivity changes with the magnitudes of the Cu surface enrichment suggests that the segregation of Cu to the electrode surface is what causes the transient selectivity changes. The driving force for the segregation of Cu to the electrode surface is hypothesized to be the stronger interaction of CO with Cu than Ag. This suggests that the Cu which segregates to the electrode surface is initially dissolved in the Ag phase. This hypothesis is corroborated by the correlation between the magnitude of the Cu surface enrichment and the fraction of Cu contained in the bimetallic electrodes that is initially dissolved in the Ag phase, which is shown in Figure S6.15C. The fraction of Cu initially dissolved in the Ag phase was calculated using the following equation:

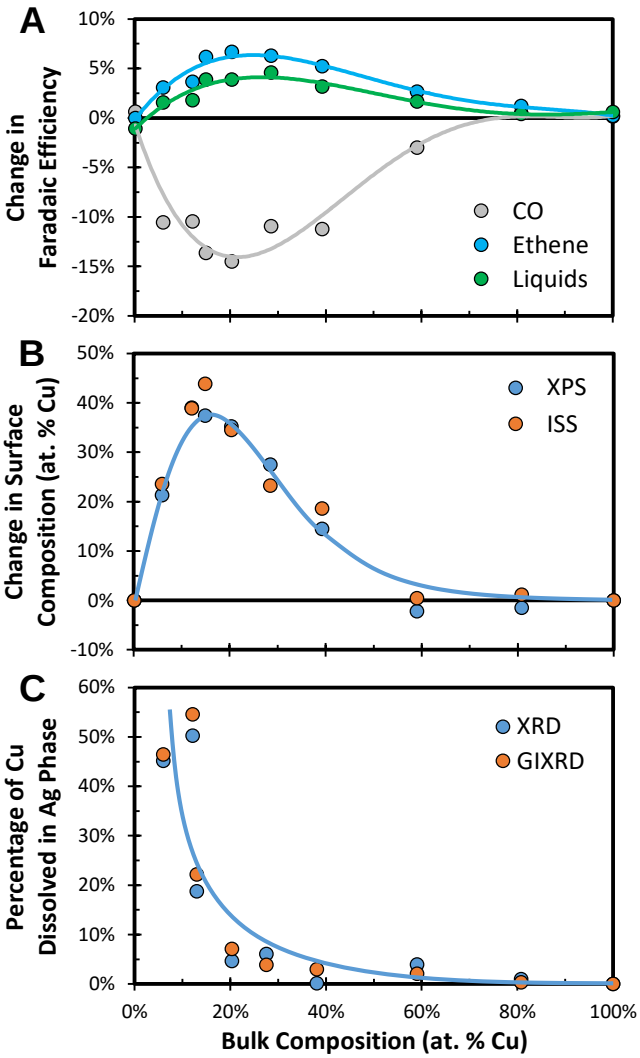

Figure S6.15 *– (A) Magnitude of the transient changes in reaction selectivity observed over the bimetallic electrodes. (B) Magnitude of the Cu surface enrichment observed over the bimetallic electrodes. (C) Percentage of Cu contained in the bimetallic electrodes that is initially dissolved in the Ag phase.*

$$\%\ Cu\ in\ Ag\ Phase = \frac{\frac{\sum I_{Ag(hlk)}}{\sum I_{Ag(hlk)} + \sum I_{Cu(hkl)}} \frac{\sum I_{Ag(hlk)} x_{Cu\ in\ Ag(hlk)}}{\sum I_{Ag(hlk)}}}{x_{Cu}}$$

Where:

% Cu in Ag Phase	Fraction of Cu Initially Dissolved in the Ag Phase
$I_{Ag(hlk)}$	Intensity of Ag(hlk) Diffraction Peak
$I_{Cu(hlk)}$	Intensity of Cu(hkl) Diffraction Peak
$x_{Cu\ in\ Ag(hlk)}$	Cu Content of Ag(hkl) Diffraction Peak (Vegard's Law)
x_{Cu}	Bulk Composition (EDS)

6.6.15 Steady State CO_2 Consumption Rates of the Bimetallic Electrodes

In order to determine the diffusion-limited flux of CO_2 to the cathode surface the CO_2 consumption rate of polycrystalline Ag was measured as a function of the applied current density. Using this method, the CO_2 diffusion limited flux of was determined to be ~35 nmol/s*cm^2, as shown in Figure S6.16A. As shown in Figure S6.16B, the CO_2 consumption rate over the bimetallic electrodes was well below the diffusion limited flux. Thus, observed product distributions are expected to be negligibly impacted by mass transfer effects.

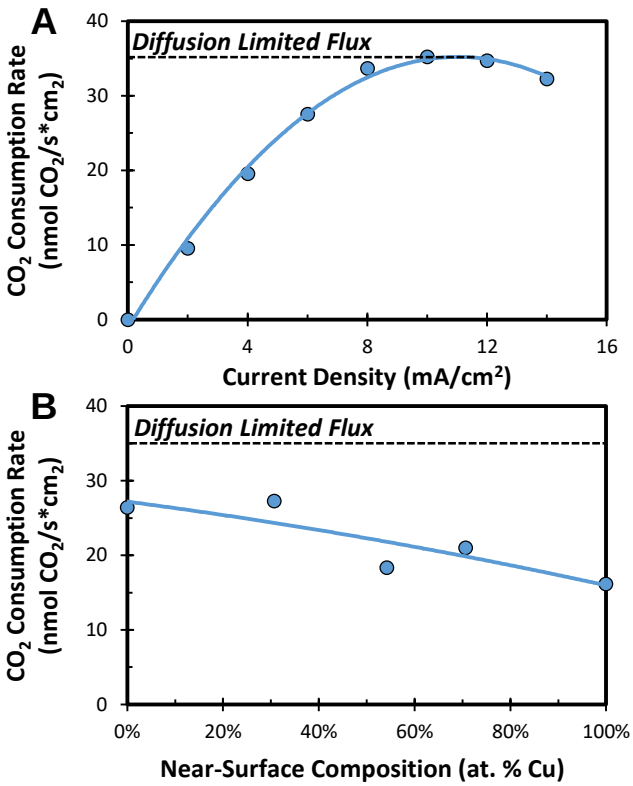

Figure S6.16 *– (A) CO_2 consumption rate over polycrystalline Ag as a function of the applied current density. (B) CO_2 consumption rate observed over the bimetallic electrodes as a function of the steady-state near-surface composition.*

6.6.16 Steady State Reaction Selectivity of the Bimetallic Electrodes

The steady state selectivity observed over the bimetallic electrodes is shown in Figure S6.17. Bimetallic electrodes with bulk compositions of 20-60 at. % Cu display a nearly equivalent reaction selectivity at steady state because they all possess the same surface composition at steady state.

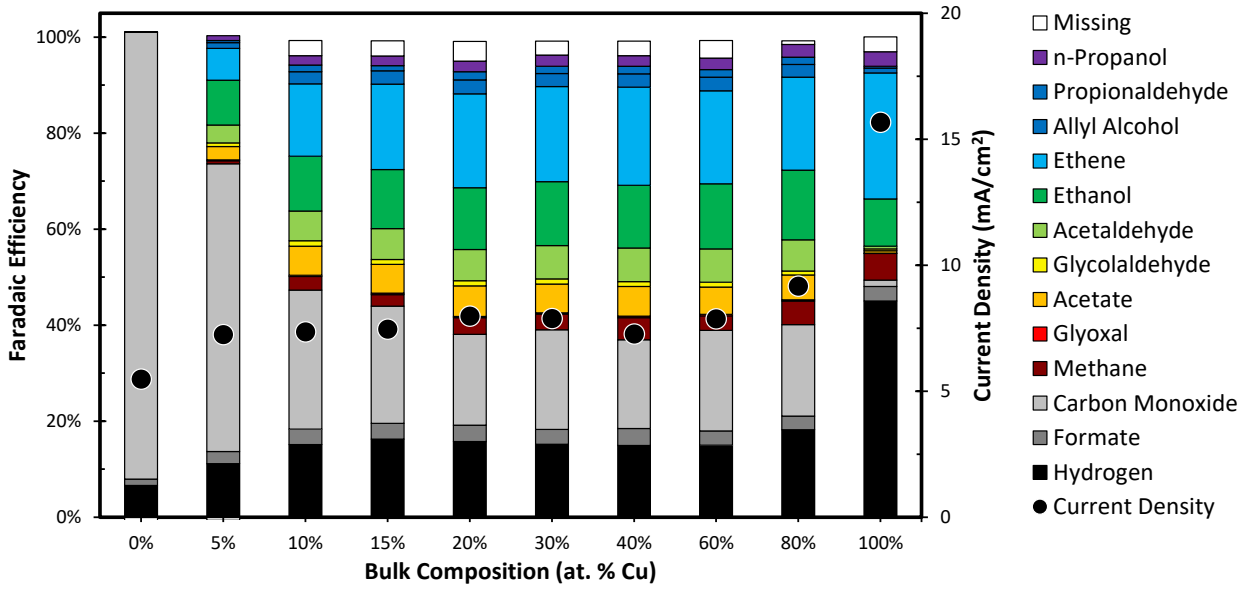

Figure S6.17 *– Steady state reaction selectivity observed over the bimetallic electrodes.*

6.6.17 Cu Foil + Ag Mesh Experiments

In order to determine if an elevated local CO concentration significantly impacts the distribution of products derived from CO over Cu, experiments were conducted over a Ag mesh backed by a Cu foil. The Cu foil and the Ag mesh were tightly pressed together in order to minimize their separation distance and to ensure electrical continuity between them. The product distribution observed over the Cu foil + Ag mesh is depicted in Figure S6.18A, along with the product distribution observed over the Cu foil, the Ag mesh, and a nominal CuAg bimetallic electrode under the same reaction conditions. The distribution of products derived from CO was calculated in order to facilitate an accurate comparison, as shown in Figure S6.18B. It is apparent that the distribution of products derived from CO observed over the Cu foil + Ag mesh closely resembles that observed over Cu foil alone, suggesting that an elevated local CO concentration is not the cause of the unique product distribution observed over the CuAg bimetallic electrodes.

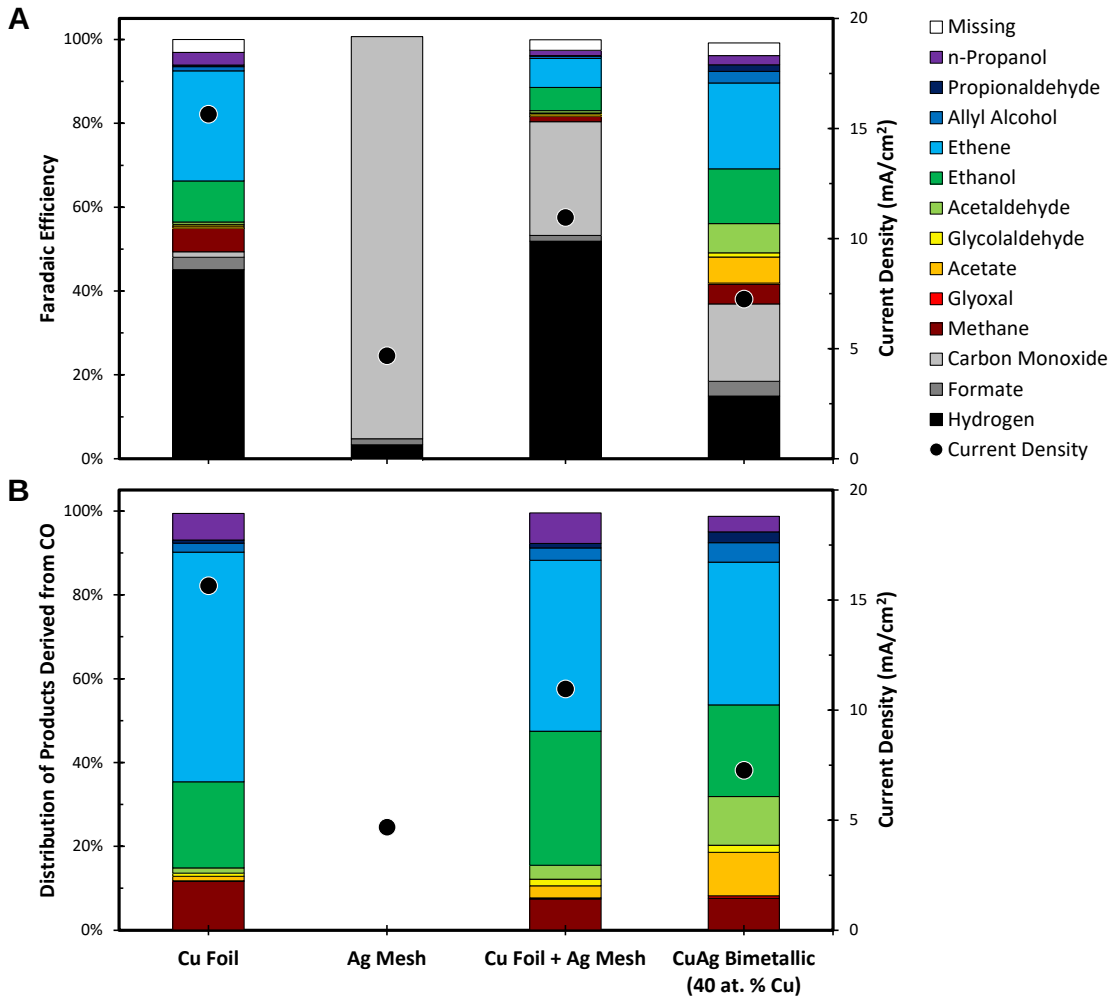

Figure S6.18 *– Comparison of a Cu foil, Ag mesh, Cu foil + Ag mesh, and a nominal CuAg bimetallic electrode at steady state: (A) reaction selectivity and (B) distribution of products derived from CO.*

6.6.18 Out-of-Plane and In-Plane X-Ray Diffraction of the Cu(100) Thin Films

Symmetric x-ray diffraction (XRD) measurements (θ/2θ) were conducted using Cu Kα radiation (40 kV, 40 mA) in order to determine the out-of-plane growth orientation of the Cu crystallites in the thin films sputtered onto Si(100). As shown in Figure S6.19A, the presence of the Cu(200) diffraction peak and the absence of all other Cu diffraction peaks indicates that the Cu thin films are oriented in the (100) direction with the relationship Cu(100)‖Si(100).

In-plane phi scans were conducted at the Bragg conditions corresponding to Si(111) and Cu(111) in order to determine if the Cu crystallites were preferentially oriented with respect to the Si single crystal substrates. As shown in Figure S6.19B, the in-plane Cu(111) intensity displayed the 4-fold symmetry characteristic of Cu(100). Furthermore, the Cu(111) and Si(111) reflections were offset by 45°. These results suggest that the Cu thin film has been deposited epitaxially on the Si(100) substrate.

Out-of-plane rocking curve scans were conducted at the Bragg condition corresponding to Cu(200) in order to determine the degree of misorientation in the epitaxial films deposited on Si(100), as shown in Figure S6.19C. The fwhm of the resulting rocking curve scan was ~2.3°, which is in agreement with what has been reported elsewhere.[5,6]

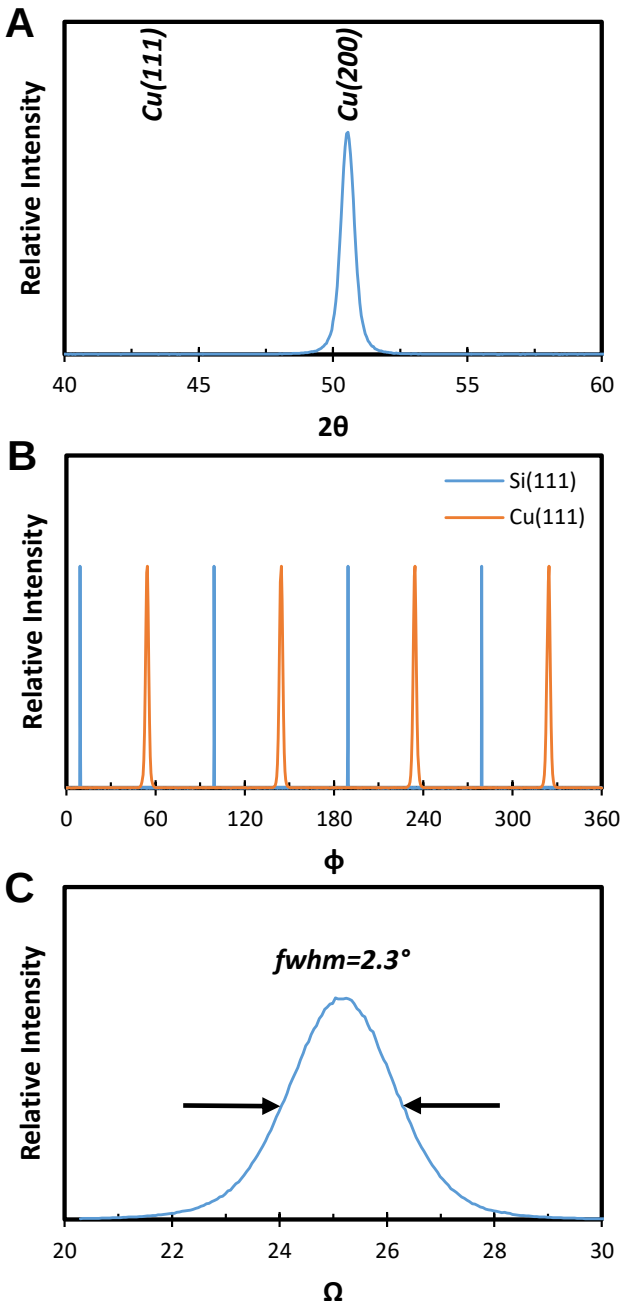

Figure S6.19 *– XRD scans of the Cu thin films sputter deposited onto Si(100): (A) Symmetric out-of-plane scan. (B) In-plane phi scan at the Bragg conditions corresponding to Si(111) and Cu(111). (C) Rocking curve scan at the Bragg condition corresponding to Cu(200).*

6.6.19 X-Ray Photoelectron Spectroscopy of the Cu(100)+Ag Electrodes

X-ray photoelectron spectroscopy (XPS) was conducted in order to quantify the near-surface composition of the Cu(100)+Ag electrodes. All spectra were acquired using monochromatized Al Kα radiation (15 kV, 15 mA). Ar sputtering of the sample surface was avoided in order to prevent composition changes resulting from the nonequivalent sputtering rates of Cu and Ag. The energy scale of the measured core level spectra were calibrated by setting the observed C 1s binding energy to 284.8 eV. The resulting Cu 2p and Ag 3d spectra are depicted in Figures S6.20A and S6.20B, respectively. Elemental quantification was conducted by integrating the Cu 2p and Ag 3d spectral features using a Shirley background and normalizing their integrated areas by an internally calibrated relative sensitivity factor:

$$RSF = \frac{A_{Cu\ 2p,x=100\%}}{A_{Ag\ 3d,x=0\%}}$$

$$x_{Cu} = \frac{\frac{A_{Cu\ 2p}}{RSF}}{\frac{A_{Cu\ 2p}}{RSF} + A_{Ag\ 3d}}$$

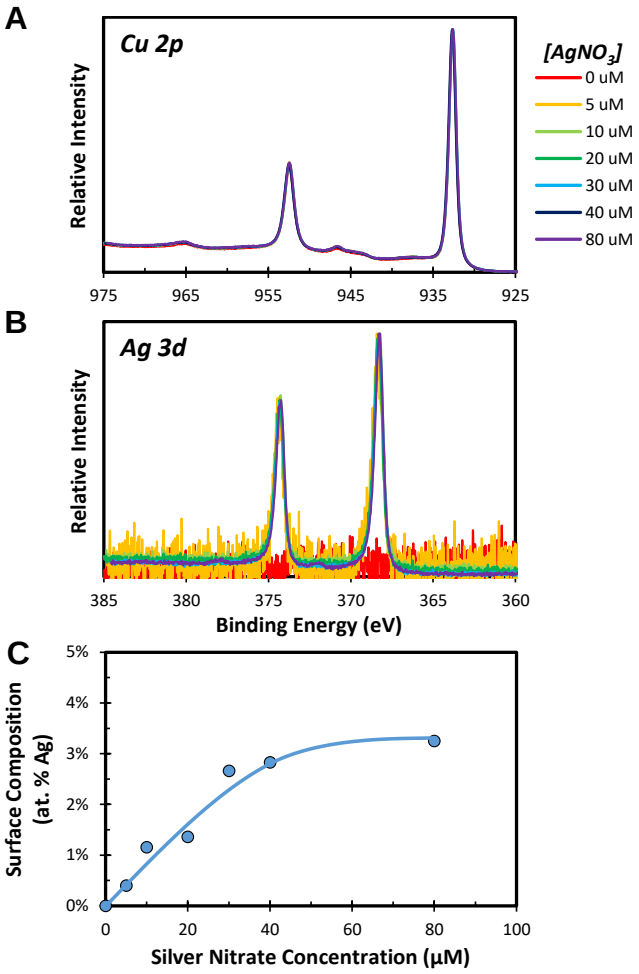

Figure S6.20 *– XPS spectra of the Cu(100)+Ag electrodes corresponding to: (A) Cu 2p and (B) Ag 3d. (C) Correlation between the near-surface compositions of the Cu(100)+Ag electrodes with the $AgNO_3$ concentration in the Galvanic exchange solution.*

Where:

RSF	Relative Sensitivity Factor
$A_{Cu\ 2p,\ x\ =\ 100\%}$	Cu 2p Area Observed over Pure Cu Film
$A_{Ag\ 3d,\ x\ =\ 0\%}$	Ag 3d Area Observed over Pure Ag Film
x_{Cu}	Near-Surface Cu Composition
$A_{Cu\ 2p}$	Observed Cu 2p Area
$A_{Ag\ 3d}$	Observed Ag 3d Area

The near-surface composition of the as-prepared Cu(100)+Ag electrodes was found to increase linearly with the concentration of $AgNO_3$ in the Galvanic exchange solution up to ~40 μM, as depicted in Figure S6.20C. The reduced rate of Ag incorporation at higher $AgNO_3$ concentrations could be a result of the saturation of the Cu(100)+Ag surface alloy.

6.6.20 Ion Scattering Spectroscopy of the Cu(100)+Ag Electrodes

Ion scattering spectroscopy (ISS) was conducted in order to obtain qualitative information about the surface composition of the Cu(100)+Ag electrodes. All spectra were acquired using a focused He ion beam (1 kV). Quantification of the surface composition was avoided due to concerns with the validity of the assumptions required to quantitatively analyze the data. However, the Ag content of the Cu(100)+Ag electrodes increased with the concentration of $AgNO_3$ in the Galvanic exchange solution, as shown in Figure S6.21A. Furthermore, the integrated area of the Ag ISS peak was observed to scale linearly with the near-surface Ag content, as shown in Figure S6.21B. This correlation suggests that all of the incorporated Ag atoms are located at the electrode surface.

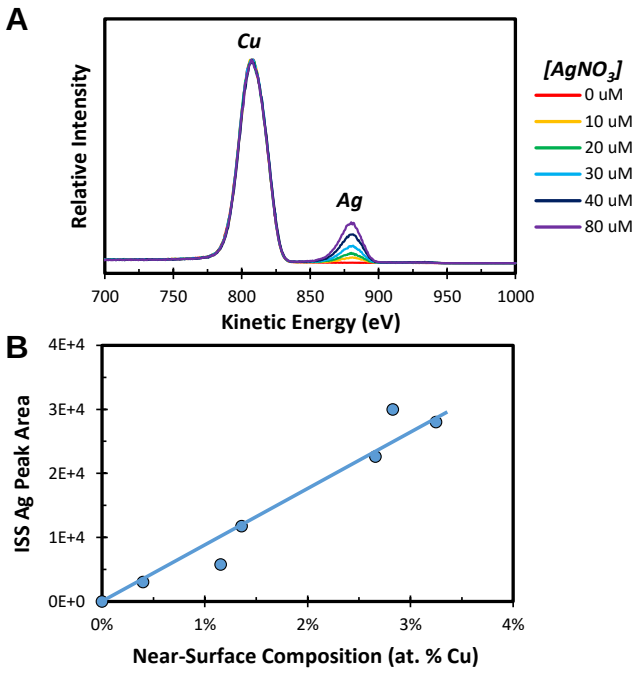

Figure S6.21 *– (A) ISS spectra of the Cu(100)+Ag electrodes. (B) Correlation between the integrated area of the Ag ISS peak and the near-surface composition, as quantified by XPS.*

6.6.21 Steady State Reaction Selectivity of the Cu(100)+Ag Electrodes

The steady state selectivity observed over the Cu(100)+Ag electrodes is shown in Figure S6.22. Unlike the CuAg bimetallic electrodes, the Cu(100)+Ag electrodes did not display significant changes in reaction selectivity with time, suggesting that they do not undergo near-surface composition changes during electrolysis.

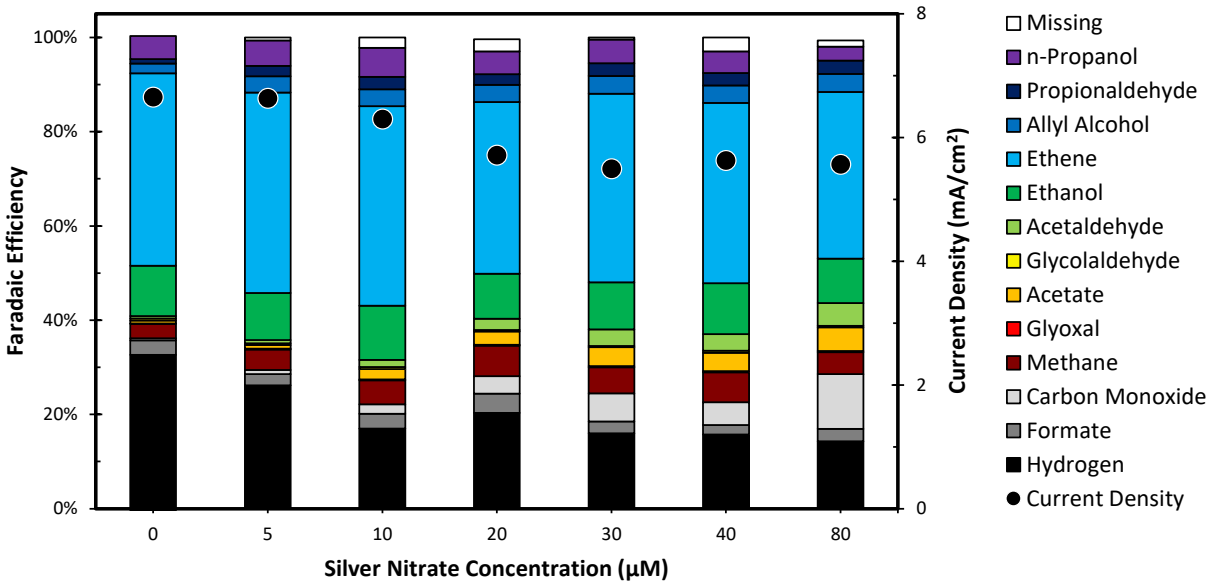

Figure S6.22 *– Steady state reaction selectivity observed over the Cu(100)+Ag electrodes.*

6.6.22 Valence Band Spectroscopy of the Bimetallic Electrodes

X-ray photoelectron spectroscopy (XPS) was utilized to measure the valence band density of states of the CuAg bimetallic electrodes.[7] All spectra were acquired using monochromatized Al Kα radiation (15 kV, 15 mA). The energy scale of the measured valence band spectra were calibrated by setting the maximum rate of signal loss to 0 eV. The valence band density of states of the bimetallic electrodes were measured by collecting photoelectrons emitted normal to the electrode surface (XPS), at an exit angle of 30° (ARXPS), and normal to the electrode surface after 30 s of Ar sputtering (Ar sputtered XPS). The observed valence bands were compared to what would have been expected to be observed had the valence band density of states of the bimetallic electrodes behaved as a linear combination of Cu and Ag. The difference between the observed and calculated spectra was utilized to identify the presence of subtle valence band modifications.

$$RSF = \frac{A_{VB,x=100\%}}{A_{VB,x=0\%}}$$

$$I = \frac{x_{Cu} I_{Cu}}{RSF} + (1 - x_{Cu}) I_{Ag}$$

Where:

RSF	Relative Sensitivity Factor
$A_{VB,x=100\%}$	Integrated Area of the Cu Valence Band
$A_{VB,x=0\%}$	Integrated Area of the Ag Valence Band
I	Intensity of the Calculated Valence Band Spectrum
x_{Cu}	Near-Surface Cu Composition
I_{Cu}	Intensity of the Cu Valence Band Spectrum
I_{Ag}	Intensity of the Ag Valence Band Spectrum

As shown in Figure S6.23, the overall shape of the valence band spectra were found to be dependent on the measurement protocol. However, the deviation of the observed spectra from ideality was found to be independent of composition when the photoelectrons were collected normal to the electrode surface. The consistency of the deviation from ideality corroborates the notion that the Cu phase in the bimetallic electrodes consists of a Cu+Ag surface alloy with a saturated Ag content. Unlike the valence band measurements in which photoelectrons were collected normal to the electrode surface, the valence bands observed when the photoelectrons were collect at a grazing exit angle of 30° did not exhibit substantial deviations from ideality. This is likely due to the fact that the electronic structure very close to the electrode surface will be dominated by perturbations associated with adsorbed O under these conditions.

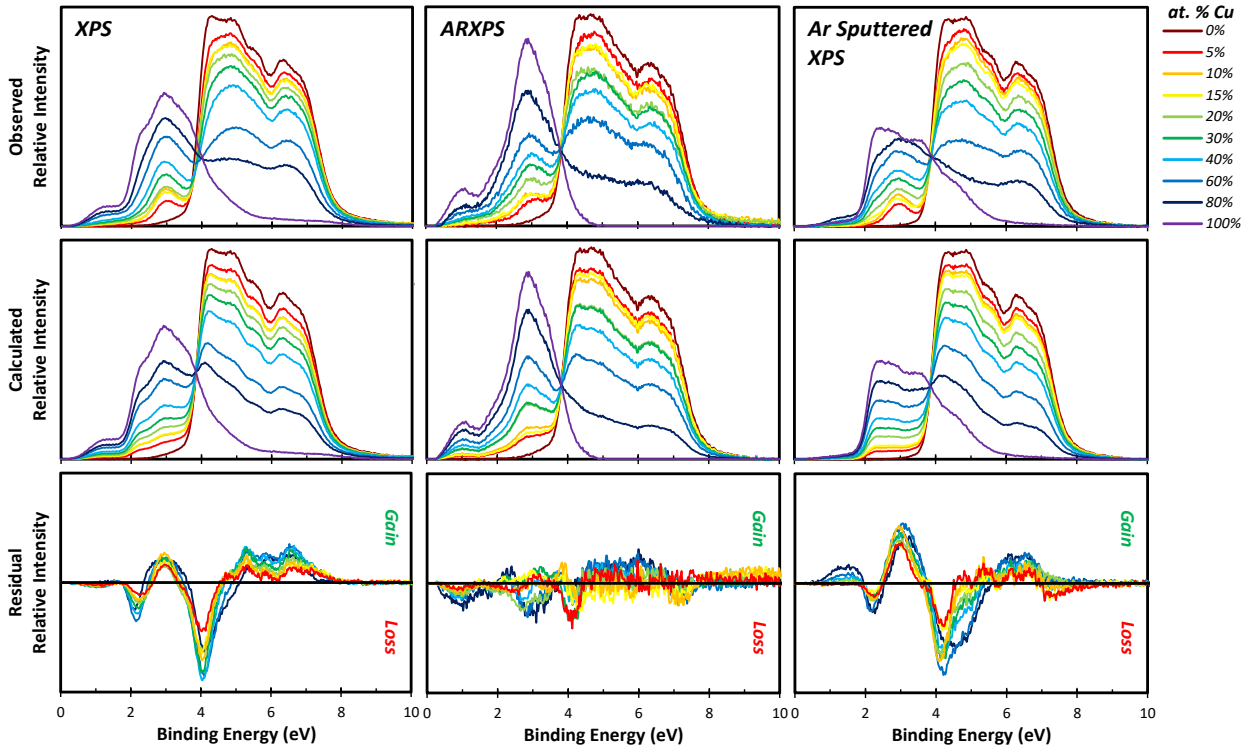

Figure S6.23 *– Valence band density of states of the CuAg bimetallic electrodes measured by XPS using different measurement protocols. The difference between the measured spectra and the calculated spectra were utilized to identify subtle electronic modifications caused by deviations from ideality.*

6.6.23 Peak Fitting of the Cu 2p Core Level Spectra

In order to determine if the near-surface Cu in the bimetallic electrodes is electronically modified by a ligand effect (i.e. a formal electron transfer from Cu to Ag) induced by intimate contact with Ag, peak fitting of the Cu 2p core level spectra was conducted. The Cu 2p core level spectra was measured by collecting photoelectrons emitted normal to the electrode surface (XPS), at an exit angle of 30° (ARXPS), and normal to the electrode surface after 30 s of Ar sputtering (Ar sputtered XPS). The

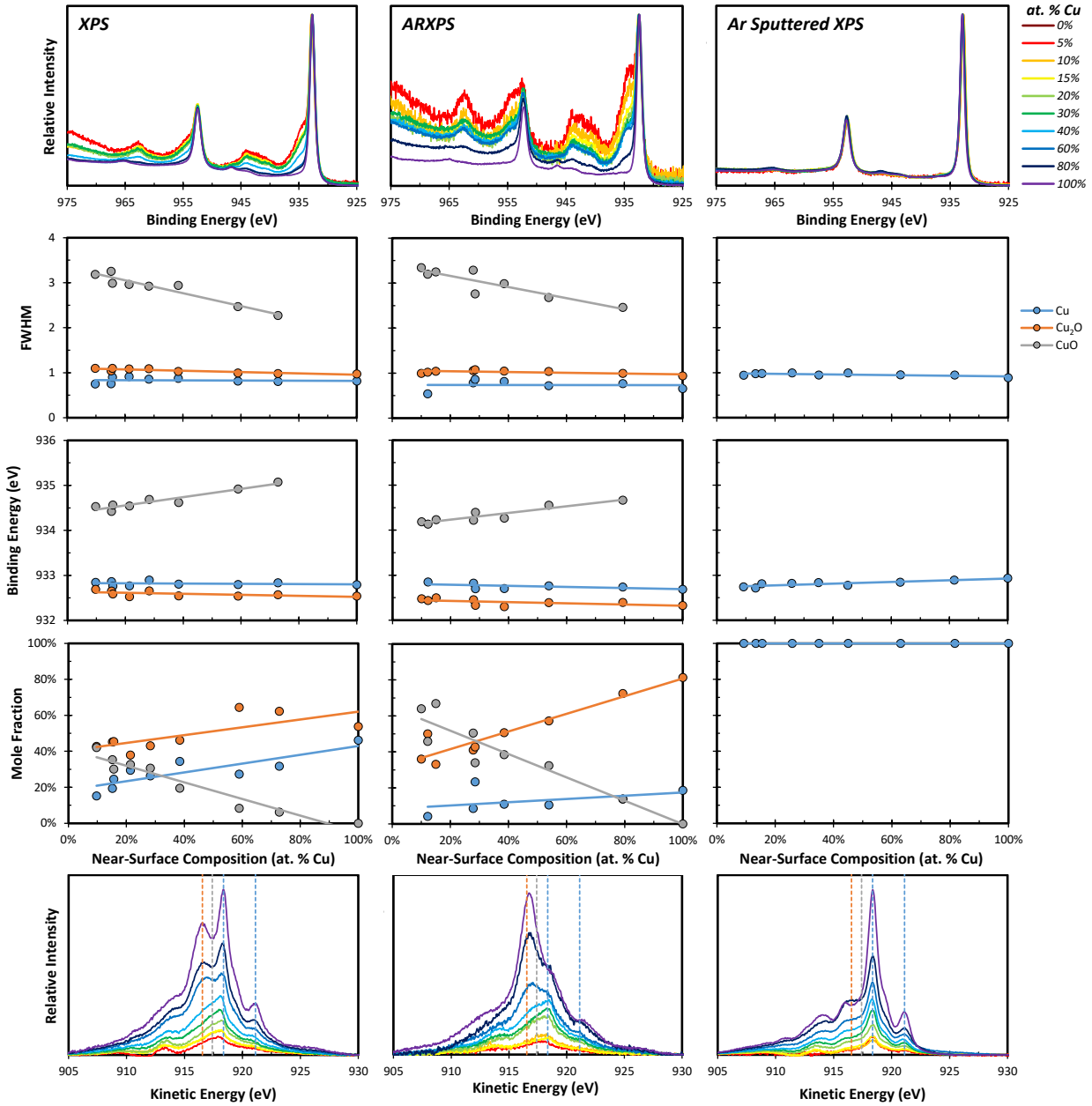

Figure S6.24 *– Cu 2p peak fitting and LMM spectra of the bimetallic electrodes obtained using different measurement protocols.*

observed Cu 2p spectra were then fit to three components representing Cu^0, Cu^{1+}, and Cu^{2+} using the CasaXPS software. The fwhms of the peaks corresponding to each oxidation state were consistent across all samples and measurement protocols, as shown in Figure S6.24. The Cu 2p core level binding energies corresponding to the Cu^0 and Cu^{1+} oxidation states were found to be independent of the near-surface composition of the bimetallic electrodes. Conversely, the Cu 2p core level binding energy corresponding to the Cu^{2+} oxidation state was observed to decrease linearly with the near-surface Ag content. Furthermore, as the near-surface Ag content of the bimetallic electrodes increased more of the near-surface Cu is present as Cu^{2+} at the expense of Cu^0. Additionally, as the penetration depth of the measurement is reduced a greater fraction of the near-surface Cu is present as Cu^{2+} at the expense of Cu^0, as demonstrated by comparing the XPS and ARXPS Cu 2p spectra.

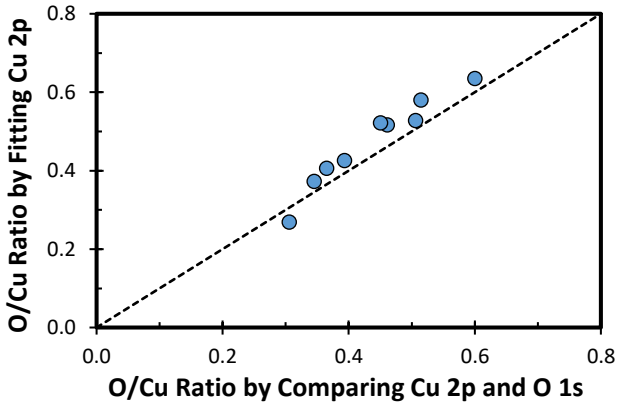

Figure S6.25 *– Comparison of the O/Cu ratio based on the peak fitting of the Cu 2p core level spectra with that calculated by comparing the integrated areas of the Cu 2p and O1s spectral features.*

In order to determine if the enhanced mole fraction of Cu^{2+} at the expense of Cu^0 is a result of a ligand effect or oxidation by O the Cu 2p spectra was measured after 30 s of Ar sputtering, which was determined to be long enough to remove ~70% of the O on the electrode surface. As shown in Figure S6.24, no oxidized Cu phases were observed after the removal of the surface O, suggesting that the oxidized Cu observed by XPS and ARXPS is not oxidized by intimate contact with Ag. To corroborate this conclusion the O/Cu ratio expected based on the fitting of the Cu 2p spectra was compared to the O/Cu ratio observed by integrating the areas of the Cu 2p and O 1s spectral regions. As shown in Figure S6.25, the agreement between the O/Cu ratio calculated using both methods confirms that the oxidized Cu is not the result of a ligand effect induced by Ag and is instead the result of a formal electron transfer from Cu to O.

6.6.24 Correlation between Oxygen Affinity and the Reduction Potential of Transition Metals

The oxophilicity of transition metal surfaces is highly correlated with the standard reduction potential of their corresponding oxides, as depicted in Figure S6.26.[8,9] Thus, the oxophilicity of a transition metal can be estimated by measuring the potential at which the corresponding oxide is reduced, with an anodic shift suggesting that the oxophilicity of the metal surface has been reduced.

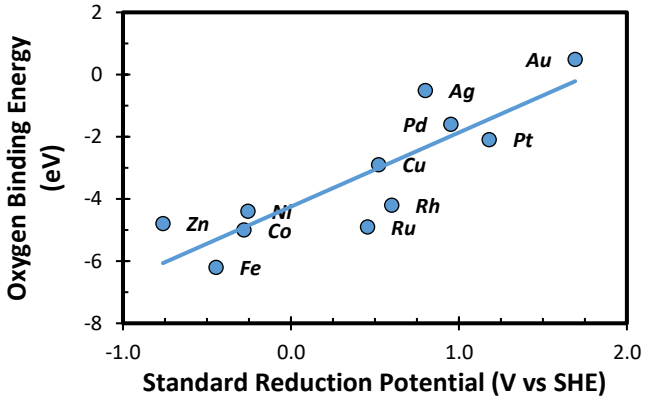

Figure S6.26 *– Correlation between the oxophilicity of transition metals with the standard reduction potential of their corresponding oxides.*

6.6.25 Electrochemical Cycling of the Bimetallic Electrodes

Cyclic voltammetry was conducted in order to determine the redox properties of the constituent metals in the CuAg bimetallic electrodes. The majority of redox waves were observed to scale as a linear combination of Cu and Ag, as shown in Figure S6.27A. However, an anodic shift of the redox wave associated with Cu^{2+}/Cu^{+} reduction was observed upon the addition of Ag into Cu, as shown in Figures S6.27B and S6.27C. The potential at which appreciable Faradaic current was observed was defined as the onset potential. The peak potential was not used since it is convoluted with kinetics effects, which change in magnitude with the composition of the surface. Interestingly, the magnitude of the anodic shift was roughly equivalent for all bimetallic electrodes, corroborating the notion that the surface of the Cu phase in the bimetallic electrodes contains a CuAg surface alloy with a saturated Ag content.

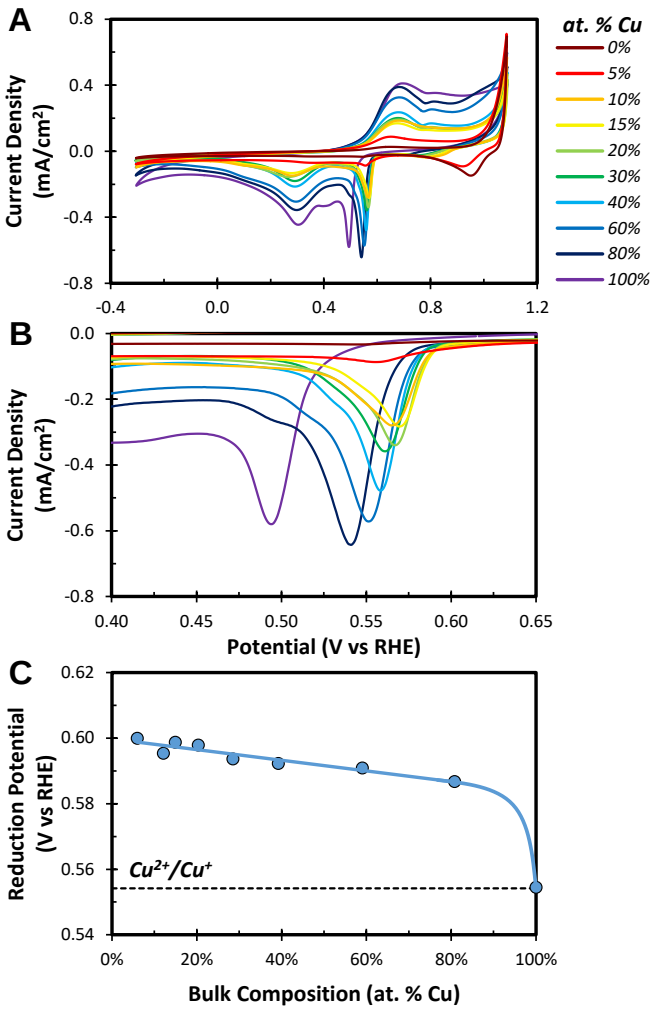

Figure S6.27 *– Results of cyclic voltammetry over the CuAg bimetallic electrodes: (A) Cyclic voltammograms, (B) Cu^{2+}/Cu^{+} reduction waves, and (C) Onset potential of Cu^{2+}/Cu^{+} reduction.*

6.6.26 Acetate to Acetaldehyde Molar Ratio

The molar ratio of acetate to acetaldehyde generated over the bimetallic electrodes was calculated in order to determine if the enhanced production of carbonyl-containing products impacts their relative abundance. As shown in Figure S6.28, the acetate to acetaldehyde ratio observed over the bimetallic electrodes is independent of the absolute generation rate of carbonyl-containing products, suggesting that these two products are mechanistically linked. In fact, it has recently been proposed that acetate forms via a "Cannizzaro-type" disproportionation of acetaldehyde in the relatively alkaline conditions found within the hydrodynamic boundary layer at the cathode surface.[10] Interestingly, the observed molar ratio of acetate to acetaldehyde is equivalent to the equilibrium constant of acetaldehyde hydration in water, suggesting that the formation of 1,1-ethanediol by hydration of acetaldehyde initiates the disproportionation reaction.

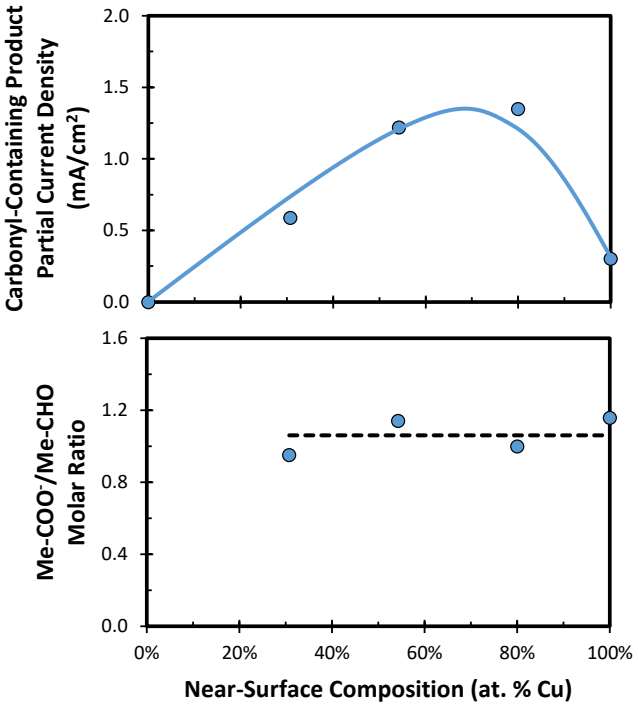

Figure S6.28 *– Total carbonyl-containing product partial current density and acetate to acetaldehyde molar ratio observed over the bimetallic electrodes. The dotted line indicates the equilibrium constant of acetaldehyde hydration in water.*

6.6.27 Supplementary Information References

(1) Singh, M. R.; Bell, A. T. Design of an Artificial Photosynthetic System for Production of Alcohols in High Concentration from CO_2. *Energy Environ. Sci.* **2016**, *9* (1), 193–199.

(2) Kuhl, K. P.; Cave, E. R.; Abram, D. N.; Jaramillo, T. F. New Insights into the Electrochemical Reduction of Carbon Dioxide on Metallic Copper Surfaces. *Energy Environ. Sci.* **2012**, *5* (5), 7050–7059.

(3) Kuhl, K. P.; Hatsukade, T.; Cave, E. R.; Abram, D. N.; Kibsgaard, J.; Jaramillo, T. F. Electrocatalytic Conversion of Carbon Dioxide to Methane and Methanol on Transition Metal Surfaces. *J. Am. Chem. Soc.* **2014**, *136* (40), 14107–14113.

(4) Subramanian, P. R.; Perepesko, J. H. The Copper-Silver System. *J. Phase Equilibria* **1993**, *14* (1), 62–63.

(5) Krastev, E. T.; Voice, L. D.; Tobin, R. G. Surface Morphology and Electric Conductivity of Epitaxial Cu(100) Films Grown on H-Terminated Si(100). *J. Appl. Phys.* **1996**, *79* (9), 6865–6871.

(6) Jiang, H.; Klemmer, T. J.; Barnard, J. A.; Payzant, E. A. Epitaxial Growth of Cu on Si by Magnetron Sputtering. *J. Vac. Sci. Technol. B* **1998**, *16* (6), 3376–3383.

(7) Hofmann, T.; Yu, T. H.; Folse, M.; Weinhardt, L.; Bar, M.; Zhang, Y.; Merinov, B. V.; Myers, D. J.; Goddard, W. A.; Heske, C. Using Photoelectron Spectroscopy and Quantum Mechanics to Determine D-Band Energies of Metals for Catalytic Applications. *J. Phys. Chem. C* **2012**, *116* (45), 24016–24026.

(8) Hummelshøj, J. S.; Abild-Pedersen, F.; Studt, F.; Bligaard, T.; Nørskov, J. K. CatApp: A Web Application for Surface Chemistry and Heterogeneous Catalysis. *Angew. Chemie - Int. Ed.* **2012**, *51* (1), 272–274.

(9) Bard, A.; Faulkner, L. *Electrochemical Methods: Fundamentals and Applications*, 2nd ed.; John Wiley & Sons, Inc., 2002.

(10) Birdja, Y. Y.; Koper, M. T. M. The Importance of Cannizzaro-Type Reactions during Electrocatalytic Reduction of Carbon Dioxide. *J. Am. Chem. Soc.* **2017**, *139* (5), 2030–2034.

Chapter 7

Outlook

7.1 Conclusions

7.1.1 Detrimental Impact of Concentration Polarization

The CO evolution activity of polycrystalline Ag was found to be dependent on the hydrodynamics of the electrochemical cell, demonstrating that the measured activity of CO_2 reduction electrocatalysts is extremely sensitive to concentration polarization. This was hypothesized to be due to CO_2 depletion from the electrolyte near the cathode by both electrochemical reduction and reaction with hydroxyl anions evolved from the electrode surface, which produces electrochemically inert bicarbonate anions. To investigate this hypothesis a DEMS cell capable of sampling products directly from the electrode-electrolyte interface was developed and utilized to relate the depletion of CO_2 within the local reaction environment to the rate of CO evolution over polycrystalline Ag. While the local CO_2 concentration declined linearly with the rate of CO evolution at low overpotentials, the local CO_2 concentrations was depleted more than would be expected based on the rate of CO evolution at more cathodic potentials. This observation suggests that another mode of CO_2 consumption is prevalent at higher current densities, under which condition the magnitude of the concentration gradients at the electrode surface will become significant.

7.1.2 Enhancing Intrinsic Activity

The activation of CO_2 involves bending the C-O-C bond, resulting in the formation of a polarizable surface adsorbed carboxyl intermediate with a significant dipole moment.[1,2] The stability of this polarizable intermediate is sensitive to the magnitude of the local electric fields present near cations in the Helmholtz plane.[1,2] The magnitude of these local electric fields was hypothesized to be dependent on the surface charge density of the electrocatalyst. This hypothesis was investigated by conducting CO evolution over Ag thin films with different crystallographic orientations. The surface charge density of these different crystallographic orientations will vary at a fixed potential due to the differences in their potentials of zero charge and surface atom densities. Consistent with the hypothesis, we observed that the intrinsic activity of the Ag(110) thin film was superior to either Ag(111) or Ag(100). This occurs because the elevated surface charge

density results in the formation of stronger local electric fields at a given potential, consistent with the original hypothesis.

7.1.3 Enhancing Oxygenate Selectivity

Acetaldehyde was hypothesized to be an intermediate reaction product in the formation of ethanol over Cu because the concentration of acetaldehyde rapidly saturates during CO_2 reduction over Cu and because the electrochemical reduction of acetaldehyde yields ethanol over Cu.[3,4] This hypothesis was investigated using a DEMS cell capable of sampling products directly from the electrode-electrolyte interface. Using this instrument, acetaldehyde was found to be present within in the immediate vicinity of the Cu cathode despite being nearly absent from the bulk electrolyte. Furthermore, the relative abundance of ethanol near the cathode was much lower than that observed in the bulk electrolyte. These observations support the conclusion that acetaldehyde is an intermediate in the mechanism of ethanol formation over Cu.

The H_2 evolution activity of Cu must be suppressed to enhance the selectivity of CO_2 reduction to desired products. Theory shows that the H adsorption energy of Cu can be reduced by introducing compressive strain in the catalyst surface.[5] Ag has been observed to spontaneously form random substitutional surface alloys with Cu at room temperature, despite near complete bulk immiscibility.[6] Interestingly, the Ag atoms in these surface alloys possess fewer Ag nearest neighbors than expected from an ideal solution, indicating that the relatively large Ag atoms incorporated into the Cu surface induce compressive surface strain in the surrounding Cu surface atoms. Thus, it was hypothesized that CO_2 reduction over Cu+Ag surface alloys would exhibit superior selectivity to multi-carbon products than pure Cu due to a suppression of H_2 evolution. This hypothesis was investigated by conducting CO_2 reduction over Cu(100)+Ag surface alloys prepared by galvanic exchange. The results suggested that incorporating less than 4 atom. % Ag into the near-surface region of Cu results in a ~40% suppression in the rate of H_2 evolution during CO_2 reduction at an applied potential of -1 V vs RHE, thereby enhancing the multi-carbon product selectivity. Interestingly, the suppression of H_2 was found to increase the selectivity of multi-carbon carbonyl containing products, such as acetaldehyde. Since acetaldehyde is typically reduced further to ethanol over Cu, the results suggest that suppressing the H_2 evolution activity of Cu is a method for reducing the degree of hydrogenation of CO_2-derived products.

7.2 Future Work

7.2.1 Explaining the Incorporation of Solvent Oxygen into Oxygenated Products

It has recently been hypothesized that solvent water is incorporated into surface adsorbed intermediates that lead to the formation of multi-carbon oxygenated products.[7] This hypothesis was based on the observation that $C^{16}O$ reduction in $H_2{}^{18}O$ resulted in the formation of oxygenated products that contained both ^{16}O and ^{18}O. While the

hypothesis was supported by DFT calculations, the authors failed to consider alternative explanations that could explain their observations. It is highly probable that the oxygenated products containing both ^{16}O and ^{18}O observed by the authors are derived from acetaldehyde. Acetaldehyde forms a geminol diol in aqueous solutions, which upon dehydration will result in isotopic scrambling with solvent water. Therefore, a portion of all products derived from acetaldehyde would be expected to contain both ^{16}O and ^{18}O. Interestingly, the authors observed that ~60% of ethanol produced contained ^{18}O from the solvent water. This fraction is very close to the fraction of acetaldehyde that is expected to be hydrated in water, supporting the hypothesis that the observations were an artifact of the measurement with no intrinsic meaning. To validate the hypothesis, $C^{18}O$ reduction in $H_2{}^{16}O$ could be conducted using our DEMS cell capable of sampling products directly from the electrode-electrolyte interface. Observation of acetaldehyde near the cathode containing both ^{16}O and ^{18}O would support the hypothesis that the incorporation of solvent oxygen into oxygenated products occurs by isotopic scrambling with transiently produced acetaldehyde.

7.2.2 Elucidating the Mechanism of C_3 Product Formation

Our observation that the enhanced relative abundance of ethanol within the local reaction environment at more cathodic potentials comes at the cost of propionaldehyde led us to hypothesize that these products share a common intermediate. Since ethanol is believed to be derived from acetaldehyde, we hypothesize that acetaldehyde is a precursor to propionaldehyde as well. For this hypothesis to be correct, acetaldehyde or an acetaldehyde-derived intermediate should be capable of C-C coupling with a CO_2-derived intermediate. To probe this idea, the reduction of $^{13}CO_2$ should be conducted in the presence of unlabeled acetaldehyde. If C_3 products are observed with 2 ^{12}C and 1 ^{13}C then the hypothesis would be supported by direct experimental evidence. This would be a significant discovery since there is currently no understanding of the mechanism by which C3 product formation occurs on the surface of Cu-based electrocatalysts. If the mechanism were found to be general and applicable to primary aldehydes of increasing carbon number, then products like n-butanol could potentially be produced by CO_2 reduction. Furthermore, if the mechanism of C_3 product formation could be elucidated then electrocatalyst properties that favor the formation of higher order products could be identified.

7.3 References

(1) Chen, L. D.; Urushihara, M.; Chan, K.; Nørskov, J. K. Electric Field Effects in Electrochemical CO2Reduction. *ACS Catal.* **2016**, *6* (10), 7133–7139.

(2) Resasco, J.; Chen, L. D.; Clark, E.; Tsai, C.; Hahn, C.; Jaramillo, T. F.; Chan, K.; Bell, A. T. Promoter Effects of Alkali Metal Cations on the Electrochemical Reduction of Carbon Dioxide. *J. Am. Chem. Soc.* **2017**, *139* (32), 11277–11287.

(3) Bertheussen, E.; Verdaguer-Casadevall, A.; Ravasio, D.; Montoya, J. H.; Trimarco, D. B.; Roy, C.; Meier, S.; Wendland, J.; Nørskov, J. K.; Stephens, I. E. L.; et al. Acetaldehyde as an Intermediate in the Electroreduction of Carbon Monoxide to Ethanol on Oxide-Derived Copper. *Angew. Chemie - Int. Ed.* **2016**, *55* (4), 1450–1454.

(4) Schouten, K. J. P.; Kwon, Y.; van der Ham, C. J. M.; Qin, Z.; Koper, M. T. M. A New

Mechanism for the Selectivity to C1 and C2 Species in the Electrochemical Reduction of Carbon Dioxide on Copper Electrodes. *Chem. Sci.* **2011**, *2* (10), 1902–1909.
(5) Nørskov, J. K.; Bligaard, T.; Logadottir, A.; Kitchin, J. R.; Chen, J. G.; Pandelov, S.; Stimming, U. Trends in the Exchange Current for Hydrogen Evolution. *J. Electrochem. Soc.* **2005**, *152* (3), J23–J26.
(6) Sprunger, P. T.; Lægsgaard, E.; Besenbacher, F. Growth of Ag on Cu(100) Studied by STM: From Surface Alloying to Ag Superstructures. *Phys. Rev. B* **1996**, *54* (11), 8163–8171.
(7) Lum, Y.; Cheng, T.; Goddard, W. A.; Ager, J. W. Electrochemical CO Reduction Builds Solvent Water into Oxygenate Products. *J. Am. Chem. Soc.* **2018**.